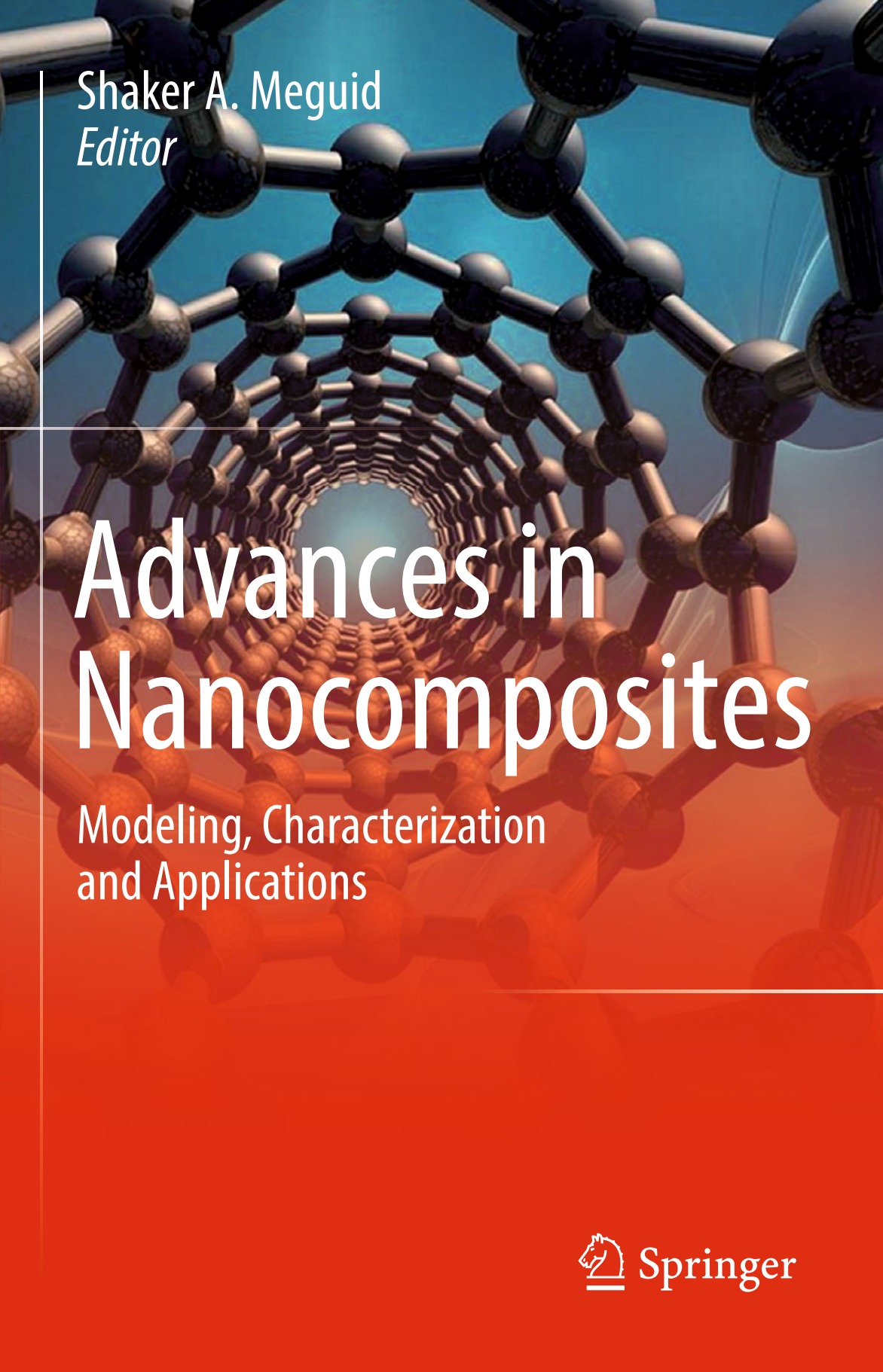
Shaker A. Meguid
Editor
Advances in Nanocomposites
Modeling, Characterization and Applications
Springer

Advances in Nanocomposites

Shaker A. Meguid
Editor

Advances in Nanocomposites

Modeling, Characterization and Applications

Springer

Editor
Shaker A. Meguid
Mechanics and Aerospace Design Laboratory
Department of Mechanical and Industrial Engineering
University of Toronto
Toronto, ON, Canada

ISBN 978-3-319-31660-4 ISBN 978-3-319-31662-8 (eBook)
DOI 10.1007/978-3-319-31662-8

Library of Congress Control Number: 2016941686

Printed on acid-free paper

This Springer imprint is published by Springer Nature
The registered company is Springer International Publishing AG Switzerland

Affectionately dedicated to Valerie Meguid
for her unlimited support
and encouragement!

Preface

Carbon nanotubes (CNTs) are lighter than aluminum, stronger than steel, and more thermally conductive than copper. Additionally, with their exceptionally large fracture strain and extremely high aspect ratio, CNTs have emerged as promising nano-particulate reinforcements that can be used to tailor the physical and mechanical properties of polymer. Due to their surface/volume ratio, nanoscopic size, and exceptional properties, it is believed that by suitably dispersing a few weight percentages of CNTs into a polymer, the physical and mechanical properties of that polymer can be significantly tailored leading to multifunctional *nanocomposites*. The unique property combinations that result from the dispersion and interactions between the properly dispersed CNTs, the interface, and the polymer provide greater opportunities for the development of novel material technologies to meet the challenges of the next century. Their applications have been demonstrated in electronic packaging, photonics, sensing, imaging, drug delivery, among others.

There are four reasons for the surge and interest in nanocomposites research. The first stems from the desire to tailor the electro-thermo-opto-mechanical properties of engineered materials to suit a specific application(s). The second from the desire to reduce our carbon print and ensure effective use of resources. The third from the current advances in computational nanomechanics and multiscale modeling. The fourth from the advances and the expanded efforts needed for conducting experiments at the nanoscopic level that would allow greater understanding of the CNT-polymer interactions.

This book is not an attempt to exhaustively cover all the relevant topics on nanocomposites. Instead, it is dedicated to recent developments in the field and the most exciting aspects of nanocomposites. It covers a range of topics that clearly demonstrate the depth, the diversity, and the breadth of this fertile area of research which is governed by size/scale, anisotropy, and morphology dependence of interacting phases that define the bulk properties of the resulting nanocomposites. It contains nine chapters authored/coauthored by some of the most talented and respected researchers in the community. Specifically, it covers multiscale modeling

of nanoreinforced composites (Chap. 1), piezoelectric response at nanoscale (Chap. 2), nanoscale mechanical characterization of 1D and 2D materials with application to nanocomposites (Chap. 3), effects of nano-porosity on the mechanical properties and applications of aerogels in composite structures (Chap. 4), smart fuzzy fiber-reinforced piezoelectric composites (Chap. 5), composite nanowires for room-temperature mechanical and electrical bonding (Chap. 6), recent developments of multiscale thermo-mechanical analysis of nanocomposites (Chap. 7), magnetoelectric coupling and overall properties of a class of multiferroic composites (Chap. 8), and snap-through buckling of micro/nanobeams in bistable micro/nanoelectromechanical systems (Chap. 9). In each chapter, the state of the art in the respective field and the future trends are covered and discussed.

This effort offers an up-to-date coverage of diverse but highly related topics on modeling, characterization, and applications of nanocomposites in a single volume. We believe that it is an excellent resource and it should be of interest to undergraduate and graduate physics and engineering students as well as researchers in academic institutions, government agencies, and industry specializing in material science, aerospace, electrical, biomedical, and mechanical engineering. We are confident that the readers will find the information covered in this book current, useful, and informative.

Finally, I wish to take this opportunity to express my gratitude to the authors for their outstanding contributions in addressing many of the exciting new concepts and developments in nanocomposites. Their informative efforts should guide both the experienced and the newcomers to this fascinating new area of research. I'm also indebted to my wife Valerie Meguid for her affectionate encouragement and support throughout the different stages of this effort.

Toronto, Canada Shaker A. Meguid

Contents

Contributors

Ahmed R. Alian Mechanics and Aerospace Design Laboratory, Department of Mechanical and Industrial Engineering, University of Toronto, Toronto, ON, Canada

Xue Chen Mechanics and Aerospace Design Laboratory, Department of Mechanical and Industrial Engineering, University of Toronto, Toronto, ON, Canada

Guillaume Colas Department of Mechanical and Industrial Engineering, University of Toronto, Toronto, ON, Canada

Yanbin Cui State Key Laboratory of Multiphase Complex System, Institute of Process Engineering, Chinese Academy of Sciences, Beijing, China

Tobin Filleter Department of Mechanical and Industrial Engineering, University of Toronto, Toronto, ON, Canada

Sunil C. Joshi School of Mechanical and Aerospace Engineering, Nanyang Technological University, Singapore, Singapore

Yang Ju Department of Mechanical Science and Engineering, Nagoya University, Nagoya, Japan

Zishun Liu International Center for Applied Mechanics, State Key Laboratory for Strength and Vibration of Mechanical Structures, Xi'an Jiaotong University, Xi'an, China

Shaker A. Meguid Mechanics and Aerospace Design Laboratory, Department of Mechanical and Industrial Engineering, University of Toronto, Toronto, ON, Canada

Teng Yong Ng School of Mechanical and Aerospace Engineering, Nanyang Technological University, Singapore, Singapore

Manas C. Ray Department of Mechanical Engineering, Indian Institute of Technology, Kharagpur, India

J.N. Reddy Department of Mechanical Engineering, Texas A&M University, College Station, TX, USA

V.U. Unnikrishnan Department of Aerospace Engineering and Mechanics, The University of Alabama, Tuscaloosa, AL, USA

G.U. Unnikrishnan Department of Mechanical Engineering, Texas A&M University, College Station, TX, USA

Yang Wang Department of Mechanical and Aerospace Engineering, Rutgers University, New Brunswick, NJ, USA

George J. Weng Department of Mechanical and Aerospace Engineering, Rutgers University, New Brunswick, NJ, USA

Jingjie Yeo A*STAR Institute of High Performance Computing, Singapore, Singapore

Jin Zhang Mechanics and Aerospace Design Laboratory, Department of Mechanical and Industrial Engineering, University of Toronto, Toronto, ON, Canada

Chapter 1
Multiscale Modeling of Nanoreinforced Composites

Ahmed R. Alian and Shaker A. Meguid

Abstract In this chapter, we present different multiscale modeling techniques to determine the elastic and interfacial properties of carbon nanotube (CNT)-reinforced polymer composites. The elastic properties of CNT-reinforced composite (hereinafter the "nanocomposite") are obtained in a two-step approach. First, at the nanoscale level, molecular dynamics (MD) and atomistic-based continuum (ABC) techniques are used to determine the effective elastic properties of a representative volume element (RVE) that is comprised of a nanofiller and its immediate surrounding. Second, at the microscale level, several micromechanics models and hybrid Monte Carlo finite-element (FE) simulations are used to determine the bulk properties of nanocomposite. The interfacial properties are determined through pullout test using MD and ABC techniques. The effect of length, diameter, agglomeration, waviness, defects, and orientation of CNTs on the elastic and interfacial properties of nanocomposites is also investigated. The development of multiscale modeling and the proper selection of simulation parameters are discussed in detail. The results of several studies are presented and compared to show the inherited limitations in each technique.

1.1 Introduction

CNTs are lighter than aluminum (density $\sim$1.4 g/cm^3; Iijima 1991; Gao et al. 1998), are stronger than steel (Young's modulus $>$1 TPa; Treacy et al. 1996; Krishnan et al. 1998; Shen and Li 2004), have large fracture strain (Wong et al. 1997; Yu et al. 2000) and high aspect ratio (Qian et al. 2000), and are more thermally conductive than copper ($>$2500 W/mK; Hone et al. 1999; Yang 2005; Awad and Ladani 2015). Due to these remarkable properties, CNTs have emerged as a promising reinforcement for polymer-based nanocomposites (Li and Chou 2003a; Shen and Li 2004; Tsai et al. 2010). It is believed that few weight percentages of

A.R. Alian • S.A. Meguid (✉)
Mechanics and Aerospace Design Laboratory, Department of Mechanical and Industrial Engineering, University of Toronto, Toronto, ON, Canada, M5S 3G8
e-mail: arowaey@mie.utoronto.ca; meguid@mie.utoronto.ca

S.A. Meguid (ed.), *Advances in Nanocomposites*,
DOI 10.1007/978-3-319-31662-8_1

CNTs can significantly improve the mechanical, thermal, and physical properties of their nanocomposites (Coleman et al. 2006a; Spitalsky et al. 2010; Rahmat and Hubert 2011).

Several experimental studies have been carried out to study the mechanical properties of nanocomposites. An earlier attempt was made by Schadler et al. (1998) to measure the mechanical properties of nanocomposite under tension and compression loadings. They reported that the compression modulus is higher than that of the tensile modulus, indicating the load transfer to CNTs from the matrix is higher in compression. Allaoui et al. (2002) managed to double Young's modulus and yield strength of the nanocomposite by adding 1 and 4 wt% of multiwalled CNTs, respectively, compared to the pure epoxy matrix. Uniform dispersion of CNTs resulted in a 250–300 % increase in the storage modulus of epoxy nanocomposite at 20–30 wt% of CNTs due to the strong interfacial bonding between CNTs and epoxy resin (Gou et al. 2004). Qian et al. (2000) investigated the load transfer in multiwalled CNT–polystyrene composites and reported an increase in the tensile modulus and strength by ∼39 and 25 %, respectively, at 1 wt% of CNTs. Meguid and Sun (2004) showed that the homogeneous dispersion of CNTs in the epoxy matrix can improve the tensile and shear strengths of the resulting synthesized nanocomposite. However, at higher CNT concentrations, the mechanical properties of the nanocomposite were found to deteriorate due to the formation of CNT agglomerates, which act as stress concentrators. The multifunctionality of nanocomposites was also investigated experimentally. For example, Park et al. (2002) synthesized a polyimide composite reinforced with CNTs and reported improved mechanical, thermal, electrical, and optical properties.

The mechanical performance of nanocomposites is significantly influenced by the interfacial cohesion between the CNT and the surrounding matrix. Higher interfacial shear strength (ISS) is an indicator of better stress transfer from the polymer matrix to the embedded CNTs and hence an enhanced reinforcement effect (Desai and Haque 2005). Several experimental studies used direct methods such as pullout test and indirect methods such as fragmentation test and Raman spectroscopy to investigate the interfacial characteristics of nanocomposites. For instance, Wagner et al. (1998) estimated the interfacial shear stress between the multiwalled CNTs and the polymer based on the fragmentation test to be as high as 500 MPa, which is more than one order of magnitude compared to the conventional composites. Micro-Raman spectroscopy was used by Ajayan et al. (2000) to measure the local mechanical behavior of single-walled CNT bundles in the epoxy nanocomposite. They noticed that the efficiency of stress transfer and hence the enhancement of the mechanical properties is lower than expected due to the sliding of CNTs within the bundle. Cooper et al. (2002) used scanning probe microscope tip to pull out individual single- and multiwalled CNT ropes from epoxy matrix. The ISS of both the cases was found in the range of 35–376 MPa. This relatively high value of the ISS was attributed to the formation of strong ultrathin epoxy layer at the interface. This layer exits as a result of the formation of covalent bonds between CNTs and the surrounding polymer molecules, which originate from the defects on the CNTs.

The efficiency of CNTs in reinforcing the matrix depends on several parameters such as chirality, aspect ratio, defects, alignment, degree of waviness, chemical functionalization, agglomeration, and aggregation in the prepared nanocomposite system (Gojny et al. 2005; Coleman et al. 2006b; Wang et al. 2012). A significant number of experimental and numerical studies have been conducted so far to study the influence of these parameters on the mechanical performance of nanocomposites. Due to the atomic nature of CNTs, we cannot use the existing analytical and numerical techniques of traditional reinforced fiber composites for studying the mechanical properties of nanocomposites (Zeng et al. 2008). In nanocomposites, the bonding between the embedded CNTs and the polymer originates mainly from the weak nonbonded van der Waals (vdW) and Coulombic interactions (Han and Elliott 2007). However, chemical functionalization of CNTs can introduce some strong interfacial covalent bonds between the nanotube walls and the polymer chains leading to a stronger nanocomposite (Xiao et al. 2015). Due to these inherited limitations in conventional modeling techniques of composite materials, different multiscale modeling techniques were developed to address the length scale effect and to determine the effective properties of nanocomposites.

In general, multiscale modeling of nanocomposites is carried out in two stages, as shown in Fig. 1.1 (Wernik 2013). The first stage usually addresses different issues related to the atomic structure of CNTs and the surrounding polymer at the nanoscale level. Mainly, MD simulations and ABC modeling technique are used in the first stage. Because of the nonbonded interactions between the CNT and the matrix and the formation of a strong ultrathin polymer layer at their interface, a representative volume element (RVE) is needed to capture the interfacial and mechanical properties of the resulting nanocomposite (Alian et al. 2015a). The results of the atomistic simulations are then used as an input to the second stage. Analytical and numerical micromechanical techniques are used in the second stage to determine the bulk properties of the nanocomposite (Wernik and Meguid 2014). The RVE from the first stage is used here as an equivalent effective fiber embedded in the bulk matrix.

In this chapter, we cover the basics of multiscale modeling techniques utilized for CNT-reinforced composites. In particular, the application of each model in studying the elastic and interfacial properties is presented. The results predicted by

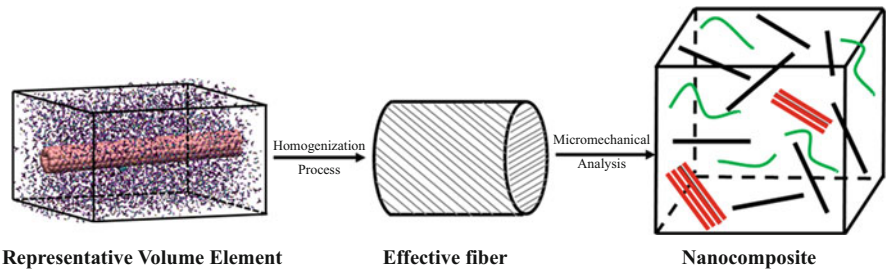

Fig. 1.1 Modeling steps involved in the multiscale model

multiscale models have been validated with those of experimental data reported in the literature. The influence of CNT morphology and dispersion on the interfacial and mechanical properties is investigated to determine the best method to prepare nanocomposites with optimal properties. The effect of CNT dispersion is investigated considering the two cases: aligned and randomly distributed CNTs, while the effect of agglomeration is investigated by considering CNT bundles of different sizes. CNTs with different curvatures are modeled as well to study the effect of their waviness on the mechanical behavior of nanocomposites. The results of the conducted investigations are presented and compared to show the inherited limitations in each modeling technique.

This chapter is organized as follows. Following this Introduction, the basics of MD and its applications in nanocomposites are described in Sect. 1.2. The basics of ABC technique and its application in determining the elastic and interfacial properties of nanocomposites are presented in Sect. 1.3. The micromechanical procedure based on Mori–Tanaka technique is reviewed and subsequently used to study the effect of CNT agglomeration, waviness, and dispersion on the bulk properties of nanocomposite in Sect. 1.4. Finally, Monte Carlo method and FE technique are then combined in Sect. 1.5 as an alternative method to Mori–Tanaka technique. Numerical and analytical results are presented for each modeling technique at the end of each section.

1.2 Molecular Modeling

MD simulations offer an appropriate and effective means to deal with large nanoscale systems and relatively longer simulation times compared to density functional theory (DFT) simulations and have been extensively used for determining the interfacial and mechanical properties of nanocomposites. MD has been also a very valuable tool for studying the effect of CNT agglomeration, waviness, aspect ratio, defects, and functionalization on the mechanical behavior of nanocomposites. For example, Frankland et al. (2003a) used MD simulations to calculate the longitudinal and transverse Young's moduli of polymer nanocomposite reinforced with long and short CNTs. Grujicic et al. (2007) studied the effect of chemical functionalization on the mechanical properties of multiwalled CNT–vinyl ester epoxy composites using MD simulations. Their results showed that introducing covalent bonds between CNTs and the surrounding polymer results in significant improvements in the transverse elastic properties of the nanocomposite. Alian et al. (2015b) studied the effect of CNT agglomeration on the elastic properties of CNT–epoxy composites by modeling different RVEs reinforced with bundles of CNTs. Their results showed that the CNT agglomerates dramatically reduce the effective properties of epoxy nanocomposites.

1.2.1 Basics of MD Simulations

MD is a computational method that was firstly introduced into theoretical physics by Alder and Wainwright (1957) to simulate elastic collisions between hard spheres. Since then, MD has become an important and attractive computational tool for many research fields including chemical physics, biochemistry, and materials science. MD allows to study relatively large molecular systems that cannot be simulated using quantum mechanics-based techniques such as DFT and ab initio approaches due to the enormous computational cost (Srivastava et al. 2003). The main purpose of MD simulations is to simulate the time-dependent behavior of the system by calculating the current and future position and velocity of each atom using Newton's equations of motion. This information can be used later to calculate the averaged mechanical, physical, and thermal properties of the system (van Gunsteren and Berendsen 1990).

The initial position and velocity of each atom of the system must be known at the beginning of the MD simulation. This initial data is randomly generated based on statistical mechanics and the required average temperature of the system. Then, the trajectories of the atoms are determined by solving the Newton's equations of motion of the interacting atoms of the system:

$$\vec{F}_i = m_i \, \vec{a}_i \tag{1.1}$$

where $\vec{F}_i$, m_i, and $\vec{a}_i$ are the acting force, mass, and acceleration of atom i, respectively. The interatomic forces are the gradient of the total potential energy, V, of the system:

$$\vec{F}_i = -\nabla V\left(\vec{r}\right) \tag{1.2}$$

The velocity, $\vec{v}_i$, and displacement vector, $\vec{r}_i$, of each atom are the first and second derivatives of the acceleration:

$$\vec{a}_i = \frac{d\vec{v}_i}{dt} \tag{1.3}$$

$$\vec{v}_i = \frac{d\vec{r}_i}{dt} \tag{1.4}$$

Using Eqs. (1.1), (1.3), and (1.4), we obtain the following differential equation:

$$-\nabla V\left(\vec{r}\right) = m_i \frac{d^2\vec{r}_i}{dt^2} \tag{1.5}$$

The most popular algorithm to integrate the resulting equations of motion of the system is the Verlet algorithm (Verlet 1967). In this algorithm, Newton's equations of motion are approximated by a Taylor series expansion as a time series:

$$r(t+\delta t) = r(t) + v(t)\,\delta t + \frac{1}{2}a(t)\,\delta t^2 + \frac{1}{6}\frac{d^3r(t)}{dt^3}\,\delta t^3 + \mathrm{O}\left(\delta t^4\right) \tag{1.6}$$

$$r(t-\delta t) = r(t) - v(t)\,\delta t + \frac{1}{2}a(t)\,\delta t^2 - \frac{1}{6}\frac{d^3r(t)}{dt^3}\,\delta t^3 + \mathrm{O}\left(\delta t^4\right) \tag{1.7}$$

Adding the above two equations and moving the $r(t-\delta t)$ term to the right-hand side, we obtain

$$r(t+\delta t) = 2r(t) - \mathrm{r}(t-\delta t) + a(t)\,\delta t^2 + \mathrm{O}\left(\delta t^4\right) \tag{1.8}$$

This is the general form of the Verlet algorithm for MD, where δt is the time step of the analysis; accuracy significantly increases with the decrease in this time step because it is a function of the fourth order of δt. The value of $a(t)$ is determined from Eq. (1.5), which depends on the location of the atom. Here, we use the positions from the previous and current time steps and acceleration of the current step to predict the trajectory of the atom. The instantaneous velocity $v(t)$ of each atom can be later calculated using Taylor series expansion, as follows:

$$v(t) = \frac{r(t+\delta t) - r(t-\delta t)}{2\delta t} + \mathrm{O}\left(\delta t^3\right) \tag{1.9}$$

The accuracy of the velocity is a function of δt^3 implying that it has lower accuracy than the position which is a function of δt^4. The kinetic energy $K(t)$ and the averaged instantaneous temperature T of the system, based on the equipartition theory, can be calculated using the obtained velocities using the following relations:

$$K(t) = \frac{1}{2}\sum\nolimits_i m_i\,(v_i(t))^2 \tag{1.10}$$

$$T(t) = \frac{2}{3}\frac{K(t)}{N\,K_\mathrm{B}} \tag{1.11}$$

where K_B is the Boltzmann constant. The averaged stress tensor of the MD unit cell is defined in the form of virial stress (Zhou 2003), as follows:

$$\sigma = \frac{1}{V}\sum\nolimits_{i=1}^{N}\left(\frac{m_i}{2}{v_i}^2 + F_i\,r_i\right) \tag{1.12}$$

where V is the volume of the MD unit cell and v_i, m_i, r_i, and F_i are the velocity, mass, position, and force acting on the ith atom, respectively.

The total potential energy of the system can be defined by interatomic potentials or molecular mechanics force fields which describe how the atoms interact with each other (LeSar 2013). The selected interatomic potential or force field for the system under investigation must be very accurate for the quantum mechanical process and to yield reliable results. These potentials and force fields have been developed by several researchers based on quantum mechanics calculations and then validated by comparing their results with experimental tests (Brenner 2000; LeSar 2013). The general expression for the total atomistic potential energy of the system can be written as a many-body expansion that depend on the position of one, two, three atoms or more at a time (LeSar 2013):

$$V\left(\vec{r}_1, \vec{r}_2, \ldots, \vec{r}_N\right) = \sum_i^N V_1\left(\vec{r}_i\right) + \sum_{i,j}^N V_2\left(\vec{r}_i, \vec{r}_j\right) + \sum_{i,j,k}^N V_3\left(\vec{r}_i, \vec{r}_j, \vec{r}_{ik}\right) + \ldots \tag{1.13}$$

where V_1 is the one-body term (energy of the isolated atom i due to an external force field such as the electrostatic force), V_2 is the two-body term (pairwise interactions of the atoms i and j such as Lennard–Jones potential (Jones 1924)), V_3 is the three-body term (three-body interactions and usually called many-body interactions such as Tersoff and Brenner potentials), N is the number of atoms in the system, and $\vec{r}_i$ is the position vector of atom i (Tersoff 1988; Brenner 1990). However, most of the polymeric systems need a more generalized interatomic potential which is mainly defined based on geometrical parameters such as bond lengths, angles, and rotation. To tackle this problem, many force fields were developed (LeSar 2013). The total energy in force fields consists of two parts: the first one is concerned with the bonded interactions of the covalently bonded atoms, and the second is concerned with the nonbonded interactions originating from the relatively weak long-range electrostatic and vdW forces:

$$V = \underbrace{\sum V_r + \sum V_\theta + \sum V_\varphi}_{V_{\text{bonded}}} + \underbrace{\sum V_{\text{vdW}} + \sum V_{\text{elec}}}_{V_{\text{non-bonded}}} \tag{1.14}$$

where V_r term is for oscillations about the equilibrium bond length (i.e., bond stretching), V_θ term is for oscillations of 3 atoms about an equilibrium bond angle (i.e., bond angle bending), V_φ term is for torsional rotation of 4 atoms about a central bond (i.e., dihedral angle torsion), V_{vdW} term is for a nonbonded vdW interactions, and V_{ele} term is for a nonbonded electrostatic interactions (Li and Chou 2003a). The components of the potential energy due to the bonded interactions are shown in Fig. 1.2.

All MD simulations are being conducted under specified conditions. These ensembles are characterized by fixed values of the following thermodynamic variables: potential energy, temperature, pressure, volume, and total number of particles. The most commonly used ensembles in MD simulations are:

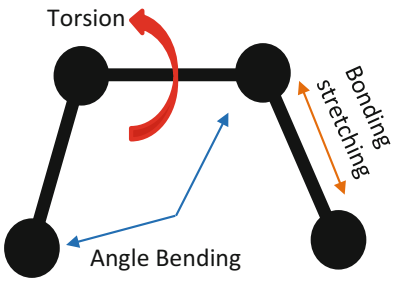

Fig. 1.2 Schematic of both bonded and nonbonded interactions between the atoms of a small molecule

- Micro-canonical ensemble: constant number of atoms, volume, and energy (*N*,*V*,*E*)
- Isothermal–isobaric ensemble: constant number of atoms, temperature, and pressure (*N*,*T*,*P*)
- Canonical ensemble: constant number of atoms, temperature, and volume (*N*,*V*,*T*)

There is a common sequence that can be followed to build an MD model and perform a successful simulation. The first step is to build the initial structure of the system using software such as NanoEngineer, Materials Studio, Packmol, etc. This step consumes a significant time of the work as it usually requires the building of small units of the system and dispersing them in a large MD unit cell. The second step is to minimize the structure by changing the initial location of the atoms to reduce the total potential energy of the system and to relieve the residual stresses. The third step is assigning an initial velocity to each atom based on the targeted average temperature of the system. The fourth is to equilibrate the minimized structure to obtain the system at targeted initial conditions (pressure, volume, temperature). Finally, conducting the required analysis and measuring the system properties of interest.

1.2.2 Modeling of Nanocomposite and Its Constituents

In this section, we will present modeling of CNTs, epoxy, and nanocomposites using MD simulations (see Fig. 1.3). The main objective is to obtain the atomic-level elastic and interfacial properties of the nanocomposite. All MD simulations will be performed with large-scale atomic/molecular massively parallel simulator (LAMMPS; Plimpton 1995) using either the consistent valence force field (CVFF; Dauber-Osguthorpe et al. 1988) or the adaptive intermolecular reactive bond order (AIREBO) potential (Stuart et al. 2000). CVFF has been used successfully by several researchers to predict the mechanical properties of CNTs, epoxy polymers, and CNT–epoxy composites (Alian et al. 2015b; Li et al. 2012; Tunvir et al. 2008). AIREBO has been also used by many researchers for CNTs, hydrocarbons, and polymers consisting of only carbon and hydrogen such as polyethylene (Coluci et al. 2007; Zang et al. 2009). Conjugate gradient algorithm is used to minimize the total potential energy of the initial configurations. The structure is considered to be optimized once the change in the total potential energy of the system between

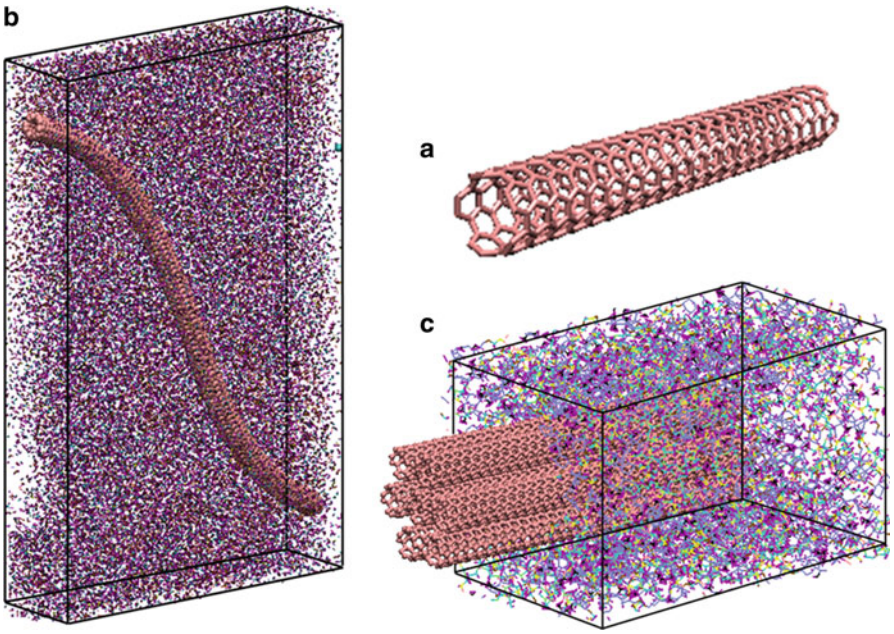

Fig. 1.3 Molecular structures of (**a**) (5,5) armchair CNT, (**b**) RVE consists of SWCNT embedded in polymer, and (**c**) pullout of CNT bundle from epoxy matrix

subsequent steps is less than 1.0×10^{-10} kcal/mol. Velocity Verlet algorithm is used to integrate the equations of motion in all MD simulations. Periodic boundary conditions are imposed on all directions of the MD unit cells. The cutoff distance for the nonbonded interaction is set to 14.0 Å (Haghighatpanah and Bolton 2013).

1.2.2.1 Modeling of CNTs

In this section, MD simulations are conducted to determine the elastic properties of pristine SWCNTs using AIREBO interatomic potential. The effect of CNT diameter size on its mechanical properties is investigated considering different armchair SWCNTs, with diameter ranging from ~6 to ~35 Å, as shown in Fig. 1.4.

The transversely isotropic elastic moduli of the armchair CNTs are determined using the strain energy density–elastic constant relations. The following four loading conditions are imposed on the CNT: axial tension for axial Young's modulus (E_1) and major Poisson's ratio (ν_{12}), torsional moment for axial shear modulus (G_{12}), in-plane biaxial tension for plane strain bulk modulus (K_{23}), and in-plane shear for in-plane shear modulus (G_{23}). Schematic representations of these loading conditions are depicted in Fig. 1.5. The equations written underneath the figures indicate the respective strain energy densities (U) stored in the CNT due to the applied strain.

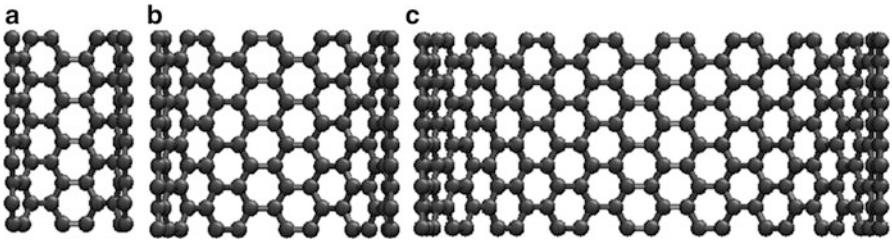

Fig. 1.4 Schematics of different CNTs adopted in the study: (**a**) (5, 5) CNT, (**b**) (10, 10) CNT, and (**c**) (20, 20) CNT

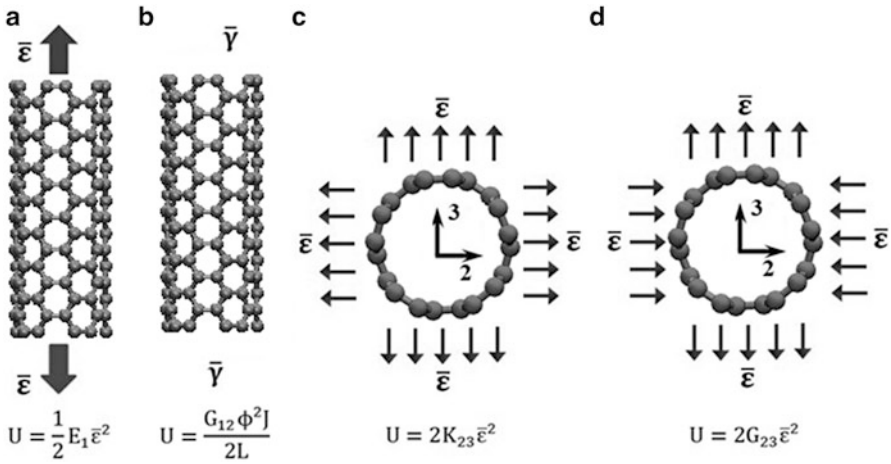

Fig. 1.5 Loading conditions used to determine the elastic constants of the CNT: (**a**) tensile, (**b**) twist, (**c**) in-plane biaxial tension, and (**d**) in-plane shear

The equivalent-continuum structure of a CNT is assumed to be annular cylinder by considering its effective wall thickness as 3.4 Å (Hao et al. 2008), and its area is determined as $A = 2\pi rt$, where r is the outer radius of the CNT and t is its wall thickness. The sequence of the MD simulations is as follows: first, the initial structures of the generated CNTs are first optimized using the conjugate gradient algorithm to obtain the nanotube configurations of minimum energy. Subsequently, the minimized structures of the CNTs are equilibrated for 50 ps in the constant temperature and volume canonical (NVT) ensemble using a 0.5 fs time step at 300 K. Then, a defined strain increment of 0.1 % is applied to the CNTs followed by potential energy minimization. During each loading step, one end of the CNT is fixed, while a prescribed load/displacement is applied to the other end. In case of axial tension, an incremental axial displacement is applied to the top end. In case of twisting moment, an incremental tangential displacement was applied to the top end while constraining its motion in the radial direction to maintain the presumed

cylindrical shape of the CNT. In case of in-plane biaxial tension, all atoms of the CNT were subjected to two-dimensional plane strain condition by axially constraining the two ends of the CNT. In case of in-plane shear condition, the CNT is subjected to in-plane shear in such a way that its circular cross section deforms into an elliptical shape. Finally, this loading step is repeated until the strain reaches up to 3 %. Under each strain increment, the change in potential energy that is equivalent to the stored strain energy in the CNTs is used to determine the elastic properties based on the relation between the deformation energy density and the elastic constants.

Five types of armchair CNTs (5, 5), (10, 10), (15, 15), (20, 20), and (25, 25) are considered in the current analysis to study the effect of nanotube diameter on the elastic moduli of CNTs. The MD results show that the elastic coefficients of the CNTs decrease as the diameter of a CNT increases (see Fig. 1.6a–d).

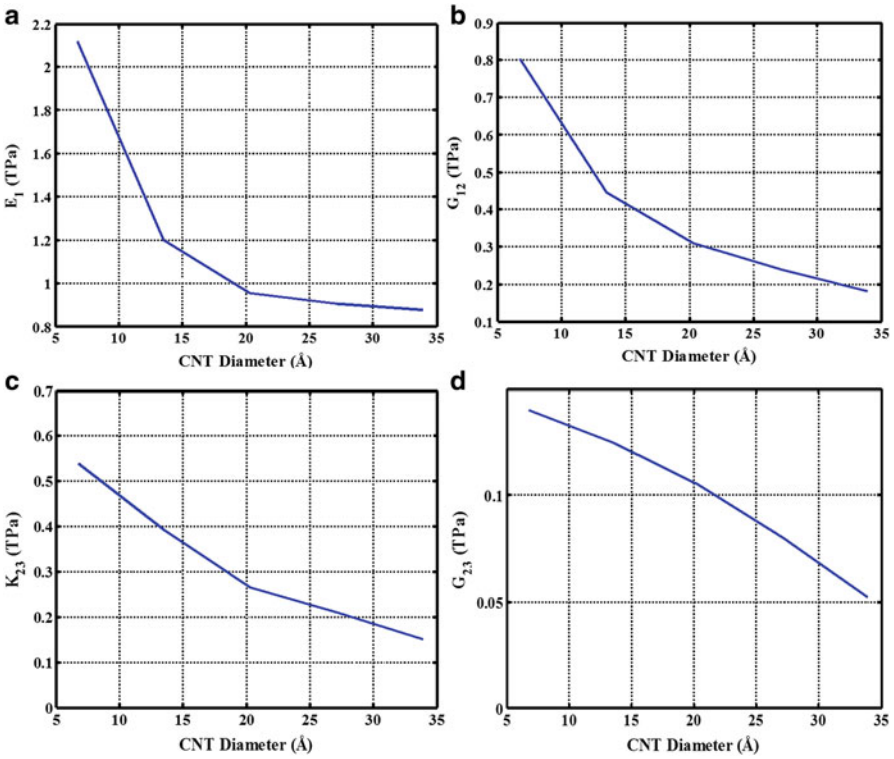

Fig. 1.6 Effect of vacancy defects on (**a**) axial Young's modulus, (**b**) axial shear modulus, (**c**) plane strain bulk modulus, and (**d**) in-plane shear modulus of (5,5) armchair CNT

1.2.2.2 Modeling of Pure Epoxy

MD simulations are conducted to determine the isotropic elastic moduli of epoxy material using CVFF. We will model a specific two-component epoxy material based on diglycidyl ether of bisphenol A (DGEBA) epoxy resin and triethylenetetramine (TETA) curing agent, which is typically used in the aerospace industry (see Fig. 1.7). The volumetric bulk (K) and shear (G) moduli of the epoxy will be determined by applying volumetric and three-dimensional shear strains, respectively.

During the curing process, the hydrogen atoms in the amine groups of the curing agent react with the epoxide groups of the resin forming covalent bonds, which result in a highly cross-linked epoxy structure. The resin/curing agent weight ratio in the epoxy polymer was set to 2:1 in order to achieve the best elastic properties (Wernik 2013). The cross-linked polymer structure consisted of 80 DGEBA molecules cross-linked with 40 molecules of curing agent TETA. The cross-linked structure was utilized to form a 3D structure of epoxy. This structure was then used to build the epoxy system in the subsequent MD simulations of both neat epoxy and CNT–epoxy composite.

The neat epoxy model was generated by randomly placing 5 cross-linked structures in a cubic simulation box of size 150 Å × 150 Å × 150 Å to form a system containing ~25,000 atoms, as shown in Fig. 1.8a. The MD unit cell was compressed gradually to the targeted dimensions of 60 Å × 60 Å × 60 Å through 25 consecutive steps. At each compression step, the atoms coordinates were remapped to fit inside the compressed box, and then the updated structure was optimized by minimizing its potential energy to obtain a relaxed configuration, as shown Fig. 1.8b.

The optimized system was then equilibrated at room temperature in the constant temperature and volume canonical (NVT) ensemble over 200 ps using a 0.5 fs time step at 300 K. The compressed system was equilibrated for another 200 ps in the isothermal–isobaric (NPT) ensemble at 300 K and 1 atm to generate an epoxy system with the correct density. This equilibration step resulted in an equilibrated amorphous structure with an average density of 1.1 g/cm^3. At the end, the structure is again equilibrated for another 200 ps in the NVT ensemble at 300 K. In order to

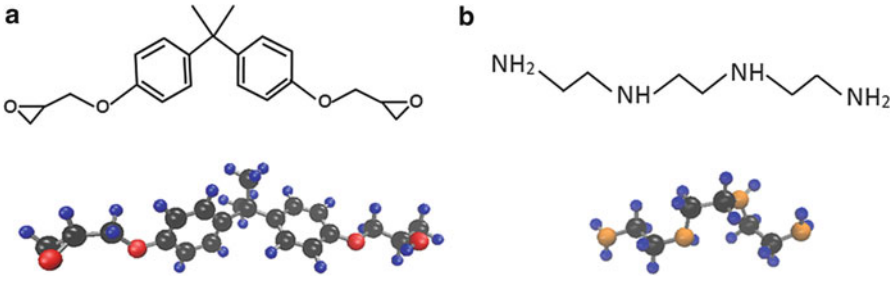

Fig. 1.7 Molecular structures of (**a**) epoxy resin (DGEBA) and (**b**) curing agent (TETA)

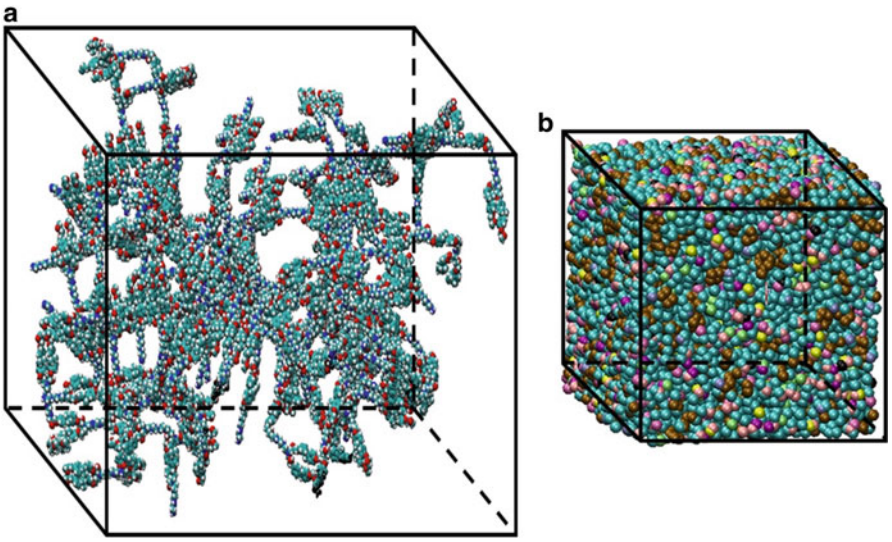

Fig. 1.8 The simulation box containing 400 chains of DGEBA and 200 chains of TETA (**a**) placed randomly in a simulation box of size 150 Å × 150 Å × 150 Å and (**b**) equilibrated after being compressed into a cube of size 60 Å × 60 Å × 60 Å

determine the bulk modulus of the epoxy, the simulation box was volumetrically strained in both tension and compression by applying equal uniform strains along the three axes. The bulk modulus was calculated by

$$K = \frac{\sigma_h}{\varepsilon_v} \tag{1.15}$$

where ε_v and σ_h are the volumetric strain and the averaged hydrostatic stress, respectively. In order to determine the average shear modulus, equal shear strains were applied on the simulation box in *xy*, *xz*, and *yz* planes. The shear modulus was calculated by

$$G = \frac{\tau_{ij}}{\gamma_{ij}}, \quad i \neq j \tag{1.16}$$

where τ_{ij} and γ_{ij} denote the averaged shear stress and shear strain, respectively. In each loading case, strain increments of 0.25 % were applied along a particular direction by uniformly expanding or shearing the simulation box and updating the atoms coordinates to fit within the new dimensions. After each strain increment, the MD unit cell was equilibrated using the NVT ensemble at 300 K for 10 ps. Then, the stress tensor is averaged over an interval of 10 ps to reduce the effect of fluctuations. These steps were repeated again in the subsequent deformation increments. The procedure was stopped when the total strain reached up to 2.5 %.

Table 1.1 Elastic moduli of the epoxy material

	Young's modulus (GPa)	Shear modulus (GPa)	Bulk modulus (GPa)	Poisson's ratio
MD simulations	3.2	1.1	4.8	0.39
Experimental work (Littell et al. 2008)	2.9	1.07	3.3	0.35

Based on the calculated bulk and shear moduli, Young's modulus (E) and Poisson's ratio (ν) were determined as follows:

$$E = \frac{9KG}{3K + G} \quad \text{and} \quad \nu = \frac{3K - 2G}{2(3K + G)} \tag{1.17}$$

The predicted elastic properties of the epoxy from the conducted MD simulations are found to be consistent with the experimentally measured moduli of a similar epoxy, as summarized in Table 1.1 (Littell et al. 2008).

1.2.2.3 Modeling of CNT–Epoxy Interface

The structure of the polymer matrix at the vicinity of the CNT surface differs from the bulk polymer far from the interface due to the formation of an ultrathin polymer layer at the CNT–epoxy polymer (Cooper et al. 2002). This ultrathin layer consists of a highly packed crystalline polymer, which has higher elastic properties than the amorphous bulk polymer (Coleman et al. 2004). In this section, the interface thickness of the CNT–epoxy composites will be determined using MD simulations. In order to obtain the actual CNT–epoxy properties using multiscale modeling technique, the size of the RVE must be large enough to incorporate the interface layer. Armchair (5,5) CNT of length 76 Å is used in the present study. Interface thickness is an important parameter in calculating the actual volume fraction of CNTs in composite. The cylindrical molecular structure of the (5,5) SWCNT is treated as an equivalent solid cylindrical fiber (Kundalwal and Ray 2012; Thostenson and Chou 2003) for determining its volume fraction in the nanocomposite RVE:

$$v_{\text{CNT}} \cong \frac{f_n N_{\text{CNT}} \pi (D_{\text{CNT}} + h_{\text{vdW}})^2 L_{\text{CNT}}}{4V_{\text{cell}}} \tag{1.18}$$

where D_{CNT} and L_{CNT} denote the respective diameter and length of a CNT, h_{vdW} is the vdW equilibrium distance between a CNT and the surrounding polymer matrix, N_{CNT} is the number of CNTs in the bundle, f_n is a factor based on the shape of the bundle of CNTs, and V_{cell} is the volume of the RVE.

In order to determine the thickness of the interface layer, we performed MD simulations for a system consisting of a CNT surrounded by epoxy structures using

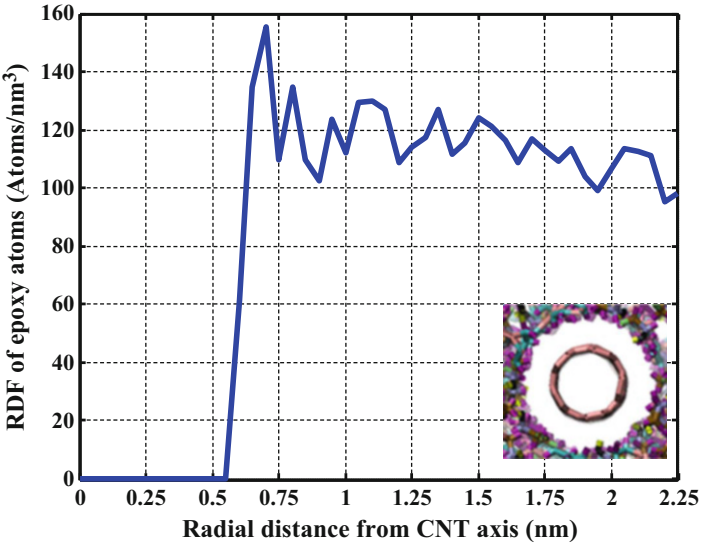

Fig. 1.9 RDF of the epoxy atoms around the embedded CNT

the same steps as adopted in the pure epoxy case without any further chaining between the epoxy molecules. This approach does not address how the interfacial layer thickness changes with the epoxy chain growth during reaction curing, but we can determine the average interfacial layer thickness when the MD system reaches an equilibrium state. Figure 1.9 shows the radial distribution function (RDF) of the epoxy atoms surrounding the embedded CNT after the equilibration. The variation of the RDF along the radial direction represents the change of the epoxy structure in the vicinity of the embedded CNT. It may be observed from Fig. 1.9 that the RDF of the epoxy atoms is zero at a radial distance of 0.56 nm and reaches its maximum value of 160 atoms/nm^3 at the radial distance of 0.77 nm. Then, it starts to fluctuate around an average value of 110 atoms/nm^3. This result indicates that the value of the vdW equilibrium distance h_{vdW} is ∼2.75 Å and the thickness of CNT–epoxy matrix interface layer is ∼3.0 Å. The obtained values of the interfacial layer thickness and the equilibrium separation distance were used to select the appropriate RVE sizes for MD simulations of nanocomposites in the next section.

1.2.2.4 Modeling of Nanocomposite Containing Agglomerated CNTs

CNTs have a tendency to agglomerate and aggregate into bundles due to poor dispersion of CNTs and their high surface energy and surface area (Dumlich et al. 2011). The presence of CNT agglomerates and aggregates deteriorates the interfacial properties of the nanocomposite resulting in limited stress transfer and load sharing (Alian et al. 2015b). Therefore, the issue of agglomeration of CNTs

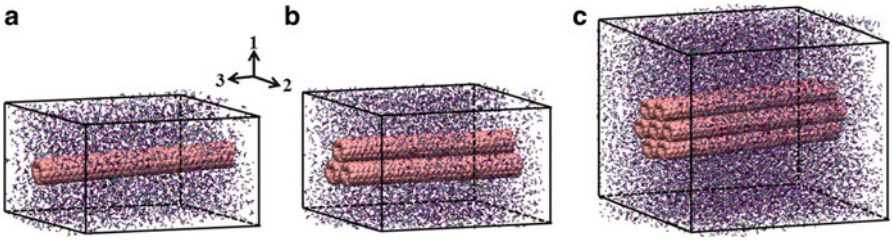

Fig. 1.10 MD unit cells containing a (**a**) single CNT, (**b**) bundle of three CNTs, and (**c**) bundle of seven CNTs

needs to be addressed. The effect of agglomeration is investigated by modeling RVEs reinforced with CNT bundles of different sizes. Three RVEs are constructed to represent an epoxy matrix containing a (1) single CNT, (2) bundle of three CNTs, and (3) bundle of seven CNTs (see Fig. 1.10). Each RVE will be used as an effective fiber in the micromechanical model to calculate the effective elastic moduli of the nanocomposite at the microscale level, as shown in Fig. 1.1. All MD simulations are conducted using CVFF force field.

The initial distance between the adjacent CNTs in the bundle was taken to be 3.4 Å, which is equivalent to the intertube separation distance in multiwalled CNTs. The RVEs are assumed to be transversely isotropic with the 3-axis being the axis of symmetry. Therefore, only five independent material constants are required to fully define the elastic stiffness matrix. The constitutive relationship of the transversely isotropic RVE is given by

$$\begin{bmatrix} \sigma_{11} \\ \sigma_{22} \\ \sigma_{33} \\ \sigma_{23} \\ \sigma_{13} \\ \sigma_{12} \end{bmatrix} = \begin{bmatrix} C_{11} & C_{12} & C_{13} & 0 & 0 & 0 \\ C_{12} & C_{11} & C_{13} & 0 & 0 & 0 \\ C_{13} & C_{13} & C_{33} & 0 & 0 & 0 \\ 0 & 0 & 0 & C_{44} & 0 & 0 \\ 0 & 0 & 0 & 0 & C_{44} & 0 \\ 0 & 0 & 0 & 0 & 0 & (C_{11} - C_{12})/2 \end{bmatrix} \begin{bmatrix} \varepsilon_{11} \\ \varepsilon_{22} \\ \varepsilon_{33} \\ \varepsilon_{23} \\ \varepsilon_{13} \\ \varepsilon_{12} \end{bmatrix} \tag{1.19}$$

where σ_{ij} and ε_{ij} are the respective stress and strain components with ($i, j = 1, 2, 3, 4, 5, 6$) and C_{ij} represents the elastic coefficients of the RVE. The MD simulation box in each case was constructed by randomly placing cross-linked epoxy structures around an individual CNT or a CNT bundle. The CNT volume fraction is kept the same in all RVE ~6.5 %. The details of the three RVEs are summarized in Table 1.2. To determine the five elastic constants, the RVEs were subjected to five different loading conditions: longitudinal tension, transverse tension, in-plane tension, in-plane shear, and out-of-plane shear. The steps involved in the MD simulations of the RVEs are the same as adopted in the previous section for pure epoxy. The boundary and loading conditions that have been applied to the RVE to determine the corresponding five independent elastic coefficients of the RVE are listed in Table 1.3.

Table 1.2 Parameters used in the RVE

Parameter	Single CNT	Bundle of three CNTs	Bundle of seven CNTs
CNT type	(5, 5)	(5, 5)	(5, 5)
Number of CNTs	1	3	7
Length of a CNT (Å)	73	73	76
CNT volume fraction	6.5 %	6.5 %	6.5 %
RVE dimensions (Å^3)	$31 \times 31 \times 76$	$55 \times 55 \times 76$	$88 \times 88 \times 76$
Total number of DGEBA molecules	120	320	960
Total number of TETA molecules	60	160	480
Total number of atoms	7836	21116	62028

Table 1.3 Effective elastic coefficients of the RVEs and corresponding displacement fields

Elastic coefficients	Applied strains	Applied displacement
C_{11}	$\varepsilon_{11} = e$	$u_1 = ex_1$
C_{33}	$\varepsilon_{33} = e$	$u_3 = ex_3$
C_{44}	$\varepsilon_{23} = e/2$	$u_2 = \frac{e}{2}x_3,\ u_3 = \frac{e}{2}x_2$
C_{66}	$\varepsilon_{12} = e/2$	$u_1 = \frac{e}{2}x_2,\ u_2 = \frac{e}{2}x_1$
$K_{12} = \frac{C_{11} + C_{12}}{2}$	$\varepsilon_{11} = \varepsilon_{22}$	$u_1 = ex_1,\ u_2 = ex_2$

Table 1.4 Material properties of the nanocomposite RVE containing either an individual CNT or its bundle

RVE	CNT volume fraction in RVE (v_{CNT})	C_{11} (GPa)	C_{12} (GPa)	C_{13} (GPa)	C_{33} (GPa)	C_{44} (GPa)	C_{66} (GPa)
Single CNT	6.5 %	11.8	7.1	5.6	47.35	3.16	2.35
Bundle of three CNTs		10.5	6.6	4.5	37.4	1.89	1.95
Bundle of seven CNTs		9.1	5.9	3.5	29.2	1.48	1.6

Table 1.4 summarizes the outcome of the MD simulations. It may be observed from the results that the elastic properties of the RVEs are significantly higher than those of the neat epoxy. It is also clear from the results that the CNT agglomeration reduces the reinforcing effect of the embedded CNTs, which eventually degrades the bulk elastic moduli of the nanocomposites. The axial elastic coefficients, C_{33}, of the RVEs containing bundles of three and seven CNTs decreased by some 21 and 38.5 %, respectively, as compared with the RVE containing an individual CNT. The CNT agglomeration is also found to reduce the transverse elastic coefficients of the RVEs. For example, the transverse elastic coefficient, C_{11}, of the RVEs containing bundles of three and seven CNTs decreased by 11.0 and 22.9 %, respectively, compared with the RVE containing an individual CNT.

The effective elastic moduli of the RVE are related to the effective elastic stiffness components as follows:

$$E_{33} = C_{33} - \frac{2C_{23}^2}{C_{12} + C_{11}} \tag{1.20}$$

$$E_{11} = E_{22} = \frac{(C_{11} - C_{12})\left(C_{11}C_{33} + C_{12}C_{33} - 2C_{23}^2\right)}{C_{11}C_{33} - C_{23}^2} \tag{1.21}$$

$$G_{12} = \frac{(C_{11} - C_{12})}{2} \tag{1.22}$$

$$G_{13} = G_{23} = C_{44} \tag{1.23}$$

$$K_{12} = \frac{C_{11} + C_{12}}{2} \tag{1.24}$$

where E_{33}, E_{11}, G_{23}, G_{12}, and K_{12} are the effective axial Young's, transverse Young's, axial shear, transverse shear, and bulk moduli of the nanocomposite, respectively.

1.2.2.5 Modeling of Nanocomposite Containing Wavy CNTs

CNTs have a tendency to bend in the prepared nanocomposites due to their relatively high aspect ratio and low bending stiffness (Falvo et al. 1997). In order to investigate the effect of CNT waviness on the mechanical performance of their nanocomposites, we conducted MD simulations to determine the elastic moduli of nanocomposites reinforced with straight and wavy CNTs using CVFF force field. Sinusoidal armchair (5,5) CNT of shape factor α (a/λ) 0.77 and length 256 Å is used in the simulations (see Fig. 1.11a). Due to the symmetry of the appiled boundary and loading conditions, only half of a complete sine-wave CNT was modeled (Matveeva et al. 2014). The MD simulation box in each case was constructed by randomly placing cross-linked epoxy structures around the embedded CNT (see Fig. 1.11b), and its size in each case was adjusted in such a way that the CNT volume fraction remains constant at 2.5 %. The details of the seven RVEs are summarized in Table 1.5.

Curved CNTs have reinforcement effects on both the chord and the transverse directions; therefore, the RVE is considered to be orthotropic. Nine independent material constants are required to fully define the elastic stiffness tensor of the orthotropic RVE. The constitutive relationship of the orthotropic RVE is given by

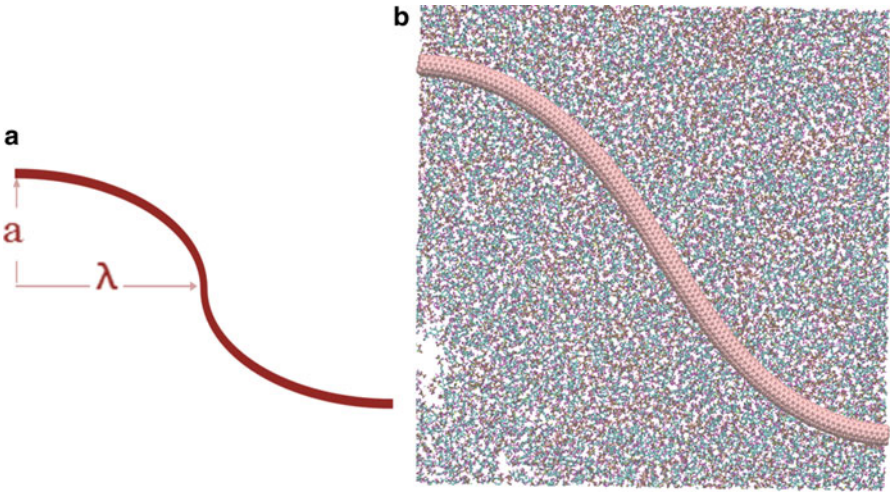

Fig. 1.11 (**a**) A schematic representation of a wavy CNT showing the main parameters that control curvature.(**b**) MD unit cell reinforced with wavy CNT ($\alpha = 0.8$)

Table 1.5 Parameters used in the RVEs

a (Å)	λ (Å)	Shape parameter ($\alpha = a/\lambda$)	No. of DGEBA resins	No. of TETA curing agents	Total no. of atoms
0	128	0.0	1476	738	96480
75	94	0.77			

$$\begin{bmatrix} \sigma_{11} \\ \sigma_{22} \\ \sigma_{33} \\ \sigma_{23} \\ \sigma_{13} \\ \sigma_{12} \end{bmatrix} = \begin{bmatrix} C_{11} & C_{12} & C_{13} & 0 & 0 & 0 \\ C_{12} & C_{22} & C_{23} & 0 & 0 & 0 \\ C_{13} & C_{23} & C_{33} & 0 & 0 & 0 \\ 0 & 0 & 0 & C_{44} & 0 & 0 \\ 0 & 0 & 0 & 0 & C_{55} & 0 \\ 0 & 0 & 0 & 0 & 0 & C_{66} \end{bmatrix} \begin{bmatrix} \varepsilon_{11} \\ \varepsilon_{22} \\ \varepsilon_{33} \\ \varepsilon_{23} \\ \varepsilon_{13} \\ \varepsilon_{12} \end{bmatrix} \tag{1.25}$$

The nine independent stiffness constants can be determined by applying six loading conditions on the RVE: uniaxial tension and compressions in all directions and in-plane shears in 1–2, 2–3, and 1–3 planes. The steps involved in the MD simulations are the same as those adopted for the pure epoxy and RVE reinforced with agglomerated CNTs. The boundary and loading conditions applied to the RVE are listed in Table 1.6.

Table 1.7 summarizes the outcome of the MD simulations. It may be observed from the results that the CNT waviness reduces the reinforcing effect of CNTs, which eventually degrades the bulk elastic moduli of the nanocomposites.

Table 1.6 Effective elastic coefficients of the RVEs and corresponding displacement fields

Elastic coefficients	Applied strains	Applied displacement
C_{11}, C_{12}, C_{13}	$\varepsilon_{11} = e$	$u_1 = ex_1$
C_{22}, C_{12}, C_{13}	$\varepsilon_{22} = e$	$u_2 = ex_2$
C_{33}, C_{13}, C_{23}	$\varepsilon_{33} = e$	$u_3 = ex_3$
C_{44}	$\varepsilon_{23} = e/2$	$u_2 = \frac{e}{2}x_3, u_3 = \frac{e}{2}x_2$
C_{55}	$\varepsilon_{13} = e/2$	$u_1 = \frac{e}{2}x_2, u_3 = \frac{e}{2}x_3$
C_{66}	$\varepsilon_{12} = e/2$	$u_1 = \frac{e}{2}x_2, u_2 = \frac{e}{2}x_1$

Table 1.7 Material properties of the nanocomposite RVE containing straight or wavy CNT at ~1.8 vol.%

Waviness parameter (α)	C_{11}	C_{22}	C_{33}	C_{12}	C_{13}	C_{23}	C_{44}	C_{55}	C_{66}
0.0	9.72	9.72	41.89	7.61	7.81	7.97	2	2	2.32
0.77	10.42	11.81	19.92	8.53	7.04	7.56	1.69	2.22	2.29

1.2.2.6 CNT Pullout Simulations

The mechanical performance of nanocomposites depends on the efficiency of stress transfer between the polymer matrix and the embedded CNTs. Due to the difficulties associated with experimental studies of the interfacial properties of nanocomposites on the atomic scale, a significant number of analytical models have been developed, and numerical studies have also been conducted to study these nanocomposites (Wernik et al. 2012). For instance, in an effort to understand the main factors that govern the interfacial adhesion, Lordi and Yao (2000) used force-field-based molecular mechanics calculations to determine the binding energies and sliding frictional stresses between CNTs and a range of polymer matrices. Their results show that binding energies and frictional forces slightly affect the strength of the interface. Liao and Li (2001) used molecular mechanics simulations to study the interfacial characteristics of a CNT-reinforced polystyrene composite due to nonbonded electrostatic and vdW interactions and reported the interfacial shear stress approximately to be ~160 MPa. Frankland and Harik (2003b) used MD simulations to pull out a CNT from a crystalline polymer matrix. Based on their MD results, they developed an interfacial friction model based on the pullout force, an effective viscosity, and the strain rate. Li et al. (2011) studied the effects of CNT length, diameter, and wall number on the interfacial properties of CNT–polyethylene composite using MD simulations. Their results showed that the ISS does not depend on the CNT length, but it is proportional to the CNT diameter.

In this section, we will determine the ISS of an epoxy nanocomposite using MD simulations. The MD simulation box is constructed using the same steps as mentioned previously herein. During the pullout simulation, one end of the fully embedded CNT is extracted from the matrix at constant velocity of 1×10^{-5} Å/fs

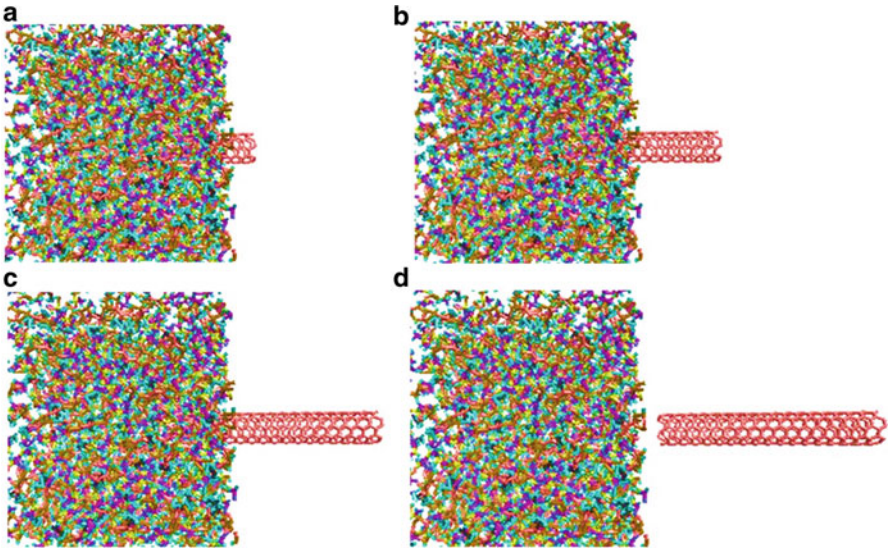

Fig. 1.12 Snapshots of CNT-reinforced epoxy composite at various displacements during the CNT pullout simulation

in the NVT ensemble at 300 K (Yang et al. 2012a). The periodic boundary conditions were removed along the axial direction of the CNT, and the polymer atoms are constrained during the pullout simulation (Li et al. 2011). The pullout force and the average ISS are then determined based on the work done during the pullout test. Typical snapshots during CNT pullout from the epoxy matrix are shown in Fig. 1.12. The corresponding ISS is determined by dividing the pullout force by the initial interfacial area, $A = \pi\, d_{\mathrm{CNT}}\, l_{\mathrm{CNT}}$, where d_{CNT} and l_{CNT} are the diameter and length of the embedded CNT, respectively.

Five different CNT lengths up to 200 Å were modeled to study the effect of CNT length on the interfacial properties. Figure 1.13 shows the effect of embedded CNT lengths on the ISS of a nanocomposite with an interfacial thickness of 3.4 Å. The ISS of the CNT–polymer composite system exhibits a decaying length trend similar to traditional fiber composites (Herrera-Franco and Drzal 1992).

The effect of CNT size on the interfacial properties was investigated by modeling RVEs reinforced with SWCNT of different diameters. The smallest CNT is of (5, 5) chirality and 6.78 Å diameter, while the largest is of (18, 18) chirality and 24.4 Å diameter. Figure 1.14 shows that the ISS decreases approximately linearly with the increase of the CNT diameter. The effect of the interface thickness on the ISS of nanocomposite is investigated by modeling the CNT–epoxy RVEs with different interface thicknesses ranging from 2.2 to 4.25 Å. The measured ISS was found to decrease with increasing the interfacial thickness, as shown in Fig. 1.15. This dependence is attributed to the fact that vdW interactions between any two atoms become weaker with the increase of their atomic separation distance.

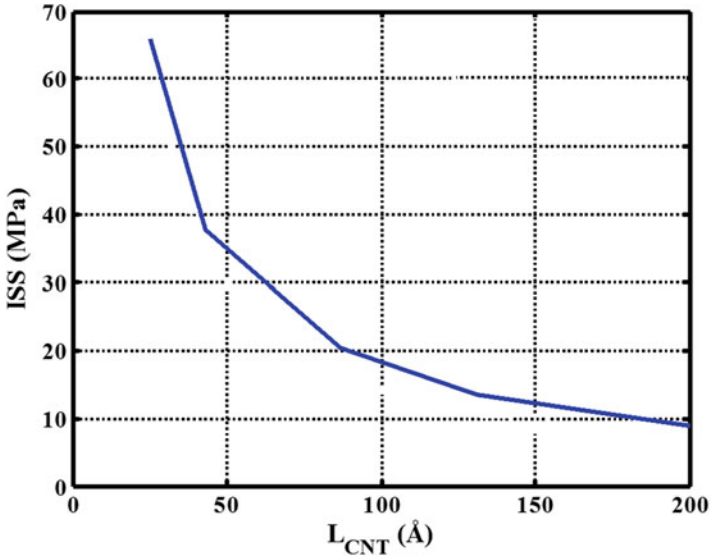

Fig. 1.13 Effect of CNT length on the ISS

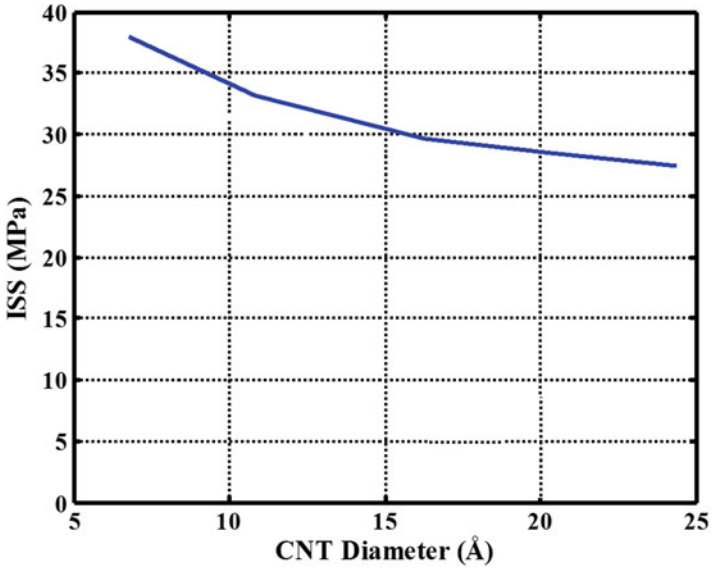

Fig. 1.14 Effect of CNT diameter on the ISS

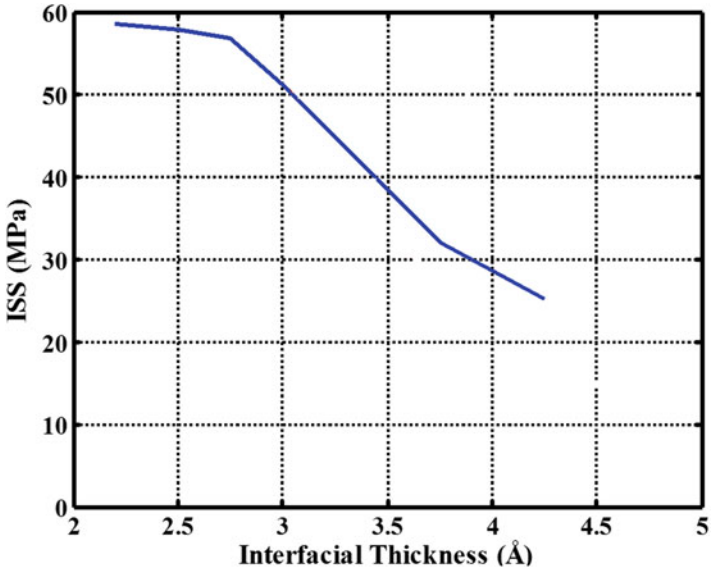

Fig. 1.15 Effect of interface thickness on the ISS

1.3 ABC Mechanics Technique

Due to the computational cost of MD simulations, another atomistic technique was developed to model CNT and its nanocomposite by replacing their structures with equivalent-continuum elements. In this method, in contrast to the traditional continuum modeling techniques, the discrete nature of the structure is considered by replacing the carbon–carbon covalent bond and the interatomic interaction with beam and truss elements, respectively. In general, ABC simulations are conducted using conventional finite element analysis (FEA) packages by modeling (1) CNTs as space frame structures; (2) bonded interactions using beam, truss, and spring elements; and (3) nonbonded interactions using nonlinear truss elements (Nasdala and Ernst 2005).

1.3.1 Basics of ABC Technique

At the nanoscale level, the total interatomic potential energy of the system can be described as the sum of individual energy contributions from bonded- and nonbonded interactions:

$$V = \sum V_r + \sum V_\theta + \sum V_\varphi + \sum V_\omega + \sum V_{\text{vdW}} \tag{1.26}$$

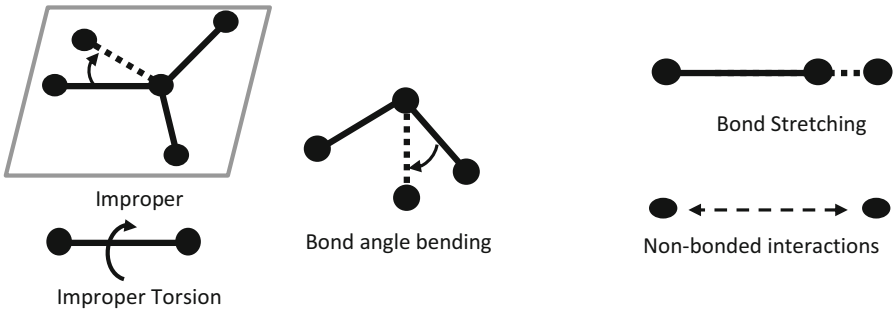

Fig. 1.16 Interatomic interactions in atomic structures

where the terms V_r, V_θ, V_φ, V_ω, and V_{vdW} represent the bond-stretch interaction, bond angle bending, dihedral angle torsion, improper (out-of-plane) torsion, and nonbonded vdW interaction, respectively (Li and Chou 2003a). Figure 1.16 shows schematic representations of these interatomic potential energies.

Li and Chou (2003a) modeled the deformation of CNTs by modeling their structures as geometrical frame-like structures in which each atom acts as a joint of connecting load-bearing beam members which represent C–C covalent bonds where the interatomic potential energies are linked to the strain energies. They described the first four terms of the interatomic potential energy for the bonded interactions using harmonic approximation assuming only small deformations. In addition, they merged the potential energy from the dihedral angle torsion and the improper torsion into a single equivalent term. As a result, the total potential energy due to the covalent bonding can be calculated using only three terms as follows:

$$V_r = \frac{1}{2} k_r (r - r_{\text{o}})^2 = \frac{1}{2} k_r \Delta r^2 \tag{1.27}$$

$$V_\theta = \frac{1}{2} k_\theta (\theta - \theta_{\text{o}})^2 = \frac{1}{2} k_\theta \Delta\theta^2 \tag{1.28}$$

$$V_\tau = V_\varphi + V_\omega = \frac{1}{2} k_\tau \Delta\varphi^2 \tag{1.29}$$

where k_r is the bond-stretching force constant, k_θ is the bond angle-bending force constant, k_τ is the torsional resistance, Δr is the bond-stretching increment, $\Delta\theta$ is the bond angle change, and $\Delta\varphi$ is the angle change of bond twisting. Then, they used beam elements to replace C–C bonds by equating the beam strain energy due to axial deformation, pure bending, and pure torsion due to the total potential energy of the bond. The governing parameters that characterize the beam elements are axial stiffness (EA), bending stiffness (EI), and torsional stiffness (GJ) (see Fig. 1.17) and can be calculated as follows:

$$\frac{\text{EA}}{L} = k_r, \quad \frac{\text{EI}}{L} = k_\theta, \quad \frac{\text{GJ}}{L} = k_\tau \tag{1.30}$$

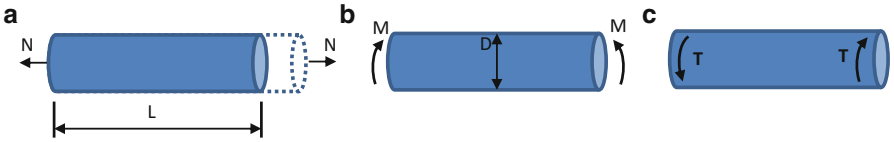

Fig. 1.17 Beam element under (**a**) axial tension, (**b**) pure bending, and (**c**) torsion

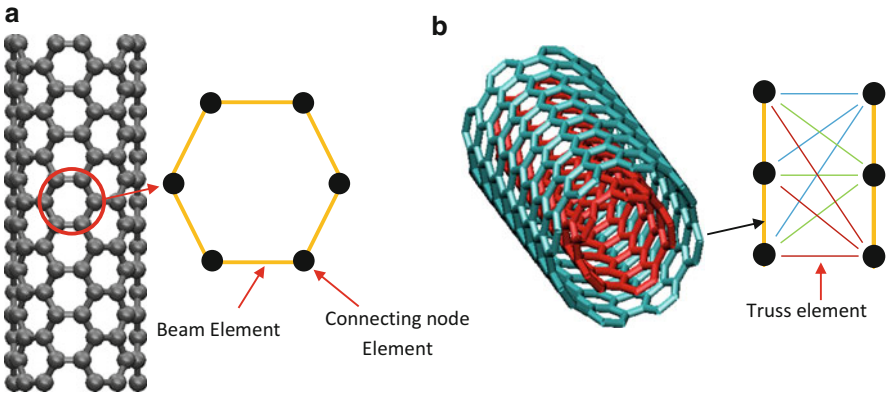

Fig. 1.18 (**a**) CNT modeled as a frame-like structure based on beam elements and (**b**) a double-wall CNT and a schematic representation of the truss elements used to model the intertube vdW interactions

Later, Li and Chou (2003b) determined the elastic properties of multiwalled CNTs by modeling them as space frame structures using connected beam elements where the vdW interactions between the CNT walls were modeled as nonlinear truss elements (see Fig. 1.18).

1.3.2 Modeling of Nanocomposites

A more advanced and generalized ABC model was developed by Wernik and Meguid (2010) based on the modified Morse potential to study the nonlinear elastic response of SWCNTs under tensile and torsional loadings. The stretching and angle-bending components in the interatomic potential were modeled by nonlinear rotational spring and beam elements, respectively, as shown in Fig. 1.19. The following equations were used to describe the bond-stretching and angle-bending components of the modified Morse potential:

$$V_{\text{modified\_morse\_potential}} = V_{\text{bond\_stretching}} + V_{\text{angle\_bending}} \tag{1.31}$$

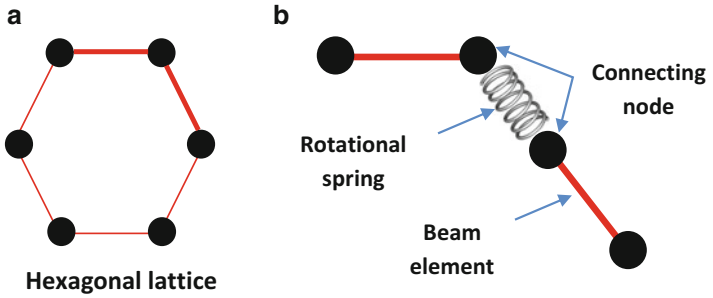

Fig. 1.19 Schematic representations of (**a**) a hexagonal lattice of CNT and (**b**) the connecting structural elements used to model C–C covalent bond

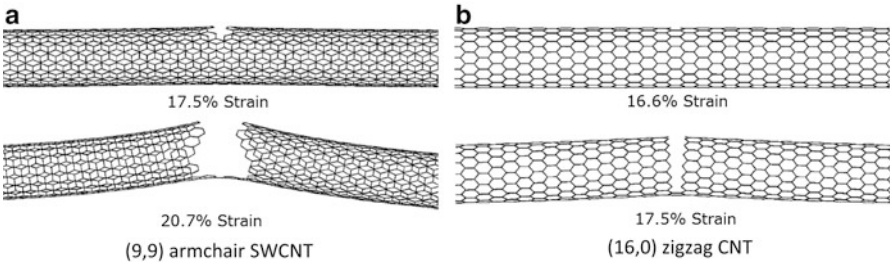

Fig. 1.20 CNTs at different fracture stages under tensile loading condition (Wernik and Meguid 2010)

$$V_{\text{bond\_stretching}} = D_e\left(\left[1-\exp^{-\beta(r-r_o)}\right]^2 - 1\right) \tag{1.32}$$

$$V_{\text{angle\_bending}} = \frac{1}{2}\,k_\theta(\theta-\theta_o)^2\left[1+k_{\text{sextic}}\,(\theta-\theta_o)^4\right] \tag{1.33}$$

where r, θ, D_e, β, k_θ, and k_{sextic} are parameters of the potential.

The results of their ABC simulations showed that armchair CNTs offer a better reinforcement for the nanocomposite due to their superior properties compared to all other types of CNTs. For example, the induced initial damage on the CNT wall expanded more rapidly in the case of zigzag CNTs, as shown in Fig. 1.20. However, zigzag CNTs showed a higher resistance to torsional buckling by having a higher angle of twist for each buckling mode in comparison to the armchair CNTs (see Fig. 1.21).

Meguid et al. (2013) extended their model to incorporate vdW interactions between neighboring atoms of the CNT and the polymer matrix by modeling the weak nonbonded interactions as truss elements. They used the modified model to study the interfacial and mechanical properties of nanocomposites. They used LJ interatomic potential to describe the vdW interactions between the embedded CNT and the surrounding polymer matrix, as given below:

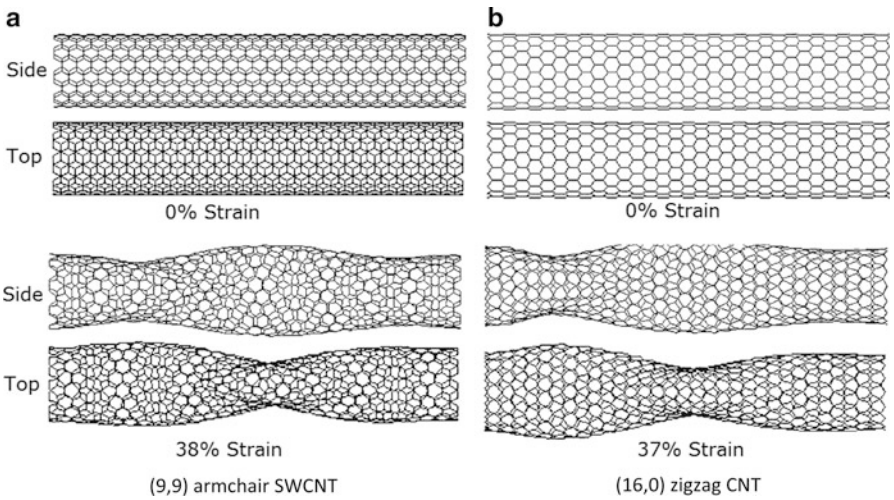

Fig. 1.21 CNTs buckling under torsional loading (Wernik and Meguid 2010)

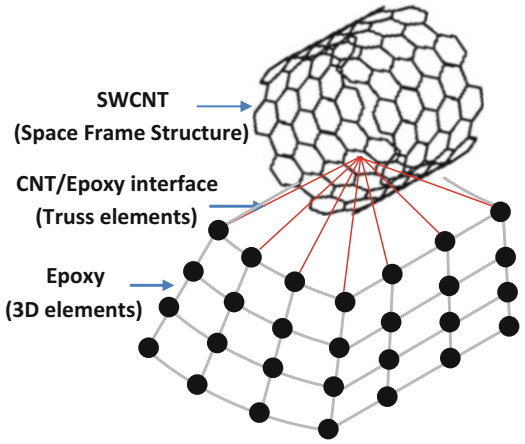

Fig. 1.22 Schematic representation of the CNT–epoxy interface

$$V_{\mathrm{LJ}} = 4\mu\left[\left(\frac{\psi}{r}\right)^{12} - \left(\frac{\psi}{r}\right)^{6}\right] \tag{1.34}$$

where μ is the depth of energy well and its value indicates the bond strength, ψ is the distance at which E_{LJ} is zero and known as the effective diameter of the hard sphere atom, and r is the distance between the two atoms. To model the surrounding polymer matrix, a specific two-component epoxy was used based on a DGEBA and TETA formulation. The Young's modulus and Poisson's ratio of the epoxy matrix were taken to be 1.07 GPa and 0.28, respectively. The epoxy was modeled using higher-ordered 3D, 10-node solid tetrahedral elements with quadratic displacement behavior as shown in Fig. 1.22.

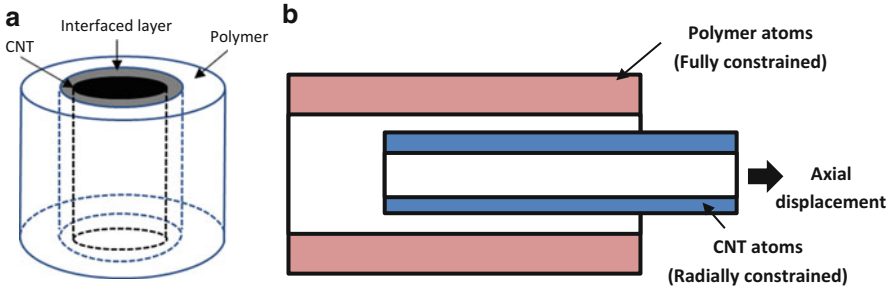

Fig. 1.23 Schematic drawing showing (**a**) the three-phase model that consists of the polymer, the reinforcing CNT, and interface layer; (**b**) pullout of a CNT from matrix to determine the ISS of the nanocomposite

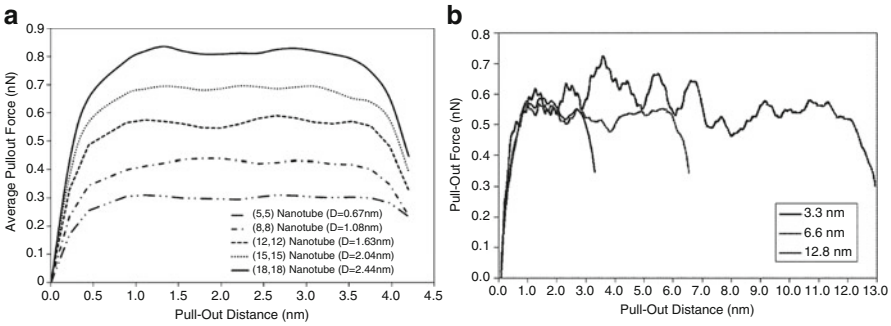

Fig. 1.24 Effect of geometrical parameters on the pullout force of a SWCNT from epoxy matrix. (**a**) Effect of CNT diameter. (**b**) Effect of CNT length (Meguid et al. 2013)

Figure 1.23 shows a schematic of the displacement boundary conditions applied during the pullout process. The nodes in the CNT are constrained from any radial displacements, and an incremental axial displacement boundary condition is applied to the top of CNT nodes to initiate the pullout process. The force required to withdraw the CNT from the matrix is evaluated over the course of the pullout process by summing the reaction forces at the upper CNT nodes. The corresponding ISS was determined by dividing the maximum pullout force by the initial interfacial area, $A = \pi dl$, where d and l are the diameter and length of the embedded CNT, respectively. The pullout model was used to study the effect of CNT length and diameter on the pullout force and the interfacial shear strength (Figs. 1.24 and 1.25). The pullout force was found to increase with increasing CNT diameter, while it was found to be independent of the CNT length. The ISS was found to decrease with increasing the CNT diameter and length.

Wernik and Meguid (2014) then used their model to determine the elastic properties of a transversely isotropic nanoscale RVE consists of a SWCNT, the surrounding polymer matrix, and their interface (see Fig. 1.26). The five stiffness constants required to fully describe the elastic behavior of the RVE were

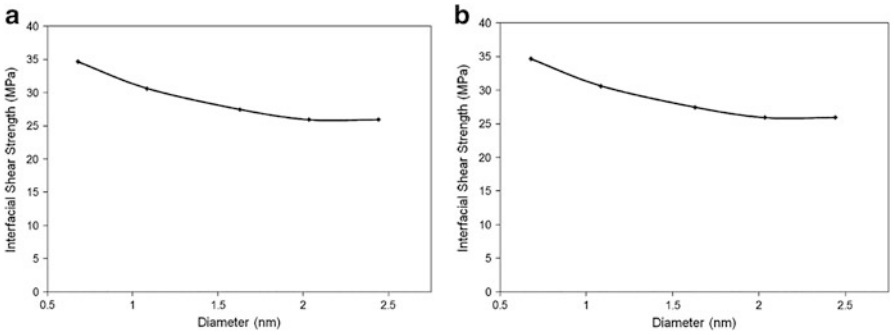

Fig. 1.25 Effect of geometrical parameters on the ISS of CNT–epoxy composite. (**a**) Effect of CNT diameter. (**b**) Effect of CNT length (Meguid et al. 2013)

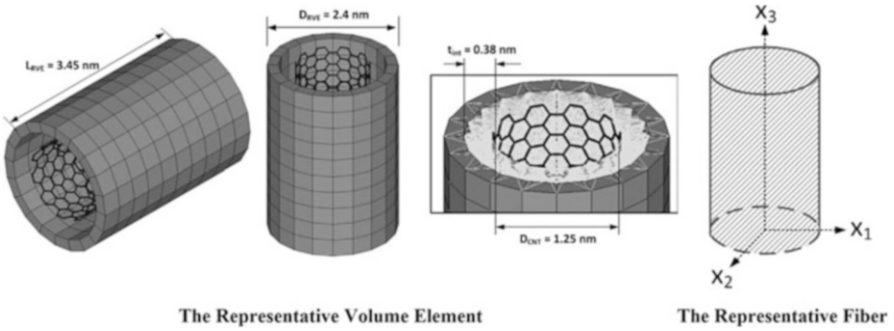

Fig. 1.26 Geometrical dimensions of the RVE and the equivalent effective fiber represent CNT–epoxy composite with 32 % CNT volume fraction (Wernik and Meguid 2014)

Table 1.8 Stiffness constants and the corresponding elastic moduli of the RVE from the ABC simulations

Elastic constants	Value (GPa)	Stiffness constants	Value (GPa)
Transverse shear modulus (G_T)	7.2	C_{11}	469.3
Plane-strain bulk modulus (K_T)	14.3	C_{12}	7.3
Longitudinal shear modulus (G_L)	26.0	C_{22}	21.5
		C_{23}	7.0
Longitudinal Young's modulus ($(E_L$)	465.6	C_{66}	26.0

determined by applying five different sets of boundary conditions on the RVE and equating the total strain energies of the RVE and an equivalent representative fiber, exhibiting the same geometrical and mechanical characteristics, under identical sets of loading conditions as listed in Table 1.3 (assuming 2–3 planes of symmetry in the current case). Table 1.8 summarizes the obtained stiffness constants and the corresponding elastic moduli of the RVE from the ABC simulations.

1.4 Micromechanics Modeling

Multiscale modeling of nanocomposites can be conducted using a two-step scheme. First, the effective elastic properties of a RVE that account for the nanofiller and its immediate surrounding are determined using an appropriate atomistic modeling technique. This RVE is subsequently homogenized into an effective fiber with the same dimensions but with uniform properties (Yang et al. 2012b). Second, established micromechanical techniques such as Mori–Tanaka technique are then used to determine the mechanical properties of the nanocomposites on a macroscopic scale using the effective fiber as the reinforcing fiber in the polymer matrix. Odegard and coworkers (2003, 2005) developed a sequential multiscale model in which the CNT, polymer matrix, and interface were all combined and modeled as an effective continuum fiber using an equivalent-continuum modeling method. Then Mori–Tanaka method was employed to determine the bulk properties of a nanocomposite reinforced with aligned and randomly orientated effective fibers for varied CNT lengths and concentrations. Selmi et al. (2007) compared the predicted elastic properties of CNT-based polymers using different micromechanical techniques including various extensions of the Mori–Tanaka method. Their comparative study showed that the two-level Mori–Tanaka/Mori–Tanaka (MT–MT) approach delivers the most accurate predictions compared to experimental results. In this section, we will use Mori–Tanaka method to scale up the elastic properties of the pure epoxy and the effective fiber, which are determined using MD simulations, to the bulk level. This method has been successfully employed to similar problems by many researchers (Jam et al. 2013; Sobhani Aragh et al. 2012).

Mori–Tanaka model can be developed by utilizing the elastic properties of the nanocomposite containing transversely isotropic aligned CNT or the orthotropic wavy CNT and the isotropic elastic properties of the pure epoxy. In case of two-phase composite, where the inhomogeneity is randomly orientated in the three-dimensional space, the following relation can be used to determine the effective stiffness tensor $[C]$ of the nanocomposite:

$$[C] = [C^m] + v_{\mathrm{RVE}}\left\langle \left(\left[C^{\mathrm{RVE}}\right] - [C^m] \right) \right\rangle \left([A][v_m[I] + v_{\mathrm{RVE}} \langle [A] \rangle]^{-1} \right) \tag{1.35}$$

in which the mechanical strain concentration tensor $[A]$ is given by

$$[A] = \left[[I] + \left[S^{\mathrm{RVE}}\right] ([C^m])^{-1} \left(\left[C^{\mathrm{RVE}}\right] - [C^m] \right) \right]^{-1} \tag{1.36}$$

where $[C^m]$ and [CRVE] are the stiffness tensors of the epoxy matrix and the RVE, respectively; $[I]$ is an identity matrix; v_m and v_{RVE} represent the volume fractions of the epoxy matrix and the RVE, respectively; and $[S^{\mathrm{RVE}}]$ indicate the Eshelby tensor (Mori and Tanaka 1973). The specific form of the Eshelby tensor for the RVE inclusion given by Qiu and Weng (1990) is utilized herein.

It may be noted that the elastic coefficient matrix $[C]$ directly provides the values of the effective elastic properties of the nanocomposite, where the RVE is aligned

with the 3-axis. In case of random orientations of CNTs, the terms enclosed with angle brackets in Eq. (1.35) represent the average value of the term over all orientations defined by transformation from the local coordinate system of the RVE to the global coordinate system. The transformed mechanical strain concentration tensor for the RVEs with respect to the global coordinates is given by

$$\left[\tilde{A}_{ijkl}\right] = t_{ip}t_{jq}t_{kr}t_{ls}\left[A_{pqrs}\right] \tag{1.37}$$

where t_{ij} are the direction cosines for the transformation and are given by

$$t_{11} = \cos\phi\ \cos\psi - \sin\phi\ \cos\gamma\ \sin\psi,\ t_{12} = \sin\phi\ \cos\psi + \cos\phi\ \cos\gamma\ \sin\psi,$$
$$t_{13} = \sin\psi\ \sin\gamma,\ t_{21} = -\cos\phi\ \sin\psi - \sin\phi\ \cos\gamma\ \cos\psi,$$
$$t_{22} = -\sin\phi\ \sin\psi + \cos\phi\ \cos\gamma\ \cos\psi,\ t_{23} = \sin\gamma\ \cos\psi,\ t_{31} = \sin\phi\ \sin\gamma,$$
$$t_{32} = -\cos\phi\ \sin\gamma, \text{ and } t_{33} = \cos\gamma$$

Consequently, the random orientation average of the dilute mechanical strain concentration tensor $[A]$ can be determined by using the following equation:

$$\langle[A]\rangle = \frac{\int_{-\pi}^{\pi}\int_{0}^{\pi}\int_{0}^{\pi/2}\left[\tilde{A}\right](\phi,\ \gamma,\ \psi)\ \sin\gamma\ \mathrm{d}\phi\mathrm{d}\gamma\mathrm{d}\psi}{\int_{-\pi}^{\pi}\int_{0}^{\pi}\int_{0}^{\pi/2}\sin\gamma\ \mathrm{d}\phi\mathrm{d}\gamma\mathrm{d}\psi} \tag{1.38}$$

where ϕ, γ, and ψ are the Euler angles as shown in Fig. 1.27. It may be noted that the averaged mechanical strain concentration tensors given by Eqs. (1.36) and (1.38) are used for the cases of aligned and random orientations of CNTs, respectively, in Eq. (1.35).

The effect of CNT orientation on the bulk properties was investigated by considering polymer reinforced with aligned and randomly oriented CNTs, as shown in Fig. 1.28. The effect of CNT agglomeration was investigated by considering effective fibers representing RVEs reinforced with bundle of three CNTs and

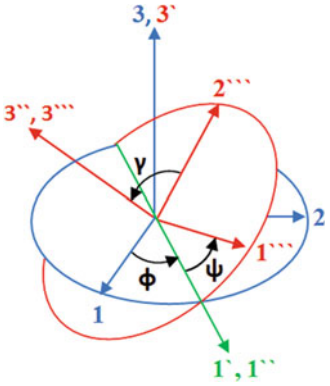

Fig. 1.27 Relationship between the local coordinates (1, 2, 3) of the RVE and the global coordinates (1′, 2′, 3′) of the bulk composite

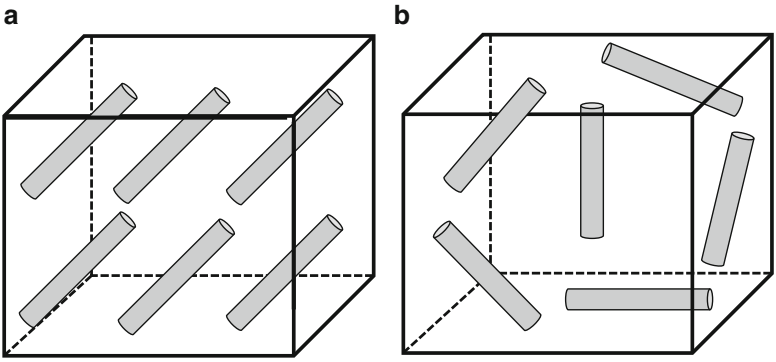

Fig. 1.28 Schematic representations of RVE reinforced with (**a**) aligned CNTs and (**b**) randomly dispersed CNTs

bundle of seven CNTs. The maximum CNT volume fraction (V_{CNT}) considered in the nanocomposite is 5 % because CNT concentrations above this loading are not normally realized (Wernik and Meguid 2014).

Unless otherwise stated, the bulk elastic properties of the nanocomposite are relate to the aligned nanocomposite RVEs along the 3-axis. Let us first demonstrate the effect of agglomeration of CNTs on the effective elastic properties of the aligned CNT-reinforced epoxy composite. Figure 1.29a–d shows the variations of the effective axial Young's modulus (E_{33}), the transverse Young's modulus (E_{11}), the effective axial shear modulus (G_{23}), and the transverse shear modulus (G_{12}) of the nanocomposite with the CNT volume fraction. The elastic moduli increase with increasing CNT volume fraction and decrease with increasing the CNT bundle size. The results show clearly that the CNT agglomerates significantly reduce the elastic moduli.

The orientations of the CNT reinforcement in the polymer matrix can vary over the volume of the nanocomposite. Therefore, studying the properties of nanocomposites reinforced with randomly oriented CNTs is of a great importance. For such investigation, CNTs or their bundles are considered to be randomly dispersed in the epoxy matrix over the volume of the nanocomposite. As expected, this case provides the isotropic elastic properties for the resulting nanocomposite. Figure 1.30a, b illustrates the variations of the effective Young's (E) and shear (G) moduli of the nanocomposite with the CNT loading. These results clearly demonstrate that the randomly dispersed CNTs improve the effective Young's and shear moduli of the nanocomposite over those of the transverse Young's modulus (E_{11}) and the shear moduli (G_{12} and G_{23}) of the nanocomposite reinforced with aligned CNTs. This is attributed to the fact that the CNTs are homogeneously dispersed in the epoxy matrix in the random case, and hence, the overall elastic properties of the resulting nanocomposite improve in comparison to the aligned case. These findings are also consistent with the previously reported findings by Odegard et al. (2003) and Wernik and Meguid (2014). It may also be observed that both E and G decrease with the increase of the number of CNTs in the bundle, and this effect becomes more pronounced at higher CNT volume fractions.

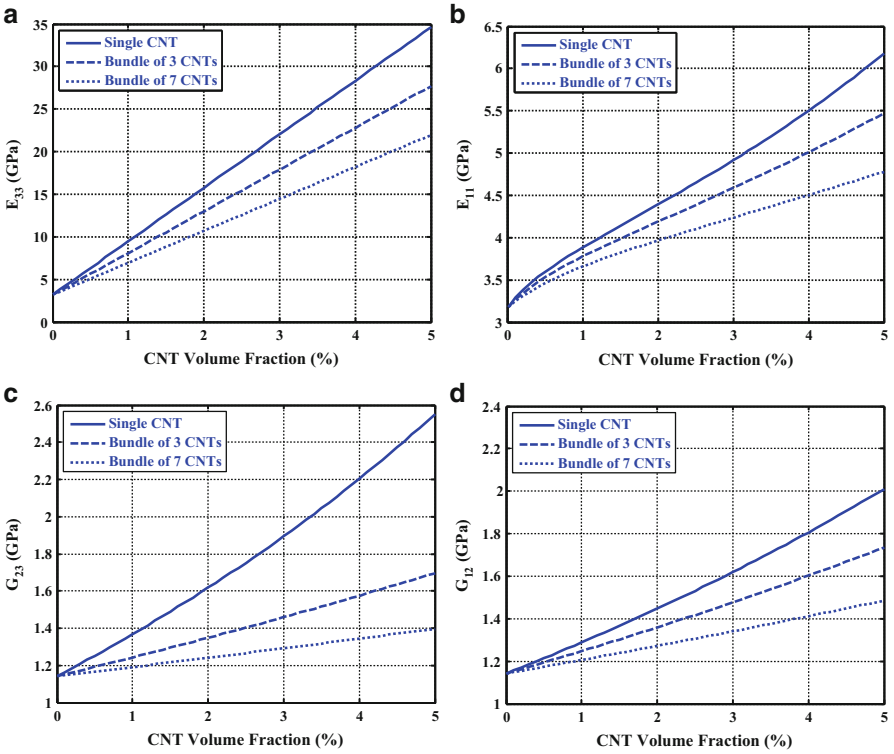

Fig. 1.29 Variation of the (**a**) axial Young's modulus, (**b**) the transverse Young's modulus, (**c**) the effective axial shear modulus, and (**d**) the transverse shear modulus of the nanocomposite containing aligned CNTs with the CNT volume fraction

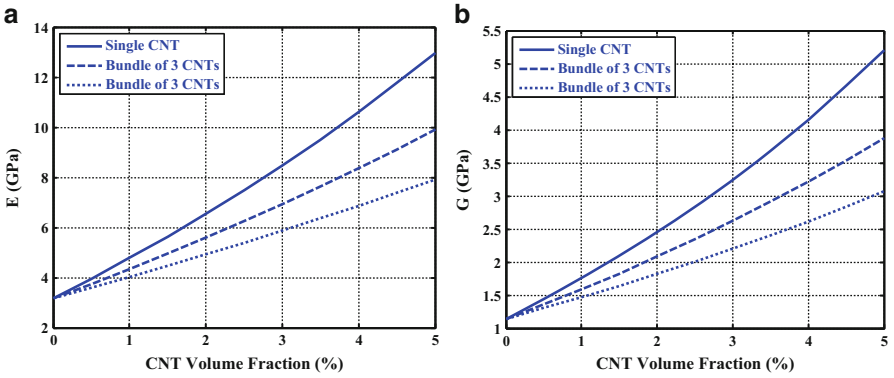

Fig. 1.30 Variation of the (**a**) Young's modulus and (**b**) the shear modulus of the nanocomposite containing randomly oriented CNTs with the CNT volume fraction

1.5 Large-Scale Hybrid Monte Carlo FEA Simulations

Finite element (FE) analysis with the aid of Monte Carlo technique offers a unique opportunity to study the local mechanical behavior and also the overall properties of CNT-reinforced polymer composites under large deformations and specific boundary conditions (Wernik 2013). Complementary to the traditional micromechanical techniques, large-scale three-dimensional (3D) FE models of polymer matrix reinforced with enough number of randomly oriented CNTs are used to predict the average properties of the nanocomposite at a certain CNT volume fraction. Simulation is carried out for several times to yield better averaged results with less scattering. This technique uses the effective elastic moduli of the RVE and the pure epoxy obtained from the atomistic simulations as an input into the analysis.

Here, we will describe the large-scale FE model developed by Wernik and Meguid (2014) to study CNT–epoxy composites. First, a constitutive model for both the effective fiber and the surrounding epoxy polymer that accounts for the material nonlinearities was determined using ABC technique. They benefited from the available nonlinear material models which represent an advantage over the linear elastic micromechanical models. The multi-linear elastic material model was used to describe the nonlinear behavior of the nanocomposite constituents allowing the full response of the composite to be determined when subjected to large deformations. Figure 1.31 shows a FE unit cell that represents a composite loaded with 1.0 % CNT volume fraction.

Higher-ordered 3D, 10-node solid tetrahedral elements with quadratic displacement behavior were used to mesh both the polymer and representative fibers.

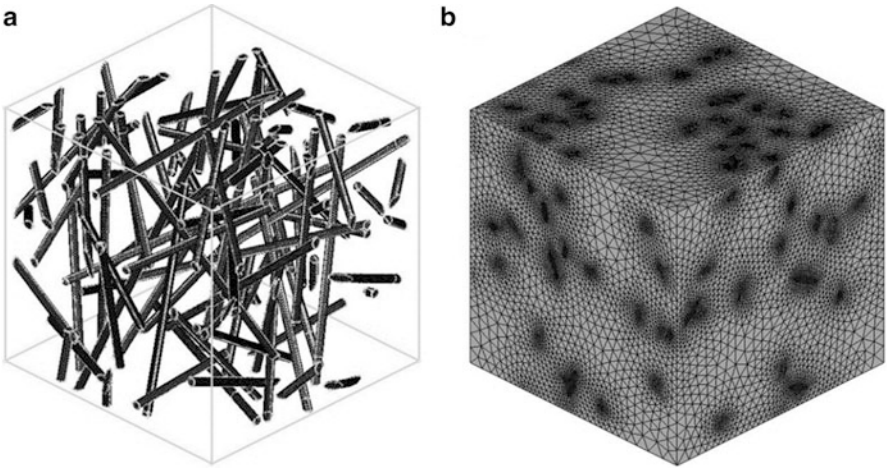

Fig. 1.31 Hybrid Monte Carlo FEA computational cell model in its (**a**) unmeshed and (**b**) fully meshed form. The model utilizes a CNT volume fraction of 1.0 % and a CNT aspect ratio of 100 (from Wernik 2013)

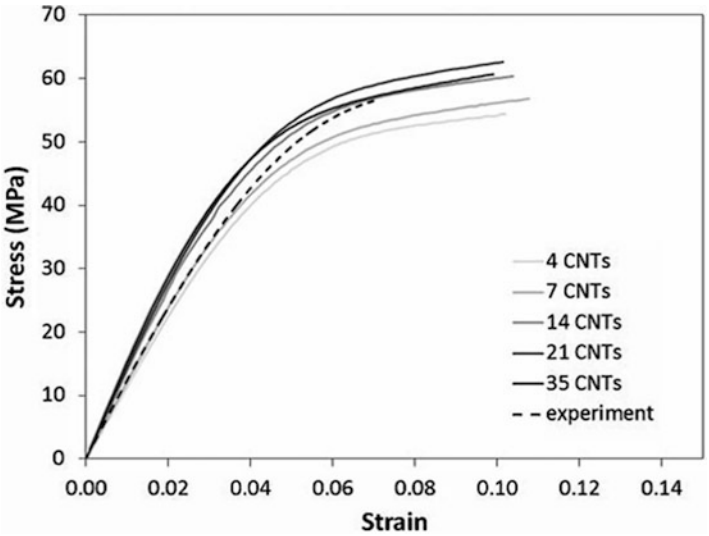

Fig. 1.32 Predicted constitutive response of nano-reinforced adhesives under tensile load (from Wernik 2013)

Periodic boundary conditions were imposed on the FE computational cell. This model represents perfectly straight reinforcing representative fibers of diameter 2.4 nm and aspect ratio of 100. The main disadvantage of this method is the enormous computational cost that is required for such simulations. As a result, a great attention should be given in selecting the cell size that provides accurate results with reasonable computational cost. The RVE was then subjected to a tensile strain up to 10 % by displacing the nodes located at the upper surface while fixing the nodes located at the lower surface. The constitutive relations of the RVE were then evaluated by dividing the total reaction force by the cross-sectional area at each iteration of the simulation. Figure 1.32 shows the predicted constitutive response of the FE unit cell under tensile load plotted against experimental measurements for an epoxy matrix reinforced with the same CNT concentration (0.5 wt%).

References

Ajayan, P.M., Schadler, L.S., Giannaris, C., Rubio, A.: Single-walled carbon nanotube-polymer composites: strength and weakness. Adv. Mater. **12**, 750–753 (2000). doi:10.1002/(SICI)1521-4095(200005)12:10<750::AID-ADMA750>3.0.CO;2-6

Alder, B.J., Wainwright, T.E.: Phase transition for a hard sphere system. J. Chem. Phys. **27**, 1208–1211 (1957). doi:10.1063/1.1743957

Alian, A.R., Kundalwal, S.I., Meguid, S.A.: Interfacial and mechanical properties of epoxy nanocomposites using different multiscale modeling schemes. Compos. Struct. **131**, 545–555 (2015a). doi:10.1016/j.compstruct.2015.06.014

Alian, A.R., Kundalwal, S.I., Meguid, S.A.: Multiscale modeling of carbon nanotube epoxy composites. Polymer **70**, 149–160 (2015b). doi:10.1016/j.polymer.2015.06.004

Allaoui, A., Bai, S., Cheng, H.M., Bai, J.B.: Mechanical and electrical properties of a MWNT/epoxy composite. Compos. Sci. Technol. **62**, 1993–1998 (2002). doi:10.1016/S0266-3538(02)00129-X

Awad, I., Ladani, L.: Mechanical integrity of a carbon nanotube/copper-based through-silicon via for 3D integrated circuits: a multi-scale modeling approach. Nanotechnology **26**, 485705 (2015). doi:10.1088/0957-4484/26/48/485705

Brenner, D.W.: Empirical potential for hydrocarbons for use in simulating the chemical vapor deposition of diamond films. Phys. Rev. B **42**, 9458–9471 (1990). doi:10.1103/PhysRevB.42.9458

Brenner, D.W.: The art and science of an analytic potential. Phys. Status Solidi B **217**, 23–40 (2000). doi:10.1002/(SICI)1521-3951(200001)217:1<23::AID-PSSB23>3.0.CO;2-N

Coleman, J.N., Cadek, M., Blake, R., Nicolosi, V., Ryan, K.P., Belton, C., Fonseca, A., Nagy, J.B., Gun'ko, Y.K., Blau, W.J.: High performance nanotube-reinforced plastics: understanding the mechanism of strength increase. Adv. Funct. Mater. **14**, 791–798 (2004). doi:10.1002/adfm.200305200

Coleman, J.N., Khan, U., Blau, W.J., Gun'ko, Y.K.: Small but strong: a review of the mechanical properties of carbon nanotube-polymer composites. Carbon **44**, 1624–1652 (2006a). doi:10.1016/j.carbon.2006.02.038

Coleman, J.N., Khan, U., Gun'ko, Y.K.: Mechanical reinforcement of polymers using carbon nanotubes. Adv. Mater. **18**, 689–706 (2006b). doi:10.1002/adma.200501851

Coluci, V.R., Dantas, S.O., Jorio, A., Galvão, D.S.: Mechanical properties of carbon nanotube networks by molecular mechanics and impact molecular dynamics calculations. Phys. Rev. B **75**, 075417 (2007). doi:10.1103/PhysRevB.75.075417

Cooper, C.A., Cohen, S.R., Barber, A.H., Wagner, H.D.: Detachment of nanotubes from a polymer matrix. Appl. Phys. Lett. **81**, 3873 (2002). doi:10.1063/1.1521585

Dauber-Osguthorpe, P., Roberts, V.A., Osguthorpe, D.J., Wolff, J., Genest, M., Hagler, A.T.: Structure and energetics of ligand binding to proteins: Escherichia coli dihydrofolate reductase-trimethoprim, a drug-receptor system. Proteins Struct. Funct. Genet. **4**, 31–47 (1988). doi:10.1002/prot.340040106

Desai, A.V., Haque, M.A.: Mechanics of the interface for carbon nanotube-polymer composites. Thin-Walled Struct. **43**, 1787–1803 (2005). doi:10.1016/j.tws.2005.07.003

Dumlich, H., Gegg, M., Hennrich, F., Reich, S.: Bundle and chirality influences on properties of carbon nanotubes studied with van der Waals density functional theory. Phys. Status Solidi B **248**, 2589–2592 (2011). doi:10.1002/pssb.201100212

Falvo, M.R., Clary, G.J., Taylor, R.M., Chi, V., Brooks, F.P., Washburn, S., Superfine, R.: Bending and buckling of carbon nanotubes under large strain. Nature **389**, 582–584 (1997). doi:10.1038/39282

Frankland, S.J.V., Harik, V.M.: Analysis of carbon nanotube pull-out from a polymer matrix. Surf. Sci. **525**, L103–L108 (2003). doi:10.1016/S0039-6028(02)02532-3

Frankland, S.J.V., Harik, V.M., Odegard, G.M., Brenner, D.W., Gates, T.S.: The stress–strain behavior of polymer–nanotube composites from molecular dynamics simulation: modeling and characterization of nanostructured materials. Compos. Sci. Technol. **63**, 1655–1661 (2003). doi:10.1016/S0266-3538(03)00059-9

Gao, G., Çagin, T., Goddard, W.A.: Energetics, structure, mechanical and vibrational properties of single-walled carbon nanotubes. Nanotechnology **9**, 184–191 (1998). doi:10.1088/0957-4484/9/3/007

Gojny, F., Wichmann, M., Fiedler, B., Schulte, K.: Influence of different carbon nanotubes on the mechanical properties of epoxy matrix composites—a comparative study. Compos. Sci. Technol. **65**, 2300–2313 (2005). doi:10.1016/j.compscitech.2005.04.021

Gou, J., Minaie, B., Wang, B., Liang, Z., Zhang, C.: Computational and experimental study of interfacial bonding of single-walled nanotube reinforced composites. Comput. Mater. Sci. **31**, 225–236 (2004). doi:10.1016/j.commatsci.2004.03.002

Grujicic, M., Sun, Y.-P., Koudela, K.L.: The effect of covalent functionalization of carbon nanotube reinforcements on the atomic-level mechanical properties of poly-vinyl-ester-epoxy. Appl. Surf. Sci. **253**, 3009–3021 (2007). doi:10.1016/j.apsusc.2006.06.050

Haghighatpanah, S., Bolton, K.: Molecular-level computational studies of single wall carbon nanotube-polyethylene composites. Comput. Mater. Sci. **69**, 443–454 (2013). doi:10.1016/j.commatsci.2012.12.012

Han, Y., Elliott, J.: Molecular dynamics simulations of the elastic properties of polymer/carbon nanotube composites. Comput. Mater. Sci. **39**, 315–323 (2007). doi:10.1016/j.commatsci.2006.06.011

Hao, X., Qiang, H., Xiaohu, Y.: Buckling of defective single-walled and double-walled carbon nanotubes under axial compression by molecular dynamics simulation. Compos. Sci. Technol. **68**, 1809–1814 (2008). doi:10.1016/j.compscitech.2008.01.013

Herrera-Franco, P.J., Drzal, L.T.: Comparison of methods for the measurement of fibre/matrix adhesion in composites. Composites **23**, 2–27 (1992). doi:10.1016/0010-4361(92)90282-Y

Hone, J., Whitney, M., Piskoti, C., Zettl, A.: Thermal conductivity of single-walled carbon nanotubes. Phys. Rev. B **59**, 2514–2516 (1999). doi:10.1103/PhysRevB.59.R2514

Iijima, S.: Helical microtubules of graphitic carbon. Nature **354**, 56–58 (1991). doi:10.1038/354056a0

Jam, J.E., Pourasghar, A., kamarian, S., Maleki, S.: Characterizing elastic properties of carbon nanotube-based composites by using an equivalent fiber. Polym. Compos. **34**, 241–251 (2013). doi:10.1002/pc.22401

Jones, J.E.: On the determination of molecular fields. II. From the equation of state of a gas. Proc. R. Soc. Math. Phys. Eng. Sci. **106**, 463–477 (1924). doi:10.1098/rspa.1924.0082

Krishnan, A., Dujardin, E., Ebbesen, T.W., Yianilos, P.N., Treacy, M.M.J.: Young's modulus of single-walled nanotubes. Phys. Rev. B **58**, 14013–14019 (1998). doi:10.1103/PhysRevB.58.14013

Kundalwal, S.I., Ray, M.C.: Effective properties of a novel continuous fuzzy-fiber reinforced composite using the method of cells and the finite element method. Eur. J. Mech. A Solids **36**, 191–203 (2012). doi:10.1016/j.euromechsol.2012.03.006

LeSar, R.: Introduction to Computational Materials Science: Fundamentals to Applications. Cambridge University Press, Cambridge, NY (2013)

Li, C., Chou, T.-W.: A structural mechanics approach for the analysis of carbon nanotubes. Int. J. Solids Struct. **40**, 2487–2499 (2003a). doi:10.1016/S0020-7683(03)00056-8

Li, C., Chou, T.-W.: Elastic moduli of multi-walled carbon nanotubes and the effect of van der Waals forces: modeling and characterization of nanostructured materials. Compos. Sci. Technol. **63**, 1517–1524 (2003b). doi:10.1016/S0266-3538(03)00072-1

Li, Y., Liu, Y., Peng, X., Yan, C., Liu, S., Hu, N.: Pull-out simulations on interfacial properties of carbon nanotube-reinforced polymer nanocomposites. Comput. Mater. Sci. **50**, 1854–1860 (2011). doi:10.1016/j.commatsci.2011.01.029

Li, C., Medvedev, G.A., Lee, E.-W., Kim, J., Caruthers, J.M., Strachan, A.: Molecular dynamics simulations and experimental studies of the thermomechanical response of an epoxy thermoset polymer. Polymer **53**, 4222–4230 (2012). doi:10.1016/j.polymer.2012.07.026

Liao, K., Li, S.: Interfacial characteristics of a carbon nanotube-polystyrene composite system. Appl. Phys. Lett. **79**, 4225–4227 (2001). doi:10.1063/1.1428116

Littell, J.D., Ruggeri, C.R., Goldberg, R.K., Roberts, G.D., Arnold, W.A., Binienda, W.K.: Measurement of epoxy resin tension, compression, and shear stress–strain curves over a wide range of strain rates using small test specimens. J. Aerosp. Eng. **21**, 162–173 (2008). doi:10.1061/(ASCE)0893-1321(2008)21:3(162)

Lordi, V., Yao, N.: Molecular mechanics of binding in carbon-nanotube-polymer composites. J. Mater. Res. **15**, 2770–2779 (2000). doi:10.1557/JMR.2000.0396

Matveeva, A.Y., Pyrlin, S.V., Ramos, M.M.D., Böhm, H.J., van Hattum, F.W.J.: Influence of waviness and curliness of fibres on mechanical properties of composites. Comput. Mater. Sci. **87**, 1–11 (2014). doi:10.1016/j.commatsci.2014.01.061

Meguid, S., Sun, Y.: On the tensile and shear strength of nano-reinforced composite interfaces. Mater. Des. **25**, 289–296 (2004). doi:10.1016/j.matdes.2003.10.018

Meguid, S.A., Wernik, J.M., Al Jahwari, F.: Toughening mechanisms in multiphase nanocomposites. Int. J. Mech. Mater. Des. **9**, 115–125 (2013). doi:10.1007/s10999-013-9218-x

Mori, T., Tanaka, K.: Average stress in matrix and average elastic energy of materials with misfitting inclusions. Acta Metall. **21**, 571–574 (1973). doi:10.1016/0001-6160(73)90064-3

Nasdala, L., Ernst, G.: Development of a 4-node finite element for the computation of nano-structured materials. Comput. Mater. Sci. **33**, 443–458 (2005). doi:10.1016/j.commatsci.2004.09.047

Odegard, G.M., Gates, T.S., Wise, K.E., Park, C., Siochi, E.J.: Constitutive modeling of nanotube-reinforced polymer composites: modeling and characterization of nanostructured materials. Compos. Sci. Technol. **63**, 1671–1687 (2003). doi:10.1016/S0266-3538(03)00063-0

Odegard, G.M., Frankland, S.-J.V., Gates, T.S.: Effect of nanotube functionalization on the elastic properties of polyethylene nanotube composites. AIAA J. **43**, 1828–1835 (2005). doi:10.2514/1.9468

Park, C., Ounaies, Z., Watson, K.A., Crooks, R.E., Smith, J., Lowther, S.E., Connell, J.W., Siochi, E.J., Harrison, J.S., Clair, T.L.S.: Dispersion of single wall carbon nanotubes by in situ polymerization under sonication. Chem. Phys. Lett. **364**, 303–308 (2002). doi:10.1016/S0009-2614(02)01326-X

Plimpton, S.: Fast parallel algorithms for short-range molecular dynamics. J. Comput. Phys. **117**, 1–19 (1995). doi:10.1006/jcph.1995.1039

Qian, D., Dickey, E.C., Andrews, R., Rantell, T.: Load transfer and deformation mechanisms in carbon nanotube-polystyrene composites. Appl. Phys. Lett. **76**, 2868–2870 (2000). doi:10.1063/1.126500

Qiu, Y.P., Weng, G.J.: On the application of Mori-Tanaka's theory involving transversely isotropic spheroidal inclusions. Int. J. Eng. Sci. **28**, 1121–1137 (1990). doi:10.1016/0020-7225(90)90112-V

Rahmat, M., Hubert, P.: Carbon nanotube-polymer interactions in nanocomposites: a review. Compos. Sci. Technol. **72**, 72–84 (2011). doi:10.1016/j.compscitech.2011.10.002

Schadler, L.S., Giannaris, S.C., Ajayan, P.M.: Load transfer in carbon nanotube epoxy composites. Appl. Phys. Lett. **73**, 3842 (1998). doi:10.1063/1.122911

Selmi, A., Friebel, C., Doghri, I., Hassis, H.: Prediction of the elastic properties of single walled carbon nanotube reinforced polymers: a comparative study of several micromechanical models. Compos. Sci. Technol. **67**, 2071–2084 (2007). doi:10.1016/j.compscitech.2006.11.016

Shen, L., Li, J.: Transversely isotropic elastic properties of single-walled carbon nanotubes. Phys. Rev. B **69**, 045414 (2004). doi:10.1103/PhysRevB.69.045414

Sobhani Aragh, B., Nasrollah Barati, A.H., Hedayati, H.: Eshelby–Mori–Tanaka approach for vibrational behavior of continuously graded carbon nanotube-reinforced cylindrical panels. Compos. Part B Eng. **43**, 1943–1954 (2012). doi:10.1016/j.compositesb.2012.01.004

Spitalsky, Z., Tasis, D., Papagelis, K., Galiotis, C.: Carbon nanotube-polymer composites: chemistry, processing, mechanical and electrical properties. Prog. Polym. Sci. **35**, 357–401 (2010). doi:10.1016/j.progpolymsci.2009.09.003

Srivastava, D., Wei, C., Cho, K.: Nanomechanics of carbon nanotubes and composites. Appl. Mech. Rev. **56**, 215–230 (2003). doi:10.1115/1.1538625

Stuart, S.J., Tutein, A.B., Harrison, J.A.: A reactive potential for hydrocarbons with intermolecular interactions. J. Chem. Phys. **112**, 6472–6486 (2000). doi:10.1063/1.481208

Tersoff, J.: Empirical interatomic potential for silicon with improved elastic properties. Phys. Rev. B **38**, 9902–9905 (1988). doi:10.1103/PhysRevB.38.9902

Thostenson, E.T., Chou, T.-W.: On the elastic properties of carbon nanotube-based composites: modelling and characterization. J. Phys. Appl. Phys. **36**, 573–582 (2003). doi:10.1088/0022-3727/36/5/323

Treacy, M.M.J., Ebbesen, T.W., Gibson, J.M.: Exceptionally high Young's modulus observed for individual carbon nanotubes. Nature **381**, 678–680 (1996). doi:10.1038/381678a0

Tsai, J.-L., Tzeng, S.-H., Chiu, Y.-T.: Characterizing elastic properties of carbon nanotubes/polyimide nanocomposites using multi-scale simulation. Compos. Part B Eng. **41**, 106–115 (2010). doi:10.1016/j.compositesb.2009.06.003

Tunvir, K., Kim, A., Nahm, S.H.: The effect of two neighboring defects on the mechanical properties of carbon nanotubes. Nanotechnology **19**, 065703 (2008). doi:10.1088/0957-4484/19/6/065703

van Gunsteren, W.F., Berendsen, H.J.C.: Computer simulation of molecular dynamics: methodology, applications, and perspectives in chemistry. Angew. Chem. Int. Ed. Engl. **29**, 992–1023 (1990). doi:10.1002/anie.199009921

Verlet, L.: Computer "experiments" on classical fluids. I. Thermodynamical properties of Lennard-Jones molecules. Phys. Rev. **159**, 98–103 (1967). doi:10.1103/PhysRev.159.98

Wagner, H.D., Lourie, O., Feldman, Y., Tenne, R.: Stress-induced fragmentation of multiwall carbon nanotubes in a polymer matrix. Appl. Phys. Lett. **72**, 188–190 (1998). doi:10.1063/1.120680

Wang, Z., Colorad, H.A., Guo, Z.-H., Kim, H., Park, C.-L., Hahn, H.T., Lee, S.-G., Lee, K.-H., Shang, Y.-Q.: Effective functionalization of carbon nanotubes for bisphenol F epoxy matrix composites. Mater. Res. **15**, 510–516 (2012). doi:10.1590/S1516-14392012005000092

Wernik, J.: Multiscale Modeling of Nano-reinforced Aerospace Adhesives (PhD). University of Toronto, Toronto, ON (2013)

Wernik, J.M., Meguid, S.A.: Atomistic-based continuum modeling of the nonlinear behavior of carbon nanotubes. Acta Mech. **212**, 167–179 (2010). doi:10.1007/s00707-009-0246-4

Wernik, J.M., Meguid, S.A.: Multiscale micromechanical modeling of the constitutive response of carbon nanotube-reinforced structural adhesives. Int. J. Solids Struct. **51**, 2575–2589 (2014). doi:10.1016/j.ijsolstr.2014.03.009

Wernik, J.M., Cornwell-Mott, B.J., Meguid, S.A.: Determination of the interfacial properties of carbon nanotube reinforced polymer composites using atomistic-based continuum model. Int. J. Solids Struct. **49**, 1852–1863 (2012). doi:10.1016/j.ijsolstr.2012.03.024

Wong, E.W., Sheehan, P.E., Lieber, C.M.: Nanobeam mechanics: elasticity, strength, and toughness of nanorods and nanotubes. Science **277**, 1971–1975 (1997). doi:10.1126/science.277.5334.1971

Xiao, T., Liu, J., Xiong, H.: Effects of different functionalization schemes on the interfacial strength of carbon nanotube polyethylene composite. Acta Mech. Solida Sin. **28**, 277–284 (2015). doi:10.1016/S0894-9166(15)30014-8

Yang, X.-S.: Modelling heat transfer of carbon nanotubes. Model. Simul. Mater. Sci. Eng. **13**, 893–902 (2005). doi:10.1088/0965-0393/13/6/008

Yang, L., Tong, L., He, X.: MD simulation of carbon nanotube pullout behavior and its use in determining mode I delamination toughness. Comput. Mater. Sci. **55**, 356–364 (2012a). doi:10.1016/j.commatsci.2011.12.014

Yang, S., Yu, S., Kyoung, W., Han, D.-S., Cho, M.: Multiscale modeling of size-dependent elastic properties of carbon nanotube/polymer nanocomposites with interfacial imperfections. Polymer **53**, 623–633 (2012b). doi:10.1016/j.polymer.2011.11.052

Yu, M.-F., Lourie, O., Dyer, M.J., Moloni, K., Kelly, T.F., Ruoff, R.S.: Strength and breaking mechanism of multiwalled carbon nanotubes under tensile load. Science **287**, 637–640 (2000). doi:10.1126/science.287.5453.637

Zang, J.-L., Yuan, Q., Wang, F.-C., Zhao, Y.-P.: A comparative study of Young's modulus of single-walled carbon nanotube by CPMD, MD and first principle simulations. Comput. Mater. Sci. **46**, 621–625 (2009). doi:10.1016/j.commatsci.2009.04.007

Zeng, Q.H., Yu, A.B., Lu, G.Q.: Multiscale modeling and simulation of polymer nanocomposites. Prog. Polym. Sci. **33**, 191–269 (2008). doi:10.1016/j.progpolymsci.2007.09.002

Zhou, M.: A new look at the atomic level virial stress: on continuum-molecular system equivalence. Proc. R. Soc. Math. Phys. Eng. Sci. **459**, 2347–2392 (2003). doi:10.1098/rspa.2003.1127

Chapter 2
Piezoelectric Response at Nanoscale

Jin Zhang and Shaker A. Meguid

Abstract Considerable efforts were invested to study the piezoelectricity at the nanoscale, which serves as a physical basis for a wide range of smart nanodevices and nanoelectronics. This chapter reviews the recent progress in characterizing the effective piezoelectric property in a nanoworld and the influence of the piezoelectric effect on the mechanical responses of nanoscale structures. Extremely strong piezoelectric responses of piezoelectric nanomaterials were reported in experiments, and the size dependence was observed in atomistic simulations. Attempts were also made to reveal the physics behind these unique features, but the universal theory has not yet been established. Among the proposed mechanisms, the theory of surface piezoelectricity is widely accepted and thus used to derive two effective piezoelectric coefficients (EPCs) for investigating the effect of piezoelectricity on (1) stress or strain and (2) the effective elastic moduli of piezoelectric nanomaterials. The EPCs are found to be size-dependent and also deformation-selective. The obtained results also show that at the nanoscale the surface piezoelectricity can enhance the piezoelectric potential of nanostructures when subjected to a static deformation. In addition, the intrinsic loss of oscillating piezoelectric nanostructures can be mitigated through the piezoelectric effect at the nanoscale.

2.1 Introduction

The discovery of advanced nanomaterials has greatly accelerated the development of nanoscience and nanotechnology. Among these nanomaterials are the family of carbon nanomaterials (Kroto et al. 1985; Iijima 1991; Ebbesen and Ajayan 1992; Geim and Novoselov 2007) and that of piezoelectric nanomaterials (PNs) (Wang 2009; Faucher et al. 2009; Smith et al. 2008; Dunn 2003). In particular, the last decade has witnessed increasing interest in PNs, such as nanoscale zinc oxide (ZnO) (Wang 2009), gallium nitride (GaN) (Faucher et al. 2009), barium titanate ($BaTiO_3$) (Smith et al. 2008), and lead zirconate titanate (PZT) (Dunn 2003). These

J. Zhang • S.A. Meguid (✉)
Mechanics and Aerospace Design Laboratory, Department of Mechanical and Industrial Engineering, University of Toronto, Toronto, ON, Canada, M5S 3G8
e-mail: jinzhang@mie.utoronto.ca; meguid@mie.utoronto.ca

S.A. Meguid (ed.), *Advances in Nanocomposites*,
DOI 10.1007/978-3-319-31662-8_2

PNs form different configurations (e.g., nanodotes, nanowires, nanofilms, nanorings, and nanotubes) and have great potential for constructing a wide range of smart piezoelectronic nanosystems, e.g., piezoelectric nanoresonators, nanosensors/actuators, nanogenerators, and nanoelectromechanical systems (Wang 2009; Faucher et al. 2009; Smith et al. 2008; Dunn 2003), which are highly expected to excite ground-breaking innovations in the twenty-first century. Nano-piezoelectricity thus has become a current topic of great interest in recent research (Zhao et al. 2004; Fan et al. 2006; Wang et al. 2006b; Zhu et al. 2008; Bdikin et al. 2010; Espinosa et al. 2012; Fang et al. 2013; Zhang et al. 2014; Xiang et al. 2006; Li et al. 2007; Dai et al. 2010, 2011; Momeni et al. 2012; Momeni and Attariani 2014).

Until now, experimental techniques (Zhao et al. 2004; Fan et al. 2006; Wang et al. 2006b; Zhu et al. 2008; Bdikin et al. 2010; Espinosa et al. 2012; Fang et al. 2013; Zhang et al. 2014) and atomistic simulations (Espinosa et al. 2012; Fang et al. 2013; Zhang et al. 2014; Xiang et al. 2006; Li et al. 2007; Dai et al. 2010, 2011; Momeni et al. 2012; Momeni and Attariani 2014) have been utilized to measure the effective piezoelectric coefficients (EPCs) and examine their size dependence for different sizes and configurations of PNs. Various physical mechanisms were proposed, and especially the theory of surface piezoelectricity (Zhang et al. 2014; Zhang 2014; Zhang and Meguid 2015a, b) was established to interpret the existing data at the nanoscale. However, large discrepancy remains among these studies. For example, EPCs obtained for ZnO nanocrystals differ by up to orders of magnitude and exhibit the size dependence qualitatively different from one another. Specifically, existing piezoelectric measurement was focused on the EPCs describing the electric field-stress relation in the constitutive equations of PNs. The ones characterizing the effect of piezoelectricity on the effective elastic moduli (EEM) of PNs as nanostructures were never considered although they may be of significance for PNs as engineering nanostructures. This situation as it currently stands indeed provides an impulsion to summarize the latest developments, capture the major issues that need to be resolved, and identify the future direction in studying nanoscale piezoelectricity. In addition, further study of the EPCs of PNs by considering both the electric field-stress relation and the electromechanical coupling is essential for the development of PNs and their smart nanosystems.

To achieve these goals, we present this review of the latest developments of nano-piezoelectricity and the derivation of size-dependent and deformation-selective EPCs. The materials are organized as follows: First, a critical review was conducted in Sect. 2.2 regarding the experimental measurements of EPCs and atomistic simulations on the size dependence of EPCs for different configurations of PNs. In Sect. 2.3 we summarized the physical mechanisms proposed in earlier studies for the interpretation of the unique behavior of EPCs. Particular attention was placed on the investigation of the effect of surface piezoelectricity of PNs. Analytical models were derived in Sect. 2.4 for the EPCs and EEM of PNs. Two types of EPCs were obtained in this section reflecting the electric field-stress relation and the electromechanical coupling of PNs. The importance of two EPCs was also evaluated for existing PNs. The influence of the nanoscale piezoelectricity on the mechanical responses (statics and dynamics) of piezoelectric nanostructures was discussed in Sect. 2.5. Finally, the conclusion remarks were given in Sect. 2.6.

2.2 Measurement of Nano-piezoelectricity

ZnO nanocrystal exhibits the strongest piezoelectric effect among the tetrahedrally bonded semiconductors, which thus makes it the most studied PNs in the literature (Wang 2009). Throughout the paper, we shall mainly focus our attention on the piezoelectric characterization of ZnO nanocrystals. In 2004 the first piezoelectric measurement of nanoscale ZnO was reported by Zhao et al. (2004) where the piezoelectric force microscope (PFM) was employed to excite the local transverse vibration (the amplitude A_f) on the ZnO nanobelts (tens of nanometers in thickness) by applying AC voltage (the amplitude U_f) in the thickness direction. The effective e_{33} calculated by $e_{33} = A_f/U_f$ was found to increase from 14.3 to 26.7 pm/V while the driving vibration frequency significantly decreased from 150 to 30 kHz. In other words, obtained e_{33} was found to be frequency-dependent and 40–160 % greater than that of bulk ZnO. Four years later, Zhu et al. (2008) measured e_{33} of ZnO nanowires of diameter ~230 nm using a nanoelectromechanical oscillating system. Their study reported the value of $e_{33} = 3 - 12$ nm/V along the c-axis [0001] using $e_{33} = \Delta l/V_{\mathrm{sd}}^{\mathrm{bias}}$, where $V_{\mathrm{sd}}^{\mathrm{bias}}$ is a DC bias voltage applied in the axial direction and Δl is the axial extension due to $V_{\mathrm{sd}}^{\mathrm{bias}}$. These values are found to be two to three orders of magnitude greater than the bulk value and those reported for ZnO nanobelts by Zhao et al. (2004). In addition, the giant e_{33} up to 100 pm/V was also achieved by Wang et al. (2006b) for the ZnO nanofilms of thickness ~200 nm doped with ferroelectric vanadium. This value is lower than those reported by Zhu et al. (2008) but still around an order of magnitude greater than the bulk value. The study by Zhao et al. (2004) indicated the rising of EPC with decreasing deriving frequency, and it was attributed to the pinning of spontaneous polarization or imperfect electrical contacts at high frequency. Based on this frequency dependency, the DC bias voltage was thought to be responsible for the extreme value of e_{33} reported by Zhu et al. (2008). Wang et al. (2006b) obtained the giant e_{33}, and they attributed this to the switchable spontaneous polarization induced by voltage dopants and the accompanying relatively high permittivity. In contrast to the observations in Zhao et al. (2004), Wang et al. (2006b), and Zhu et al. (2008), e_{33} measured for large ZnO nanopillar (300 nm in diameter and 2 mm in height) in Fan et al. (2006) was around 7.5 pm/V, which was lower than the bulk value. In early studies (Zhao et al. 2004; Fan et al. 2006; Wang et al. 2006b; Zhu et al. 2008), piezoelectric measurement was centered on the ZnO single nanocrystalline. The characterization of the polycrystalline at the nanoscale was not reported until 2010, where the EPCs were measured for the polycrystalline ZnO nanofilms (around 200 nm in thickness and 2 μm in length) based on PFM (Bdikin et al. 2010). The obtained effective value of e_{33} is found to be 12 pm/V, almost the same as the accepted bulk value.

As reviewed above, EPCs were measured for individual PNs in experiments, but the possible size dependence of EPCs have not yet been investigated experimentally. This is probably due to lack of suitable techniques to control the geometric size of synthesized PNs. To circumvent this hurdle, theoretical studies were performed to calculate the EPC for a group of ZnO nanofilms and nanowires

where the geometric size varies monotonically. Xiang et al. (2006) conducted a density functional study of ZnO nanowires with diameter up to 2.8 nm. In their study, the atomic averaged effective e_{33} is defined as $e_{33} = (V_{\text{scell}}/N)dP/d\varepsilon$ for one-dimensional nanowires, where ε is the axial compression or tension, P is the polarization induced by ε, V_{scell} is the volume, and N represents the number of atoms in the supercell. It was found that the effective e_{33} exhibits a significant but nonmonotonic diameter dependence, i.e., with the increasing diameter, e_{33} first decreases to reach its minimum value, then rises, and finally stabilizes when the diameter exceeds 2.8 nm. Here the obtained e_{33} falls in the range 1837–2025 (unit: 10^{-16} μCA/ion), which is 20–40 % greater than that of the bulk ZnO. Likewise, density functional theory (DFT) was used by Li et al. (2007) to calculate the effective e_{33} for ZnO nanofilms of a thickness (h) up to 2.9 nm. They expressed effective e_{33} as $(\partial P_3/\partial \varepsilon_3)_u + (\partial P_3/\partial u)_\varepsilon (du/d\varepsilon_3)$, where ε_3 and P_3 are the strain and polarization in the c-axis, respectively, and u is the internal parameter. In this expression, the contributions to the piezoelectric polarization from both the clamped ion and the internal strain have been considered. The results showed that the effective e_{33} increases monotonically with increasing thickness. It becomes greater than the bulk value only when the value of h exceeds 2.4 nm. At the maximum thickness of $h = 2.9$ nm studied, e_{33} was found to be increased by 11 % in comparison to the bulk value. Beyond this limit, the authors expected that e_{33} would further increase to the maximum value and then decrease with increasing h to approach the bulk value at large h. This again suggested a nonmonotonic dependence of e_{33} on the feature size of the ZnO nanofilms.

So far, in the existing works, the first-principle calculation remains computationally expensive. Thus, measurements based on this technique (Xiang et al. 2006; Li et al. 2007) are limited to very small ZnO nanocrystal, e.g., feature size less than 2.8 nm (Xiang et al. 2006) and 2.9 nm (Li et al. 2007). To further improve the efficiency and expand the scope of the study, Dai et al. (2010; 2011), Momeni et al. (2012), and Momeni and Attariani (2014) computed the EPC of ZnO nanofilms/nanowires by utilizing molecular dynamics simulations (MDS) based on the empirical core-shell potential. This more efficient technique enabled the authors to consider the nanofilms/nanowires with the thickness up to 10 nm (Dai et al. 2011). The maximum size that can be handled by MDS, however, is still very small as compared with the feature size of synthesized PNs that is of the order of tens to hundreds of nanometers (Zhao et al. 2004; Fan et al. 2006; Wang et al. 2006b; Zhu et al. 2008; Bdikin et al. 2010). A study by Dai et al. (2011) reveals that the magnitudes of the effective e_{33} and e_{31} increase monotonically with increasing thickness h and approach the bulk values gradually at large thickness, $h \geq 10$ nm. As compared with the DFT studies, the MDS predicted the small magnitude and qualitatively different size dependence of the EPC (Dai et al. 2010; Dai et al. 2011; Momeni et al. 2012; Momeni and Attariani 2014). In particular, the magnitudes of the MDS results are always found to be lower than the bulk values.

To show the large scattering of the obtained results, we have summarized the aforementioned experimental and atomistic simulations on (undoped) single ZnO nanocrystal (see Table 2.1). Note that the strong piezoelectric response was

Table 2.1 Effective piezoelectric coefficients measured for (undoped) single-crystalline ZnO nanofilms and nanowires in exiting experiments and atomistic simulations

	Nanowires (diameter d or thickness h)			Nanofilms (thickness h)			
d or h	~230 nm	~230 nm	0.3–2.8 nm	Tens nm	0.48–2.9 nm	0.48–2.4 nm	1.2–9.6 nm
e_{33}	~7.5 (pm/V)	3–12 (nm/V)	1837–2025 (10^{-16} μCA/ion)	14.3–26.7 (pm/V)	0.5–1.4 (C/m^2)	0.28–1.17 C/m^2)	0.3–1.2 (C/m^2)
		374.6–1498.5 (C/m^2)	1.56–1.73 (C/m^2)	1.79–3.33 (C/m^2)			
e_{31}						−0.2 to −0.5 (C/m^2)	−0.1 to −0.5 (C/m^2)
Method	Exp.	Exp.	DFT	Exp.	DFT	DFT	MDS
Ref.	Fan et al. (2006)	Zhu et al. (2008)	Xiang et al. (2006)	Zhao et al. (2004)	Li et al. (2007)	Dai et al. (2011)	

reported in the experiments (Zhao et al. 2004; Fan et al. 2006; Zhu et al. 2008) and DFT studies (Xiang et al. 2006; Li et al. 2007; Dai et al. 2011), where the obtained values of e_{33} were found to be larger than the bulk value. In Zhao et al. (2004), the enhanced piezoelectric response was partially attributed to the perfect single crystallinity and the low density of defects at the nanoscale. This theory, to some extent, is confirmed by the fact that e_{33} of the polycrystalline ZnO nanofilms is almost the same as the bulk value (Bdikin et al. 2010) and also in accordance with Fan et al. (2006) where the authors believed that small e_{33} (smaller than the bulk value) obtained might be a result of relatively high density of defects in the large ZnO films. The free boundary conditions on the lateral surface of nanowires or nanofilms (Zhao et al. 2004; Xiang et al. 2006) were also considered as a physical origin leading to the strong piezoelectric response at the nanoscale, i.e., the free relaxation of the surface atoms along the lateral direction of nanofilms/nanowires would lead to an increase of the strain, which, in turn, yields an effective $e_{33} = e_{33}^b - \nu e_{13}^b > e_{33}^b$ where ν (>0) is Poisson's ratio and e_{13}^b (<0) and e_{33}^b are piezoelectric coefficients of bulk ZnO. However, the small e_{33} of the polycrystalline ZnO nanofilms indicates that the perfect single crystallinity is more important in determining the piezoelectric effect of ZnO nanocrystal (Bdikin et al. 2010). Moreover, as mentioned before the atomistic simulations in Li et al. (2007) and Dai et al. (2011) predicted weak piezoelectric responses for the perfect ZnO single nanocrystal (i.e., no defects) with the relaxation of surface atoms, which can also be observed from Table 2.1. Obviously, the small EPCs obtained in these simulations cannot be understood based on the physical mechanisms proposed above. Thus, further efforts were made to reveal the physics behind the unique piezoelectric effect at the nanoscale. Following this, the effect of the surface piezoelectricity was identified as one of the major factors that would exert significant influence on the electromechanical behavior of PNs (Dai et al. 2011; Miller and Shenoy 2000; Wang and Feng 2009, 2010; Liu and Rajapakse 2010; Assadi et al. 2010; Assadi and Farshi 2010; Huang and Yu 2006; Yan and Jiang 2010, 2011; Li et al. 2011; Zhang and Wang 2012; Zhang et al. 2012a, b).

2.3 Effect of Piezoelectric Surface Layer

It is understood that the miniaturization of materials into the nanoscale significantly increases their surface-to-volume ratio and, thus, substantially enhances the effect of thin surface layers, where atoms experience an environment different than that in the inner section. As reviewed above, one of the surface effects, i.e., the free relaxation of the surface atoms in lateral direction, was thought to be responsible for the enhanced piezoelectric effect at the nanoscale (Zhao et al. 2004; Xiang et al. 2006). In addition to the less constrained atoms, the surface layer also experiences structural changes (e.g., the change in atomic bond length) relative to the bulk materials at the inner sections. In general, these alterations lead to nonzero

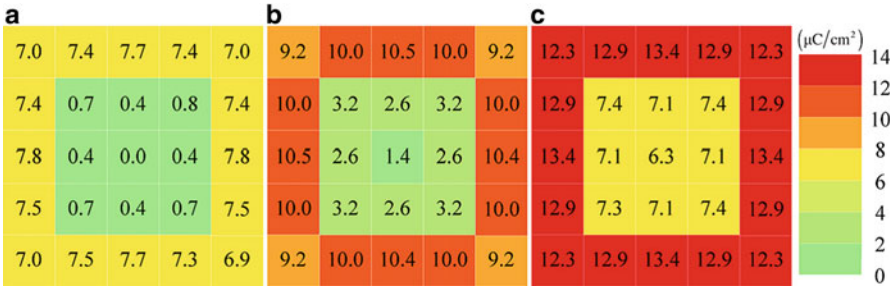

Fig. 2.1 Evolution of axial polarization distribution along the cross section of a $BaTiO_3$ nanowire under different axial strains. (**a**) −0.5 % strain, (**b**) 0.0 % strain, and (**c**) 0.5 % strain (Zhang et al. 2010)

residual surface stress and the surface material properties distinct from those of the bulk materials. To examine the effect of elastic surface layer(s), a core-shell or core-surface (CS) model was developed and efficiently utilized to examine the effect of residual surface stress and surface elasticity on the elastic properties and the mechanical responses of nanomaterials (Miller and Shenoy 2000; Wang and Feng 2009, 2010; Liu and Rajapakse 2010; Assadi et al. 2010; Assadi and Farshi 2010). In the CS model, nanomaterials are treated as equivalent composite materials consisting of the bulk material wrapped by a two-dimensional (2D) surface layer.

The "core-surface" concept was extended by Huang and Yu (2006) to evaluate the effect of piezoelectric surface on the structural responses of PNs. Along with the surface residual stress and surface elasticity, the surface piezoelectricity was considered for the first time in the analysis of PNs. The significant influence of surface piezoelectricity was further confirmed based on ab initio and MDS studies (Zhang et al. 2009, 2010). For example, the distributions of polarization due to strain were obtained in Zhang et al. (2010) for a 2 nm thick $BaTiO_3$ nanowire. As shown in Fig. 2.1, the results of Zhang et al. (2010) indicated that the strain-induced polarization on the surface is greater than that found in the core (bulk) section. Motivated by the study of Huang and Yu (2006), Yan and Jiang (2010, 2011) and Li et al. (2011) incorporated the surface piezoelectricity into the CS beam model and studied the bending, vibration, and buckling of one-dimensional (1D) piezoelectric nanowires and nanofilms. Most recently, a sandwich-plate model was developed based on the "core-surface" concept to study the static and dynamic behaviors of 2D piezoelectric nanofilms (Zhang and Wang 2012; Zhang et al. 2012a, b). The influence of the surface piezoelectricity on the EPCs was also discussed briefly in the works of Zhang and Wang (2012) and Zhang et al. (2012a, b).

A general theoretical framework of surface piezoelectricity was formulated by Shen and Hu (2010) for PNs. Consistent with the existing piezoelectric CS models, they stated that the total internal energy density (W) consists of the surface energy density (U_s) and the energy density of the core section (U_b). As a result, the piezoelectricity of both the surface layer and the core section contributes to the

effective piezoelectric properties or the EPCs of PNs. This theory of surface piezoelectricity enabled Dai et al. (2011) to conduct a comprehensive study on the effect of piezoelectric surface on EPCs. Based on $W = U_s/h + U_b$, they derived the analytical formulae for the EPCs (e_{ij3}^{eff}) of the nanofilms with thickness h (Dai et al. 2011):

$$e_{ij3}^{\text{eff}} = e_{ij3}^{b} + n\frac{e_{ij3}^{s}}{h} \tag{2.1}$$

where e_{ij3}^{b} and e_{ij3}^{s} are the piezoelectric coefficients of the inner bulk material and 2D surface layer, respectively, and n denotes the number of the contributing surfaces. It is interesting to see that the MDS and DFT simulations in Li et al. (2007) and Dai et al. (2011) were well fitted into Eq. (2.1) with almost constant e_{ij3}^{b} and e_{ij3}^{s} for $n = 2$ or 4 and h increasing from 0.3 to 10 nm. For a given $e_{31}^{b} = -0.59\,\text{C/m}^2$ and $e_{33}^{b} = 1.22\,\text{C/m}^2$ of bulk ZnO, the DFT (or MDS) yields $e_{31}^{s} = 0.1 \times 10^{-9}$ C/m, $\left(0.29 \times 10^{-9}\ \text{C/m}\right)$, and $e_{33}^{s} = -0.15 \times 10^{-9}$ C/m $\left(-0.29 \times 10^{-9}\ \text{C/m}\right)$ for surface layers of ZnO nanofilms. In these studies, the EPCs were also calculated for $BaTiO_3$ and $SrTiO_3$ nanofilms and similar size dependence was also achieved. These results, to a large extent, confirm that the size-dependent EPCs obtained for the PNs attributed to the surface piezoelectricity (Dai et al. 2011). In other words, the piezoelectric CS model can be used for the interpretation of the atomistic simulations on relatively large PNs studied in Dai et al. (2011). Furthermore, it is noted that the surface layer and the bulk materials of ZnO exhibit reverse piezoelectric effects characterized by the piezoelectric coefficients of opposite signs. Thus, the surface piezoelectricity reduces the overall piezoelectric effect of ZnO nanocrystals and leads to the EPCs lower than the bulk values. This is in contrast to the effect of free relaxations of the surface atoms, which, as argued in Zhao et al. (2004) and Xiang et al. (2006), would enhance the resultant piezoelectric effect. We believe that the above two effects of the surface layers were considered naturally in the DFT and MDS studies (Dai et al. 2011). Thus, the low EPCs suggest that the effect of surface piezoelectricity could be even stronger than that of free relaxation of the surface atoms.

On the other hand, the theory of surface piezoelectricity (see Eq. (2.1)) is unable to explain the enhancement of piezoelectric response observed in the experiments (Zhao et al. 2004; Zhu et al. 2008; Bdikin et al. 2010) and earlier atomistic simulations (Xiang et al. 2006; Li et al. 2007) for ZnO nanocrystal. It thus still remains a big challenge to develop a universal theory that is able to account for the large scattering of the EPCs summarized in Table 2.1 and the different size dependence predicted in the simulations (Xiang et al. 2006; Li et al. 2007; Dai et al. 2011). The current authors believe that, in addition to the uncertainty in the experiments and the discrepancy in the simulation theories, the difference among the existing studies may be due to the fact that multifactors instead of single factor influence the piezoelectric responses of PNs. Specifically, in different cases, e.g., at distinct size scale, the key factor may switch from one to another. For example, as

far as very thin PNs (e.g., the feature size is of the order of 1 nm) are concerned with the quantum effect may be predominant over the surface effects. The change of the crystal constant of such thin PNs with their geometric size may also affect their EPCs significantly (Xiang et al. 2006). The effect of these factors, however, is negligible for relatively large PNs (e.g., the feature size of the order of 10 nm) where the surface piezoelectricity dominates. Moreover, for synthesized PNs with geometric size of up to hundred nanometers, the surface effect should also decline as the surface energy decreases at large size. The exceptional piezoelectric effect of synthesized PNs (Zhao et al. 2004; Zhu et al. 2008) is likely due to the specific microstructures of the tested samples, the boundary conditions enforced in the experiments, as well as other factors in the experimental setups due to some unknown physical mechanisms. Indeed, great efforts are required to further advance the physics of the piezoelectricity in a nanoscale world.

2.4 Piezoelectricity of Nanostructures

Evidently the continuous attempts to estimate the size-dependent EPCs for PNs are crucial for the design of the PN-based smart nanodevices and nanoelectromechanical systems. Here, it should be emphasized that when put into practical use, PNs serve as not only materials characterized by material constants but also structures (e.g., beams, plates, or cylinders) which are able to sustain different external loadings, e.g., extension, bending, and torsion. As reported previously, in the latter case, the nanostructures may exhibit effective material properties depending on the deformation patterns (or loading conditions). The typical examples are the loading condition-dependent Young's modulus of carbon nanotubes (Huang et al. 2006) and ZnO nanowires (He et al. 2009; Xu et al. 2010). Nevertheless, in all existing theoretical and experimental measurement of EPCs, effective e_{33} and e_{31} were extracted by considering the uniform normal deformation (stresses) generated by an electric field (voltage) or vice versa. Bending or torsion associated with nonuniform deformation (stresses) has never been used. The EPCs obtained in this scenario are the effective material constants relating an electric field to the stresses (stains) in the constitutive relations. The possible loading condition or deformation dependence of EPCs and its influence on the EEM of PNs however have not received enough attention so far.

In fact, as pointed out in Zhang and Wang (2012), Zhang et al. (2012a, b), and Yan and Jiang (2010), (2011), the piezoelectricity of an engineering structure affects its structural responses not only by the voltage (V)-induced stresses (strains) due to the converse piezoelectric effect but also via the electromechanical coupling that changes the EEM associated with specific structural stiffnesses. Consequently, both effects of the piezoelectricity should be taken into consideration in calculating the EPCs of PNs as nanostructures. In what follows two piezoelectric nanostructures studied in Yan and Jiang (2010), (2011), Zhang and Wang (2012), and Zhang et al. (2012a, b) will be considered herein: (1) the 2D piezoelectric

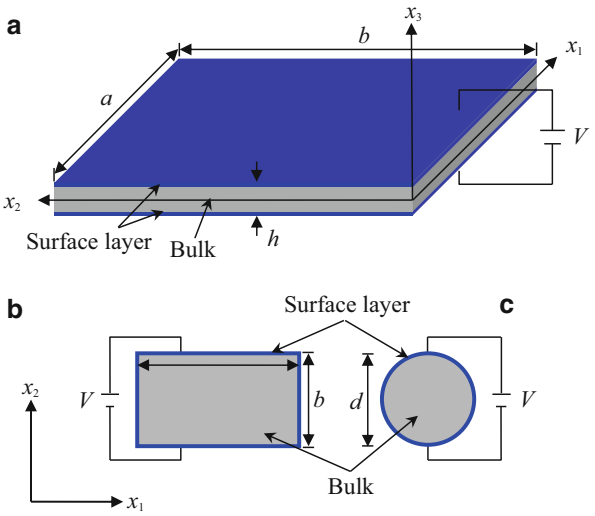

Fig. 2.2 Schematic illustrations of (**a**) a piezoelectric rectangular nanofilm, (**b**) a piezoelectric nanobeam with rectangular cross section, and (**c**) a piezoelectric nanobeam with circular cross section subjected to an electric voltage V

rectangular nanofilms with thickness h and an electric voltage V applied in their thickness direction (Zhang and Wang 2012; Zhang et al. 2012a, b) (Fig. 2.2a) and (2) the 1D piezoelectric nanowires (films) subjected to an electrical voltage V across their cross sections (Yan and Jiang 2010, 2011) (Fig. 2.2b, c). It was shown in Zhang and Wang (2012) and Zhang et al. (2012a, b) that the overall structural responses of the piezoelectric nanofilms are controlled by the membrane stress, N_{ij}; the off-plane stiffness, D_{ijkl}; and in-plane stiffness, K_{ijkl}:

$$N_{ij} = K_{ijkl}\gamma_{kl} + 2\sigma_{ij}^0 + \left(e_{ij3}^b + 2\frac{e_{ij3}^s}{h}\right)V \tag{2.2}$$

$$K_{ijkl} = \left(c_{ijkl} + 2\frac{c_{ijkl}^s}{h}\right)h \tag{2.3}$$

$$D_{ijkl} = \left[c_{ijkl} + 6\frac{c_{ijkl}^s}{h} + \frac{e_{ij3}^b}{k_{33}}\left(d_{kl3}^b + 6\frac{e_{kl3}^s}{h}\right)\right]\frac{h^3}{12} \tag{2.4}$$

Here c_{ijkl}^b and c_{ijkl}^s are elastic moduli, e_{ijkl}^b and e_{ijkl}^s are piezoelectric constants, and k_{33} is dielectric constant. Superscripts b and s represent the parameters of the bulk material and surface layer, respectively. Subscripts i, j, k, and l are equal to 1 or 2. γ_{kl} and σ_{ij}^0 represent in-plane strain and surface residual stresses, respectively. In addition, Yan and Jiang (2010, 2011) showed that for beam-like piezoelectric nanowires, the structural responses are determined by the applied axial force, P; the extensional stiffness, EA; and the bending stiffness, EI. For the nanowires with rectangular cross section of width a and height b (see Fig. 2.2b), we have (Yan and Jiang 2011)

$$P = EA\varepsilon_0 + \left[2\sigma_{11}^0 + \left(e_{31}^b + 2\frac{e_{31}^s}{b}\right)V\right]a \tag{2.5}$$

$$EA = \left(c_{11}^b + 2\frac{c_{11}^s}{b}\right)ab \tag{2.6}$$

$$EI = \left\{c_{11}^b + \left(\frac{6}{b} + \frac{2}{a}\right)c_{11}^s + \frac{e_{31}}{k_{33}}\left[e_{31}^b + \left(\frac{6}{b} + \frac{2}{a}\right)e_{31}^s\right]\right\}\frac{ab^3}{12} \tag{2.7}$$

Those derived for the nanowires with circular cross section of diameter d (Fig. 2.2c) are as follows (Yan and Jiang 2011):

$$P = EA\varepsilon_0 + \left[2\sigma_{11}^0 + \left(e_{31}^b + \frac{8}{\pi}\frac{e_{31}^s}{d}\right)\frac{\pi}{4}V\right]d \tag{2.8}$$

$$EA = \left(c_{11}^b + \frac{8}{\pi}\frac{c_{11}^s}{d}\right)\frac{\pi d^2}{4} \tag{2.9}$$

$$EI = \left[c_{11}^b + 8\frac{c_{11}^s}{d} + \frac{e_{31}^b}{k_{33}}\left(e_{31}^b + 8\frac{e_{31}^s}{d}\right)\right]\frac{\pi d^4}{64} \tag{2.10}$$

2.4.1 *Effective Piezoelectric Coefficients* $\mathbf{e}_{31}^{e1}$ *and* $\mathbf{e}_{31}^{e2}$

Based on Eqs. (2.2) to (2.10), we will first derive e_{31}^{e1} of the PNs considering the contribution of piezoelectricity to the EEM of the PNs. This effect of piezoelectricity has never been considered before in piezoelectric measurement. We shall first obtain the formulae of EEM. In the structural stiffness Eqs. (2.3), (2.4), (2.5), (2.7), (2.9), and (2.10), the coefficients represent the EEM of the nanostructures and thus are tabulated in Table 2.2. As noted in Table 2.2, EEM not only depends on the feature size of the PNs (e.g., the thickness h or the diameter d) but also varies with the deformation of the PNs. The origin of these unique features is the surface piezoelectricity and/or surface elasticity, whose effect is inversely proportional to the geometric size of the PNs and turns out to be more significant for the EEM associated with off-plane deformation, e.g., bending or off-plane torsion. It is also noted that the piezoelectricity of the PNs only contributes to c_{11} (note $c_{11} = c_{22}$ for an isotropic material) associated with bending but has no influence on the EEM associated with uniform tension/compression or torsion.

Next, let us calculate e_{31}^{e1} characterizing the electromechanical coupling of the nanostructures, i.e., the effect of piezoelectricity on the EEM. To this end, we shall concentrate on the piezoelectric terms found in the function of c_{11}^{e1} and c_{11}^{e2} (see Table 2.2). First $e_{31}^b\left[e_{31}^b + (6/h)e_{31}^s\right]/k_{33}$ can be obtained for the piezoelectric nanoplates (films). At $e_{31}^s = 0$ it reduces to $(e_{31}^b)^2/k_{33}$ providing the effect of

Table 2.2 Formulae derived for the effective elastic modulus c_{11}^{e1} and c_{11}^{e2}, and effective piezoelectric coefficients e_{31}^{e1} and e_{31}^{e2} of piezoelectric nanofilms and nanobeams subjected to various deformations

	Nanofilms	Nanobeams (rectangular)	Nanobeams (circular)
c_{11}^{e1}	$c_{11}^{b}+2\frac{c_{11}^{s}}{h}$	$c_{11}^{b}+2\frac{c_{11}^{s}}{h}$	$c_{11}^{b}+\frac{8}{\pi d}c_{11}^{s}$
c_{11}^{e2}	$c_{11}^{b}+6\frac{c_{11}^{s}}{h}+\frac{e_{31}^{b}}{k_{33}}\left(e_{31}^{b}+\frac{6}{h}e_{31}^{s}\right)$	$c_{11}^{b}+\left(\frac{6}{b}+\frac{2}{a}\right)c_{11}^{s}+\frac{e_{31}^{b}}{k_{33}}\left[e_{31}^{b}+\left(\frac{6}{b}+\frac{2}{a}\right)e_{31}^{s}\right]$	$c_{11}^{b}+\frac{8}{\pi d}c_{11}^{s}+\frac{e_{31}^{b}}{k_{33}}\left(e_{31}^{b}+\frac{8}{\pi d}e_{31}^{s}\right)$
e_{31}^{e1}	$\sqrt{\left(e_{31}^{b}\right)^{2}+\left(\frac{6}{h}\right)e_{31}^{b}e_{31}^{s}}$	$\sqrt{\left(e_{31}^{b}\right)^{2}+\left(\frac{6}{h}+\frac{2}{b}\right)e_{31}^{b}e_{31}^{s}}$	$\sqrt{\left(e_{31}^{b}\right)^{2}+\left(\frac{8}{\pi h}\right)e_{31}^{b}e_{31}^{s}}$
e_{31}^{e2}	$e_{31}^{b}+2\frac{e_{31}^{s}}{h}$	$e_{31}^{b}+2\frac{e_{31}^{s}}{h}$	$e_{31}^{b}+\frac{8}{\pi h}e_{31}^{s}$

piezoelectricity on c_{11} of classical piezoelectric plates without surface piezoelectricity. Therefore, considering the nanofilms as equivalent classical plates with piezoelectric constant e_{31}^{e1}, one can have $\left(e_{31}^{e1}\right)^2 = e_{31}^b\left[e_{31}^b + (6/h)e_{31}^s\right]$ which yields $e_{31}^{e1} = \sqrt{e_{31}^b\left[e_{31}^b + (6/h)e_{31}^s\right]}$. Following a similar procedure, one is able to derive e_{31}^{e1} for the two nanobeams studied here. The results are also shown in Table 2.2.

Subsequently, we shall turn to e_{31}^{e2} characterizing the V-induced forces on the piezoelectric nanofilms and nanowires, i.e., the relation between the stresses (deformation) and an electric voltage (field). This is the piezoelectric effect we usually refer to and was considered in previous piezoelectric measurements of PNs (Zhao et al. 2004; Fan et al. 2006; Wang et al. 2006a, b; Zhu et al. 2008; Bdikin et al. 2010; Espinosa et al. 2012; Fang et al. 2013; Zhang et al. 2014). The V-induced forces of the PNs extracted from Eqs. (2.2), (2.5), and (2.8) are $\left(e_{ij3}^b + 2e_{ij3}^s/h\right)V$, $\left(e_{31}^b + 2e_{31}^s/b\right)aV$, and $\left[e_{31}^b + (8/\pi)e_{31}^s/d\right]\pi dV/4$, respectively. By assuming $e_{ij3}^s = 0$ the V-induced forces of the corresponding macroscopic structures can be achieved as $e_{ij3}^b V$, $e_{31}^b aV$, and $e_{31}^b \pi dV/4$. Subsequently, e_{31}^{e2} of PNs can be easily obtained by equating the V-induced forces of PNs to the forces of corresponding macroscopic structures. The results are presented in Table 2.2 in comparison with e_{31}^{e1}.

It may be observed from Table 2.2, EPCs of PNs are also size-dependent as a result of the effect of surface piezoelectricity. Such an effect increases with decreasing geometric size of the nanofilms or nanobeams. In particular, it is noted that e_{31}^{e2} achieved for the quasi-2D piezoelectric nanofilms via the voltage-stress relation is identical to Eq. (2.1) (Dai et al. 2011) derived based on the theory of surface piezoelectricity (Zhang et al. 2009). Other formulae in Table 2.2 are reported for the first time in the literature. From Table 2.2 it follows that, in principle, the general form of EPC function does not exist. Thus, a particular form of EPC should be selected for corresponding deformation experienced by the PNs. For example, when uniform tension or compression is concerned, e_{31}^{e2} should be incorporated, whereas e_{31}^{e1} is not required as there is no bending. However, both e_{31}^{e1} and e_{31}^{e2} may be used when more general cases are considered, e.g., the transverse vibration or the buckling of nanofilms and nanobeams, where both bending stiffness and normal prestresses may significantly influence (Yan and Jiang 2010, 2011; Zhang and Wang 2012; Zhang et al. 2012a, b).

2.4.2 *Importance of Coefficients* $\mathbf{e_{31}^{e1}}$ *and* $\mathbf{e_{31}^{e2}}$

As shown in Sect. 2.4.1, in nano-piezoelectricity theory, there exist two types of EPCs for PNs, i.e., e_{31}^{e1} and e_{31}^{e2}, which reflect different physical mechanisms of the piezoelectric effect. It is thus of interest to evaluate (1) the effect of the surface piezoelectricity on the two EPCs and (2) the importance of the two EPCs for

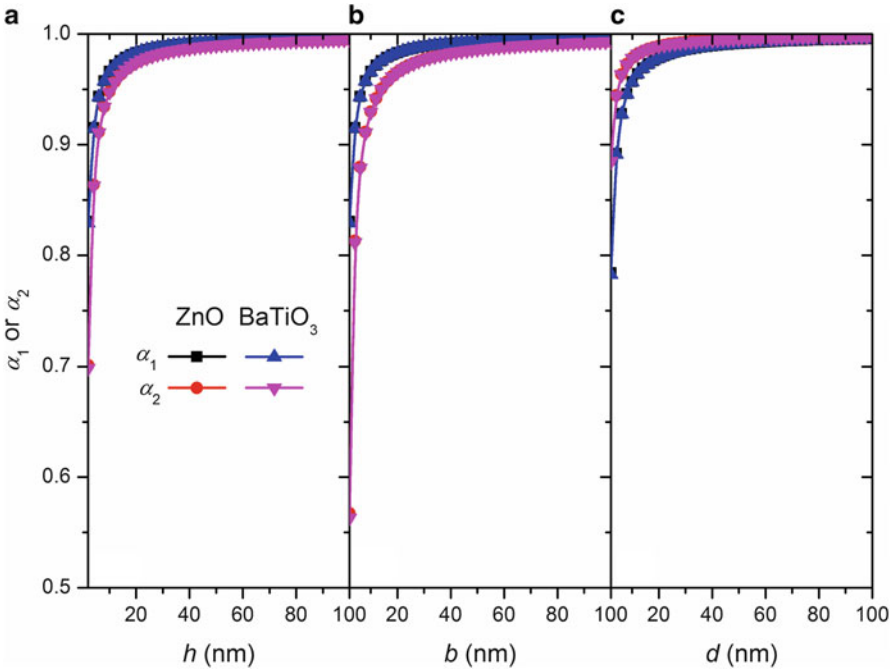

Fig. 2.3 The ratios $\alpha_1 = e_{31}^{e1}/e_{31}^{b}$ and $\alpha_2 = e_{31}^{e2}/e_{31}^{b}$ calculated for ZnO and $BaTiO_3$ (**a**) nanofilms with thickness h (Fig. 2.2a), (**b**) nanowires with rectangular cross section of height b (Fig. 2.2b), and (**c**) nanowire with circular cross section of diameter d (Fig. 2.2c)

Table 2.3 Material properties of ZnO and $BaTiO_3$ used in Figs. 2.3, 2.4, and 2.5

	ZnO	$BaTiO_3$
c_{11} (GPa)	209.7	222
e_{31}^{b} (C/m^2)	−0.59	−4.1
e_{31}^{s} (10^{-9} C/m)	0.1	0.7
k_{33} (pF/m)	78.89	1142.17

c_{11} is the elastic modulus, e_{31}^{b} and e_{31}^{s} are the piezoelectric constants for the bulk materials and surface layer, and k_{33} is dielectric constant

existing PNs of different configurations. To achieve the first goal, the ratios $\alpha_1 = e_{31}^{e1}/e_{31}^{b}$ and $\alpha_2 = e_{31}^{e2}/e_{31}^{b}$ are calculated in Fig. 2.3 for nanofilms and nanobeams against their feature size. The material properties of ZnO and $BaTiO_3$ considered in Fig. 2.3 are summarized in Table 2.3. It is seen from Fig. 2.3 that α_1 and $\alpha_2 < 0.95$, i.e., e_{31}^{e1} and $e_{31}^{e2} < 0.95e_{31}^{b}$, at the feature size around 10 nm or smaller. Thus, the surface piezoelectricity affects the EPCs of ZnO and $BaTiO_3$ nanocrystal significantly (say, >5 %) when the feature size is of the order of 10 nm. In Fig. 2.3 such an effect increases to 10 % (i.e., α_1 and $\alpha_2 < 0.9$ or e_{31}^{e1} and $e_{31}^{e2} < 0.9e_{31}^{b}$) when the feature size is down to around 5 nm. On the other hand, at the feature size much

larger than 10 nm, the effect of the surface piezoelectricity becomes negligible. These results are found to be in a good agreement with those predicted by Dai et al. (2011).

According to the definition illustrated above, e_{31}^{e2} characterizes the contribution of piezoelectricity to the initial stress on the PNs. The surface residual stress σ^0 of ~1 N/m (Zhang and Wang 2012; Zhang et al. 2012a, b) is also a part of this initial stress and is identified as a major factor that can substantially affect the structural responses of PNs (Yan and Jiang 2010, 2011; Zhang and Wang 2012; Zhang et al. 2012a, b). Thus, to show the significance of e_{31}^{e2}, we computed the ratio $\beta = \sigma/\sigma^0$ in Fig. 2.4 for the same PNs studied in Fig. 2.3. Here $\sigma = e_{31}^{e2}V$ is the V-induced initial stress and σ^0 (~1 N/m) represents the surface residual stress. Figure 2.4 shows that at low voltage $V = 0.1$–0.5 V, σ is up to 1.2 ($BaTiO_3$) and 2 (ZnO) times that of σ^0 and will further increase at higher V. The importance of e_{31}^{e2} can thus be manifested here as σ due to e_{31}^{e2} which can be even greater than σ^0. Next, the importance of e_{31}^{e1} was evaluated in Fig. 2.5 by calculating the ratio $\gamma = \left(e_{31}^{e1}e_{31}^{e1}/k_{33}\right)/c_{11}$, where $e_{31}^{e1}e_{31}^{e1}/k_{33}$ is the increase of c_{11} (associated with bending in Table 2.2) due to the electromechanical coupling characterized by e_{31}^{e1}. Figure 2.5 shows that the increase of the elastic modulus is considerable (~6 %) for ZnO nanocrystal but negligible (~2 %)

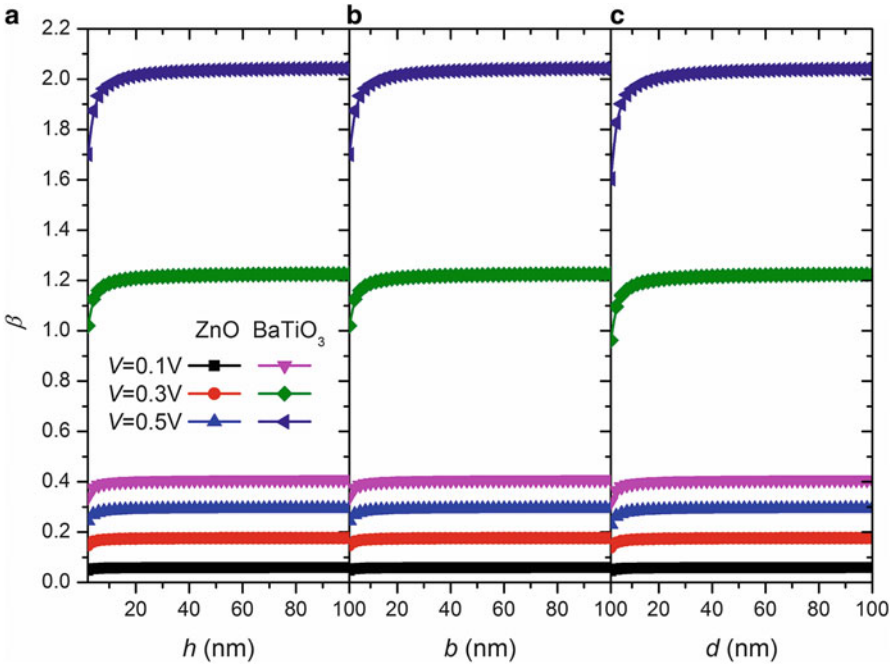

Fig. 2.4 The ratio of $\beta = \sigma/\sigma^0$ calculated for ZnO and $BaTiO_3$ (**a**) nanofilms with thickness h (Fig. 2.2a), (**b**) nanowires with rectangular cross section of height b (Fig. 2.2b), and (**c**) nanowires with circular cross section of diameter d (Fig. 2.2c). Here $e_{31}^{e2}V$ is the stress induced by an electrical voltage V due to e_{31}^{e2} and σ^0 (~1 N/m) is the residual surface stress

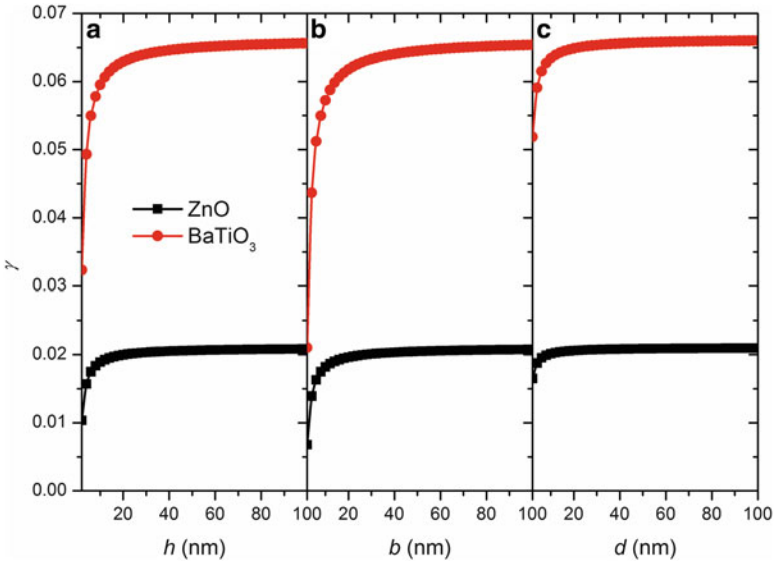

Fig. 2.5 The ratio $(e_{31}^{e1}e_{31}^{e1}/k_{33})/c_{11}$ calculated for ZnO and $BaTiO_3$ nanofilms with thickness h (Fig. 2.2a), nanowires with rectangular cross section of height b (Fig. 2.2b), and nanowires with circular cross section of diameter d (Fig. 2.2c). Here $e_{31}^{e1}e_{31}^{e1}/k_{33}$ represents the contribution of piezoelectricity to the effective elastic modulus c_{11}^{e2} and c_{11} is the elastic modulus of the bulk materials

for the $BaTiO_3$ nanostructures. Here it is worth noting that in Figs. 2.3, 2.4, and 2.5, the values of piezoelectric constants determined using MDS (Dai et al. 2011) are shown, which are even lower than the bulk values. Nevertheless, the existing experiments (Zhao et al. 2004; Wang et al. 2006a, b; Zhu et al. 2008) showed that the e_{33} of ZnO at the nanoscale can be increased to one to three orders of magnitude greater than the bulk value, by, e.g., doping with ferroelectric vanadium (Wang et al. 2006a, b). In this case, the value of e_{31}^{e1} and e_{31}^{e2} would also increase and thus greatly increase the ratios $\beta = \sigma/\sigma^0$ and $\gamma = \left(e_{31}^{e1}e_{31}^{e1}/k_{33}\right)/c_{11}$. In other words, the EEM (Table 2.2) and σ of PNs would rise by orders of magnitude. In these particular cases, both e_{31}^{e1} and e_{31}^{e2} play a critical role in structural responses of PNs and thus have to be taken into consideration in static deformation and vibration and buckling analyses of PNs.

2.5 Influence of Piezoelectricity on Mechanical Responses of Nanostructures

In preceding sections we have summarized the measurement of the piezoelectricity at the nanoscale and also compared the piezoelectricity at the nanoscale to that at the macroscale. In this section we will discuss how the nanoscale piezoelectricity

influences the mechanical responses (statics and dynamics) of piezoelectric nanostructures. Specifically, regarding the static behavior, we will study the piezoelectric potential of GaN nanotubes. In terms of the dynamics, we will show the piezoelectric effect on the intrinsic dissipation in oscillating GaN nanobelts.

2.5.1 *On the Piezoelectric Potential of GaN Nanotubes*

2.5.1.1 Material Properties of GaN Nanotubes

In this section, MDS were employed to calculate the equivalent elastic, piezoelectric, and dielectric properties of GaN nanotubes. In this study, we consider the most common GaN nanotube whose growth direction is along the [001] crystalline direction. The nanotubes have hexagonal cross sections with a sixfold symmetry and lateral surfaces {100} (Han et al. 2000) as shown in Fig. 2.6a. Such shapes have been observed in GaN nanotubes grown by chemical-thermal evaporation (Han et al. 2000). Initially, Ga and N atoms are arrayed in a single-crystalline wurtzite structure with the lattice constants, $a = 3.19$ Å and $c = 5.20$ Å (Bere and Serra

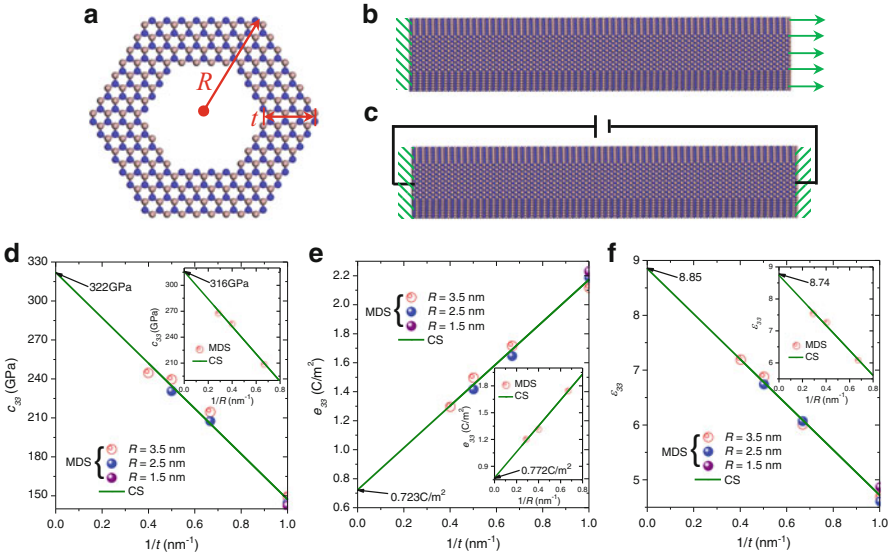

Fig. 2.6 (**a**) Molecular representation of the cross section of a GaN nanotube. The radius is R and the wall thickness is t. The simulation setup for the measurement of (**b**) the elastic property, and (**c**) the piezoelectric and dielectric properties of GaN nanotubes. (**d**) The elastic constant c_{33}, (**e**) the piezoelectric coefficient e_{33}, and (**f**) the dielectric constant ε_{33} as a function of the inverse of the wall thickness, $1/t$, of the nanotubes with various radii R, which are based on MDS and CS model. The insets in (**d**)–(**f**) show the corresponding results for solid GaN nanowire as a function of the inverse of their radius, $1/R$ (Zhang and Meguid 2015a)

2006). The length L of the nanotubes is fixed at 30 nm, whereas the radius R and the wall thickness t of the hexagonal cross section were allowed to change to study the size-dependent material properties of nanotubes.

Classical MDS were conducted in this study, and the NVT ensemble (constant number of particles, volume, and temperature) was employed to update the positions and velocities of the atoms after each time step by using the Nosé-Hoover temperature thermostat (Nosé 1984). The interactions between Ga-Ga, N-N, and Ga-N were described by the Stillinger-Weber (SW) potential (Stillinger and Weber 1985), which contains a two-body term φ_2 and a three-body term φ_3, as follows:

$$\varphi_2(r_{ij}) = A\delta\left(B\left(\frac{r_{ij}}{d}\right)^{-4} - 1\right)\exp\left(\left(\frac{r_{ij}}{d} - r\right)^{-1}\right), \frac{r_{ij}}{d} < r, \tag{2.11}$$

$$\varphi_2(r_{ij}) = 0, \frac{r_{ij}}{d} \geq r, \tag{2.12}$$

$$\varphi_3(r_{ij}, r_{ik}, \theta_{ijk}) = \delta C\exp\left(\gamma(r_{ij} - r)^{-1} + \gamma(r_{ik} - r)^{-1}\right)\left(\cos\theta_{ijk} + \frac{1}{3}\right)^2 \tag{2.13}$$

Here, subscripts i, j, and k represent the different atoms in the system; δ is the cohesive energy of the bond; d is the length unit; r is the cutoff distance; r_{ij} is the length of the bond ij; and θ_{ijk} is the angle formed by the ji and the jk bonds. Other parameters, A, B, and C, are dimensionless fitting parameters adjusted to match the material properties. The values used in this study are taken from Bere and Serra (2006). The SW potentials have been used to reproduce bulk structures and mechanical properties; they have been successfully employed to evaluate the material properties of single-crystal GaN nanowires (Zhang et al. 2013; Zhang 2014; Minary-Jolandan et al. 2012; Wang et al. 2007) and fracture of single-crystal GaN nanotubes (Wang et al. 2006a, 2008). These calculations have demonstrated that the empirical SW potentials for GaN can be employed to study the mechanical behaviors of single-crystal GaN structures. In addition, the potentials can handle dangling bonds, wrong bonds, and excess bonds in bulk GaN very well. Therefore, these potentials are proven to be reliable in characterizing the mechanical responses of GaN nanotubes.

As a quasi-1D nanostructure, the elastic, piezoelectric, and dielectric properties of the GaN nanotubes in the axial direction (c-axis) are of major concern and can be, respectively, characterized by the axial elastic constant c_{33}, piezoelectric coefficient e_{33}, and dielectric constant k_{33}. At the beginning of all simulations of these material properties, the equilibrium of the initial structure was achieved corresponding to the lowest energy of the nanotube structure in 100 ps. After the full relaxation, different treatments were applied to calculate the material properties (see Fig. 2.6b, c) and are discussed briefly below. Here all MDS were conducted using the open-source LAMMPS (Plimpton 1995) under room temperature (300 K) and without periodic boundary conditions.

Determination of the Elastic Property

To measure the elastic constant c_{33}, one end of the nanotube was pulled along the axial direction while the other end was fixed (Fig. 2.6b). The deformation of the nanotube was then measured by the axial strain λ_3, which generated a tensile stress σ_3 in the nanotubes. Here, the tensile stress σ_3 was taken as the arithmetic mean of the local stresses on all atoms, as follows:

$$\sigma_3 = \frac{1}{N}\sum_{i=1}^{N}\frac{1}{V_i}\left(m_i v_3^i v_3^i + \frac{1}{2}\sum_{j\neq i}^{N} F_3^{ij} r_3^{ij}\right) \tag{2.14}$$

Here m_i is the mass of atom i; v_3^i is the velocity component in the axial direction of atom i; F_3^{ij} refers to the axial component of the interatomic force between atoms i and j; r_3^{ij} is the interatomic distance in the axial direction between atoms i and j; V_i refers to the volume of atom i, which is assumed as a hard sphere in a closely packed undeformed crystal structure; and N is the number of atoms. For small strain case, i.e., $\lambda_3 \leq 0.01$, the elastic constant c_{33} can be obtained from the slope of the linear $\sigma_3 - \lambda_3$ curve since $c_{33} = \partial\sigma_3/\partial\lambda_3$ for structure under small deformation.

Determination of the Piezoelectric Property

In the measurement of the piezoelectric coefficient e_{33}, we fixed the two ends of the nanotubes. It is worth mentioning that simulation process was conducted after its initial relaxation to avoid prestraining the nanotube structure. Then, an electric field E_3 was applied to the nanotubes along the axial direction (see Fig. 2.6c). The external force on ion i due to the electric field can be expressed as $F_i = q_i E_3$, where q_i is the charge on ion i. Finally, the nanotube was relaxed again to reach a new equilibrium state. Following that, the stress σ_3 in the axial direction is calculated based on Eq. (2.12). The piezoelectric coefficient e_{33} can then be calculated as the negative slope of the $\sigma_3 - E_3$ curve, since it is defined as $e_{33} = -\partial\sigma_3/\partial E_3$ (Zhang et al. 2013).

Determination of the Dielectric Property

The dielectric constant k_{33} can be defined as $k_{33} = k_0(1 + \chi_{33})$ with $\chi_{33} = (\partial P_3/\partial E_3)/k_0$ being the electric susceptibility of the material (Zhang 2014). Here k_0 is the vacuum permittivity and P_3 is the axial polarization density. It is noted that the axial polarization P_3 is mainly determined by the polarization due to the relative displacement between Ga and N atoms, since the polarization between the nucleus and electron cloud is negligible (Zhang 2014). The axial polarization density vector can thus be further written as $P_3 = \sum_{i=1}^{N} x_3^i q_i/\overline{V}$, where x_3^i is the

coordinate along the axial direction of atom i and $\overline{V}$ is the volume of the nanotube. To obtain χ_{33} and k_{33}, we fixed the two ends of the nanotubes after the initial relaxation and applied an electric field E_3 to the nanotube in the axial direction (see Fig. 2.6c). Following this, the nanotube was relaxed again to reach a new equilibrium state. The axial polarization density vector P_3 of this new equilibrium state was obtained according to the above definition. Finally, the dielectric constant k_{33} can thus be determined from the slope of the obtained linear $P_3 - E_3$ curve.

The elastic constant c_{33}, piezoelectric coefficient e_{33}, and relative dielectric constant ε_{33} ($\varepsilon_{33} = k_{33}/k_0$) obtained from the approaches described above are plotted in Fig. 2.6d–f (solid circles) as a function of the inverse of the wall thickness, $1/t$, of nanotubes with various radii R. In addition, based on similar simulation techniques described above, the corresponding results of their solid nanowire counterparts are also measured and presented as insets in Fig. 2.6d–f (solid circles) against the inverse of their radius, $1/R$. It is well known that for the solid nanowire, its cross section is determined based on its radius. As a result, its material properties are generally found to only depend on the nanowire radius due to the small-scale effect (Zhang et al. 2013; Zhang 2014). For example, we can see from the insets of Fig. 2.6d–f that c_{33} and ε_{33} of the nanowires, respectively, increase by 28 and 23 % as their R increases from 1.5 to 3.5 nm. Similarly, in this process, e_{33} is found to decrease by 30 %. Concerning the nanotube structures, we notice that their cross section is not only characterized by R but also by their wall thickness t (see Fig. 2.6a). From Fig. 2.6d–f, we can observe that in nanotubes, the wall thickness t rather than the radius R becomes the major geometric parameter that dominates their material properties. For instance, when $t = 1.5$ nm, all measured c_{33}, e_{33}, and ε_{33} of the nanotubes were found to be around 146 GPa, 2.18 C/m^2, and 4.73, respectively, as R increases from 1.5 to 3.5 nm. However, when R is fixed at 3.5 nm, c_{33} and ε_{33} of the nanotubes increased by 63 and 53 %, respectively, and e_{33} decreased by 39 % as t increases from 1 to 2.5 nm.

2.5.1.2 Core-Surface Model

To understand the size-dependent material properties observed in Sect. 2.5.1.1, we will introduce a CS model in this section. It is known that the reduction in the size of materials to the nanoscale increases their surface-to-volume ratio and substantially enhances the influence of thin surface layers, where atoms experience structure reconstruction. In general, the surface reconstruction leads to a distinct surface layer that is different than its bulk. For example, in Fig. 2.7a we have shown the potential energy distribution of the cross section of a GaN nanotube after the full relaxation. Figure 2.7a illustrates that nanotubes usually hold two surfaces (inner and outer surfaces) and note that the potential energy of these two surfaces is almost the same. However, the potential energy of these two surfaces is different from that of their bulk counterpart. In fact, the potential energy of the two surfaces is about 23 % greater than that of their bulk counterpart (see Fig. 2.7a). It is believed that the

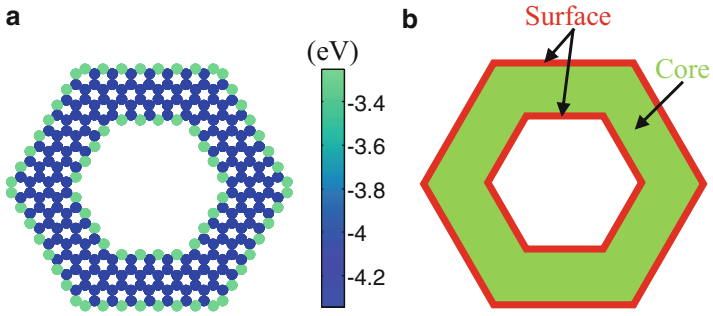

Fig. 2.7 (**a**) The potential energy distribution of the cross section of the GaN nanotube after the full relaxation. (**b**) An equivalent core-surface model of the GaN nanotube (Zhang and Meguid 2015a)

difference of the physics between the surface layer and the bulk part of the nanostructures results in distinct material properties in layer and bulk and is responsible for the size-dependent material properties observed at the nanoscale (Zhang et al. 2014). Inspired by this idea, a CS model was developed to characterize the size-dependent material properties observed in nanowires (Chen et al. 2006; Xu et al. 2010; Zhang et al. 2013; Zhang 2014; Yang et al. 2012; Yao et al. 2012), where a nanowire is modeled as a composite beam consisting of the core section of the bulk material and the surface layer with two distinct properties. In this section, we will extend the idea of the CS model from the nanowire to the present nanotube structure, which holds two surface layers, as depicted in Fig. 2.7b.

The internal energy density W (incorporating surface contributions) is $W = U^b + 6U^s(2R - t)/S$ for the present nanotube with a hexagonal cross section and $W = U^b + 6U^sR/S$ for its solid nanowire counterpart, where U^b is the bulk internal energy density function and U^s is the surface internal energy density. Here S is the area of the cross section and equals to $3\sqrt{3}(2R - t)t/2$ for the nanotube and $3\sqrt{3}R^2/2$ for the nanowire. Thus, the internal energy density can be rewritten as:

For nanotube:

$$W = U^b + \frac{4\sqrt{3}}{3}\frac{U^s}{t}, \tag{2.15}$$

For nanowire:

$$W = U^b + \frac{4\sqrt{3}}{3}\frac{U^s}{R} \tag{2.16}$$

Comparing Eqs. (2.15) with (2.16), we can observe that the geometric parameter determining the size dependency has changed from the radius R for the nanowire to the wall thickness t for the nanotube, which is consistent with the results demonstrated in the MDS (see Fig. 2.6d–f).

Following Huang and Yu (2006), the internal surface energy density can be written as

$$U^s(\lambda_\alpha, E_i) = U^s(0, 0) + \sigma^0_\alpha \lambda_\alpha + \frac{1}{2} c^s_{\alpha\beta} \lambda_\alpha \lambda_\beta + D^0_i E_i + \frac{1}{2} k^s_{ij} E_i E_j + e^s_{\alpha k} \lambda_\alpha E_k \quad (2.17)$$

where σ^0_α and D^0_i can be termed as the surface stress and the surface electric displacement without applying strain and electric field, respectively; $c^s_{\alpha\beta}$, k^s_{ij}, and $e^s_{\alpha k}$, respectively, can be defined as the surface stiffness tensor, surface dielectric tensor, and surface piezoelectric tensor; and λ_α and E_i are the strain and electric field vectors, respectively. After substituting Eq. (2.13) into Eqs. (2.15) and (2.16) and considering $c_{33} = \partial^2 W / \partial \lambda_3^2$ (Xu and Pan 2006), $e_{33} = \partial^2 W / (\partial \lambda_3 \partial E_3)$ (Dai et al. 2010), and $k_{33} = \partial^2 W / \partial E_3^2$ (Zhang 2014), we can obtain the equivalent material properties of the nanotube and nanowire from the CS model as follows:

$$\rho_{33} = \rho^b_{33} + \frac{4\sqrt{3}}{3} \frac{\rho^s_{33}}{\varsigma} \quad (2.18)$$

where ρ^b_{33} and ρ^s_{33} are the bulk and surface elastic constant, piezoelectric coefficient, or relative dielectric constant with $\rho \in (c,\ e,\ \varepsilon)$ and $\varsigma = t$ for the nanotube and $\varsigma = R$ for the nanowire. According to Eq. (2.14), a linear curve fitting to the data was used in the MDS depicted in Fig. 2.6d–f. Following that, we were able to present the bulk elastic constant c^b_{33}, the piezoelectric coefficient e^b_{33}, and the relative dielectric constant ε^b_{33} in Fig. 2.6d–f (the values at $1/t = 0$ or $1/R = 0$). It is to be noted that the respective bulk values c^b_{33}, e^b_{33}, and ε^b_{33} obtained from the present MDS-based CS model are ~319 GPa, ~0.748 C/m^2, and ~8.8, respectively, and are in good agreement with the experimental and ab initio findings ($c^b_{33} = 311$ GPa, $e^b_{33} = 0.73$ C/m^2, and $\varepsilon^b_{33} = 9.7$, respectively) (reported in Levinshtein et al. 2001; Schwarz and Khachaturyan 1997; Bernardini and Fiorentini 1997). Moreover, the results in Fig. 2.6d–f (solid lines) of the present CS model are applicable to large-scale structure, where MDS are not feasible.

2.5.1.3 Piezoelectric Potential in GaN Nanotubes

In this section, the material properties measured in Sect. 2.5.1.1 are employed to study the piezoelectric potential generated in GaN nanotubes under compression. Here, as shown in Fig. 2.8, a GaN nanotube is fixed and grounded at the substrate. Then, an axial force F is applied to the free surface of the nanotube to produce the piezoelectric polarization in the GaN nanotube. Theoretically, to obtain the piezoelectric potential, one needs to solve the following constitutive relations for GaN nanotubes (Zhang 2014):

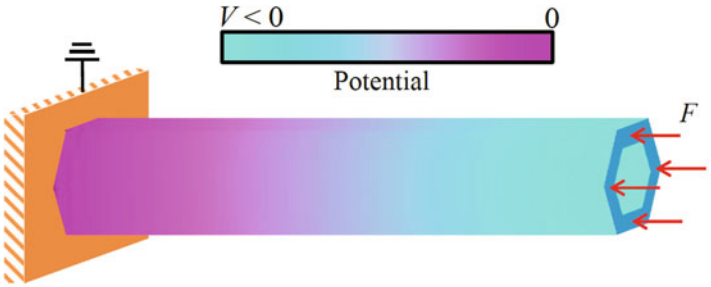

Fig. 2.8 Piezoelectric potential distribution of a GaN nanotube subjected to the uniaxial compression (Zhang and Meguid 2015a)

$$\sigma_\alpha = c_{\alpha\beta}\lambda_\beta - e_{\alpha k}E_k \tag{2.19}$$

$$D_i = e_{i\beta}\lambda_\beta + k_{ik}E_k \tag{2.20}$$

where $c_{\alpha\beta}$, $e_{\alpha k}$, and k_{ik} are the linear elastic constant, the piezoelectric coefficient, and the dielectric constant, respectively. D_i and σ_α are the electric displacement and the stress vectors, respectively. Incorporating constitutive Eqs. (2.19) and (2.20) with the equilibrium equation, geometrical compatibility equation, and Gauss equation in Gao and Wang (2007), we have calculated the piezoelectric potential in the deformed nanotube from the finite element method (FEM). In the present study, the FEM calculation was carried out using the commercial software ANSYS. In this process, the SOLID5 element was selected to describe the piezoelectric nanotubes, and 12,000 elements were chosen after conducting element convergence analysis. The electric potential distribution in a deformed GaN nanotube obtained from the FEM calculation is plotted in Fig. 2.8. It is found that when a compression force is uniformly applied on the free surface of the nanotube, it creates a negative potential between the nanotubes and the substrate. A similar FEM calculation was also conducted to the nanowire to develop its piezoelectric potential. The obtained electric potential distribution of nanowires is found to be comparable to nanotubes, where the potential drops linearly only along the length direction.

To quantitatively evaluate the difference in the piezoelectric potential between nanotubes and nanowires, we have normalized the potential V of the nanotubes by the potential V_0 of the nanowires to be the ratio α. Such a piezoelectric potential ratio is then calculated in Fig. 2.9 (shown in solid squares) as a function of the wall thickness-to-radius ratio, t/R, of the nanotube. Here, the nanotubes and nanowires are assumed to have the same length (30 nm) and radius (3.5 nm) and are subjected to the same force (10 nN). It can be seen from Fig. 2.9 that α increases from 1.34 to 10.27 as t/R decreases from 0.71 to 0.29. In other words, the piezoelectric potential generated in the nanotubes can be up to over nine times greater than that in the nanowires even though they have the same radii. Based on this observation, we can conclude that the nanotubes, especially those with thin wall thickness, can generate much higher piezoelectric potential than their nanowire counterparts. Thus,

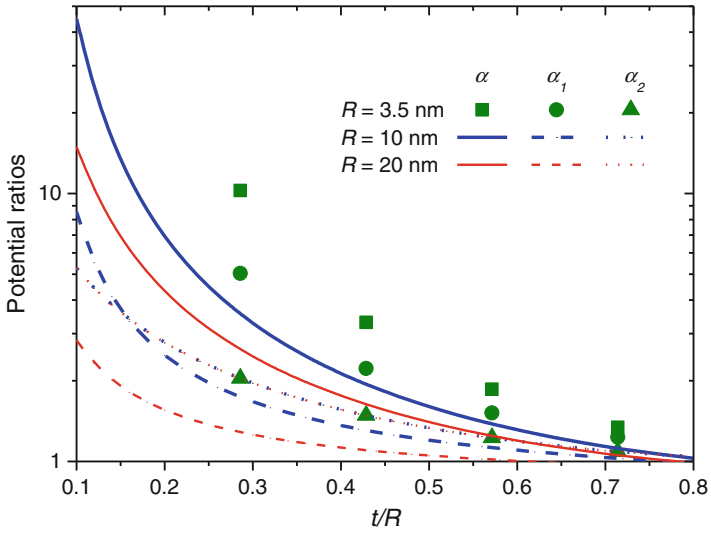

Fig. 2.9 Piezoelectric potential ratios α, α_1, and α_2 as a function of the wall thickness-to-radius ratio, t/R, of the GaN nanotubes with various radii R (Zhang and Meguid 2015a)

compared with its mostly used nanowire counterpart, the nanotube can be considered as a better candidate for building piezotronic nanodevices in terms of its piezoelectric potential generation.

In principle, the difference between the nanowires and nanotubes may originate from their different material properties (see Fig. 2.6d–f) and geometrical properties (different cross sections). To better quantitatively understand the influence of these two factors, we have focused our attention to the following two piezoelectric potential ratios, $\alpha_1 = V_1/V_0$ and $\alpha_2 = V_2/V_0$. Here V_1 is the piezoelectric potential calculated based on the nanotube's material properties and the nanowire's geometrical properties, and V_2 is the piezoelectric potential obtained based on the nanotube's geometrical properties and the nanowire's material properties. Thus, α_1 and α_2 measure the contribution of material and geometrical properties of the nanotubes, respectively. The results of α_1 (solid circles) and α_2 (solid triangles) are plotted in Fig. 2.9 for the nanotubes with $R = 3.5$ nm and t/R decreasing from 0.71 to 0.29. This figure illustrates that the different material and geometrical properties of nanotubes, compared to nanowires, enhance the piezoelectric potential of nanotubes, and this effect becomes more significant for the nanotubes with smaller t/R. Moreover, from Fig. 2.9, we can also observe that the resultant effect of the material and geometrical properties is much stronger than their individual effect. For example, the resultant influence (α) from the material and geometrical properties can enhance the piezoelectric potential of nanotubes with $t/R = 0.29$ by nine times. However, the influence of the material (α_1) properties increases the piezoelectric potential by 400 %, while the influence of the geometrical properties (α_2) increases the piezoelectric potential by 108 %. Thus, it is of interest to examine how these two factors influence the resultant potential. In what follows, we will provide

an analytical expression of the piezoelectric potential of GaN nanotubes/nanowires under compression.

Suppose an axial force F is applied on the GaN nanotube/nanowire, it will produce a uniform uniaxial strain since $\lambda_3 = -F/(c_{33}S)$. Under this uniaxial compressive strain, the wurtzite GaN cell will be deformed so that a bound charge will be generated at both ends of the structure, thus creating a dipole-like piezoelectric potential along the c-axis x_3. Due to the piezoelectric effect, the strain produces a polarization field, $P_3 = e_{33}\lambda_3$. It is known that the lateral and the free surfaces are constrained to have zero surface charge when the base of the nanotube or nanowire is connected to the ground and is at the reference potential. Under this condition, the piezoelectric potential is constant along the cross-sectional area (see Fig. 2.8), and its trend along the c-axis can be obtained by solving the 1D Poisson's equation (Romano et al. 2011): $\partial(k_{33}\partial\varphi/\partial x_3 - P_3)/\partial x_3 = 0$. This equation gives a linear potential profile, $\varphi = P_3 x_3/k_{33}$, where the conditions $E_3(x_3 = L) = -P_3/k_{33}$ and $\varphi(x_3 = 0) = 0$ have been used. The piezoelectric potential is therefore

$$V = \varphi(L) = -F\frac{e_{33}}{c_{33}k_0k_{33}}\frac{L}{S} \tag{2.21}$$

From Eq. (2.17), we can observe that the resultant influence of the material properties and geometrical properties can be considered as the product of their individual effect, i.e., $\alpha = \alpha_1 \cdot \alpha_2$.

In addition, Eq. (2.17) also provides a convenient way to predict the piezoelectric potential of a relatively large nanotube/nanowire by incorporating the CS model (see Eq. (2.14)) into it. Using this technique, we are able to calculate the piezoelectric potential ratios, α, α_1, and α_2, for relatively large nanotubes, e.g., $R = 10$ and 20 nm. The results are plotted as a function of their t/R ratios in Fig. 2.9 (shown by lines). This figure demonstrates that α_2 is independent of R and is only determined by the ratio, t/R. However, α_1 is found to depend on both the ratio t/R and the radius R. Specifically, α_1 decreases with increasing R and almost vanishes ($\alpha_1 \approx 1$) when $R > 135$ nm even for nanotube with extremely small wall thickness-to-radius ratio, e.g., $t/R = 0.1$. This observed R-dependent α_1 and R-independent α_2 further lead to a reduction in α with increasing R as it finally approaches α_2 when R is relatively large, i.e., $R > 135$ nm. In addition, we can also observe from this figure that the contribution of the material properties (measured by α_1) is stronger than that of the geometrical properties (measured by α_2) for a relatively small radius of nanotube, e.g., $R = 3.5$ nm. However, due to the R-dependent α_1 and R-independent α_2, the contribution of the material properties is negligible compared to the geometrical properties when a relatively large nanotube is considered, e.g., $R = 20$ nm.

Finally, it is worth mentioning that the present calculation (Figs. 2.8 and 2.9, and Eq. (2.17)) is based on Lippmann theory, since we assume that there are no free charge carriers and the whole system is isolated. However, according to recent studies, the piezoelectric potential in a strained GaN nanostructure would be screened by the free charge carriers, since the as-grown GaN nanostructure always shows an n-type semiconducting behavior (Gao and Wang 2009; Romano

et al. 2011; Araneo et al. 2012). In order to overcome this screening effect, the idea of controlling the screening effect by imposing external surface charges on the nanowire/nanotube system has recently been invalidated theoretically and experimentally (Kim et al. 2012; Sohn et al. 2013). Existing numerical simulations reveal that this surface functionalization can fully deplete the free carriers (electrons) and make the piezoelectric potential of nanowires/nanotubes recover to their intrinsic case (Kim et al. 2012; Sohn et al. 2013). In addition, the numerical results also indicate that the full coverage of surface charges surrounding the nanotubes increases the piezoelectric output potential exponentially within a relatively smaller range of charge density compared to the case of nanowires for a typical donor concentration (Kim et al. 2012). This efficient surface functionalization of nanotubes could be another advantage of GaN nanotubes serving as a building block of piezotronic nanodevices, especially the nanogenerators compared with their mostly used nanowire counterparts.

2.5.2 *Piezoelectric Effect on the Intrinsic Dissipation in Oscillating GaN Nanobelts*

In this section, classical MDS have been employed to study the piezoelectric effect on the dynamic response of GaN nanobelts (see Fig. 2.10). Special attention was paid to the piezoelectric effect on the intrinsic energy dissipation of such vibrating

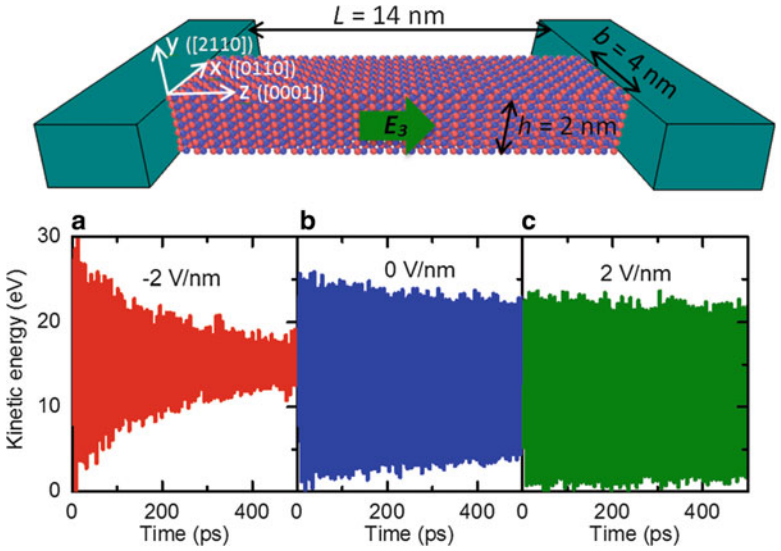

Fig. 2.10 Top: A schematic of a doubly clamped GaN nanobelt resonator subjected to an electric field E_3. Here L, b, and h are the respective length, width, and thickness of the nanobelt. Bottom: kinetic energy time history of the vibrating nanobelts under (**a**) $E_3 = -2$ V/nm, (**b**) no electric field ($E_3 = 0$ V/nm), and (**c**) $E_3 = 2$ V/nm (Zhang and Meguid 2015b)

GaN nanobelts, since the intrinsic energy loss sets a fundamental limit for the performance of nanodevices (Imboden and Mohanty 2014). In the present study, we considered the most common GaN nanobelts (Yu et al. 2012) whose growth direction is the c-axis [0001] with the top surface being [2110] and the side surface being [0110], as shown in Fig. 2.10. In this figure, the x-, y-, and z-axes are, respectively, taken along the [0110], [2110], and [0001] directions. The nanobelts studied here have a dimension of $14\ \text{nm} \times 4\ \text{nm} \times 2\ \text{nm}$. The interactions between Ga-Ga, N-N, and Ga-N were described by the SW potential (see Eqs. (2.11)–(2.13)). After obtaining the energy-minimized configuration of GaN nanobelts from the conjugate gradient method, our simulation was conducted using the following four steps. First, the initial configuration was relaxed at a specified temperature ranging from 10 to 300 K to reach its equilibrium state in 100 ps. Here, the NVT ensemble (constant number of particles, volume, and temperature) was employed to update the positions and velocities of the atoms after each time step using a Nosé-Hoover temperature thermostat (Nosé 1984). Second, to simulate the piezoelectric effect, the two ends of the relaxed nanobelt were fixed, and an electric field E_3 was applied along the axial direction (see Fig. 2.10), which produces an external force $f_i = q_i E_3$ on ion i, where q_i is the charge of ion i. Subsequently, another relaxation with 100 ps was utilized to get the new equilibrium state. Third, after the second thermal equilibration, a point bending force was applied along the y-axis at the midpoint of a nanobelt to deflect it to a certain displacement, which is less than 2 % of the nanobelt length to avoid the influence of the geometric nonlinearity. Fourth, this bending force was removed, and the vibration of the nanobelt was then achieved under a constant energy (NVE) ensemble.

In Fig. 2.10a–c, we illustrate the kinetic energy time history of the vibrating nanobelts at room temperature (300 K) under different electric fields: $E_3 = -2\ \text{V/nm}$ in Fig. 2.10a, no electric field applied ($E_3 = 0\ \text{V/nm}$) in Fig. 2.10b, and $E_3 = 2\ \text{V/nm}$ in Fig. 2.10c. It is worth mentioning that in Fig. 2.10a–c the total kinetic energy E_k is composed of two parts: one is the external kinetic energy for the flexural mode E_{ek} and the other is the internal kinetic energy E_{ik} due to thermal vibrations. The oscillation in the kinetic energy reflects the vibration of nanobelts. Specifically, the kinetic energy vibrates at a frequency of $2f$, where f is the natural frequency of the flexural mode of the nanobelts.

After applying the fast Fourier transform to the obtained kinetic energy time history in Fig. 2.10a–c, we obtain their corresponding frequency spectrum in Fig. 2.11a. From this figure we can see that the frequency of the nanobelts is shifted by the applied electric field through the piezoelectric effect. Similar piezoelectric effect-induced frequency shift phenomenon was also observed in recent experiments and treated as a novel method to tune the frequency of nanoelectromechanical system resonators (Masmanidis et al. 2007). In Fig. 2.11b, we plot the frequency f and frequency shift Δf of the nanobelts as a function of the electric field strength. It is observed that the resonant frequency shifts upward as the negative electric field is increased, while it shifts downward with increasing positive electric field. To explain this resonant frequency shift phenomenon, we show the distribution of the atomic

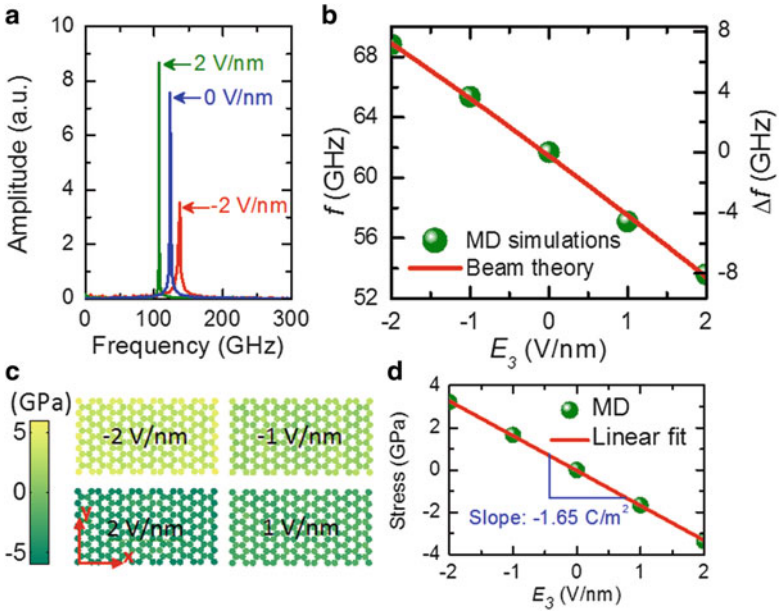

Fig. 2.11 (**a**) Fast Fourier transform of the kinetic energy time history. (**b**) The resonant frequency f and frequency shift Δf as a function of the electric field strength E_3. (**c**) Distribution of the normal stress in the cross section of nanobelts subjected to different electric fields. (**d**) The average normal stress as a function of E_3 (Zhang and Meguid 2015b)

level stress on the cross section of GaN nanobelts subjected to different electric fields in Fig. 2.11c. We can observe from this figure that due to the piezoelectric effect, a positive stress is generated in the nanobelt by a negative electric field, and thus, according to the classical beam theory (Olsson 2010), it increases the frequency of the nanobelt. On the contrary, a negative stress is produced by a positive electric field, leading to a reduction in the frequency. In addition, according to the classical piezoelectric theory (Zhang 2014; Zhang and Meguid 2015a, b), the stress σ in the nanobelt due to the piezoelectric effect is $\sigma = -e_{33}E_3$, where e_{33} is the piezoelectric coefficient. In Fig. 2.11d, we fit this expression to the results obtained from our MDS. After curve fitting the results, we obtain $e_{33} = 1.65\ \ \mathrm{C/m^2}$, which closely agrees with the predicted values for GaN nanowires with the same cross-sectional size using first-principle calculations (Hoang et al. 2013).

Moreover, analogous to the experimental observation (Masmanidis et al. 2007), an almost linear relationship between the frequency shift and the electric field strength is also observed in the present MDS results (see Fig. 2.11b). To shed light on this observation, we resort to the classical piezoelectric and Euler beam theories, which give the resonant frequency f as

$$f = f_0\sqrt{1 - \frac{E_3 e_{33} A L^2}{4\pi^2 EI}} \tag{2.22}$$

where A is the cross-sectional area, I is the second moment of area, L is the length of the nanobelt, E is Young's modulus, and $f_0 = 3.56\sqrt{EI/(\rho AL^4)}$ (ρ being the mass density) is the frequency of the nanobelt without piezoelectric effect. Under small electrical perturbations, the frequency shift obtained from Eq. (2.18) is $\Delta f = -f_0 E_3 e_{33} AL^2/(8\pi^2 EI)$. This expression shows a linear relationship between Δf and E_3, which agrees with our MDS results (see Fig. 2.11b). In addition, we obtain the piezoelectric coefficient of the present GaN nanobelts as $e_{33} = 1.7$ C/m^2 by fitting the f - E_3 curve in Fig. 2.11b with Eq. (2.18). The obtained piezoelectric coefficient is consistent with the value calculated by above direct measurements (Fig. 2.11d).

Next, we will turn our attention to the energy dissipation (the quality factor) of the GaN nanobelt resonator. In Fig. 2.10a–c, the decay of the oscillation amplitude in the kinetic energy represents the energy dissipation in the nanobelt resonators. Assuming that the quality factor Q is constant during vibration, i.e., after n vibration cycles, the maximum external kinetic energy $E_{ek}(n)$ is related to the initial external kinetic energy $E_{ek}(0)$ by the relation $E_{ek}(n) = E_{ek}(0)(1 - 2\pi/Q)^n$ (Jiang et al. 2004). This expression is used in the present work to determine the quality factors of the nanobelt resonators based on their kinetic energy time history (Fig. 2.10a–c). In addition, comparing Fig. 2.10a–c, we can observe that the nanobelt resonator that is subjected to a negative electric field (Fig. 2.10a) demonstrates considerable higher energy dissipation than its counterpart without an electric field (Fig. 2.10b). On the contrary, the nanobelt resonator subjected to a positive electric field (Fig. 2.10c) holds much lower energy dissipation. These results suggest that the piezoelectric effect can greatly influence the energy dissipation and thus the quality factor of the nanobelt resonators. Indeed, we calculated Q of a nanobelt resonator as a function of the electric field strength E_3 in Fig. 2.12a. It can be seen from Fig. 2.12a that Q is increased by up to 12 times as E_3 increases from -2 to 2 V/nm. In other words, a negative electric field significantly decreases the quality factor, while a positive one increases it. This result suggests that applying a negative electric field can mitigate the intrinsic loss of GaN nanobelt resonators via their piezoelectric effect.

To provide some possible explanation to the above observed phenomenon, we will present a brief discussion based on the classical theory of energy dissipation at the nanoscale. Among various sources of the energy dissipation, it is believed that at relatively high temperature (>100 K), the thermoelastic dissipation is the dominant mechanism for a nanobeam oscillator involving bending deformation (Jiang et al. 2004). Based on Zener's work on rectangular reeds (Li et al. 2010), the thermoelastic dissipation in the flexural mode of the present nanobelt can be approximated by (Jiang et al. 2004)

$$\frac{1}{Q} = \frac{2E\alpha^2 h^2}{\pi k} Tf \tag{2.23}$$

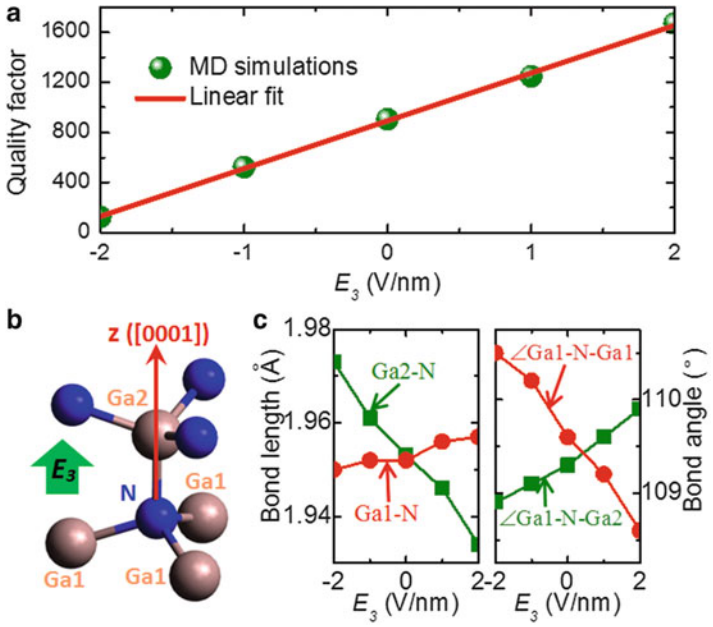

Fig. 2.12 (**a**) The quality factor as a function of the electric field strength E_3. (**b**) The bond configuration of the wurtzite GaN. (**c**) The evolution of bond length and bond angle of the wurtzite GaN subjected to E_3 (Zhang and Meguid 2015b)

where α is the coefficient of thermal expansion, k is the thermal conductivity, h is the thickness of the nanobelt, and T is the temperature. Equation (2.19) shows that the quality factor Q increases with the decrease in the resonant frequency f since $Q \propto 1/f$. This trend is consistent with our MDS results, where a negative E_3 increases f but reduces Q and a positive E_3 decreases f but improves Q. In addition, it is also expected from Eq. (2.19) that the relative change in $1/Q$ should be close to the relative change in f. Nevertheless, from Figs. 2.11b to 2.12a, we can observe that $1/Q$ can be reduced by up to 92 % as E_3 increases from -2 to 2 V/nm. However, in this process f is found to be decreased by only 22 %. In other words, if compared with f, the change of Q is more sensitive to the change of the applied electric field. This observation implies that the figure of merit $(f \cdot Q)$ of the nanobelt resonator can be efficiently tuned by applying an electric field, and specifically a negative electric field can improve the performance of the resonator. On the other hand, the more sensitive Q (compared with f) to the electric field also suggests that the piezoelectric effect may influence the thermoelastic dissipation and the quality factor through some other factors, including f. To shed some light on this issue, let us examine the atomic details of the wurtzite GaN subjected to an electric field, whose atomic structure is illustrated in Fig. 2.12b. For this purpose, we measured the variation of bond lengths and angles with different applied electric fields and plotted the measured results in Fig. 2.12c. It can be seen from Fig. 2.12c that due to the

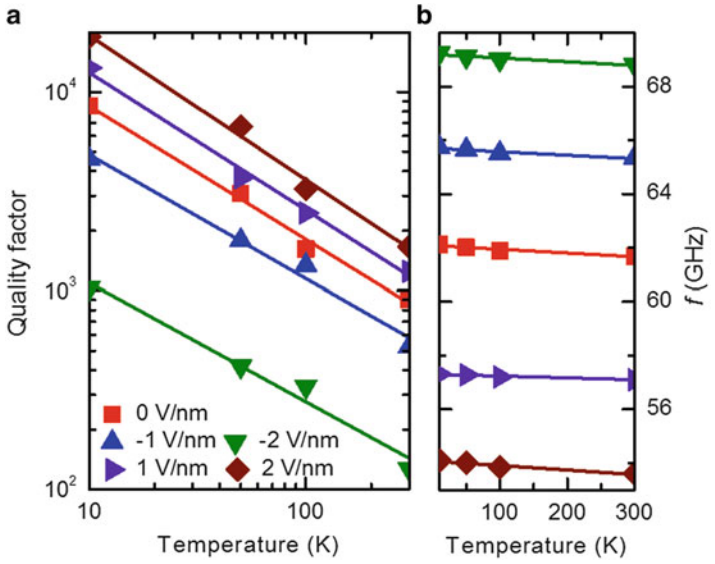

Fig. 2.13 (**a**) The quality factor and (**b**) the resonant frequency f as a function of the temperature for GaN nanobelts subjected to different electric fields (Zhang and Meguid 2015b)

piezoelectric effect, the bond lengths and angles of wurtzite GaN significantly vary with the changing electric field. It has been proven from previous studies on carbon nanotubes (Li et al. 2010), graphene sheets (Li et al. 2010), and semiconductor nanowires (Li et al. 2010) that the varied bond lengths and angles of nanostructures greatly shift their phonon spectra and thus significantly influence their thermal conductivity. Thus, based on this discussion together with Eq. (2.19), we can conclude that the changed thermal conductivity k of GaN nanobelts due to the piezoelectric effect can be regarded as another possible explanation for the electric field-dependent quality factor detected in the present study.

Finally, we will study the dependence of the dynamic behaviors (Q and f) on the temperature T. We display Q of nanobelts subjected to various electric fields against T in Fig. 2.13a. From this figure we can deduce that Q increases exponentially with decreasing T and can be described by the following relation, $Q \propto 1/T^{\beta}$, where the thermoelastic damping exponent β is in the range 0.59–0.72, and depends on the electric field strength. Such deduction relationship of the quality factor with increasing temperature deviates from the $1/T$ dependence obtained from the classical description of thermoelastic loss for bulk materials (Eq. (2.19)). This discrepancy is attributed to a surface effect, which results in dynamic behaviors of the surface layer of the nanobelt that is distinctly different from its bulk counterpart (Zhang et al. 2012b). In addition, although the initial temperatures are fixed in the simulations, a small raise of the temperature is still unavoidable because of the nature of the simulations in the micro-canonical ensemble. This slight temperature increase could be another explanation for the above observed discrepancy.

It is noted here that $\beta = 0.67$ for GaN nanobelts without an applied electric field is close to that of 0.7 as obtained from MDS of silicon nanowires (Georgakaki et al. 2014). Moreover, β is found to significantly depend on the electric field strength, E_3. This E_3-dependent β can be attributed to the pyroelectric character of the wurtzite GaN crystal, which makes the piezoelectric effect of GaN nanobelts temperature dependent (Zhang et al. 2013; Zhang and Meguid 2015a). We further determined the influence of the temperature on the resonant frequency of GaN nanobelts. Owing to the so-called thermal-softening effect on the elastic properties and/or the pyroelectric effect, f is found to decrease with increasing T (Fig. 2.13b). However, the effect of T on f almost can be ignored, since f is reduced by no more than 1 % when T increases from 10 to 300 K. Similar negligible influence of temperature on the resonant frequency was also observed in a recent experimental study of GaN nanowire resonators (Montague et al. 2012).

2.6 Conclusion Remarks

Piezoelectric response in a nanoscale world has attracted considerable attention in recent research. Effort has been made to characterize the piezoelectricity of PNs in different configurations. Experimental techniques were used for synthesized PNs of the feature size tens to hundreds of nanometers, while the atomistic simulations are focused on small PNs of the feature size 0.5–10 nm. Due to unknown physical mechanisms, strong or extreme piezoelectric response was reported for ZnO PNs, characterized by the EPCs orders of magnitude greater than the bulk values. In particular the EPCs at the nanoscale are not constants but vary significantly with the geometric size of PNs. On the other hand, large discrepancy is found among the existing studies in measuring the values of EPCs and predicting their size dependence.

In addition, various mechanisms have been proposed as possible physical origins of unique piezoelectric response at the nanoscale, such as the quantum effects, single or polycrystallinity, the density of defects, the free relaxation of surface atoms, and the piezoelectricity of the surface layers. The effect of individual factor may vary drastically in different cases, e.g., length scales. Specifically, the theoretical framework of the surface piezoelectricity has been established and was found to be in good agreement with some atomistic simulations. Thus, surface piezoelectricity can be accepted as a major factor that determines the magnitudes and behavior of the EPCs of PNs, at least, in some cases. Nevertheless, it still remains a challenge to formulate a universal theoretical framework that is able to achieve physical insights into the scattering of the obtained results.

Moreover, based on the structural models accounting for the effect of the surface piezoelectricity, two types of EPCs of PNs are derived for the first time characterizing the relation of an electric field to the initial stress and the contribution of piezoelectricity to EEM. Both of them are found to vary with not only the geometric size of PNs but also the deformation experienced by the PNs.

Finally, the influence of the nanoscale piezoelectricity on the mechanical responses (statics and dynamics) of piezoelectric nanostructures was also discussed. It is found that at the nanoscale, the surface piezoelectricity can enhance the piezoelectric potential of nanostructures when they are subjected to a static deformation. In addition, the intrinsic loss of oscillating piezoelectric nanostructure can be mitigated through the piezoelectric effect at the nanoscale.

Acknowledgments This work was supported by the Natural Sciences and Engineering Research Council of Canada (NSERC) and the Discovery Accelerator Supplements.

References

Araneo, R., Lovat, G., Burghignoli, P., Falconi, C.: Piezo-semiconductive quasi-1D nanodevices with or without anti-symmetry. Adv. Mater. **24**, 4719–4724 (2012)

Assadi, A., Farshi, B.: Vibration characteristics of circular nanoplates. J. Appl. Phys. **108**, 074312 (2010)

Assadi, A., Farshi, B., Alinia-Ziazi, A.: Size dependent dynamic analysis of nanoplates. J. Appl. Phys. **107**, 124310 (2010)

Bdikin, I.K., Gracio, J., Ayouchi, R., Schwarz, R., Kholkin, A.L.: Local piezoelectric properties of ZnO thin films prepared by RF-plasma-assisted pulsed-laser deposition method. Nanotechnology **21**, 235703 (2010)

Bere, A., Serra, A.: On the atomic structures, mobility and interactions of extended defects in GaN: dislocations, tilt and twin boundaries. Philos. Mag. **86**, 2159–2192 (2006)

Bernardini, F., Fiorentini, V.: Spontaneous polarization and piezoelectric constants of III-V nitrides. Phys. Rev. B **56**, R10024 (1997)

Chen, C.Q., Shi, Y., Zhang, Y.S., Zhu, J., Yan, Y.J.: Size dependence of Young's modulus in ZnO nanowires. Phys. Rev. Lett. **96**, 075505 (2006)

Dai, S.X., Dunn, M.L., Park, H.S.: Piezoelectric constants for ZnO calculated using classical polarizable core-shell potentials. Nanotechnology **21**, 445707 (2010)

Dai, S.X., Gharbi, M., Sharma, P., Park, H.S.: Surface piezoelectricity: size effects in nanostructures and the emergence of piezoelectricity in non-piezoelectric materials. J. Appl. Phys. **110**, 104305 (2011)

Dunn, S.: Strain behaviour of thin film PZT (30/70) examined through piezoforce microscopy (P-AFM). J. Appl. Phys. **94**, 5964–5968 (2003)

Ebbesen, T.W., Ajayan, P.M.: Large-scale synthesis of carbon nanotubes. Nature **358**, 220–222 (1992)

Espinosa, H.D., Bernal, R.A., Minary-Jolandan, M.: A review of mechanical and electromechanical properties of piezoelectric nanowires. Adv. Mater. **24**, 4656–4675 (2012)

Fan, H.J., Lee, W., Hauschild, R., Alexe, M., Le Rhun, G., Scholz, R., Dadgar, A., Nielsch, K., Kalt, H., Krost, A., Zacharias, M., Gosele, U.: Template-assisted large-scale ordered arrays of ZnO pillars for optical and piezoelectric applications. Small **2**, 561–568 (2006)

Fang, X.Q., Liu, J.X., Gupta, V.: Fundamental formulations and recent achievements in piezoelectric nano-structures: a review. Nanoscale **5**, 1716–1726 (2013)

Faucher, M., Grimbert, B., Cordier, Y., Baron, N., Wilk, A., Lahreche, H., Bove, P., François, M., Tilmant, P., Gehin, T., Legrand, C., Werquin, M., Buchaillot, L., Gaquière, C., Théron, D.: Influence of carrier concentration on piezoelectric potential in a bent ZnO nanorod. Appl. Phys. Lett. **94**, 233506 (2009)

Gao, Y., Wang, Z.L.: Electrostatic potential in a bent piezoelectric nanowire. The fundamental theory of nanogenerator and nanopiezotronics. Nano Lett. **7**, 2499–2505 (2007)

Gao, Y., Wang, Z.L.: Equilibrium potential of free charge carriers in a bent piezoelectric semiconductive nanowire. Nano Lett. **9**, 1103–1110 (2009)
Geim, A.K., Novoselov, K.S.: The rise of graphene. Nat. Mater. **6**, 183–191 (2007)
Georgakaki, D., Ziogos, O.G., Polatoglou, H.M.: Vibrational and mechanical properties of Si/Ge nanowires as resonators: a molecular dynamics study. Phys. Status Solidi A **211**, 267–276 (2014)
Han, W.Q., Redlich, P., Ernst, F., Ruhle, M.: Synthesis of GaN-carbon composite nanotubes and GaN nanorods by arc discharge in nitrogen atmosphere. Appl. Phys. Lett. **76**, 652–654 (2000)
He, M.R., Shi, Y., Zhou, W., Chen, J.W., Yan, Y.J., Zhu, J.: Diameter dependence of modulus in zinc oxide nanowires and the effect of loading mode: in situ experiments and universal core-shell approach. Appl. Phys. Lett. **95**, 091912 (2009)
Hoang, M.T., Yvonnet, J., Mitrushchenkov, A., Chambaud, G.: First-principles based multiscale model of piezoelectric nanowires with surface effects. J. Appl. Phys. **113**, 014309 (2013)
Huang, G.Y., Yu, S.W.: Effect of surface piezoelectricity on the electromechanical behaviour of a piezoelectric ring. Phys. Status Solidi B **243**, R22–R24 (2006)
Huang, Y., Wu, J., Hwang, K.C.: Thickness of graphene and single-wall carbon nanotubes. Phys. Rev. B **74**, 245413 (2006)
Iijima, S.: Helical microtubules of graphitic carbon. Nature **354**, 56–58 (1991)
Imboden, M., Mohanty, P.: Dissipation in nanoelectromechanical systems. Phys. Rep. **534**, 89–146 (2014)
Jiang, H., Yu, M.F., Liu, B., Huang, Y.: Intrinsic energy loss mechanisms in a cantilevered carbon nanotube beam oscillator. Phys. Rev. Lett. **93**, 185501 (2004)
Kim, S.M., Kim, H., Nam, Y., Kim, S.: Effects of external surface charges on the enhanced piezoelectric potential of ZnO and AlN nanowires and nanotubes. AIP Adv. **2**, 042174 (2012)
Kroto, H.W., Heath, J.R., O'Brien, S.C., Curl, R.F., Smalley, R.E.: C60: Buckminsterfullerene. Nature **318**, 162–163 (1985)
Levinshtein, M.E., Rumyantsev, S.L., Shur, M.S.: Properties of advanced semiconductor materials: GaN, AlN, InN, BN, SiC, SiGe. Wiley, New York (2001)
Li, C., Guo, W.L., Kong, Y., Gao, H.J.: Size-dependent piezoelectricity in zinc oxide nanofilms from first-principles calculations. Appl. Phys. Lett. **90**, 033108 (2007)
Li, X.B., Maute, K., Dunn, M.L., Yang, R.G.: Strain effects on the thermal conductivity of nanostructures. Phys. Rev. B **81**, 245318 (2010)
Li, Y.H., Fang, B., Zhang, J.Z., Song, J.Z.: Surface effects on the wrinkling of piezoelectric films on compliant substrates. J. Appl. Phys. **110**, 114303 (2011)
Liu, C., Rajapakse, R.K.N.D.: Surface energy incorporated continuum models for static and dynamic response of nanoscale beams. IEEE Trans. Nanotechnol. **9**, 422–431 (2010)
Masmanidis, S.C., Karabalin, R.B., De Vlaminck, I., Borghs, G., Freeman, M.R., Roukes, M.L.: Multifunctional nanomechanical systems via tunably coupled piezoelectric actuation. Science **317**, 780–783 (2007)
Miller, R.E., Shenoy, V.B.: Size-dependent elastic properties of nanosized structural elements. Nanotechnology **11**, 139–147 (2000)
Minary-Jolandan, M., Bernal, R.A., Kuljanishvili, I., Parpoil, V., Espinosa, H.D.: Individual GaN nanowires exhibit strong piezoelectricity in 3D. Nano Lett. **12**, 970–976 (2012)
Momeni, K., Attariani, H.: Electromechanical properties of 1D ZnO nanostructures: nanopiezotronics building blocks, surface and size-scale effects. Phys. Chem. Chem. Phys. **16**, 4522–4527 (2014)
Momeni, K., Odegard, G.M., Yassar, R.S.: Finite size effect on the piezoelectric properties of ZnO nanobelts: a molecular dynamics approach. Acta Mater. **60**, 5117–5124 (2012)
Montague, J.R., Bertness, K.A., Sanford, N.A., Bright, V.M., Rogers, C.T.: Temperature-dependent mechanical-resonance frequencies and damping in ensembles of gallium nitride nanowires. Appl. Phys. Lett. **101**, 173101 (2012)
Nosé, S.: A unified formulation of the constant temperature molecular dynamics methods. J. Chem. Phys. **81**, 511–519 (1984)

Olsson, P.A.T.: Transverse resonant properties of strained gold nanowires. J. Appl. Phys. **108**, 034318 (2010)

Plimpton, S.J.: Fast parallel algorithms for short-range molecular dynamics. J. Comput. Phys. **117**, 1–19 (1995)

Romano, G., Mantini, G., Di Carlo, A., D'Amico, A., Falconi, C., Wang, Z.L.: Piezoelectric potential in vertically aligned nanowires for high output nanogenerators. Nanotechnology **22**, 465401 (2011)

Schwarz, R.B., Khachaturyan, K.: Elastic moduli of gallium nitride. Appl. Phys. Lett. **70**, 1122–1124 (1997)

Shen, S., Hu, S.: A theory of flexoelectricity with surface effect for elastic dielectrics. J. Mech. Phys. Solids **58**, 665–677 (2010)

Smith, M.B., Page, K., Siegrist, T., Redmond, P.L., Walter, E.C., Seshadri, R., Brus, L.E., Steigerwald, M.L.: Crystal structure and the paraelectric-to-ferroelectric phase transition of nanoscale BaTiO3. J. Am. Chem. Soc. **130**, 6955–6963 (2008)

Sohn, J.I., Cha, S.N., Song, B.G., Lee, S., Kim, S.M., Ku, J., Kim, H.J., Park, Y.J., Choi, B.L., Wang, Z.L., Kim, J.M., Kim, K.: Engineering of efficiency limiting free carriers and an interfacial energy barrier for an enhancing piezoelectric generation. Energ. Environ. Sci. **6**, 97–104 (2013)

Stillinger, F.H., Weber, T.A.: Computer simulation of local order in condensed phases of silicon. Phys. Rev. B **31**, 5262–5271 (1985)

Wang, Z.L.: ZnO nanowire and nanobelt platform for nanotechnology. Mater. Sci. Eng. R **64**, 33–71 (2009)

Wang, G.F., Feng, X.Q.: Timoshenko beam model for buckling and vibration of nanowires with surface effects. J. Phys. D Appl. Phys. **42**, 155411 (2009)

Wang, G.F., Feng, X.Q.: Effect of surface stresses on the vibration and buckling of piezoelectric nanowires. Europhys. Lett. **91**, 56007 (2010)

Wang, Z.G., Zu, X.T., Gao, F., Weber, W.J.: Atomistic simulation of brittle to ductile transition in GaN nanotubes. Appl. Phys. Lett. **89**, 243123 (2006a)

Wang, X.B., Song, C., Li, D.M., Geng, K.W., Zen, F., Pan, F.: The influence of different doping elements on microstructure, piezoelectric coefficient and resistivity of sputtered ZnO film. Appl. Surf. Sci. **253**, 1639–1643 (2006b)

Wang, Z.G., Zu, X.T., Yang, L., Gao, F., Weber, W.J.: Atomistic simulations of the size, orientation, and temperature dependence of tensile behavior in GaN nanowires. Phys. Rev. B **76**, 045310 (2007)

Wang, Z.G., Zu, X.T., Gao, F., Weber, W.J.: Mechanical behavior of gallium nitride nanotubes under combined tension-torsion: an atomistic simulation. J. Appl. Phys. **103**, 013505 (2008)

Xiang, H.J., Yang, J.L., Hou, J.G., Zhu, Q.S.: Piezoelectricity in ZnO nanowires: a first-principles study. Appl. Phys. Lett. **89**, 223111 (2006)

Xu, B., Pan, B.C.: The effect of atomic vacancies and grain boundaries on the mechanical proper. J. Appl. Phys. **99**, 104314 (2006)

Xu, F., Qin, Q.Q., Mishra, A., Gu, Y., Zhu, Y.: Mechanical properties of ZnO nanowires under different loading modes. Nano Res. **3**, 271–280 (2010)

Yan, Z., Jiang, L.Y.: Surface effects on the electromechanical coupling and bending behaviours of piezoelectric nanowires. J. Phys. D Appl. Phys. **44**, 075404 (2010)

Yan, Z., Jiang, L.Y.: The vibrational and buckling behaviors of piezoelectric nanobeams with surface effects. Nanotechnology **22**, 245703 (2011)

Yang, Y., Guo, W., Wang, X., Wang, Z., Qie, J., Zhang, Y.: Size dependence of dielectric constant in a single pencil-like ZnO nanowire. Nano Lett. **12**, 1919–1922 (2012)

Yao, H.Y., Yun, G.H., Bai, N.: Influence of exponentially increasing surface elasticity on the piezoelectric potential of a bent ZnO nanowire. J. Phys. D Appl. Phys. **45**, 285304 (2012)

Yu, R.M., Dong, L., Pan, C.F., Niu, S.M., Liu, H.F., Liu, W., Chua, S.J., Chi, D.Z., Wang, Z.L.: Piezotronic effect on the transport properties of GaN nanobelts for active flexible electronics. Adv. Mater. **24**, 3532–3537 (2012)

Zhang, J.: Small-scale effect on the piezoelectric potential of gallium nitride nanowires. Appl. Phys. Lett. **104**, 253110 (2014)
Zhang, J., Meguid, S.A.: On the piezoelectric potential of gallium nitride nanotubes. Nano Energ. **12**, 322–330 (2015a)
Zhang, J., Meguid, S.A.: Piezoelectric effect on the intrinsic dissipation in oscillating gallium nitride nanobelts. Europhys. Lett. **112**, 26003 (2015b)
Zhang, J., Wang, C.Y.: Vibrating piezoelectric nanofilms as sandwich nanoplates. J. Appl. Phys. **111**, 094303 (2012)
Zhang, Y.H., Hong, J.W., Liu, B., Fang, D.N.: Molecular dynamics investigations on the size-dependent ferroelectric behavior of BaTiO3 nanowires. Nanotechnology **20**, 405703 (2009)
Zhang, Y.H., Hong, J.W., Liu, B., Fang, D.N.: Strain effect on ferroelectric behaviors of BaTiO3 nanowires: a molecular dynamics study. Nanotechnology **21**, 015701 (2010)
Zhang, J., Wang, C.Y., Adhikari, S.: Surface effect on the buckling of piezoelectric nanofilms. J. Phys. D Appl. Phys. **45**, 285301 (2012a)
Zhang, J., Wang, C.Y., Chowdhury, R., Adhikari, S.: Small-scale effect on the mechanical properties of metallic nanotubes. Appl. Phys. Lett. **101**, 093109 (2012b)
Zhang, J., Wang, C.Y., Chowdhury, R., Adhikari, S.: Size-and temperature-dependent piezoelectric properties of gallium nitride nanowires. Scr. Mater. **68**, 627–630 (2013)
Zhang, J., Wang, C.Y., Bowen, C.: Piezoelectric effects and electromechanical theories at the nanoscale. Nanoscale **6**, 13314–13327 (2014)
Zhao, M.H., Wang, Z.L., Mao, S.X.: Piezoelectric characterization of individual zinc oxide nanobelt probed by piezoresponse force microscope. Nano Lett. **4**, 587–590 (2004)
Zhu, R., Wang, D.Q., Xiang, S.Q., Zhou, Z.Y., Ye, X.Y.: Piezoelectric characterization of a single zinc oxide nanowire using a nanoelectromechanical oscillator. Nanotechnology **19**, 285712 (2008)

Chapter 3
Nanoscale Mechanical Characterization of 1D and 2D Materials with Application to Nanocomposites

Guillaume Colas and Tobin Filleter

Abstract In this chapter the critical recent advances in the area of nanoscale mechanical characterization of 1D and 2D nanostructures with application to nanocomposites are presented. CNTs and graphene have been the most widely studied within this class of materials; however, a number of additional 1D and 2D nanostructures such as molybdenum disulfide (MoS_2) ultrathin films have also recently emerged and will be discussed. The chapter will cover a variety of nanomechanical characterization techniques that have been developed recently, with a particular focus on methods which characterize the nature of interactions (shear strength, interfacial friction, etc.) between the nanocomposite constituents which can play a significant role in governing macroscopic nanocomposite behavior.

3.1 Introduction

Over the last decade, the diversity of usage of graphene, graphene oxides (GOs), and carbon nanotubes (CNTs) has grown exponentially and covers a wide range of applications. For example, CNTs, which can be classified as pseudo 1D nanostructures, can be used as building blocks to form bundles, yarns, and large-scale fibers (Kwon et al. 2015; Meng et al. 2012; Mirzaeifar et al. 2015; Dong et al. 2011; Compton et al. 2012; Vilatela et al. 2011; Liu et al. 2015; Naraghi et al. 2010; Qiu et al. 2013; Alemán et al. 2015) and composites materials (Mirjalili et al. 2014) for lightweight structures. They are also found useful to create actuators (Kwon et al. 2015; Mirzaeifar et al. 2015) and electronics (Azoubel and Magdassi 2014). 2D nanostructures, such as graphene and its less expensive cousin GO, have attracted a great deal of interest for bendable electronics, light emission, and super-elastic electronics (Wang et al. 2015; Kim et al. 2015); as sensors using the

G. Colas • T. Filleter (✉)
Department of Mechanical and Industrial Engineering, University of Toronto, Toronto, ON, Canada, M5S 3G8
e-mail: guillaume.colas@utoronto.ca; filleter@mie.utoronto.ca

S.A. Meguid (ed.), *Advances in Nanocomposites*,
DOI 10.1007/978-3-319-31662-8_3

vibrational response of graphene to molecules (Rodrigo et al. 2015), evolution of resistivity of GO to water to create humidity sensor (Borini et al. 2013); for wettability control of surfaces (Boddeti et al. 2013); and also as lubricants at the nano-/microscale (Chen and Filleter 2015; Lee et al. 2010) and even at the macroscale (Berman et al. 2014, 2015). Many of these applications require the 1D and 2D nanostructures to be integrated within other matrix materials or connected by heterogeneous cross-links as nanocomposites, which is particularly true for the applications of CNTs and graphene as reinforcement elements in structural nanocomposites (Qian et al. 2010; Coleman et al. 2006).

To achieve such a wide range of already available and potential future nanocomposite applications, there is a need to characterize the nanostructure materials individually (single-layer graphene, single-layer GO, individual SWCNT and MWCNT, etc.), then as building blocks comprised of the same nature individuals (multilayer graphene, multilayer GO, yarn of CNTs) or comprised of mixed materials (graphene/GO, graphene/CNTs, GO/CNTs, etc.), and finally with the surrounding extra materials or matrix (polymers, silicon, metals, etc.). For many applications, this characterization must be both mechanical and chemical in nature and focused on the different interactions existing between each of the individual components of the nanocomposite material. In this chapter we will present a summary of the critical recent advances in the area of nanoscale mechanical characterization of this class of materials. While CNTs and graphene have been the most widely studied within this class, a number of other 1D and 2D nanostructures such as molybdenum disulfide (MoS_2) and boron nitride (BN) nanotubes and sheets have also emerged recently. A particular focus of the chapter will be put on characterizing the nature of interactions (shear strength, interfacial friction, etc.) between the nanocomposite constituents which can play a significant role in governing their macroscopic behavior.

3.2 In Situ Mechanical Characterization of 1D and 2D Nanomaterials

3.2.1 MEMS-Based In Situ Characterization

One of the great challenges of characterizing the interfacial properties of nanostructures and nanostructured composite materials is developing and applying experimental techniques that can both handle and deform such small structures, as well as measure interaction forces in the nN range. One research direction that has emerged over the last decade is utilizing micro-electro-mechanical systems (MEMS) to operate as miniaturized mechanical testing setups to accomplish this (Haque and Saif 2002; Lu et al. 2010; Espinosa et al. 2012a; Zhang et al. 2014). An additional benefit to MEMS devices is that they are small enough to operate in situ high-resolution imaging tools such as scanning electron

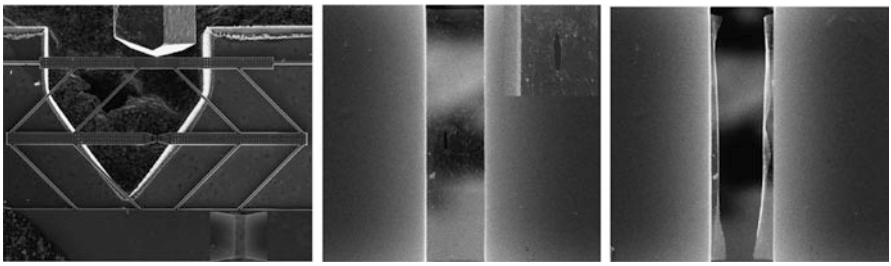

Fig. 3.1 MEMS-based testing of the fracture toughness of graphene films. *Left*: In situ SEM MEMS device. *Middle*: Graphene film prior to testing with a predefined crack. *Right*: Graphene film after fracture. Reproduced from Zhang et al. (2014)

microscopes (SEM) and transmission electron microscopes (TEM). This enables both testing of interfacial properties and direct visualization of deformational and structural changes in the nanostructures.

MEMS testing has played a significant role in developing an understanding of shear interactions and the mechanical properties of graphene- and CNT-based materials used as reinforcement elements in structural nanocomposites. The fracture toughness of graphene, which is an extremely important material property to be considered in graphene-based nanocomposite design, has recently been measured using an in situ TEM MEMS device (Zhang et al. 2014). Figure 3.1 shows the MEMS device used for fracture toughness measurements, as well as images of graphene films before and after fracture. In situ TEM MEMS-based tensile testing systems have also been applied to study 1D carbon-based nanomaterials such as CNTs. It has been demonstrated recently that the weak van der Waals interactions between adjacent MWNT shells and CNT within CNT bundles can be strengthened through covalent bonding via electron irradiation (Peng et al. 2008; Filleter et al. 2011). The strength and stiffness improvements for CNT bundles demonstrated via electron irradiation are predicted to translate to significant improvements in the composite strength and modulus for both CNT/polymer and CNT/epoxy nanocomposites (Filleter et al. 2011).

3.2.2 In Situ Shear and Peeling Techniques

Miniaturized testing systems can also be applied using in situ SEM and TEM to measure the cleavage and adhesion behavior of layered 2D nanomaterials. Recent studies on MoS_2 cleavage have directly measured the surface energy of atomically thin MoS_2 layers under observation of the TEM (Tang et al. 2014). In the future, similar techniques can be applied for 2D carbon-based nanostructures such as graphene and GO. Peeling experiments, conducted using in situ SEM, have also been used in conjunction with numerical modeling to study interfacial interactions of CNTs and graphene. In these measurements, one end of a CNT is attached to the

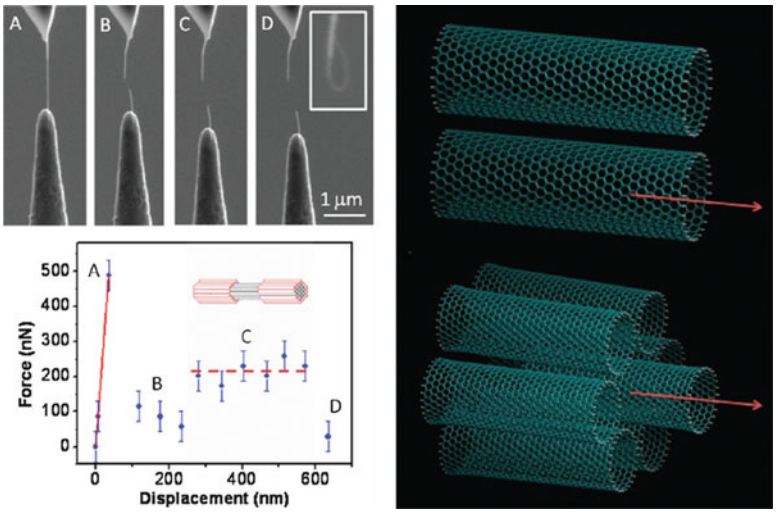

Fig. 3.2 (*Left*) In situ SEM shear testing of CNT bundles. (*Right*) Molecular mechanics simulation of CNT bundles used to study the shear interactions between CNTs. Reproduced from Filleter et al. (2012)

tip of an AFM cantilever which is brought away from the surface until the CNT detached itself from the surface in order to measure adhesion. This has demonstrated CNTs functionalized to exhibit high adhesion toward graphene-based nanocomposites (Roenbeck et al. 2015). In addition to peeling, the shear interactions between adjacent CNTs within CNT bundles can also be measured using a similar technique in situ SEM. Figure 3.2 shows the pullout force recorded during a shear experiment conducted on a CNT bundle using in situ SEM.

3.2.3 In Situ Raman Spectroscopy Techniques

Spectroscopy techniques based on the inelastic scattering of light upon interaction with nanostructures have been used to characterize interfaces between carbon nanostructures and composite matrix materials. Raman spectroscopy is one of the most common techniques used to characterize structural characteristics of carbon-based nanostructures such as graphene, CNTs, and GOs. For example, Raman spectroscopy can be used to measure the wall diameters within CNTs by measuring the vibrational breathing mode frequencies (Dresselhaus et al. 2005), and it can be used to identify the number of layers in few-layer graphene (Malard et al. 2009; Ferrari and Basko 2013). The nature of Raman spectroscopy also allows for the identification of variations in strain of the carbon honeycomb lattice, enabling in situ Raman studies of load transfer at the interface of the nanostructures and the composite matrix (Cooper et al. 2001; Gong et al. 2012). Gong et al. demonstrated

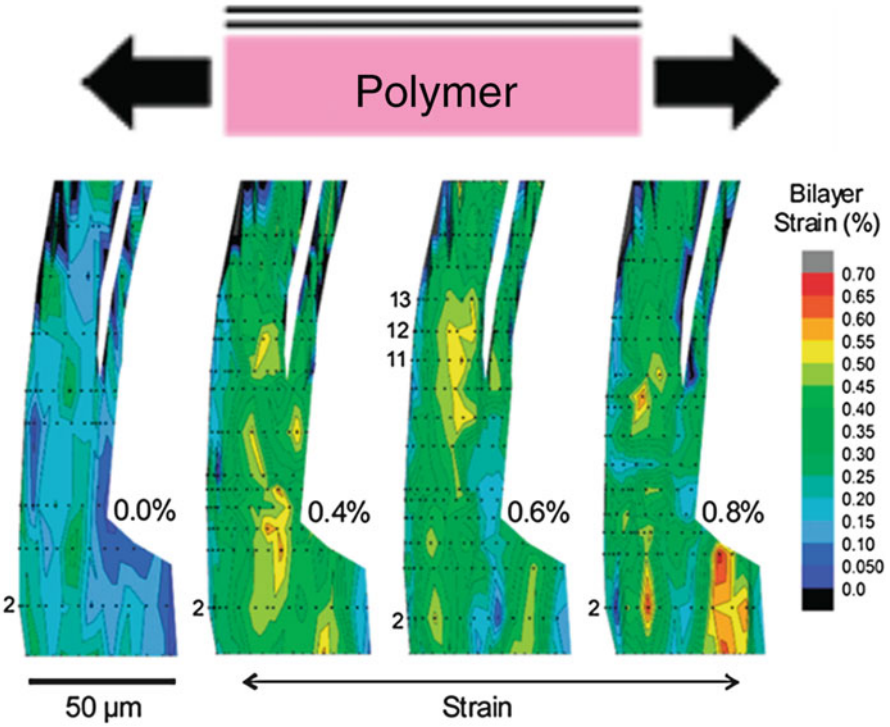

Fig. 3.3 In situ Raman spectroscopy strain mapping of bilayer graphene flake attached to a PMMA underlying substrate in tension. Reproduced from Gong et al. (2012)

an in situ Raman method to study the load transfer between multilayer graphene flakes and a PMMA matrix during tensile testing (Gong et al. 2012). By monitoring the stress-induced shift in the 2D band from Raman measurements, the local strain within the graphene layers was mapped during tensile loading of the composite material. Figure 3.3 shows this local strain mapping for a bilayer graphene region on a polymer substrate which shows the nonhomogeneity of the load transfer between the underlying PMMA matrix layer and the graphene layers (Gong et al. 2012).

3.3 Probe-Based Mechanical Characterization of Nanocomposite Materials

3.3.1 Friction Force Microscopy and Shear Testing

Friction is a particularly important parameter to take into account when considering the interactions within nanocomposite materials. When 1D (CNTs) and 2D

materials (graphene, GO, MoS2, etc.) are used as building blocks, they will necessarily interact with each other and friction plays an important role in those interactions. To characterize friction at the nano- and microscale, atomic force microscopy (AFM) operated in a friction force microscopy (FFM) mode is typically used due to the possibility to conduct experiments at very low normal load (few to hundreds of nN) and measure friction forces in the nano-Newton range. Extensively used for many years for characterizing local friction at surfaces of "bulk" materials (Bharat et al. 2000; Bhushan 2005; Santos et al. 2001; Samyn et al. 2010; Sahoo and Biswas 2009), the versatility of the AFM allows working in different environments and with functionalized cantilevers, which make it a predilection tool for studying 1D and 2D material friction. AFM was used to demonstrate both that graphene can exhibit exceptionally low friction and that the layer thickness of multilayer 2D nanostructures can influence the frictional behavior (Lee et al. 2010; Filleter et al. 2009). Figure 3.4 shows AFM-based friction measurements of graphene and MoS_2 multilayer films which clearly exhibit a thickness dependence on the measured friction. Layer thicknesses of approximately 4 monolayers are found to exhibit friction similar to their corresponding bulk materials (Lee et al. 2010). Chen et al. (2015) notably terminated an AFM cantilever with 70 μm colloidal glass beads to perform quantitative friction tests on graphene and GO. Obtaining reliable quantitative measurements is a hard task and requires calibration of the cantilever as well as the consideration of the adhesion force between the bead and the material.

Similar friction test experiments demonstrated that GO tribological behavior (friction coefficient and wear) is highly related to the nature and amount of functional groups on the GO (Chen and Filleter 2015). This technique also highlighted that some other phenomena such as a reversible negative compressibility may occur when few-layer graphene, MoS_2, or hexagonal boron nitride is submitted to shear (Barboza et al. 2012). If the number of layers is high, only a few 5–6 top layers might contribute to this phenomenon. Interestingly, some other materials such as mica and Bi_2Se_3 are not found to exhibit such behavior.

3.3.2 Ultrathin Film Deflection and AFM-Based Methods

In addition to friction testing using AFM, a number of AFM-based techniques have also been developed through the years to measure the intrinsic mechanical properties of nanomaterials at the different scales. A well-known approach is the indentation of suspended structures to measure force–displacement curves and calculate the Young's modulus, toughness, etc., of single-layer and multilayer graphene (Wei and Kysar 2012; Cao et al. 2014), GO (Suk et al. 2010; Cao et al. 2015), single-layer (Bertolazzi et al. 2011) and multilayer MoS_2 (Castellanos-Gomez et al. 2012), and multilayer heterogeneous materials (Liu et al. 2014). Figure 3.5 shows AFM-based indentation measurements of the 2D modulus measured for a variety of single-layer and multilayer MoS_2 and graphene materials (Liu et al. 2014). In all of these

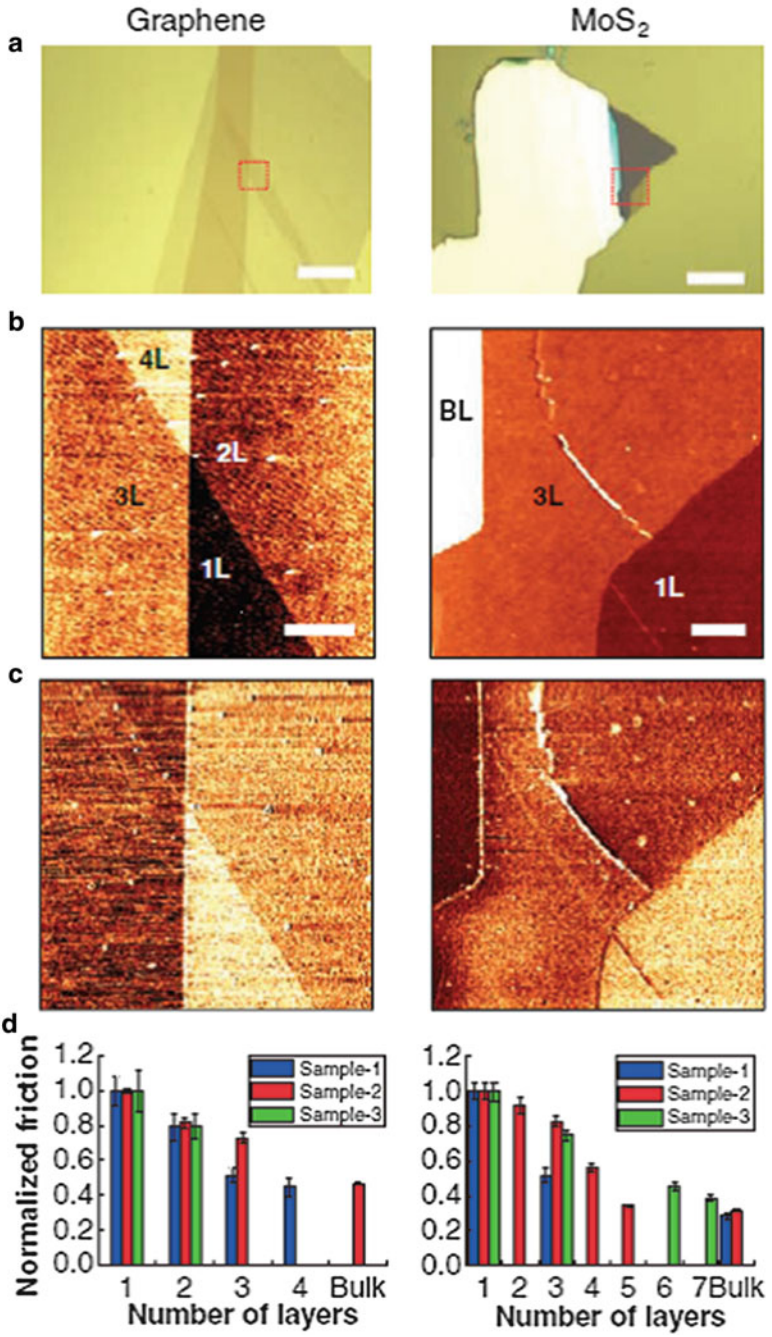

Fig. 3.4 AFM-based friction measurements of graphene (*left*) and MoS_2 (*right*) multilayer films. Reproduced from Lee et al. (2010)

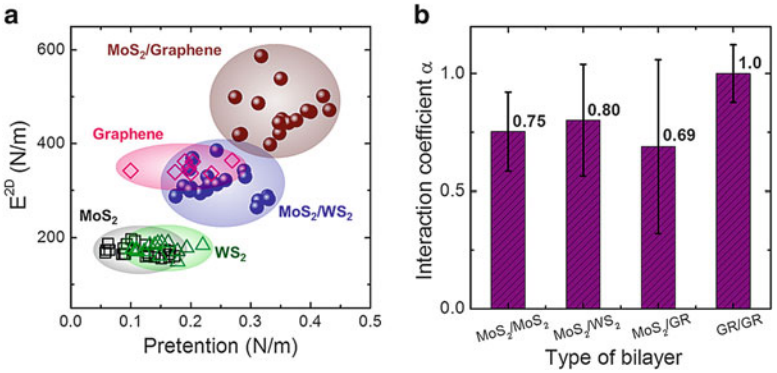

Fig. 3.5 Comparison of elastic properties of different 2D layers. (**a**) Experimental data of 2D modulus and pretension for various 2D layers and heterostructures. (**b**) Interaction coefficients for different types of bilayers. Figure and caption reproduced from Liu et al. (2014)

Table 3.1 Comparison of estimated Young's modulus measurements of MoS_2

Study	Monolayer MoS_2		Multilayer		Comment
	E^{2D} (N/m)	E (GPa)	E^{2D} (N/m)	E (GPa)	
(Liu et al. 2014)	171 ± 11	–	300 ± 13[a]	–	[a]Bilayer with interaction coefficient of 0.75 between layers
(Bertolazzi et al. 2011)	180 ± 60	270 ± 100	260 ± 70[b]	200 ± 60	[b]Bilayer
(Castellanos-Gomez et al. 2012)	–	–	–	330 ± 70[c]	[c]Tests with 5–25 layers

studies, the material is held in place only by the adhesion forces between the films, and the holey substrate and sequential indentation are usually performed in different places on the suspended structure. Indeed, localizing the center of the structure is difficult and performing several measurements allows diminishing the error. With those measures, stress–strain behavior can be extracted, and properties such as the Young's modulus and ultimate strength can be calculated and/or directly measured.

In the case of measuring the Young's modulus of MoS_2 materials, studies of Liu et al. (2014) and Bertolazzi et al. (2011) appear to be consistent with one another although, contrary to Bertolazzi et al. (2011), Liu et al. (2014) define an interaction coefficient between the two layers of the bilayer structure for the sake of determining the contribution of each to the total. Castellanos-Gomez (Castellanos-Gomez et al. 2012) estimations are much higher than the two other studies. Table 3.1 shows a detailed summary of different Young's modulus measurements of MoS_2 monolayers and multilayers. For comparison, Suk et al. (2010) and Cao et al. (2015) found a Young's modulus of 145.3 ± 16.4 N/m (207.6 ± 23.4 GPa) for monolayer

GO with C/O ratio of 5:1. For monolayer graphene, Liu et al. (2014) measured a Young's modulus of 349 ± 12 N/m (1,000 GPa). Interestingly, in their study, they showed that when they stacked two different materials, one layer of each, the pretention of the bilayer structure is close to the sum of both the values from each layer; however, the Young's modulus of the bilayer structure was found to be lower.

CNTs have also been tested using AFM deflection measurements of structures suspended over a hole and indented (Kis et al. 2004). Kis et al. used this method to measure the bending stiffness of CNT bundles revealing the benefits of irradiation-induced covalent cross-linking between CNTs on increasing the stiffness of CNT bundles (Kis et al. 2004). However, due to their size and cylindrical shape, it is extremely difficult to indent CNTs and CNT bundles at a precise location. Consequently, other testing methods have been developed. Another pseudo AFM-based technique consists of gluing one end of the CNT or CNT bundle to a rigid and extremely stiff support and gluing the other end to an AFM cantilever (Filleter et al. 2012). Those tests are generally performed using in situ SEM to be able to follow the deflection of the cantilever (load applied) and the elongation of the CNT (strain). Thus, "classical" tensile tests can be performed. Such a tensile testing technique has also been applied to other materials. Recently, it has been used to characterize GO paper (Wang et al. 2013). In this study beams of constant length and thickness but with variable width were FIB milled at the edge of a large GO paper. Each beam has then been successively glued to an AFM cantilever to perform the tensile test using in situ SEM.

3.3.3 Adhesion Characterization

As mentioned previously, the adhesion can play an important role in friction (Chen and Filleter 2015) but also within structures made of individual 1D and 2D component (multilayer structures, DW- and MWCNTs, etc.) (Dong et al. 2011; Liu et al. 2014; Gao et al. 2011) and between materials and the surrounding materials used for the application such as the switchable blister (Boddeti et al. 2013). It is also of great importance for some specific mechanical studies where monolayer and few-layer materials are fixed to the surface only by adhesion forces. A good example is the indentation of suspended structure to calculate from the force–displacement curve the Young's modulus and strength of single-layer and multilayer graphene (Wei and Kysar 2012; Cao et al. 2014), GO (Suk et al. 2010; Cao et al. 2015), single-layer (Bertolazzi et al. 2011) and multilayer MoS_2 (Castellanos-Gomez et al. 2012), and multilayer heterogeneous materials (Liu et al. 2014). In all those studies, the material is held in place only by the adhesion forces between them and the holed substrate.

Adhesion between nanostructures can be measured with the well-known pull-off force measurement protocol with an AFM which consists in approaching a cantilever with a regular or functionalized tip into contact with the material to

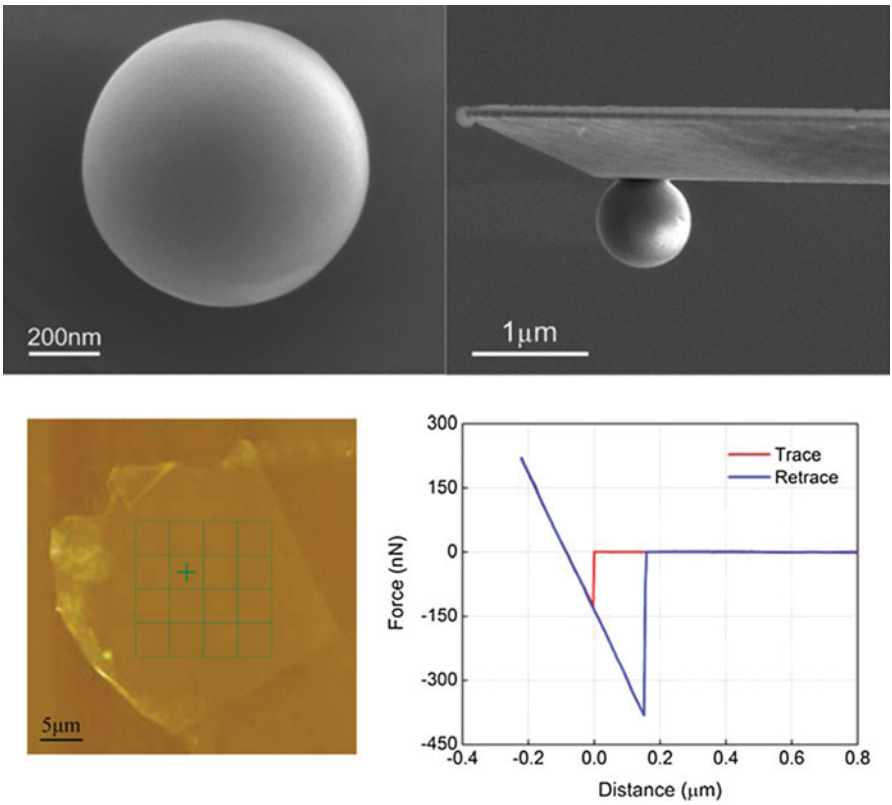

Fig. 3.6 (*Top*) Spherical AFM probe used for adhesion measurements on graphene. (*Bottom*) AFM image of a graphene film and force vs. distance curve recorded to measure the adhesion of graphene. Reproduced from Jiang and Zhu (2015)

characterize and measure the pull-off force when the tip is pulled away from the surface (Chen and Filleter 2015; Lee et al. 2010; Bharat et al. 2000; Sahoo and Biswas 2009; Jiang and Zhu 2015; Jacobs et al. 2015a, b; Lin et al. 2007). Figure 3.6 shows an example of AFM-based adhesion measurements conducted on graphene films (Jiang and Zhu 2015). When the cantilever is brought into contact with the material, it is done at low loads in order to remain in the elastic regime. However, adhesion is a general term to define how much force will be needed to separate two surfaces that have been brought into contact. Adhesion can be influenced by long-range and short-range forces and bonds (van der Waals forces, Coulomb forces, capillary forces, etc.) (Israelachvili 1992). Consequently, the pull-off force is a convolution of a variety of influences which can make it difficult to interpret. Controlling experimental parameters becomes of critical importance as well as defining which theoretical model should be used to extract adhesion data from the pull-off force measurement. The main models used to extract the data and define the real contact areas are the well-known JKR, DMT, and Maugis–Dugdale which

is a transition model between JKR and DMT (Chen and Filleter 2015; Bharat et al. 2000; Lin et al. 2007; Israelachvili 1992). However, those contact mechanics models require assumption that perfect flat surfaces are used, which is practically impossible to achieve experimentally, and some assumption regarding the tip geometry. To obtain more physical data such as the equilibrium distance of adhesion between two materials or the real work of adhesion, other models based on chemical and physical aspects (surface tension, Lennard–Jones potential, etc.) are needed. But most of the time, from pull-off force data, knowing the contact area will be required.

The Persson convention (Persson and Tosatti 2001), used by Jacobs et al. (2015a, b), dissociates adhesion into the effective work of adhesion and the intrinsic work of adhesion. The former is defined as pull-off force between two rough surfaces (the globally encountered measure), while the latter corresponds to the pull-off force between two perfectly flat surfaces. Several models have been developed to take into account the roughness and the exact tip geometry in the extraction of adhesion parameters from the pull-off force. The modified Rumpf model (Jiang and Zhu 2015; Jacobs et al. 2013; Rabinovich et al. 2000) which takes into account the roughness at the nanoscale (by hemispherical approximation of it) was demonstrated to give a better estimation of the effective work of adhesion. Comparisons between MD simulation and in situ TEM experimental data post treated using the modified Rumpf model showed good agreements (Jacobs et al. 2013). Indeed, the decrease by 50 % of the work of adhesion predicted by the MD simulation when the RMS roughness changed from 0.03 to 0.1 nm was found experimentally. Recently, Jacobs et al. (2015a, b) developed a mathematical approach to measure the strength and length of adhesive interactions between rigid materials using the real geometry of the tip. Their approach notably allows measurement of both the $z0$ distance and the intrinsic work of adhesion. In the review done in Jacobs et al. (2015b), the authors notably explain that whatever the approach developed up to now, even in situ TEM measurements, requires an assumption of the $z0$ distance. The in situ TEM experiments reported show huge difference in determination of work of adhesion compared to conventional AFM pull-off measurement which demonstrates the importance to be cautious when relying only on reference values for conventional calculations.

Numerous direct and non-direct techniques exist to measure and estimate adhesion forces between bodies. However, the question that one must ask is "which adhesion, value of adhesion, is representative of the system I am working on?" For large-scale application where surface roughness is completely unavoidable, the classical pull-off force to get the effective adhesion might suffice. On the contrary, for nanocomposite applications where atomically thick materials are to be used, the intrinsic work of adhesion must be known. Finally, the question of the material to be used is of interest, and the interactions depend on the nature of the materials brought into contact. For example, Biswas et al. (Sahoo and Biswas 2009) measured adhesion between MoS_2 particles and glass beads. As it is for a micro-/macroscale tribological application, the adhesion measured is the effective adhesion directly linked to the pull-off force, which is fine considering the scale and the application.

However, in many applications of MoS_2 as a solid lubricant layer, the real contact is steel vs. MoS_2 and not glass vs. MoS_2 which greatly limits the transposition of the data to the real application.

Throughout the previous sections on friction and adhesion, the discussion mentioned different models to define adhesion, for example. But some of those models, like JKR or DMT, require the knowledge of the mechanical properties of the material tested. Moreover, to employ those materials in large-scale applications such as the bendable electronics, the mechanical properties of individual 1D and 2D component and their assembly must be known.

3.4 Indirect Mechanical Characterization of Interfaces Within Nanocomposites

3.4.1 Dynamic Mechanical Analysis

Dynamic mechanical analysis (DMA) is another experimental technique that has been used to study the mechanical behavior of carbon nanostructure-based composite materials (Compton et al. 2010, 2012; Yang et al. 2004; Zou et al. 2004; Wang et al. 2004; Espinosa et al. 2012b; An et al. 2011). While DMA has been extensively used to measure the viscoelastic response of CNT–polymer and CNT–epoxy matrix nanocomposites as it measures both the storage and loss moduli (Yang et al. 2004; Zou et al. 2004; Wang et al. 2004; Espinosa et al. 2012b), it can also be used to indirectly study the shear interactions within other forms of carbon-based nanocomposites. An et al. used DMA to measure the stiffening effects of bio-inspired composite GO papers which were similar to borate cross-linkers. DMA measurements showed significant increases in the GO paper stiffness as a result of the inclusion of borate between the GO sheets which introduced covalent bonding increasing the bond strength and stiffness between layers (An et al. 2011). Similar stiffening effects have also been observed using DMA for polyvinyl alcohol (PVA)–GO nanocomposites. Figure 3.7 shows DMA experimental results and molecular dynamics (MD) simulations of PVA–GO composite papers with intercalated water content. The presence of an optimal concentration of water molecules between the PVA–GO layers introduces hydrogen-bonding networks at the interfaces between GO layers which act cooperatively to enhance the stress transfer between layers and ultimately modify the stiffness of the composites (Compton et al. 2012).

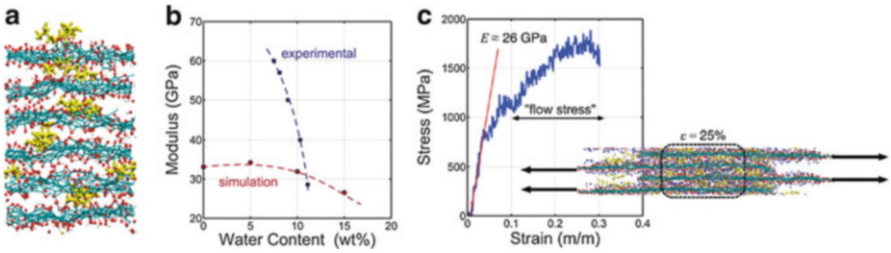

Fig. 3.7 (**a**) Molecular dynamics simulation cell for a PVA–GO nanocomposite. (**b**) Comparison between DMA storage modulus measurements and MD simulation results at varying water content levels. (**c**) MD simulation of the stress–strain response of a PVA–GO composite. Adapted with permission from Compton et al. (2012)

3.4.2 Micro Tensile Testing, Compression, and Nanoindentation

The mechanical stress–strain response under uniaxial tension can be measured for nanocomposite material via micro tensile testing. While this is often the mechanical characterization method of choice for graphene- and CNT-reinforced fibers and plates to determine the macroscopic mechanical properties, it can also be utilized indirectly to gain insights into the internal mechanisms within the composite materials. In the case of graphene-based nanocomposites, micro tensile testing, accompanied by post failure SEM imaging of fracture surfaces, has been used to identify the nature of shear interactions and fracture with the nanocomposite materials (Dikin et al. 2007; Stankovich et al. 2006). Micro tensile testing has also been heavily utilized to characterize the mechanical behavior of both pure CNT and CNT nanocomposite fibers (Naraghi et al. 2010; Koziol et al. 2007; Stano et al. 2008; Motta et al. 2005; Zhang et al. 2005; Dalton et al. 2003).

The interaction between adjacent nanostructures can also be indirectly probed by analysis of compression and nanoindentation experiments on arrays or bundles. Compression and nanoindentation studies on tightly packed CNT forests and arrays have given insights into the shear interactions between individual CNTs and bundles during loading (Ginga and Sitaraman 2013; Cao et al. 2011). Cao et al. demonstrated that the buckling behavior of CNT forests is affected by entanglements and shear interactions between the adjacent CNTs in the densely packed array structures which has an impact on the energy adsorption behavior of the materials (Cao et al. 2011).

When the thickness of the material to be characterized reaches a few hundreds of nanometers, typically for thin films, or contains different phase or structure, nanoindentation also becomes of interest. This technique allows measuring the mechanical properties of materials such as the hardness, the Young's modulus, or the yield strength at the nanoscale. Both AFM and nanoindenter can be used. However, due to the intrinsic design of both systems, nanoindenter is much stiffer

than AFM-based systems and allows working at higher loads and measuring the contact stiffness accurately and continuously during indentation. Numerous models exist to extract the different properties from the measurements. The Oliver–Pharr model (Oliver and Pharr 1992) is the most known and certainly used model for elastic plastic indentation. However, similarly to the Hertz, JKR, DMT, and Maugis models used for indentation in the elastic domain, the Oliver–Pharr model can be employed only under specific conditions, and notably in homogeneous isotropic materials, the body indented must be semi-infinite compared to the indenter, no pileup of material around the indentation, and no significant deformation of the indenter. The Oliver–Pharr model relies on the measurements of the indentation depth from the unloading curve. However, this value can be questioned if pileup occurs around the indenter or if the indentation depth is low which can induce big errors in its measurement. Guillonneau et al. (2012) developed a technique based on the detection of the second harmonic of the displacement signal to determine the mechanical properties independently of indentation depth measurement. This technique appears to be limited to constant Young's modulus materials, but appears useful to low indentation depth experiments. When both adhesion and mechanical properties, in the elastic regime, are of interest, methods based on other models like JKR can be used (Ebenstein and Wahl 2006). In this study, the authors notably extended the model to viscoelastic materials and managed to extract both the frequency-dependent and relaxed modulus of PDMS materials.

Nanoindentation can be of interest when 2D materials are stacked and the overall structure reaches a few hundred nanometers. Stempflé and von Stebut (2006) in their study of the 3rd body created from graphite showed that when the 3rd body is quasi-continuous, i.e., formed by agglomeration of cleaved basal planes, indentation showed energy dissipation but no indentation marks. This energy is dissipated via a dissipation mode by shearing of the basal planes. The thicknesses of the quasi-continuous 3rd body films tested were approximately 150, 300, and 450 nm. Despite its usefulness and widespread application, nanoindentation can suffer from limitations that may strongly influence the measurement reliability. The reader is invited to read Fischer-Cripps (2011) for a review of the different parameters (pileup, friction, substrate, roughness, system compliance, etc.) influencing the measurement reliability.

3.5 Perspectives and Future Directions for Research

A complete understanding of the mechanical properties of nanocomposite materials requires a detailed characterization of both the intrinsic behavior of the nanomaterial constituents and interfacial interactions at multiple length scales. In this chapter a number of advances in nanomechanical characterization techniques including both macroscale indirect approaches and direct in situ approaches have been summarized. In order to further advance nanoscale mechanical testing of 1D and 2D materials, progress in a number of research directions is needed. Notable

directions include conducting tribology experiments using in situ SEM and TEM as well as controlling the environmental conditions for nanomechanical testing such that they are more aligned with conditions of real applications.

Given the small length scales of the constituents with nanocomposites and the importance of interfacial properties, further advancements of in situ tribology approaches are still needed. For example, the majority of approaches to characterize friction and adhesions discussed herein have been conducted ex situ with little direct knowledge of the contact under investigation. Advanced in situ FFM techniques are needed in which SEM and TEM are used to directly measure the contact geometry and local deformation of the interfaces for which friction and adhesion are being measured. Although some significant advances have been achieved in this direction to visualize nanoscale contacts under sliding (Merkle and Marks 2007), many are currently limited to qualitative characterization and do not enable full quantitative force and stress analysis available from conventional table top AFM-based techniques.

The environment within which nanostructures are characterized can also play a significant role in the measured properties. For example, as was discussed earlier, the water content present around and within carbon-based nanocomposite materials can play a role in varying mechanical properties such as ductility and stiffness (Compton et al. 2012). Despite this important role of environment, many nanomechanical techniques are currently employed under either poorly controlled room temperature and humidity conditions or under vacuum environments that do not accurately represent application conditions. Integration of the techniques discussed herein within controlled environment chambers with careful monitoring is needed to ensure that measured properties are fully understood with respect to the presence of humidity and contaminants.

References

Alemán, B., Reguero, V., Mas, B., Vilatela, J.J.: Strong CNT fibers by drawing inspiration from polymer fiber spinning. ACS Nano **9**(7), 7392–7398 (2015)

An, Z., Compton, O.C., Putz, K.W., Brinson, L.C., Nguyen, S.T.: Bio-inspired borate cross-linking in ultra-stiff graphene oxide thin films. Adv. Mater. **23**, 3842–3846 (2011)

Azoubel, S., Magdassi, S.: Controlling adhesion properties of SWCNT-PET films prepared by wet deposition. ACS Appl. Mater. Interfaces **6**, 9265–9271 (2014)

Barboza, A.P., Chacham, H., Oliveira, C.K., Fernandes, T.F., Ferreira, E.H., Archanjo, B.S., Batista, R.J., de Oliveira, A.B., Neves, B.R.: Dynamic negative compressibility of few-layer graphene, h-BN, and MoS2. Nano Lett. **12**, 2313–2317 (2012)

Berman, D., Erdemir, A., Sumant, A.V.: Graphene: a new emerging lubricant. Mater. Today **17**, 31–42 (2014)

Berman, D., Deshmukh, S.A., Sankaranarayanan, S.K.R.S., Erdemir, A., Sumant, A.V.: Macroscale superlubricity enabled by graphene nanoscroll formation. Science **348**, 1118–1122 (2015)

Bertolazzi, S., Brivio, J., Kis, A.: Stretching and breaking of ultrathin MoS2. ACS Nano **5**, 9703–9709 (2011)

Bharat, B., Othmar, M.: Micro/nanotribology. In: Bhushan B. (ed.) Modern Tribology Handbook, vol 2, CRC Press, Boca Raton (2000)

Bhushan, B.: Nanotribology and nanomechanics. Wear **259**, 1507–1531 (2005)

Boddeti, N.G., Liu, X., Long, R., Xiao, J., Bunch, J.S., Dunn, M.L.: Graphene blisters with switchable shapes controlled by pressure and adhesion. Nano Lett. **13**, 6216–6221 (2013)

Borini, S., White, R., Wei, D., Astley, S., Spigone, E., Harris, N., Kivioja, J., Ryhanen, T.: Ultrafast graphene oxide humidity sensors. ACS Nano **7**, 11166–11173 (2013)

Cao, C.H., Reiner, A., Chung, C.H., Chang, S.H., Kao, I., Kukta, R.V., Korach, C.S.: Buckling initiation and displacement dependence in compression of vertically aligned carbon nanotube arrays. Carbon **49**, 3190–3199 (2011)

Cao, C., Sun, Y., Filleter, T.: Characterizing mechanical behavior of atomically thin films: a review. J. Mater. Res. **29**, 338–347 (2014)

Cao, C., Daly, M., Singh, C.V., Sun, Y., Filleter, T.: High strength measurement of monolayer graphene oxide. Carbon **81**, 497–504 (2015)

Castellanos-Gomez, A., Poot, M., Steele, G.A., van der Zant, H.S., Agrait, N., Rubio-Bollinger, G.: Elastic properties of freely suspended MoS2 nanosheets. Adv. Mater. **24**, 772–775 (2012)

Chen, H., Filleter, T.: Effect of structure on the tribology of ultrathin graphene and graphene oxide films. Nanotechnology **26**, 135702 (2015)

Coleman, J.N., Khan, U., Blau, W.J., Gun'ko, Y.K.: Small but strong: a review of the mechanical properties of carbon nanotube-polymer composites. Carbon **44**, 1624–1652 (2006)

Compton, O., Dikin, D.A., Putz, K.W., Brinson, L.C., Nguyen, S.T.: Electrically conductive "alkylated" graphene paper via chemical reduction of amine-functionalized graphene oxide paper. Adv. Mater. **22**, 892–896 (2010)

Compton, O.C., Cranford, S.W., Putz, K.W., An, Z., Brinson, L.C., Buehler, M.J., Nguyen, S.T.: Tuning the mechanical properties of graphene oxide paper and its associated polymer nanocomposites by controlling cooperative intersheet hydrogen bonding. ACS Nano **6**, 2008–2019 (2012)

Cooper, C.A., Young, R.J., Halsall, M.: Investigation into the deformation of carbon nanotubes and their composites through the use of Raman spectroscopy. Compos. Part A Appl. Sci. Manuf. **32**, 401–411 (2001)

Dalton, A.B., Collins, S., Munoz, E., Razal, J.M., Ebron, V.H., Ferraris, J.P., Coleman, J.N., Kim, B.G., Baughman, R.H.: Super-tough carbon-nanotube fibres-these extraordinary composite fibres can be woven into electronic textiles. Nature **423**, 703–706 (2003)

Dikin, D.A., Stankovich, S., Zimney, E.J., Piner, R.D., Dommett, G.H., Evmenenko, G., Nguyen, S.T., Ruoff, R.S.: Preparation and characterization of graphene oxide paper. Nature **448**, 457 (2007)

Dong, X., Xing, G., Chan-Park, M.B., Shi, W., Xiao, N., Wang, J., Yan, Q., Sum, T.C., Huang, W., Chen, P.: The formation of a carbon nanotube-graphene oxide core-shell structure and its possible applications. Carbon **49**, 5071–5078 (2011)

Dresselhaus, M.S., Dresselhaus, G., Saito, R., Jorio, A.: Raman spectroscopy of carbon nanotubes. Phys. Rep. **409**, 47–99 (2005)

Ebenstein, D.M., Wahl, K.J.: A comparison of JKR-based methods to analyze quasi-static and dynamic indentation force curves. J. Colloid Interface Sci. **298**, 652–662 (2006)

Espinosa, H.D., Bernal, R.A., Filleter, T.: In-situ TEM electro-mechanical testing of nanowires and nanotubes. Small **8**, 3233–3252 (2012a)

Espinosa, H.D., Filleter, T., Naraghi, M.: Multiscale experimental mechanics of hierarchical carbon-based materials. Adv. Mater. **24**, 2805–2823 (2012b)

Ferrari, A.C., Basko, D.M.: Raman spectroscopy as a versatile tool for studying the properties of graphene. Nat. Nanotechnol. **8**, 235–246 (2013)

Filleter, T., McChesney, J.L., Bostwick, A., Rotenberg, E., Emtsev, K.V., Seyller, T., Horn, K., Bennewitz, R.: Friction and dissipation in epitaxial graphene films. Phys. Rev. Lett. **102**, 086102 (2009)

Filleter, T., Bernal, R., Li, S., Espinosa, H.D.: Ultrahigh strength and stiffness in cross-linked hierarchical carbon nanotube bundles. Adv. Mater. **23**, 2855–2860 (2011)

Filleter, T., Yockel, S., Naraghi, M., Paci, J.T., Compton, O.C., Mayes, M.L., Nguyen, S.T., Schatz, G.C., Espinosa, H.D.: Experimental-computational study of shear interactions within double-walled carbon nanotube bundles. Nano Lett. **12**, 732–742 (2012)

Fischer-Cripps, A.C.: Nanoindentation. Springer, New York (2011)

Gao, Y., Liu, L.Q., Zu, S.Z., Peng, K., Zhou, D., Han, B.H., Zhang, Z.: The effect of interlayer adhesion on the mechanical behaviors of macroscopic GO papers. ACS Nano **5**, 2134–2141 (2011)

Ginga, N.J., Sitaraman, S.K.: The experimental measurement of effective compressive modulus of carbon nanotube forests and the nature of deformation. Carbon **53**, 237–244 (2013)

Gong, L., Young, R.J., Kinloch, I.A., Riaz, I., Jalil, R., Novoselov, K.S.: Optimizing the reinforcement of polymer-based nanocomposites by graphene. ACS Nano **6**, 2086–2095 (2012)

Guillonneau, G., Kermouche, G., Bec, S., Loubet, J.-L.: Determination of mechanical properties by nanoindentation independently of indentation depth measurement. J. Mater. Res. **27**, 2551–2560 (2012)

Haque, M.A., Saif, M.T.A.: In-situ tensile testing of nano-scale specimens in SEM and TEM. Exp. Mech. **42**, 123–128 (2002)

Israelachvili, J.N.: Intermolecular and Surface Forces, 2nd edn. Academic, London, UK (1992)

Jacobs, T.D.B., Ryan, K.E., Keating, P.L., Grierson, D.S., Lefever, J.A., Turner, K.T., Harrison, J. A., Carpick, R.W.: The effect of atomic-scale roughness on the adhesion of nanoscale asperities: a combined simulation and experimental investigation. Tribol. Lett. **50**, 81–93 (2013)

Jacobs, T.D.B., Lefever, J.A., Carpick, R.W.: A technique for the experimental determination of the length and strength of adhesive interactions between effectively rigid materials. Tribol. Lett. **59**, 1–11 (2015a)

Jacobs, T.D.B., Lefever, J.A., Carpick, R.W.: Measurement of the length and strength of adhesive interactions in a nanoscale silicon-diamond interface. Adv. Mater. Interfaces. **2**, 1400547 (2015b)

Jiang, T., Zhu, Y.: Measuring graphene adhesion using atomic force microscopy with a microsphere tip. Nanoscale **7**, 10760–10766 (2015)

Kim, Y.D., Kim, H., Cho, Y., Ryoo, J.H., Park, C.H., Kim, P., Kim, Y.S., Lee, S., Li, Y., Park, S. N., Shim Yoo, Y., Yoon, D., Dorgan, V.E., Pop, E., Heinz, T.F., Hone, J., Chun, S.H., Cheong, H., Lee, S.W., Bae, M.H., Park, Y.D.: Bright visible light emission from graphene. Nat. Nanotechnol. **10**, 676–681 (2015)

Kis, A., Csanyi, G., Salvetat, J.-P., Lee, T.-N., Couteau, E., Kulik, A.J., Benoit, W., Brugger, J., Forro, L.: Reinforcement of single-walled carbon nanotube bundles by intertube bridging. Nat. Mater. **3**, 153–157 (2004)

Koziol, K., Vilatela, J., Moisala, A., Motta, M., Cunniff, P., Sennett, M., Windle, A.: High-performance carbon nanotube fiber. Science **318**, 1892–1895 (2007)

Kwon, C.H., Chun, K.Y., Kim, S.H., Lee, J.H., Kim, J.H., Lima, M.D., Baughman, R.H., Kim, S. J.: Torsional behaviors of polymer-infiltrated carbon nanotube yarn muscles studied with atomic force microscopy. Nanoscale **7**, 2489–2496 (2015)

Lee, C., Li, Q.Y., Kalb, W., Liu, X.Z., Berger, H., Carpick, R.W., Hone, J.: Frictional characteristics of atomically thin sheets. Science **328**, 76–80 (2010)

Lin, D.C., Dimitriadis, E.K., Horkay, F.: Robust strategies for automated AFM force curve analysis-II: adhesion-influenced indentation of soft, elastic materials. J. Biomech. Eng. **129**, 904–912 (2007)

Liu, K., Yan, Q., Chen, M., Fan, W., Sun, Y., Suh, J., Fu, D., Lee, S., Zhou, J., Tongay, S., Ji, J., Neaton, J.B., Wu, J.: Elastic properties of chemical-vapor-deposited monolayer MoS2, WS2, and their bilayer heterostructures. Nano Lett. **14**, 5097–5103 (2014)

Liu, Z.F., Fang, S., Moura, F.A., Ding, J.N., Jiang, N., Di, J., Zhang, M., Lepro, X., Galvao, D.S., Haines, C.S., Yuan, N.Y., Yin, S.G., Lee, D.W., Wang, R., Wang, H.Y., Lv, W., Dong, C.,

Zhang, R.C., Chen, M.J., Yin, Q., Chong, Y.T., Zhang, R., Wang, X., Lima, M.D., Ovalle-Robles, R., Qian, D., Lu, H., Baughman, R.H.: Hierarchically buckled sheath-core fibers for superelastic electronics sensors and muscles. Science **349**, 400–404 (2015)

Lu, Y., Ganesan, Y., Lou, J.: A multi-step method for in situ mechanical characterization of 1-D nanostructures using a novel micromechanical device. Exp. Mech. **50**, 47–54 (2010)

Malard, L.M., Pimenta, M.A., Dresselhaus, G., Dresselhaus, M.S.: Raman spectroscopy in graphene. Phys. Rep. Rev. Sect. Phy. Lett. **473**, 51–87 (2009)

Meng, F., Zhao, J., Ye, Y., Zhang, X., Li, S., Jia, J., Zhang, Z., Li, Q.: Multifunctionalization of carbon nanotube fibers with the aid of graphene wrapping. J. Mater. Chem. **22**, 16277 (2012)

Merkle, A.P., Marks, L.D.: Friction in full view. Appl. Phys. Lett. **90**, 064101 (2007)

Mirjalili, V., Ramachandramoorthy, R., Hubert, P.: Enhancement of fracture toughness of carbon fiber laminated composites using multi wall carbon nanotubes. Carbon **79**, 413–423 (2014)

Mirzaeifar, R., Qin, Z., Buehler, M.J.: Mesoscale mechanics of twisting carbon nanotube yarns. Nanoscale **7**, 5435–5445 (2015)

Motta, M., Li, Y.L., Kinloch, I., Windle, A.: Mechanical properties of continuously spun fibers of carbon nanotubes. Nano Lett. **5**, 1529–1533 (2005)

Naraghi, M., Filleter, T., Moravsky, A., Locascio, M., Loutfy, R.O., Espinosa, H.D.: A multiscale study of high performance double-walled nanotube—polymer fibers. ACS Nano **4**, 6463–6476 (2010)

Oliver, W.C., Pharr, G.M.: An improved technique for determining hardness and elastic modulus using load and displacement sensing indentation experiments. J. Mater. Res. **7**, 1564–1583 (1992)

Peng, B., Locascio, M., Zapol, P., Li, S., Mielke, S.L., Schatz, G.C., Espinosa, H.D.: Measurements of near-ultimate strength for multiwalled carbon nanotubes and irradiation-induced crosslinking improvements. Nat. Nanotechnol. **3**, 626–631 (2008)

Persson, B.N.J., Tosatti, E.: The effect of surface roughness on the adhesion of elastic solids. J. Chem. Phys. **115**, 5597–5610 (2001)

Qian, H., Greenhalgh, E.S., Shaffer, M.S.P., Bismarck, A.: Carbon nanotube-based hierarchical composites: a review. J. Mater. Chem. **20**, 4751–4762 (2010)

Qiu, J., Terrones, J., Vilatela, J.J., Vickers, M.E., Elliott, J.A., Windle, A.H.: Liquid infiltration into CNT fibers_Effect on structure and electrical properties. ACS Nano **7**, 8412–8422 (2013)

Rabinovich, Y.I., Adler, J.J., Ata, A., Singh, R.K., Moudgil, B.M.: Adhesion between nanoscale rough surfaces. J. Colloid Interface Sci. **232**, 10–16 (2000)

Rodrigo, D., Limaj, O., Janner, D., Etezadi, D., García de Abajo, F.J., Pruneri, V., Altug, H.: Mid-infrared plasmonic biosensing with graphene. Science **349**, 165–168 (2015)

Roenbeck, M.R., Furmanchuk, A., An, Z., Paci, J.T., Wei, X., Nguyen, S.T., Schatz, G.C., Espinosa, H.D.: Molecular-level engineering of adhesion in carbon nanomaterial interfaces. Nano Lett. **15**, 4504–4516 (2015)

Sahoo, R.R., Biswas, S.K.: Microtribology and friction-induced material transfer in layered MoS2 nanoparticles sprayed on a steel surface. Tribol. Lett. **37**, 313–326 (2009)

Samyn, P., Schoukens, G., De Baets, P.: Micro- to nanoscale surface morphology and friction response of tribological polyimide surfaces. Appl. Surf. Sci. **256**, 3394–3408 (2010)

Santos, L.V., Trava-Airoldi, V.J., Iha, K., Corat, E.J., Salvadori, M.C.: Diamond-like-carbon and molybdenum disulfide nanotribology studies using atomic force measurements. Diamond Relat. Mater. **10**, 1049–1052 (2001)

Stankovich, S., Dikin, D.A., Dommett, G.H.B., Kohlhaas, K.M., Zimney, E.J., Stach, E.A., Piner, R.D., Nguyen, S.T., Ruoff, R.S.: Graphene-based composite materials. Nature **442**, 282 (2006)

Stano, K.L., Koziol, K., Pick, M., Motta, M.S., Moisala, A., Vilatela, J.J., Frasier, S., Windle, A. H.: Direct spinning of carbon nanotube fibres from liquid feedstock. Int. J. Mater. Form. **1**, 4 (2008)

Stempflé, P., von Stebut, J.: Nano-mechanical behaviour of the 3rd body generated in dry friction—feedback effect of the 3rd body and influence of the surrounding environment on the tribology of graphite. Wear **260**, 601–614 (2006)

Suk, J.W., Piner, R.D., An, J., Ruoff, R.S.: Mechanical properties of monolayer GO. ACS Nano **4**, 6557–6564 (2010)

Tang, D.M., Kvashnin, D.G., Najmaei, S., Bando, Y., Kimoto, K., Koskinen, P., Ajayan, P.M., Yakobson, B.I., Sorokin, P.B., Lou, J., Golberg, D.: Nanomechanical cleavage of molybdenum disulphide atomic layers. Nat. Commun. **5**, 3631 (2014)

Vilatela, J.J., Elliott, J.A., Windle, A.H.: A model for the strength of yarn-like carbon nanotube fibers. ACS Nano **5**, 1921–1927 (2011)

Wang, Z., Liang, Z.Y., Wang, B., Zhang, C., Kramer, L.: Processing and property investigation of single-walled carbon nanotube (SWNT) buckypaper/epoxy resin matrix nanocomposites. Compos. Part A Appl. Sci. Manuf. **35**, 1225–1232 (2004)

Wang, C., Frogley, M.D., Cinque, G., Liu, L.-Q., Barber, A.H.: Deformation and failure mechanisms in graphene oxide paper using in situ nanomechanical tensile testing. Carbon **63**, 471–477 (2013)

Wang, X., Tian, H., Mohammad, M.A., Li, C., Wu, C., Yang, Y., Ren, T.L.: A spectrally tunable all-graphene-based flexible field-effect light-emitting device. Nat. Commun. **6**, 7767 (2015)

Wei, X., Kysar, J.W.: Experimental validation of multiscale modeling of indentation of suspended circular graphene membranes. Int. J. Solids Struct. **49**, 3201–3209 (2012)

Yang, J.W., Hu, J.H., Wang, C.C., Qin, Y.J., Guo, Z.X.: Fabrication and characterization of soluble multi-walled carbon nanotubes reinforced P(MMA-co-EMA) composites. Macromol. Mater. Eng. **289**, 828–832 (2004)

Zhang, M., Fang, S.L., Zakhidov, A.A., Lee, S.B., Aliev, A.E., Williams, C.D., Atkinson, K.R., Baughman, R.H.: Strong, transparent, multifunctional, carbon nanotube sheets. Science **309**, 1215–1219 (2005)

Zhang, P., Ma, L.L., Fan, F.F., Zeng, Z., Peng, C., Loya, P.E., Liu, Z., Gong, Y.J., Zhang, J.N., Zhang, X.X., Ajayan, P.M., Zhu, T., Lou, J.: Fracture toughness of graphene. Nat. Commun. **5**, 3782 (2014)

Zou, Y.B., Feng, Y.C., Wang, L., Liu, X.B.: Processing and properties of MWNT/HDPE composites. Carbon **42**, 271–277 (2004)

Chapter 4
Effects of Nanoporosity on the Mechanical Properties and Applications of Aerogels in Composite Structures

Teng Yong Ng, Sunil C. Joshi, Jingjie Yeo, and Zishun Liu

Abstract Aerogels are ultralight solids with nanoporous structure and are one of the world's lightest materials available in the market. It is a dry gel, principally made up of 99.8 % of air and weighing just around three times that of air. The first aerogels were realized in 1931, when Kistler (J Phys Chem 36:52–64, 1932) attempted to remove liquid from a wet gel. It started out with the testing of the hypothesis that the liquid in a jelly can be replaced by a gas so as to avoid the collapse of the wet gel. He postulated that it was possible to slowly expand the supercritical fluid within a gel and obtain an air-filled non-collapsed gel structure. He subsequently succeeded in producing silica aerogels with densities in the range 20–100 kg/m^3, as well as aerogels of alumina, tungsten, ferric, and stannic oxides. Today, silica aerogel is frequently used in nanocomposites for their light weight and excellent thermal insulating properties. In this chapter, we document some of the silica aerogel-filled carbon composite sandwich structures we have recently developed and also numerically examine the underlying mechanisms which enable silica aerogels to possess extreme insulation properties and especially how pore size plays a major role.

T.Y. Ng (✉) • S.C. Joshi
School of Mechanical and Aerospace Engineering, Nanyang Technological University, 50 Nanyang Avenue, Singapore 639798, Singapore
e-mail: mtyng@ntu.edu.sg; mscjoshi@ntu.edu.sg

J. Yeo
A*STAR Institute of High Performance Computing, 1 Fusionopolis Way, #16-16 Connexis, Singapore 138632, Singapore
e-mail: yeojj@ihpc.a-star.edu.sg

Z. Liu
International Center for Applied Mechanics, State Key Laboratory for Strength and Vibration of Mechanical Structures, Xi'an Jiaotong University, Xi'an 710049, People's Republic of China
e-mail: zishunliu@xjtu.edu.cn

S.A. Meguid (ed.), *Advances in Nanocomposites*,
DOI 10.1007/978-3-319-31662-8_4

4.1 Introduction

Many novel ultralight materials have been developed over the past decades in the unending drive to construct engineering nanocomposites which are lighter, stronger, and cheaper than ever before. A method to achieve these purposes is the simultaneous reduction of the weight of the material (such as introducing extreme porosity) while maximizing its toughness and strength. One such class of materials utilizing this approach is termed aerogels. For instance, silica aerogels are highly porous materials synthesized through supercritical drying of a wet gel, originating in the early 1930s from Kistler (1932; Aegerter et al. 2011). Supercritical drying occurs at high temperatures and pressures due to the liquid–gas phase boundary becoming indistinguishable. Without supercritical drying, high surface tensions from evaporation of the liquids would result in xerogels of low porosities rather than aerogels due to shrinkage and collapsing (Fricke and Emmerling 1992). The nanoporous network of silica aerogels is formed through a multistep process of polymerization, gelation, hydrolysis, and condensation, using alkoxides of $Si(OR)_4$ as precursors. For example, a good precursor could be tetramethoxysilane (TMOS) where the R group is a methyl group CH_3, such that

$$Si(OCH_3)_4 + 2H_2O \rightarrow SiO_2 + 4CH_3OH$$

Subsequently, polycondensation and supercritical drying of the aqueous gel will form a coherent nanoporous network. Other potential precursors include tetraethyl orthosilicate (TEOS), polyethoxysilane (PEDS), perfluoroalkysilane (PFAS), and 3-(2-aminoethylamino) propyltrimethoxysilane (EDAS) (Aegerter et al. 2011). Such a wide range of choices allows the enhancement or tailoring of the desired geometrical, chemical, and mechanical properties of the end product such as the pore-size distribution, density, and strength. Other important factors in aerogel production include the nature of the solvent, the nature and concentration of the catalyst, the molar ratio of precursors to water, and the concentration of precursors (Aegerter et al. 2011). Moreover, aerogels can be produced from materials other than silica such as carbon, sodium silicate, zirconium dioxide, and many other organic and inorganic materials, resulting in a wide variety of properties for different applications. These properties can include opacity, strength and toughness, and electrical and thermal conductivity. The Aerogel Handbook is a comprehensive compendium of aerogels outside of silica aerogels (Aegerter et al. 2011).

Due to pure silica aerogels' low density and connectivity within the silica network, their mechanical properties tend to be rather poor, such that elastic contraction of approximately 50 % in comparison to their length can be attained easily. However, hybridization, doping, and aging of silica aerogels could help to alleviate some of these drawbacks (Aegerter et al. 2011). In spite of these deficiencies, their low dielectric constants and thermal conductivity enable silica aerogels to be highly suitable for applications in dielectrics for integrated circuits (ICs), passive solar energy collection devices, and thermal and acoustic insulation in

buildings and appliances (Hrubesh 1998). Silica aerogels can also substitute plastics produced from chlorofluorocarbons, used in thermal insulation of refrigerators, as they are nontoxic to the environment. Most notably, Cherenkov counters in Cherenkov radiators (Cantin et al. 1974) were made from silica aerogels. Another crucial aspect of silica aerogels is their extremely low density for a solid, which can be as low as only three times that of air at 0.003 g/cm^3. Such a low density results in dramatic weight savings when silica aerogels are employed in nanocomposites or other monolithic structures. This extreme porosity also allows silica aerogels to be utilized for nanoparticulate sorption, entrapment, storage, and release (Aegerter et al. 2011). Other structural features of silica aerogels in the nanoscale include self-similar patterns known as fractals, where aerogels display significant geometrical similarity regardless of viewing distance. Such fractal features can be characterized through the parameter known as the fractal dimension measured experimentally using a variety of methods such as small-angle neutron scattering (SANS) spectroscopy, adsorption of molecules of different cross-sectional areas, or small- or ultrasmall-angle x-ray scattering (SAXS/USAXS).

Currently, there is a great proliferation of silica aerogels as thermal insulators due to large-scale commercial production, generally as granular beads (Herrmann et al. 1995; Cabot-Corp. 2011; Jelle et al. 2011). This granular form allows silica aerogels to be embedded in other materials as nanocomposites and fillers to customize the thermal and optical properties for specific applications including passive solar windows (Wittwer 1989), cryogenic thermal insulation systems on space launch vehicles (Fesmire 2006; Jones 2006), and thermal insulation of windows (Rubin and Lampert 1983; Duer and Svendsen 1998). Theoretical calculations found that the thermal conductance of a window using just 5 mm thick aerogel insulation is potentially halved, a reduction that is much larger than that attainable by double-glass windows (Rubin and Lampert 1983). By ensuring the Rovers are kept at relative steady temperatures in spite of the 100 °C variations in temperatures on the surface of Mars, silica aerogels also played an important role in the ongoing exploration of the planet Mars by the Mars Rovers, Spirit and Opportunity, launched in 2003 (Jones 2006).

4.2 Types of Aerogels

The three most established and prevalent types of aerogels, namely, silica aerogel, alumina aerogel, and carbon aerogel, have been reported in the literature. Table 4.1 compares different properties of these aerogels.

Table 4.1 Comparison of different types of aerogels (Steiner 2015)

Parameter	Alumina aerogel (Poco et al. 2001)	Carbon aerogel (Cotet et al. 2007)	Silica aerogel (Tillotson and Hrubesh 1992)
Class and composition	Metal oxide (Al_2O_3)	Carbon (C)	Silica (SiO_2)
Density range (kg/m^3)	30–100	20–500	1.1–65.0
Surface area (m^2/g)	150–370	600–800	500–950
Primary particle size (nm)	–	3.0–20	2.0–3.0
Average pore size (nm)	–	7.0–20.0	20
Thermal conductivity at room temperature (W/mK)	29	120–320	0.016–0.03
Young's modulus (MPa)	0.55 (at 0.037 g/cm^3)	–	0.05–400

4.2.1 Alumina Aerogel

Alumina-based ceramics, in addition to its relatively high strength, offer better thermal and chemical stability. These non-silica aerogels are notably weak and fragile in monolithic form. It is especially difficult to prepare uncracked monoliths of pure alumina aerogels that are robust and moisture stable. However, by using a two-step sol–gel process, strong stable monolithic and high porosity alumina aerogels can be produced (Poco et al. 2001). Monolithic alumina aerogels could be used separately or added to other thermal protection materials to make composites with superior thermal resistance properties. Alumina aerogels are also used as catalysts for NO reduction with C_3H_6 (Hirashima et al. 1997).

4.2.2 Carbon Aerogel

Carbon aerogels are promising materials which can be electrodes for high-performance capacitors and batteries (Fu et al. 2003). They are nanoporous materials with controllable structural properties, such as low mass densities, high surface areas, and continuous porosities. Moreover, they offer the possibility to incorporate metallic species in the carbon framework. In the last decade, many efforts have been devoted to increase the graphitization of carbon aerogels in order to enhance their electrical conductivity. It was reported that transition metals incorporated into the carbon aerogels structure seem to be the best catalysts for graphitization of carbon aerogels.

4.2.3 *Silica Aerogel*

Silica aerogels (see Fig. 4.1) are marked with properties, such as high-specific surface area, high porosity, low density, high thermal insulation value, ultralow dielectric constant, and low index of refraction. Monolithic silica aerogel has been used extensively in high energy physics in radiation detectors. Other application of silica aerogels are shock wave studies at high pressures, inertial confinement fusion, radio luminescent devices, and micrometeorites (Soleimani Dorcheh and Abbasi 2008).

Another area in which silica aerogels are being applied is in solar architecture, as transparent insulation. Silica aerogel readily allows the passage of solar radiation into the solar panel but prevents the heat which is generated in the solar panel from being dissipated. Furthermore, the transparent material allows through light as well. Silica aerogel is hydrophobic, which keeps it free from atmospheric moisture. By holding air in its micron-sized pores, silica aerogel makes an excellent insulator thermally, electrically, and acoustically. The authors have used it as a core filler in various composite panels, as seen in Fig. 4.2, either as the granules or as blocks with certain binders.

Fig. 4.1 Silica aerogel granules (Sachithanadam 2015)

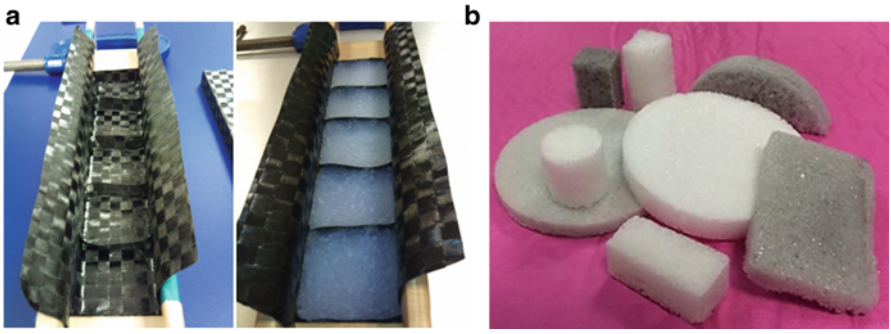

Fig. 4.2 (**a**) Granular core filler (Joshi and Xu 2010) and (**b**) lightweight aerogel blocks (Sachithanadam 2015)

4.3 Aerogel Porosity and Properties

The porous structure is an integral feature of an aerogel produced during the synthesis process. Gel preparation is the first step of aerogel production (Soleimani Dorcheh and Abbasi 2008). To obtain the silica gel, the sol–gel process has to be carried out. The sol is prepared by the addition of a catalyst to a silica solution. One of the common types of silicon derivatives used is tetramethoxysilane (TMOS). The solvent is usually alcohol or acetone. The next step is the addition of a catalyst solution to the sol–gel to carry out the hydrolysis process. There are three different catalyst methods, namely, acid catalyst, base catalyst, and two-step catalyst methods.

4.3.1 Surface Nanopores and Their Formation

Acid catalysts generally produce linear or randomly branched chains. Acid catalysts used are HCL, H_2SO_4, HNO, HF, etc. The lower the PH of the sol, the longer it will take for the sol to gel. Base catalysts generally form a network that contains uniform particles in the sol. Base catalyst used is dilute ammonia. Pore volume obtained by using base catalyst is quite large. In the two-step catalyst process, first, an acid, e.g., HCL, is added to the sol followed by a second step addition of NH_4OH. The addition of the base NH_4OH increases the rate of condensation and reduces gelation time. Generally acid catalyzed hydrolysis and condensation forms gels that have weaker branches and have more microporous structure. In the base and two-step process, cross-linking is increased resulting in lesser microporosity.

Additives like polyethylene glycol (PEG) can be added to the sol to control pore-size and mechanical properties. Aging of the wet gel is carried out to further enhance the mechanical properties for aerogel production. It was found that aging processes resulted in stronger and stiffer wet gels; however, a maximum strength and stiffness was observed after a certain aging time (Strøm et al. 2007). Drying of the gel is one of the most critical steps in production of aerogel. This is the process whereby liquid within the gel is removed, leaving behind the cross-linked silica network structure. Capillary pressure affects the drying of the gel, and capillary tension developed during the drying process leads to damage to the pores of the gel. This is unavoidable if drying is done at ambient temperature and pressure (Soleimani Dorcheh and Abbasi 2008).

To reduce the capillary tension thus protecting the network pore structure, supercritical drying method has to be used. Using supercritical drying, liquid in the pore is extracted above the critical temperature and pressure of the pore liquid. With supercritical drying, there is the elimination of the liquid vapor interface and therefore no capillary pressure is present. There are two methods of supercritical

drying: the high-temperature supercritical drying (HTSCD) and low-temperature supercritical drying (LTSCD). The HTSCD is a three-step process:

1. Wet gel containing solvent is placed in an autoclave. Temperature in the autoclave is slowly increased. Both the temperature and pressure are increased above critical points of the fluid in the gel and held constant for some time.
2. Fluid in the gel is then vented with the temperature being held constant. Pressure will decrease slowly.
3. Upon reaching the ambient pressure, the autoclave is allowed to cool to room temperature. Using this method, the liquid vapor phase boundary is not crossed at any time, and there is the elimination of capillary pressure problem. The silica aerogel structural network is not damaged in the drying process.

In LTSCD, before the drying process is carried out, the liquid in the gel is exchanged with another solvent that has a critical temperature and pressure closer to the ambient pressure and temperature. Liquid CO_2 is used to replace the liquid in the gel. Using liquid CO_2, LTSCD can be carried out at a temperature of less than 40 °C and a pressure of less than 80 bar. Here the gel with the solvent is placed in the autoclave and sealed. Liquid CO_2 is pumped into the autoclave at a temperature between 4 and 12 °C. Pumping is stopped when pressure reaches 100 bar. Outlet valve is open to allow for solvent that had been removed by the liquid CO_2 in the gel to be vented out. When all the solvent has been vented out, outlet valve is closed. The temperature is increased to 40 °C. Steps 2 and 3 are similar to that of the HTSCD method. The difference is that aerogels produced using LTSCD are hydrophilic.

4.3.2 Pore Structure

Most aerogels have pore diameter of between 2 and 50 nm. Pore sizes of this range are termed "mesopores." Aerogels have an open-pore structure and pores are interconnected. For open-pore structures, pores are "open" to fluid flow and fluids are able to travel from one pore to another and eventually flow through the whole structure (Gibson and Ashby 1999). Several methods have been employed in examining the porosity and pore structure by various researchers. The most commonly used method is the nitrogen adsorption/desorption technique or BET method (Xu et al. 2007; Ye et al. 2010). High-resolution scanning electron microscopy (SEM) and transmission electron microscopy (TEM) allow for direct examination of aerogel structure and provide estimation of the pore sizes (Moner-Girona et al. 1999; Rao et al. 2003; Xu et al. 2007). Lesser known methods of characterizing the pore structure such as ultrasmall-angle X-ray scattering (USAXS) (Reim et al. 2004) and atomic force microscopy (AFM) (Borne et al. 1995) have also been used by several researchers.

4.3.3 Properties of Silica Aerogel

Here we will briefly review the pertinent properties of silica aerogel (SA) which have made it of such immense interest to the materials research community.

4.3.3.1 Density

Density is an essential physical property of SAs. Two terms are used in characterizing the density of aerogels: bulk density and skeletal density. Bulk density (ρ_b) is defined as the ratio of aerogel's mass to its volume. The skeletal density (ρ_s) refers to the density of bulk solid of the material the aerogel is made of. The pore volume and porosity are related to ρ_b and ρ_s by

$$\text{Pore Volume}\left(\frac{\text{cm}^3}{\text{g}}\right) = \left(\frac{1}{\rho_b} - \frac{1}{\rho_s}\right) \tag{4.1}$$

$$\text{Porosity} = \left(1 - \frac{\rho_b}{\rho_s}\right) \times 100\ \% \tag{4.2}$$

4.3.3.2 Optical Properties

SAs are highly transparent for a porous material. This is due to the nanoscaled microstructure of aerogels compared to the wavelength of light (Pajonk 1998). The transparency of the aerogels can be controlled at the hydrolysis and condensation stages of the process through careful setting of parameters (Pajonk 1998).

4.3.3.3 Hydrophobicity

SAs can be either hydrophilic or hydrophobic. Both characteristics of the aerogels depend vastly on the precursors, solvents, drying methods, and silylating agents used. Hydrophilic aerogels due to its water-absorbing nature and subsequent collapse of its solid fractal component were rarely used, till recently with growing interest in drug delivery systems especially ketoprofen and griseofulvin (Smirnova et al. 2004). Thus, most of the aerogels in applications are hydrophobic. As mentioned previously, SA will lose its hydrophobic qualities at above 350 °C or after a prolonged period of time. This process of oxidation revert the aerogels back to its hydrophilic state. The thermal stability of aerogels in terms of hydrophobic degradation can be estimated by means of thermogravimetric and differential thermal analysis (TGA–DTA).

4.3.3.4 Thermal Conductivity

Thermal conductivity, λ, is the property of a material to conduct heat that is primarily governed by the Fourier's Law of heat conduction. SAs have unique properties resulting from the sol–gel method producing extremely low-density transparent solids having small pore size that has extremely high thermal resistance. When evacuated under partial vacuum (0.1 bar), the effective thermal conductivity is reduced by a factor of 3 to about 0.007 W/m-K at 280 K (van Bommel et al. 1997). Reim et al. (2004) studied the thermal and optical properties of the SA granules as compared to the monolith SA, noting the similarity in the reduction of gaseous conductivity at 0.1 bar. Typically, the thermal conductivity of SA granules ranges from 0.017 to 0.024 W/(m-K) as highlighted by Schmidt and Schwertfeger (1998). Measuring the individual mode of thermal transport, that is, conduction, convection, and radiation, can be difficult as each mode is interdependent on the other. Total thermal conductivity measurements are usually done to gage the thermal conductivity of the SAs.

4.3.3.5 Modulus and Strength

Most published literature analyzed the elastic modulus of SA by drawing inspiration from the cellular solid models. For example, Ashby and Gibson describe the open cellular foam model compressive modulus to follow power-law dependence on the relative density as shown in Eq. (4.3) where C and μ are geometric constants that depend on the topological features and microstructure undergoing cell wall bending as the dominant deformation (Gibson and Ashby 1999).

$$\left(\frac{E}{E_s}\right) = C\left(\frac{\rho}{\rho_s}\right)^{\mu} \tag{4.3}$$

4.4 Numerical Characterization of Aerogel Structures and Properties

Various numerical characterizations of the mechanical properties of silica aerogels were also performed, where the focus was on detailed mimicry of the silica aerogels' porosity and fractal features. To form fractal structures from dense amorphous silica, Kieffer and Angell (Kieffer and Angell 1988) employed molecular dynamics (MD) simulations together with an expansion scheme dubbed negative pressure rupturing by the authors, and the resulting structures had fractal dimensions reminiscent of experimental porous silica. The same expansion scheme was employed by Nakano et al. (1994) with the Vashishta interatomic potential

(Vashishta et al. 1990) to determine structural correlations such as the internal surface area, pore surface-to-volume ratio, pore-size distribution, fractal dimension, correlation length, and mean-particle size as a function of aerogel density. Subsequently, a different method of expanding, heating, and quenching dense amorphous silica was developed by Murillo et al. (2010) to characterize the mechanical properties of silica aerogels. In comparison with experimental results, this method achieved a good fit for the elastic moduli but not the strength. Methods of significantly greater complexity and computational intensity can be utilized to model silica aerogels (Pohl et al. 1995; Beckers and de Leeuw 2000; Bhattacharya and Kieffer 2005; Kieffer and Bhattacharya 2008), but scaling these methods to large simulations are challenging as the computational costs are too prohibitive. An example of this is simulations of sol–gel synthesis in an aqueous environment by Bhattacharya and Kieffer (2005), through a reactive force field in MD with charge transfer.

To determine the effects of silica aerogels in nanocomposites, the numerical methods detailed above could potentially be utilized, or other methods need to be derived to accurately reproduce silica aerogel's thermal features, such as their extremely low thermal conductivity, because the main focus of previous studies were on the geometrical, mechanical, and chemical properties of silica aerogels. Appropriate MD models have been formulated by the authors (Ng et al. 2012; Lei et al. 2013; Yeo et al. 2013) across a wide range of densities for fast and reasonable reproduction of the geometrical, mechanical, and thermal properties of bulk experimental porous silica aerogel. It will be demonstrated that differing methods of negative pressure rupturing first introduced by Kieffer and Angell (1988), as well as the heating, expanding, and quenching scheme first proposed by Murillo et al. (2010), will result in dramatic variations in thermal conductivities obtained. These are modeled using the van Beest–Kramer–van Santen interatomic potential (van Beest et al. 1990; Kramer et al. 1991) and a re-parameterized Tersoff potential (Munetoh et al. 2007), respectively. Each model's shortcomings and potential improvements will be discussed to establish the most accurate model in terms of the thermal conductivity.

The thermal transport mechanisms in aerogels have been characterized experimentally, and it was determined that separate components of gaseous, solid, and radiative thermal conductivity constitute the total thermal conductivity of monolithic silica aerogels (Lu et al. 1995; Heinemann et al. 1996; Zeng et al. 1996; Wei et al. 2011), and the coupling between these modes were negligible, together with non-convection of heat by gases within the pores (Lu et al. 1995). The extremely low solid thermal conductivity of silica aerogels was also found to be due to strong restrictions in the movement of local excitations within the aerogel's backbone due to large amounts of pores. The solid thermal conductivity was characterized as a function of density, such that

$$\lambda_s = C_\lambda \rho^\xi \tag{4.4}$$

where particle connectivity within the aerogel significantly influences the factor C_λ, and the exponent, ζ, was approximately 1.6 for silica aerogels with densities, ρ, between 0.3 and 1 g/cm^3 (Fricke 1988).

In this chapter, classical all-atom molecular dynamics is utilized to investigate silica aerogel's thermal properties, where the construction of the aerogel structures is realized through different schemes. Two simulation steps are needed: generation of percolated silica aerogel structures at various densities via either negative pressure rupturing or an expand, heat, and quench method, followed by reverse nonequilibrium molecular dynamics to determine their thermal conductivities.

4.4.1 Molecular Dynamics: Theory and Formulation

To fully model numerous physical phenomena, more than one order of time or length scales are typically needed with four main classifications as identified in Fig. 4.3. For instance, ab initio methods of quantum mechanics deal with minuscule length scales smaller than a few angstroms, while finite element methods (FEM), computational fluid dynamics (CFD), and continuum elasticity (CE) deal with phenomena that occur beyond the order of microns.

Bridging these scales is molecular dynamics (MD), where simulations can span time scales between picoseconds to a few microseconds, together with length scales of a few angstroms to several microns. As atomistic interactions in MD simulations are treated with empirical interatomic potentials, MD naturally incorporates anharmonic atomic vibrations and interactions. This is vital to our study with respect to modeling nanoscale atomic heat transport effectively and efficiently. Moreover, analytical solutions for classical many-body problems are generally not available as the complexity of the solutions rapidly escalates with increasing numbers of atoms. MD simulation is capable of employing computational power

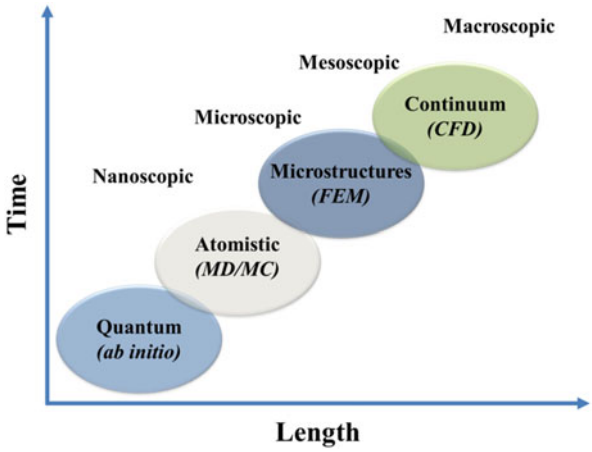

Fig. 4.3 The broad range of time and length scales that can be modeled with varying computational methods

that is currently swiftly increasing to provide meaningful solutions of atomistic behaviors without relying on experimental systems. These capabilities make MD an imperative computational tool in many fields of science, especially in areas of materials science, physics, and biochemistry (Allen and Tildesley 1989; Sadus 1999; Frenkel and Smit 2002; Rapaport 2004; Shakouri et al. 2014; Cheng et al. 2015).

4.4.1.1 Interatomic Interaction Potentials

MD is the numerical embodiment of Newtonian, Eulerian, Hamiltonian, and Lagrangian analytical mechanics. For example, Newton's second law is exemplified in the simplest case of hard spheres moving at constant velocity and experiencing perfectly elastic collisions (Alder and Wainwright 1957, 1959). More intricate systems can be treated with empirical mathematical functions to model the interactions between pairs, triplets, and even groups of atoms. These mathematical functions are known as interatomic interaction potentials, and they are typically functions of individual atomic coordinates, such that the total potential energy can be given by

$$U = \sum_i U_1(\boldsymbol{r}_i) + \sum_i \sum_{j>i} U_2(\boldsymbol{r}_i, \boldsymbol{r}_j) + \sum_i \sum_{j>i} \sum_{k>j>i} U_3(\boldsymbol{r}_i, \boldsymbol{r}_j, \boldsymbol{r}_k) + \ldots \tag{4.5}$$

where i, j, and k are individual atom indices. The forces corresponding to a potential is written as

$$f = -\nabla U(r) \tag{4.6}$$

and the equations of motions are determined from Newton's second law

$$m r_i = f_i = \sum_j^{N_m} f_{ij} \tag{4.7}$$

where m is the atomic mass of the atom under consideration. A possible choice of pair potential functions is the well-known "12-6" Lennard-Jones (LJ) potential (Jones 1924; Rapaport 2004), expressed as

$$U(r_{ij}) = \begin{cases} 4\varepsilon_{ij}\left[\left(\frac{\sigma_{ij}}{r_{ij}}\right)^{12} - \left(\frac{\sigma_{ij}}{r_{ij}}\right)^{6}\right], & \text{for } r_{ij} < r_c \\ 0, & \text{for } r_{ij} \geq r_c \end{cases} \tag{4.8}$$

where r_{ij} is the separation between atoms i and j and the parameter ε_{ij} denotes the interatomic interaction strength. There are no interactions if σ_{ij} is equivalent to r_{ij}, and similarly so if r_{ij} exceeds the interaction cutoff distance r_c.

For the purposes of modeling silica, we examined two different interatomic potentials, namely, the van Beest–Kramer–van Santen (BKS) (van Beest et al. 1990; Kramer et al. 1991) potential and the Tersoff potential (Tersoff 1988) re-parameterized to model silica (Munetoh et al. 2007). Both of these potentials are implemented on the Large-scale Atomic/Molecular Massively Parallel Simulator (LAMMPS) (Plimpton 1995), an open-source classical molecular dynamics code. The BKS potential is expressed as

$$U(r_{ij}) = \frac{q_i q_j}{r_{ij}} + A_{ij}\exp(-B_{ij}r_{ij}) - \frac{c_{ij}}{r_{ij}^6} \tag{4.9}$$

where q_i and q_j are the atomic charges and constants A_{ij}, B_{ij}, and C_{ij} varies between atom pairs i and j, as defined by van Beest et al. (1990). Numerous MD studies in the literature have used the BKS potential to model silica to study thin films, nanowires, nanoparticles, and bulk silica (Horbach and Kob 1999; Horbach et al. 1999; Jund and Jullien 1999; Shell et al. 2002; McGaughey and Kaviany 2004; Mahajan et al. 2007; Coquil et al. 2011). However, the BKS potential alone was found to be unable to handle the simulation process of quenching silica at high temperatures to obtain amorphous silica, as uncontrollable dynamics can be caused by atoms coming together too closely at these temperatures (Guissani and Guillot 1996; McGaughey and Kaviany 2004; Mahajan et al. 2007). To maintain cohesion, the BKS potential can be modified with an additional "24-6" LJ potential to obtain (Guissani and Guillot 1996)

$$U(r_{ij}) = \frac{q_i q_j}{r_{ij}} + A_{ij}\exp(-B_{ij}r_{ij}) - \frac{c_{ij}}{r_{ij}^6} + 4\varepsilon_{ij}\left[\left(\frac{\sigma_{ij}}{r_{ij}}\right)^{24} - \left(\frac{\sigma_{ij}}{r_{ij}}\right)^{6}\right] \tag{4.10}$$

with parameters from McGaughey and Kaviany (2004).

The Tersoff potential's mathematical form is

$$U = \sum_i U_i = \frac{1}{2}\sum_{i \neq j} V_{ij} \tag{4.11}$$

$$V_{ij} = f^{\mathrm{c}}(r_{ij})\left[V^{\mathrm{R}}(r_{ij}) + b_{ij}V^{\mathrm{A}}(r_{ij})\right] \tag{4.12}$$

where the function V^{R} and V^{A} are repulsive and attractive pair potentials, respectively; f^{c} is a smoothly varying cutoff function; b_{ij} is a monotonically decreasing function dependent on the coordination of atoms i and j. Details and parameters of this potential were previously reported by Munetoh et al. (2007). This potential has been used to model interactions between amorphous silica and CNTs and heterojunctions between crystalline silicon and amorphous silica, and we will also show subsequently that it reproduces the vibrational density of states (vDOS) of bulk amorphous silica (Laughlin and Joannopoulos 1977; Ong and Pop 2010; Chen et al. 2012).

4.4.1.2 Thermal Conductivity Simulations

An equilibrium method can be used in MD simulations to determine the thermal conductivity of materials through the perturbation response of a system (Allen and Tildesley 1989; Mahajan et al. 2007), expressed as

$$\lambda = \frac{1}{Vk_{\mathrm{B}}T^2}\int_0^{\infty}\left\langle j_z^{\mathrm{e}}(t)j_z^{\mathrm{e}}(0)\right\rangle \mathrm{d}t \tag{4.13}$$

However, the convergence of this method is heavily reliant on very long simulation times (Sellan et al. 2010). A simpler approach can be utilized using Fourier's Law, given by

$$\lambda = \frac{j^{\mathrm{e}}}{\mathrm{d}T/\mathrm{d}x} \tag{4.14}$$

To do so, the reverse nonequilibrium molecular dynamics (RNEMD) method (Muller-Plathe and Bordat 2004) can be applied by imposing a heat flux across the simulation cell. Firstly, atoms are binned into an even number of slabs in the direction of heat transfer. Secondly, the first slab is designated as the cold slab, while the middle slab is designated as the hot slab. Figure 4.4 illustrates this concept.

Enforcement of these hot and cold conditions requires periodic numerical interchanges of the energy of the atom with the highest kinetic energy within the cold slab with that of the atom with the lowest kinetic energy within the hot slab. Over time, a temperature gradient in the system is induced by energy flux from the more energetic middle slab to the less energetic end slabs. This energy flux can be written as

$$j^{\mathrm{e}} = \frac{1}{2tA}\sum_{N_{\mathrm{swap}}}\frac{m_i}{2}\left(v_{\mathrm{hot}}^2 - v_{\mathrm{cold}}^2\right) \tag{4.15}$$

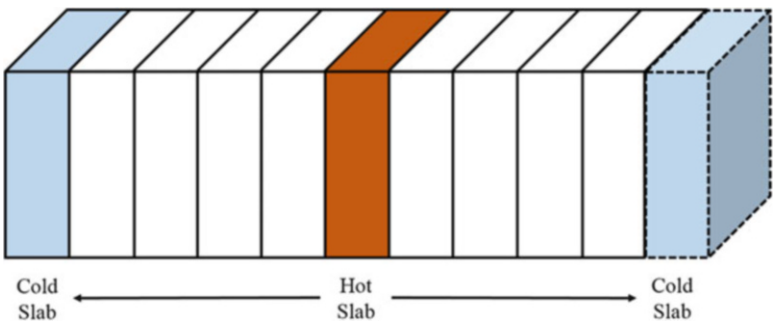

Fig. 4.4 Reverse nonequilibrium molecular dynamics (RNEMD) represented schematically, where the direction of heat flux is depicted by *arrows*. The periodic image of the cold slab is represented by *dotted lines*

where t is the total simulation time; A the cross-sectional area of the simulation cell, orthogonal to the direction of heat flux; N_{swap} the total number of swaps; m_{i} the atomic mass; and v_{hot} and v_{cold} the velocities of the hot and cold atom, respectively. Sampling of the simulation cell's temperature profile through time averaging can be performed at steady state:

$$\frac{3N_{\text{slab}}k_{\text{B}}T_{\text{slab}}}{2} = \frac{1}{2}\left\langle \sum_{i}^{N_{\text{slab}}} m_i v_i^2 \right\rangle \tag{4.16}$$

where N_{slab} is the number of atoms in the slab, T_{slab} the temperature of the slab, and k_{B} the Boltzmann's constant. Figure 4.5 depicts a typical temperature profile obtained at steady state, and linear regression can be performed on slabs that show linear variation of temperature with distance as illustrated in Fig. 4.6. Once the heat flux and temperature gradient are known, Fourier's Law can be used to determine the thermal conductivity.

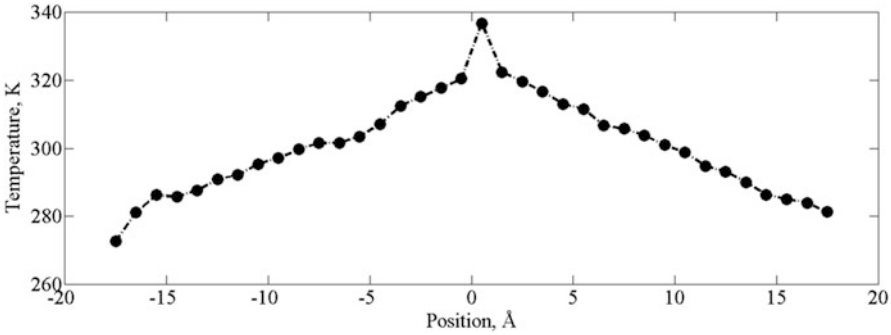

Fig. 4.5 A typical plot of the temperature distribution determined from RNEMD

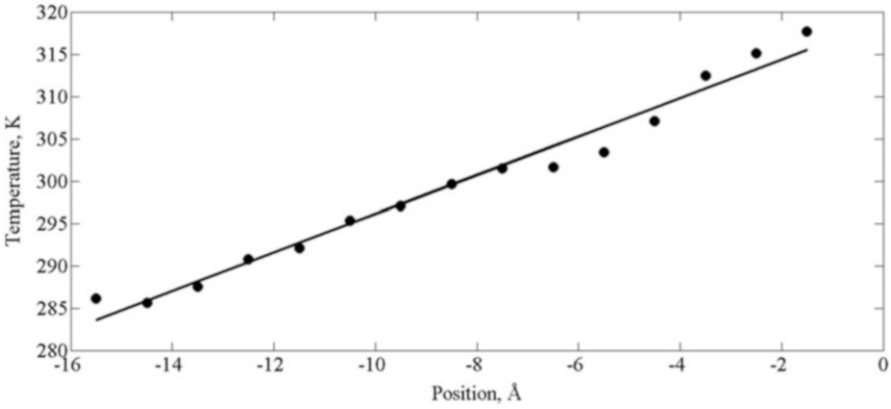

Fig. 4.6 The temperature gradient is averaged by linear regression in the region displaying linear response

4.4.2 Numerical Generation of Aerogel Structures

To obtain silica aerogel's percolated backbone, amorphous silica systems must be prepared first by quenching β-cristobalite (Wyckoff 1963) linearly from 6000 to 300 K over 500 ps. The initial crystal lattice is depicted in Fig. 4.7.

We explored two different methods of generating porous aerogel structures in our MD studies. The first method was dubbed negative pressure rupturing by Kieffer and Angell (1988), where stepwise expansion of amorphous silica brought the system to the percolation threshold. Instantaneous stretching of existing bonds beyond 10–35 % of their equilibrium at each expansion step ruptures these bonds till the desired density is obtained. Subsequently, conjugate gradient minimization was performed to bring the system to a local minimum-energy configuration, and the system is thermalized at 300 K for another 15 ps to attain the final percolated structure, as illustrated in Fig. 4.8.

The second method to generate porous silica is the expanding, heating, and quenching scheme of Murillo et al. (2010). In this scheme, instantaneous expansion of the same initial β-cristobalite lattice configuration brings the system to the

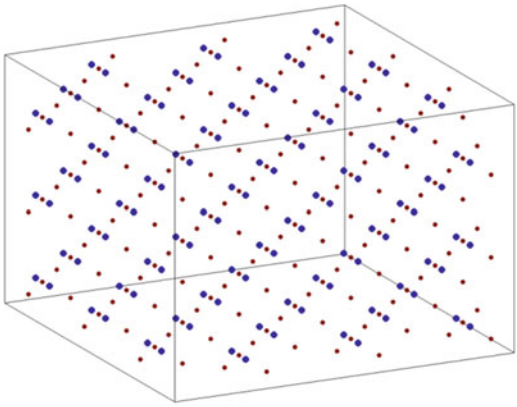

Fig. 4.7 Ideal β-cristobalite is used as the initial configuration, where small *black dots* denote oxygen atoms and *big blue dots* denote silicon

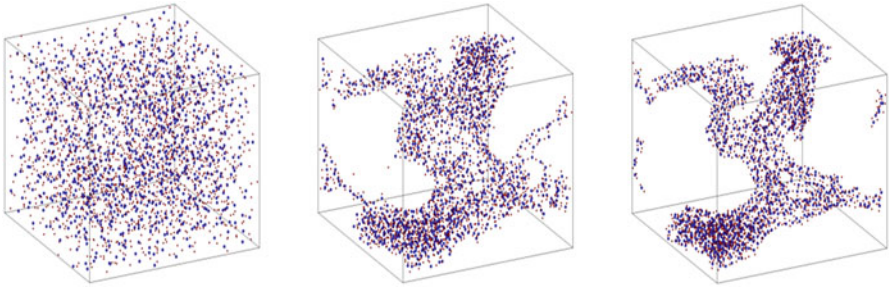

Fig. 4.8 Negative pressure rupturing produced percolated aerogel structures at varying densities of 2.17 g/cm^3, 0.50 g/cm^3, and 0.32 g/cm^3 from left to right, respectively

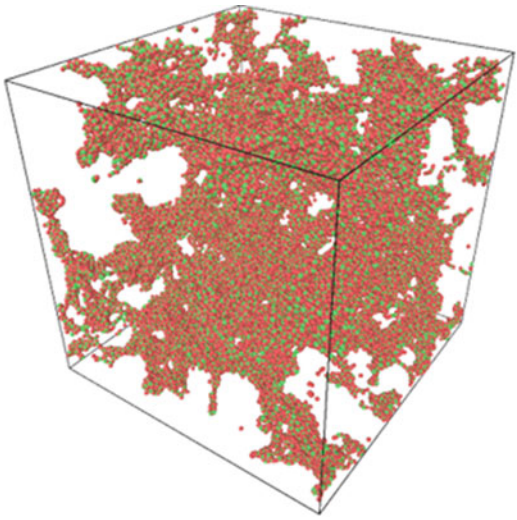

Fig. 4.9 The expanding, heating, and quenching scheme produced the percolated aerogel backbone at a density of 0.3 g/cm^3

desired density, before it is heated and quenched from 3000 to 300 K over 350 ps to produce aerogels in the density range of 0.3–1.0 g/cm^3. An example of the final equilibrated percolated state at a simulation cell volume of 5832 nm^3 and a density of 0.3 g/cm^3 is displayed in Fig. 4.9.

4.4.3 Solid Thermal Conductivity of Silica Aerogels

Following the production of the aerogels at the desired density, their thermal conductivity is determined through RNEMD as discussed earlier. All simulations were fully periodic with a time step of 0.5 fs, and energies were swapped every 50 steps to impose the heat flux. Subsequent equilibration for 500 ps leads to a linear temperature gradient and another 500 ps was ran to obtain time averages of the results. Final averaging was performed for the thermal conductivity of each sample in the x, y, and z directions.

4.4.3.1 Dense Amorphous Silica with BKS Potential

The thermal conductivity of dense amorphous silica is determined first to validate the current MD simulation scheme. A system of 216 silicon atoms and 432 oxygen atoms was quenched to obtain amorphous silica, and the thermal conductivity was found to be approximately 1.20 ± 0.07 W/(m-K) using RNEMD, in excellent agreement with previous MD results (Jund and Jullien 1999; Coquil et al. 2011). The thermal conductivity for a larger system of 3000 atoms were also determined to be 1.39 W/(m-K) at 300 K, close to the experimental value of 1.40 W/(m-K)

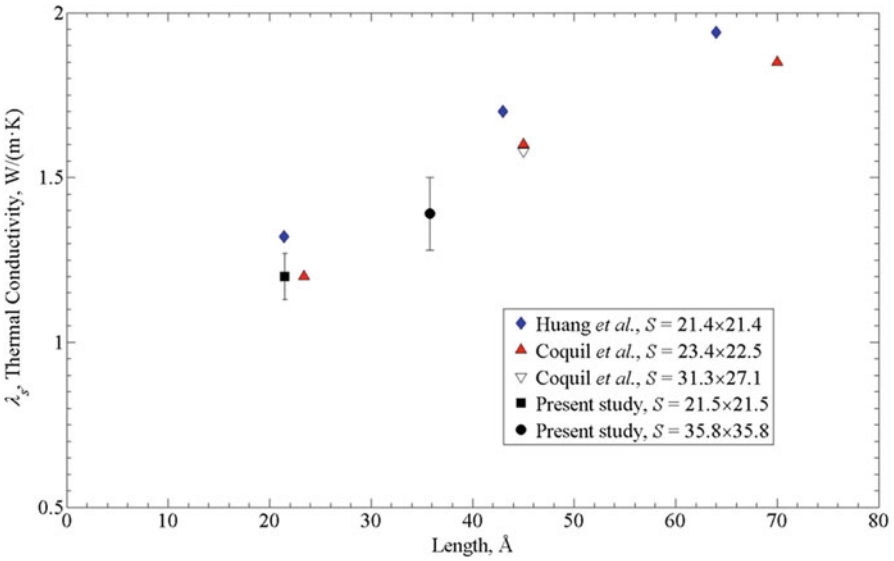

Fig. 4.10 Amorphous silica's thermal conductivity plotted with results of previously reported data by Huang et al. (2009) and Coquil et al. (2011) for various system lengths at 300 K. *S* refers to the cross-sectional area of the simulated samples in units of angstroms

(Weber 2002). This is in good agreement with studies investigating system size effects on thermal conductivity (Huang et al. 2009; Coquil et al. 2011), where thermal conductivity was found to increase with lengthening of the simulation cells, independent of the cross-sectional area. These results are shown in Fig. 4.10. Their results also indicated an overestimation of the thermal conductivity as the system size continuously increase, leading to a plateau at 2.1 W/(m-K) (Coquil et al. 2011).

4.4.3.2 Silica Aerogel with BKS Potential

Negative pressure rupturing is applied on the system of 3000 atoms to produce porous networks with densities ranging from 0.99 to 0.32 g/cm^3 while preserving axial connectivity. To determine the fractal dimension at each density using a method proposed previously (Kieffer and Angell 1988), power-law fits were performed on the total radial distributions (Le Roux and Petkov 2010) at the regions that are varying linearly in the log-scale plot of the total radial distributions. Figure 4.11 compares the fractal dimensions obtained by this method, which is in good agreement with Kieffer and Angell (1988). The experimental values of the fractal dimensions vary with aerogel processing conditions, being slightly higher at 2.2–2.4 under acidic and neutral conditions and lower under basic processing conditions at approximately 1.8 (Woignier et al. 1990).

RNEMD was used to determine the thermal conductivity at each density as shown in Fig. 4.12 with a power-law fit of the data, where thermal conductivity

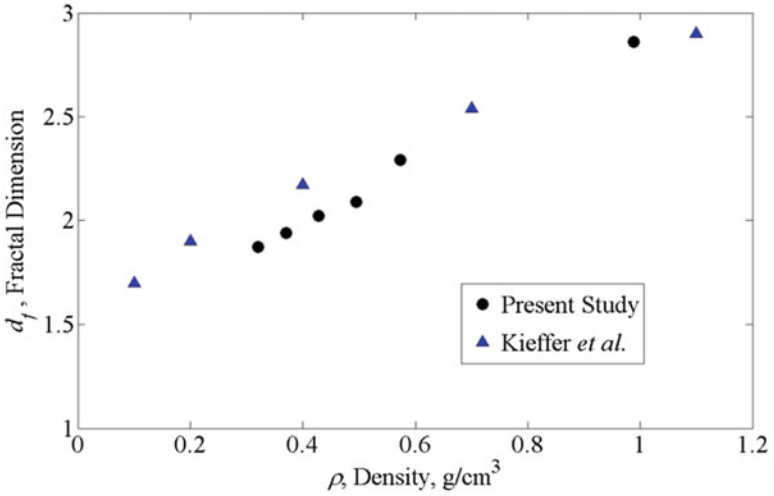

Fig. 4.11 Fractal dimensions increased with increasing density, in good agreement with results from Kieffer and Angell (1988)

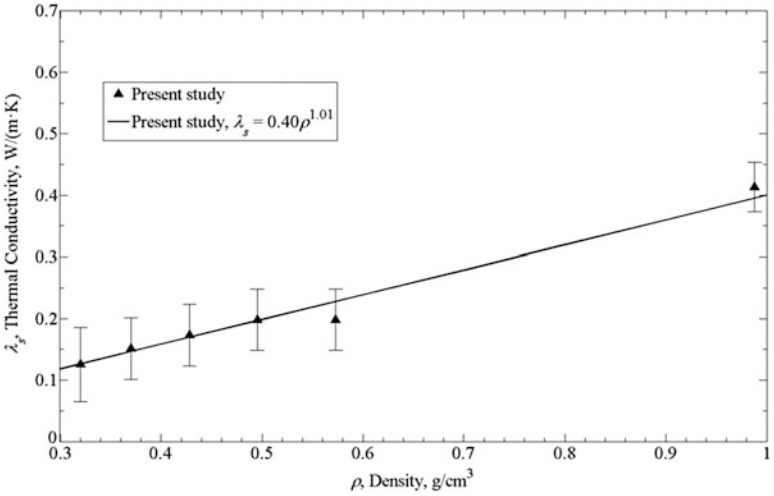

Fig. 4.12 Solid thermal conductivities of the simulated aerogel samples shows a power-law variation with density

decreases linearly with decreasing density. Negative pressure rupturing reproduced the same experimental observation of such large decreases in thermal conductivity with decreases in aerogel density, being an order of magnitude lower in comparison with dense amorphous silica at the aerogel density of 0.32 g/cm^3. However, the power-law fit produced a ζ value of 1.01 in the density range of 0.32–0.99 g/cm^3, in contrast with experimental values of 1.6 in the density range of 0.3–1.0 g/cm^3

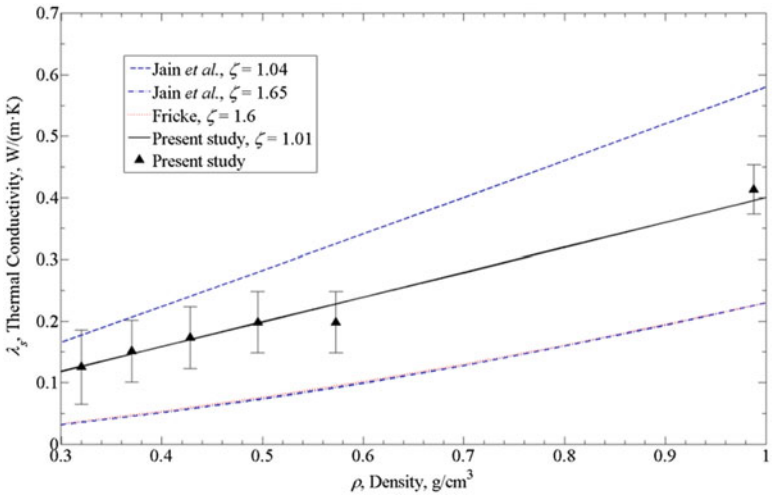

Fig. 4.13 Power-law fit of the present results in comparison with experimental data from Jain et al. (2002) and Fricke (1988)

(Fricke 1988). Furthermore, our results were an order of magnitude higher than the experimental value of 0.01 W/(m-K) (Fricke 1988) at a density of 0.3 g/cm^3. This is likely to be due to the dependence of the aerogels' thermal conductivity on their processing conditions, such that sintered aerogels had a lower ζ value of 1.04 for a density range of 0.4–1.6 g/cm^3 with a prefactor C_λ of 0.58 (Jain et al. 2002). This was in good agreement with our results. As the method of negative pressure rupturing does not reproduce the actual sol–gel conditions, it is unable to reproduce defects such as micro-cracks, impurities, and very broad pore-size distributions found in experimental aerogels. These defects are significant factors that contribute to the extremely low thermal conductivity as they scatter phonons significantly and limit the mean free path. Jain et al. (2002) verified this experimentally, where substantial amounts of defects were removed by aerogel sintering, leading to much higher thermal conductivities and an almost linear variation with density. These results are compared in Fig. 4.13.

This explanation is further reinforced through the calculated pore-size distribution (Bhattacharya and Gubbins 2006) of our simulated aerogel, as shown in Fig. 4.14 for the lowest density of 0.32 g/cm^3. The largest pore diameter that can be represented at this density is in the order of less than 30 Å, significantly lower than that found in experimental aerogels. The additional role that finite size effects may have played, together with the fact that the BKS potential may be unsuitable for modeling the thermal properties of amorphous silica, lead to an enhanced model devised and validated using an expanding, heating, and quenching scheme as discussed earlier, together with the re-parameterized Tersoff. This enhanced model improved the representation of the experimental and theoretical thermal properties of bulk experimental silica aerogel.

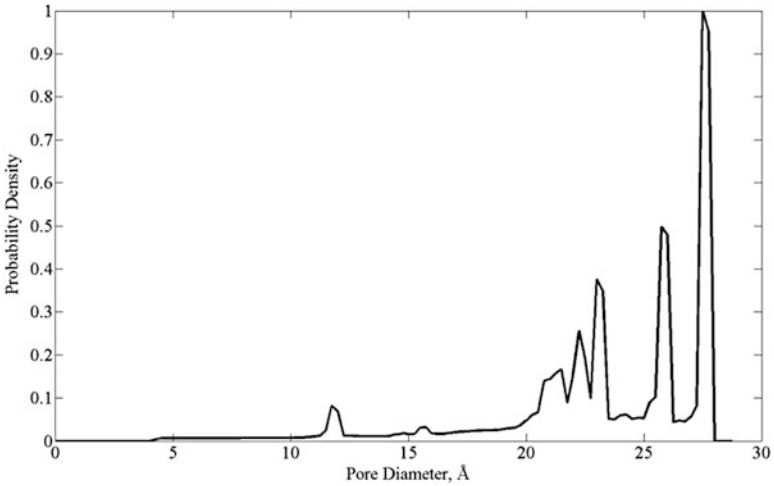

Fig. 4.14 At the lowest density of 0.32 g/cm^3, the pore-size distribution is well below 30 Å

4.4.3.3 Dense Amorphous Silica with Tersoff Potential

The thermal conductivity of amorphous silica is compared once more with experimental results for validation purposes. RNEMD was used to determine the thermal conductivities of amorphous silica of increasing system lengths, and the results were plotted in Fig. 4.15 in comparison with results from previous theoretical studies (Huang et al. 2009; Coquil et al. 2011) and with the BKS potential.

The same trend of increasing thermal conductivity with increasing system length is observed, where the Tersoff potential slightly underestimates the experimental value of 1.37–1.4 W/(m-K) for amorphous silica (Weber 2002) and plateaued at 1.10 ± 0.01 W/(m-K). In contrast, the BKS potential approximately plateaued at values between 1.89 ± 0.12 W/(m-K) and 1.94 ± 0.09 W/(m-K), significantly overshooting the experimental value. Significantly higher values were reported by previous MD studies in much smaller systems, as observed in Fig. 4.15. From these results, it can be seen that major differences in the cross-sectional areas and limited system length scales can cause finite size effects. To provide a better characterization for thermal conductivities predicted by the Tersoff and the BKS potential for bulk amorphous silica, the results can be extrapolated to an infinite length scale. This extrapolation showed that the Tersoff potential considerably improves upon the estimation of bulk thermal properties than the BKS potential as plotted in Fig. 4.16, which shows the variation of the inverse of the thermal conductivities with the inverse of the system lengths ($1/\lambda_s$ vs. $1/L$) extrapolated to zero. The inverse of the x-intercepts of each curve gave values of 2.13 W/(m-K) for the BKS potential and 1.19 W/(m-K) for the Tersoff potential, which translates into 55 % overestimation and 13 % underestimation of the experimental value, respectively. Clearly, the Tersoff potential is more desirable for better reproduction of bulk thermal properties.

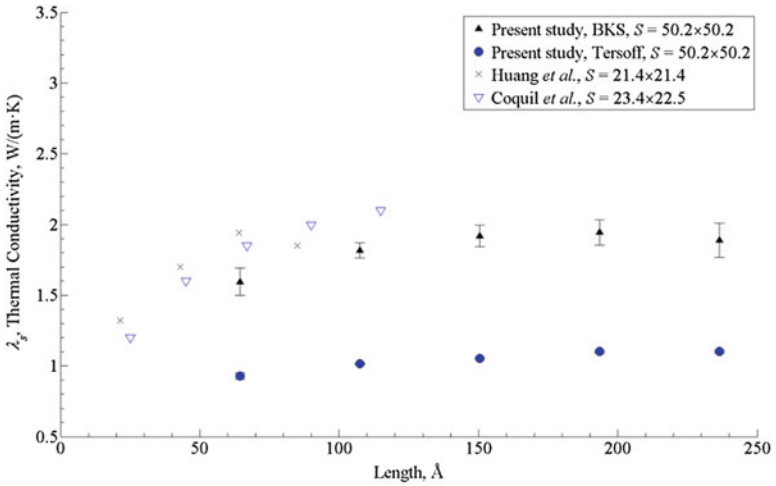

Fig. 4.15 Amorphous silica's thermal conductivity plotted with results of previously reported data by Huang et al. (2009) and Coquil et al. (2011) for various system lengths at 300 K. *S* refers to the cross-sectional area of the simulated samples in units of angstroms

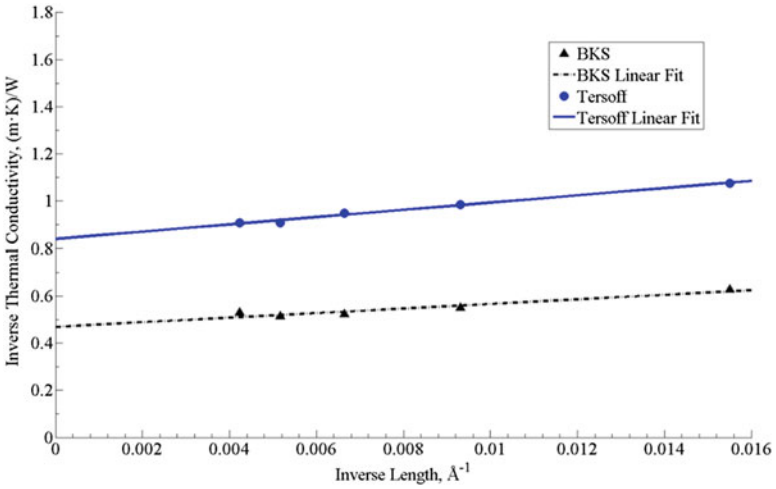

Fig. 4.16 To obtain estimates of the thermal conductivities for bulk amorphous silica, the inverse of the thermal conductivities for amorphous silica systems are linearly extrapolated to zero using the BKS and Tersoff potentials

The Tersoff potential is also capable of reproducing the vibrational density of states (vDOS) of bulk amorphous silica. The vDOS is derived from the Fourier transform of the velocity autocorrelation function (VACF) (Dove 1993), and it characterizes the excitable phonon frequencies in amorphous silica. It has been shown that the vDOS of amorphous silica has three distinct peaks near the frequencies of 10.5, 24.0, and

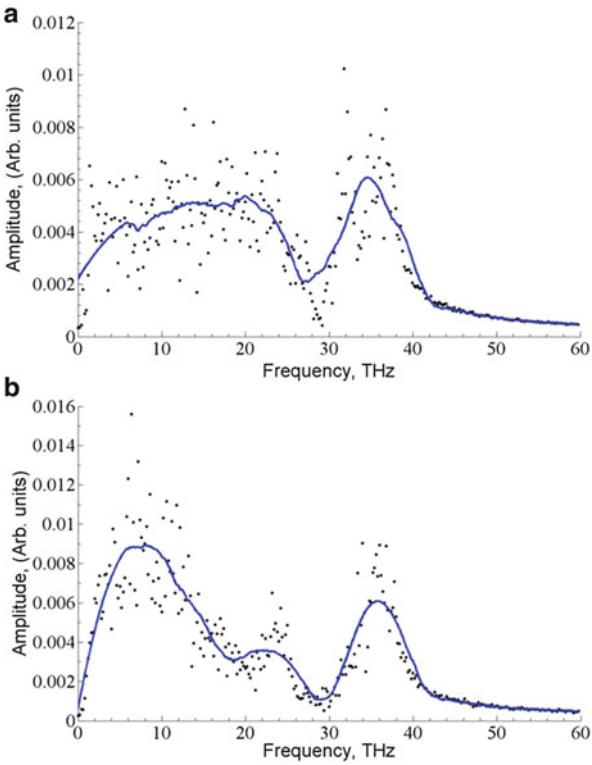

Fig. 4.17 Vibrational density of states of amorphous silica based on (**a**) the BKS potential and (**b**) the Tersoff potential

36.0 THz. Results from the Tersoff potential clearly shows these peaks as observed in Fig. 4.17b, whereas the lower frequencies were smeared for the BKS potential as seen in Fig. 4.17a, such that only the 36.0 THz peak is evident.

From these numerical data of the thermal conductivities and the vDOS of amorphous silica, we can conclude that the BKS potential is far less suitable for the thermal characterization of bulk amorphous silica than the Tersoff potential.

4.4.3.4 Silica Aerogel with Tersoff Potential

Next, the heating, expanding, and quenching scheme described earlier was used to produce the porous network of silica aerogels together with the Tersoff potential. The system is cubic with 52,728 atoms and the densities ranged from 0.3 to 1 g/cm^3. The fractal dimensions were determined and plotted in Fig. 4.18 in comparison with results from previous theoretical studies (Nakano et al. 1994; Murillo et al. 2010), where good agreement was obtained.

From RNEMD, the thermal conductivity at each density was determined and plotted on a log scale in Fig. 4.19, in comparison with results from the BKS potential and from previous experimental studies (Fricke 1988; Ng et al. 2012).

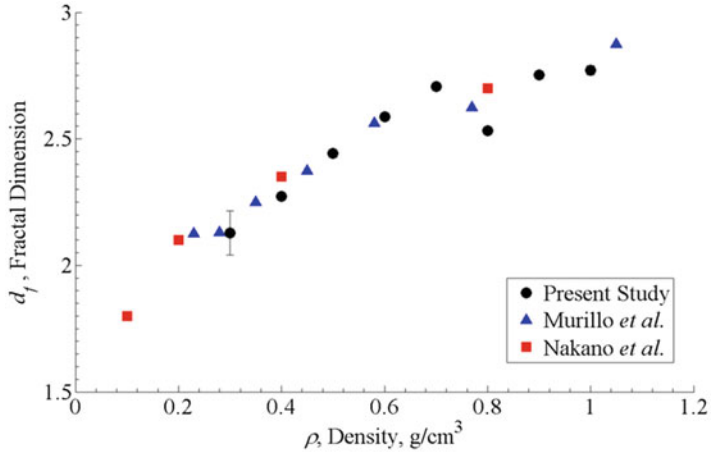

Fig. 4.18 Fractal dimensions increased with increasing density, in good agreement with results from Murillo et al. (2010) and Nakano et al. (1994)

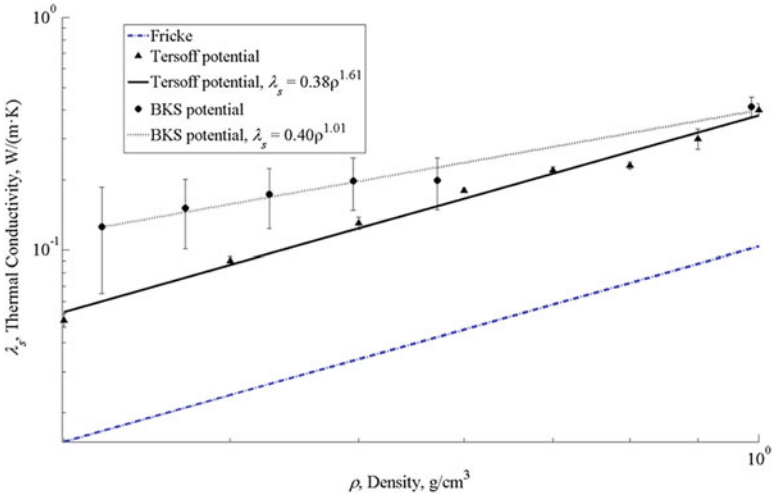

Fig. 4.19 Thermal conductivities of the simulated aerogel samples show power-law variations with density, where the power-law exponent from the Tersoff potential is in excellent agreement with experimental results from Fricke (1988)

In contrast with the BKS potential, results from the Tersoff potential showed a nonlinear reduction in the thermal conductivity with decreases in density. The lowest value obtained was 0.05 ± 0.003 W/(m-K) at the lowest density of 0.3 g/cm^3, and this value is close to 3 times lower than that obtained from the BKS potential. Furthermore, the ζ value of 1.61 is in excellent correlation with experimental results of 1.6 in the same density range of 0.3–1.0 g/cm^3 (Fricke 1988) which is a significant improvement over the ζ value of 1.01 obtained from the

BKS potential. An added advantage was that the current model can produce aerogels with densities below 0.1 g/cm^3 without any adverse effects.

The main downside observed for the current model was that the overall thermal conductivities at each density was 5 times higher than the experimental value as seen in Fig. 4.19. This can be explained by deficiencies in the pore-size distribution of the current model. Through PSDsolv (Bhattacharya and Gubbins 2006), the pore-size distribution was determined for three systems with increasing lengths of 69, 180, and 277 Å. The largest pore sizes accessible through our simulations increased in tandem with increasing system length scales from 20.75 to 32 Å in diameter as shown in Fig. 4.20.

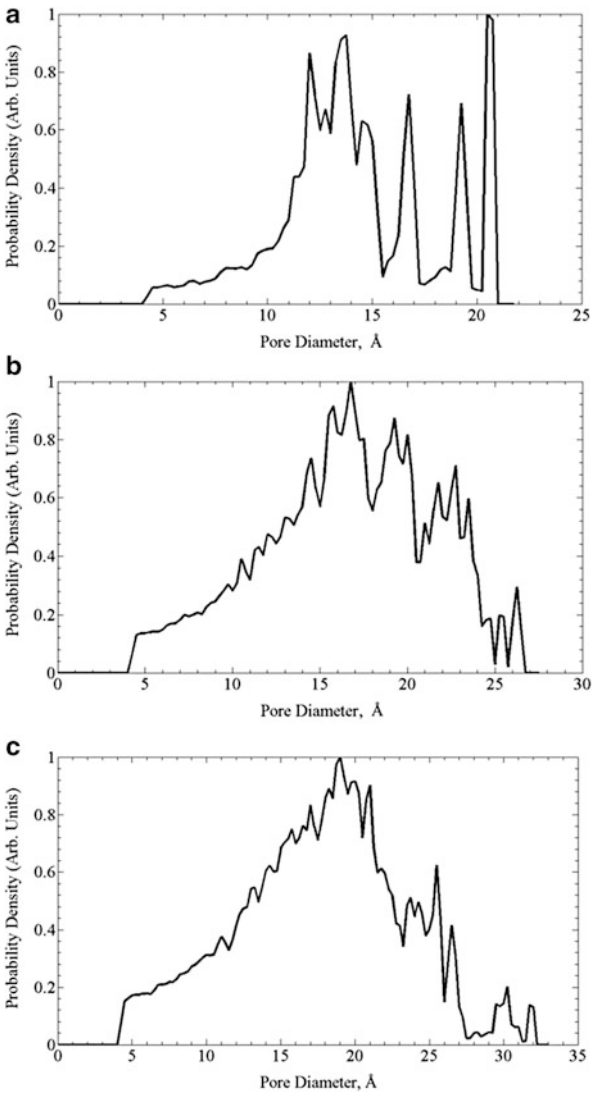

Fig. 4.20 At the lowest density of 0.3 g/cm^3 for three different system length scales of (**a**) 69 Å, (**b**) 180 Å, and (**c**) 277 Å, pore sizes are still significantly smaller than bulk experimental aerogels

However, realistic pore-size regimes in bulk experimental silica aerogels can be in the order of microns, a regime inaccessible to fully atomistic MD simulations as the maximum pore sizes accessible is increasing at a decreasing rate. A consequence of this is that the largest pore diameters only increased by approximately 50 % given a fourfold increase in system length. In order for realistic pore-size regimes to be accessible, it would require MD simulations with tens of millions of atoms for system sizes that are 1000–10,000 times larger than our current model. While such an endeavor may be deemed feasible with the current supercomputing facilities available and sheer brute force, pure MD simulations may not be the best solution given the computational intensity. It is likely that more meaningful results can be obtained in a reasonable manner through multiscale modeling techniques which utilizes the current model to characterize the thermal properties of silica aerogel in the nanoporous regime.

4.5 Conclusions

In this chapter, we reported the molecular dynamics modeling and simulation of silica aerogels used in nanocomposites to reproduce their thermal properties. The BKS potential augmented with a "24-6" Lennard-Jones potential was used to validate the model through determination of the thermal properties of nonporous amorphous silica and the results showed reasonable agreement with previously reported studies. Negative pressure rupturing was applied to create the porous backbone of silica aerogels of decreasing densities and the fractal dimensions were found to be comparable to previously reported studies. RNEMD was applied to determine the thermal conductivities, and it was found that the variation of thermal conductivity with density correlated very well with bulk sintered aerogel with values in the same order of magnitude. It does not compare as well with bulk as-prepared aerogels as our results were more than an order of magnitude higher. The pore-size distributions were determined and maximum pore sizes were found to be less than 3 nm. Together with the fact that defects such as micro-cracks were absent in the model, it explained the lack of congruence of our results with bulk as-prepared aerogels. Finite size effects could also be a significant factor as the predicted thermal conductivity of amorphous silica was found to increase with increasing system size.

To remedy these issues, an enhanced model was devised, using a combination of the Tersoff potential with an expanding, heating, and quenching scheme. It was determined that the Tersoff potential was more capable of reproducing the thermal properties of amorphous silica when compared to the BKS potential as the Tersoff potential provided a slight 13 % underestimation of bulk amorphous silica's thermal conductivity, whereas the BKS potential significantly overestimated by 55 %. Additionally, it was verified that the vDOS from the Tersoff potential was more comparable to the theoretical and experimental results of amorphous silica's vibrational spectra. Fractal dimensions of aerogels derived from this enhanced model

showed good agreement with experimental studies for densities ranging from 0.3 to 1 g/cm^3. This model showed nonlinear decrease in thermal conductivity with decreasing density, in stark contrast to the linear variation determined in the previous model. While the magnitudes of thermal conductivities were still five times higher than those determined experimentally, the power-law variation was in excellent agreement. It was verified that this model was also unable to breach larger pore-size regime by analysis of the pore-size distribution; hence, it was proposed that multiscale modeling methods should be applied for future characterizations.

Acknowledgments This work was supported by the A*STAR Computational Resource Centre through the use of its high-performance computing facilities.

References

Aegerter, M.A., Leventis, N., Koebel, M.M.: Aerogels Handbook. Springer Science + Business Media, LLC, New York (2011)

Alder, B.J., Wainwright, T.E.: Phase transition for a hard sphere system. J. Chem. Phys. **27**, 1208–1209 (1957)

Alder, B.J., Wainwright, T.E.: Studies in molecular dynamics. I. General method. J. Chem. Phys. **31**, 459–466 (1959)

Allen, M.P., Tildesley, D.J.: Computer Simulation of Liquids. Oxford University Press, New York (1989)

Beckers, J.V.L., de Leeuw, S.W.: Molecular dynamics simulation of nanoporous silica. J. - Non-Cryst. Solids **261**, 87–100 (2000)

Bhattacharya, S., Gubbins, K.E.: Fast method for computing pore size distributions of model materials. Langmuir **22**, 7726–7731 (2006)

Bhattacharya, S., Kieffer, J.: Fractal dimensions of silica gels generated using reactive molecular dynamics simulations. J. Chem. Phys. **122**, 094715 (2005)

Borne, A., Chevalier, B., Chevalier, J.L., Quenard, D., Elaloui, E., Lambard, J.: Characterization of silica aerogel with the atomic force microscope and SAXS. J. Non-Cryst. Solids **188**, 235–242 (1995)

Cabot-Corp.: "Aerogel." http://www.cabot-corp.com/aerogel (2011). Retrieved Dec 2015

Cantin, M., Casse, M., Koch, L., Jouan, R., Mestreau, P., Roussel, D., Bonnin, F., Moutel, J., Teichner, S.J.: Silica aerogels used as Cherenkov radiators. Nucl. Instrum. Methods **118**, 177–182 (1974)

Chen, J., Zhang, G., Li, B.: Thermal contact resistance across nanoscale silicon dioxide and silicon interface. J. Appl. Phys. **112**, 064319 (2012)

Cheng, Y., Koh, L.-D., Li, D., Ji, B., Zhang, Y., Yeo, J., Guan, G., Han, M.-Y., Zhang, Y.-W.: Peptide–graphene interactions enhance the mechanical properties of silk fibroin. ACS Appl. Mater. Interfaces **7**, 21787–21796 (2015)

Coquil, T., Fang, J., Pilon, L.: Molecular dynamics study of the thermal conductivity of amorphous nanoporous silica. Int. J. Heat Mass Transfer **54**, 4540–4548 (2011)

Cotet, L.C., Baia, M., Baia, L., Popescu, I.C., Cosoveanu, V., Indrea, E., Popp, J., Danciu, V.: Structural properties of some transition metal highly doped carbon aerogels. J. Alloys Compd. **434–435**, 854–857 (2007)

Dove, M.T.: Introduction to Lattice Dynamics. Cambridge University Press, Cambridge (1993)

Duer, K., Svendsen, S.: Monolithic silica aerogel in superinsulating glazings. Sol. Energy **63**, 259–267 (1998)

Fesmire, J.E.: Aerogel insulation systems for space launch applications. Cryogenics **46**, 111–117 (2006)
Frenkel, D., Smit, B.: Understanding Molecular Simulation: From Algorithms to Applications, 2nd edn. Academic, San Diego (2002)
Fricke, J.: Aerogels - highly tenuous solids with fascinating properties. J. Non-Cryst. Solids **100**, 169–173 (1988)
Fricke, J., Emmerling, A.: Aerogels. J. Am. Ceram. Soc. **75**, 2027–2036 (1992)
Fu, R., Lin, Y.-M., Rabin, O., Dresselhaus, G., Dresselhaus, M.S., Satcher Jr., J.H., Baumann, T. F.: Transport properties of copper-doped carbon aerogels. J. Non-Cryst. Solids **317**, 247–253 (2003)
Gibson, L.J., Ashby, M.F.: Cellular Solids: Structure and Properties. Cambridge University Press, Cambridge (1999)
Guissani, Y., Guillot, B.: A numerical investigation of the liquid-vapor coexistence curve of silica. J. Chem. Phys. **104**, 7633–7644 (1996)
Heinemann, U., Caps, R., Fricke, J.: Radiation conduction interaction: An investigation on silica aerogels. Int. J. Heat Mass Transfer **39**, 2115–2130 (1996)
Herrmann, G., Iden, R., Mielke, M., Teich, F., Ziegler, B.: On the way to commercial production of silica aerogel. J. Non-Cryst. Solids **186**, 380–387 (1995)
Hirashima, H., Kojima, C., Imai, H.: Application of alumina aerogels as catalysts. J. Sol-Gel Sci. Technol. **8**, 843–846 (1997)
Horbach, J., Kob, W.: Static and dynamic properties of a viscous silica melt. Phys. Rev. B Condens. Matter Mater. Phys. **60**, 3169–3181 (1999)
Horbach, J., Kob, W., Binder, K.: Specific heat of amorphous silica within the harmonic approximation. J. Phys. Chem. B **103**, 4104–4108 (1999)
Hrubesh, L.W.: Aerogel applications. J. Non-Cryst. Solids **225**, 335–342 (1998)
Huang, Z., Tang, Z., Yu, J., Bai, S.: Thermal conductivity of amorphous and crystalline thin films by molecular dynamics simulation. Phys. B **404**, 1790–1793 (2009)
Jain, A., Rogojevic, S., Ponoth, S., Gill, W.N., Plawsky, J.L., Simonyi, E., Chen, S.T., Ho, P.S.: Processing dependent thermal conductivity of nanoporous silica xerogel films. J. Appl. Phys. **91**, 3275–3281 (2002)
Jelle, B.P., Baetens, R., Gustavsen, A.: Aerogel insulation for building applications: a state-of-the-art review. Energy Build. **43**, 761–769 (2011)
Jones, J.E.: On the determination of molecular fields. II. From the equation of state of a gas. Proc. R. Soc. A. Math. Phys. Eng. Sci. **106**, 463–477 (1924)
Jones, S.M.: Aerogel: space exploration applications. J. Sol-Gel Sci. Technol. **40**, 351–357 (2006)
Joshi, S.C., Xu, K.: Fabrication and thermal performance of aerogel-filled carbon composite sandwich structures. International Symposium on Innovative Materials for Processes in Energy Systems (IMPRES), Singapore (2010)
Jund, P., Jullien, R.: Molecular-dynamics calculation of the thermal conductivity of vitreous silica. Phys. Rev. B Condens. Matter Mater. Phys. **59**, 13707–13711 (1999)
Kieffer, J., Angell, C.A.: Generation of fractal structures by negative-pressure rupturing of SiO_2 glass. J. Non-Cryst. Solids **106**, 336–342 (1988)
Kieffer, J., Bhattacharya, S.: Molecular dynamics simulation study of growth regimes during polycondensation of silicic acid: from silica nanoparticles to porous gels. J. Phys. Chem. C **112**, 1764–1771 (2008)
Kistler, S.S.: Coherent expanded aerogels. J. Phys. Chem. **36**, 52–64 (1932)
Kramer, G.J., Farragher, N.P., van Beest, B.W., van Santen, R.A.: Interatomic force fields for silicas, aluminophosphates, and zeolites: derivation based on ab initio calculations. Phys. Rev. B Condens. Matter Mater. Phys. **43**, 5068–5080 (1991)
Laughlin, R.B., Joannopoulos, J.D.: Phonons in amorphous silica. Phys. Rev. B Condens. Matter Mater. Phys. **16**, 2942–2952 (1977)
Le Roux, S., Petkov, V.: ISAACS - interactive structure analysis of amorphous and crystalline systems. J. Appl. Crystallogr. **43**, 181–185 (2010)

Lei, J., Liu, Z., Yeo, J., Ng, T.Y.: Determination of the Young's modulus of silica aerogels - an analytical-numerical approach. Soft Matter **9**, 11367–11373 (2013)
Lu, X., Caps, R., Fricke, J., Alviso, C.T., Pekala, R.W.: Correlation between structure and thermal-conductivity of organic aerogels. J. Non-Cryst. Solids **188**, 226–234 (1995)
Mahajan, S.S., Subbarayan, G., Sammakia, B.G.: Estimating thermal conductivity of amorphous silica nanoparticles and nanowires using molecular dynamics simulations. Phys. Rev. E Stat. Nonlinear Soft Matter Phys. **76**, 056701 (2007)
McGaughey, A.J.H., Kaviany, M.: Thermal conductivity decomposition and analysis using molecular dynamics simulations part II. Complex silica structures. Int. J. Heat Mass Transfer **47**, 1799–1816 (2004)
Moner-Girona, M., Roig, A., Molins, E., Martınez, E., Esteve, J.: Micromechanical properties of silica aerogels. Appl. Phys. Lett. **75**, 653–655 (1999)
Muller-Plathe, F., Bordat, P.: Reverse non-equilibrium molecular dynamics. In Novel Methods in Soft Matter Simulations, **640**, 310–326 (2004), Berlin, Heidelberg: Springer Berlin Heidelberg, ISBN: 978-3-540-39895-0, doi: 10.1007/978-3-540-39895-0_10
Munetoh, S., Motooka, T., Moriguchi, K., Shintani, A.: Interatomic potential for Si-O systems using Tersoff parameterization. Comput. Mater. Sci. **39**, 334–339 (2007)
Murillo, J.S.R., Bachlechner, M.E., Campo, F.A., Barbero, E.J.: Structure and mechanical properties of silica aerogels and xerogels modeled by molecular dynamics simulation. J. Non-Cryst. Solids **356**, 1325–1331 (2010)
Nakano, A., Bi, L.S., Kalia, R.K., Vashishta, P.: Molecular-dynamics study of the structural correlation of porous silica with use of a parallel computer. Phys. Rev. B Condens. Matter Mater. Phys. **49**, 9441–9452 (1994)
Ng, T.Y., Yeo, J.J., Liu, Z.S.: A molecular dynamics study of the thermal conductivity of nanoporous silica aerogel, obtained through negative pressure rupturing. J. Non-Cryst. Solids **358**, 1350–1355 (2012)
Ong, Z.-Y., Pop, E.: Molecular dynamics simulation of thermal boundary conductance between carbon nanotubes and SiO_{2}. Phys. Rev. B Condens. Matter Mater. Phys. **81**, 155408 (2010)
Pajonk, G.M.: Transparent silica aerogels. J. Non-Cryst. Solids **225**, 307–314 (1998)
Plimpton, S.: Fast parallel algorithms for short-range molecular-dynamics. J. Comput. Phys. **117**, 1–19 (1995)
Poco, J.F., Satcher Jr., J.H., Hrubesh, L.W.: Synthesis of high porosity, monolithic alumina aerogels. J. Non-Cryst. Solids **285**, 57–63 (2001)
Pohl, P.I., Faulon, J.L., Smith, D.M.: Molecular-dynamics computer-simulations of silica aerogels. J. Non-Cryst. Solids **186**, 349–355 (1995)
Rao, A.V., Kulkarni, M.M., Pajonk, G.M., Amalnerkar, D.P., Seth, T.: Synthesis and characterization of hydrophobic silica aerogels using trimethylethoxysilane as a co-precursor. J. Sol-Gel Sci. Technol. **27**, 103–109 (2003)
Rapaport, D.C.: The Art of Molecular Dynamics Simulation. Cambridge University Press, Cambridge (2004)
Reim, M., Reichenauer, G., Körner, W., Manara, J., Arduini-Schuster, M., Korder, S., Beck, A., Fricke, J.: Silica-aerogel granulate – structural, optical and thermal properties. J. Non-Cryst. Solids **350**, 358–363 (2004)
Rubin, M., Lampert, C.M.: Transparent silica aerogels for window insulation. Sol. Energy Mater. **7**, 393–400 (1983)
Sachithanadam, M.: Characterization of mechanical, thermal and acoustic properties of aerogel composites. Doctoral Thesis, Nanyang Technological University (2015)
Sadus, R.J.: Molecular Simulation of Fluids: Theory, Algorithms and Object-Orientation. Elsevier, New York (1999)
Schmidt, M., Schwertfeger, F.: Applications for silica aerogel products. J. Non-Cryst. Solids **225**, 364–368 (1998)

Sellan, D.P., Landry, E.S., Turney, J.E., McGaughey, A.J.H., Amon, C.H.: Size effects in molecular dynamics thermal conductivity predictions. Phys. Rev. B Condens. Matter Mater. Phys. **81**, 214305 (2010)
Shakouri, A., Yeo, J., Ng, T.Y., Liu, Z., Taylor, H.: Superlubricity-activated thinning of graphite flakes compressed by passivated crystalline silicon substrates for graphene exfoliation. Carbon **80**, 68–74 (2014)
Shell, M.S., Debenedetti, P.G., Panagiotopoulos, A.Z.: Molecular structural order and anomalies in liquid silica. Phys. Rev. E Stat. Nonlinear Soft Matter Phys. **66**, 011202 (2002)
Smirnova, I., Suttiruengwong, S., Arlt, W.: Feasibility study of hydrophilic and hydrophobic silica aerogels as drug delivery systems. J. Non-Cryst. Solids **350**, 54–60 (2004)
Soleimani Dorcheh, A., Abbasi, M.H.: Silica aerogel; synthesis, properties and characterization. J. Mater. Process. Technol. **199**, 10–26 (2008)
Steiner, S.: Website on properties of aerogels. http://www.aerogel.org/?p=103. Retrieved Dec 2015
Strøm, R.A., Masmoudi, Y., Rigacci, A., Petermann, G., Gullberg, L., Chevalier, B., Einarsrud, M. A.: Strengthening and aging of wet silica gels for up-scaling of aerogel preparation. J. Sol-Gel Sci. Technol. **41**, 291–298 (2007)
Tersoff, J.: New empirical approach for the structure and energy of covalent systems. Phys. Rev. B Condens. Matter Mater. Phys. **37**, 6991–7000 (1988)
Tillotson, T.M., Hrubesh, L.W.: Transparent ultralow-density silica aerogels prepared by a two-step sol-gel process. J. Non-Cryst. Solids **145**, 44–50 (1992)
van Beest, B.W., Kramer, G.J., van Santen, R.A.: Force fields for silicas and aluminophosphates based on ab initio calculations. Phys. Rev. Lett. **64**, 1955–1958 (1990)
van Bommel, M.J., den Engelsen, C.W., van Miltenburg, J.C.: A thermoporometry study of fumed silica/aerogel composites. J. Porous. Mater. **4**, 143–150 (1997)
Vashishta, P., Kalia, R.K., Rino, J.P., Ebbsjo, I.: Interaction potential for SiO_2 - a molecular-dynamics study of structural correlations. Phys. Rev. B Condens. Matter Mater. Phys. **41**, 12197–12209 (1990)
Weber, M.J.: Glasses. Handbook of Optical Materials. CRC Press, Boca Raton, FL (2002)
Wei, G., Liu, Y., Zhang, X., Yu, F., Du, X.: Thermal conductivities study on silica aerogel and its composite insulation materials. Int. J. Heat Mass Transfer **54**, 2355–2366 (2011)
Wittwer, V.: Translucent insulation for passive solar energy utilization in buildings. Solar Wind Technol. **6**, 419–426 (1989)
Woignier, T., Phalippou, J., Vacher, R., Pelous, J., Courtens, E.: Different kinds of fractal structures in silica aerogels. J. Non-Cryst. Solids **121**, 198–201 (1990)
Wyckoff, R.W.G.: Crystal Structures New York. John Wiley & Sons, London (1963)
Xu, Z., Gan, L., Jia, Y., Hao, Z., Liu, M., Chen, L.: Preparation and characterization of silica-titania aerogel-like balls by ambient pressure drying. J. Sol-Gel Sci. Technol. **41**, 203–207 (2007)
Ye, L., Ji, Z.-H., Han, W.-J., Hu, J.-D., Zhao, T.: Synthesis and characterization of silica/carbon composite aerogels. J. Am. Ceram. Soc. **93**, 1156–1163 (2010)
Yeo, J., Liu, Z., Ng, T.: Enhanced thermal characterization of silica aerogels through molecular dynamics simulation. Modell. Simul. Mater. Sci. Eng. **21**, 075004 (2013)
Zeng, J.S.Q., Stevens, P.C., Hunt, A.J., Grief, R., Daehee, L.: Thin-film-heater thermal conductivity apparatus and measurement of thermal conductivity of silica aerogel. Int. J. Heat Mass Transfer **39**, 2311–2317 (1996)

Chapter 5
Smart Fuzzy Fiber-Reinforced Piezoelectric Composites

Manas C. Ray

Abstract In this chapter analytical micromechanics model of a novel smart fuzzy fiber-reinforced composite (**SFFRC**) has been derived. The novel constructional feature of such **SFFRC** is that the existing vertically reinforced 1–3 piezoelectric composite has been hybridized by radially growing carbon nanotubes (**CNT**s) on the surface of the cylindrical vertical piezoelectric fibers. The model predicts that the effective in-plane piezoelectric coefficient and the elastic properties of such **SFFRC** are significantly improved over those of the existing 1–3 piezoelectric composite without reinforced with CNTs.

5.1 Piezoelectric Effects

Piezoelectric effect is an electromechanical coupling phenomenon exhibited by non-centrosymmetric dielectric materials. These materials do not possess inversion symmetry. This means that the inversion of the atomic positions alters the original crystalline structure, and different equilibrium positions of charges are associated with different polarization. Such polarization is called the piezoelectricity. Two types of piezoelectric effects exist in the piezoelectric materials. One of the effects by virtue of which the conversion of the mechanical energy into the electric energy occurs when the piezoelectric materials are deformed upon mechanical stimulus is called the direct piezoelectric effect. The other effect is called the converse piezoelectric effect by virtue of which piezoelectric materials are deformed due to the application of the electric field resulting in the conversion of the electrical energy into the mechanical energy. To exhibit piezoelectric effect, piezoelectric materials must be poled. Normally, a piezoelectric material has electric dipoles which are randomly oriented. When it is heated above a certain temperature called the Curie temperature and is subjected to a very strong electric field, the electric dipoles

M.C. Ray (✉)
Department of Mechanical Engineering, Indian Institute of Technology, Kharagpur 721302, India
e-mail: mcray@mech.iitkgp.ernet.in

S.A. Meguid (ed.), *Advances in Nanocomposites*,
DOI 10.1007/978-3-319-31662-8_5

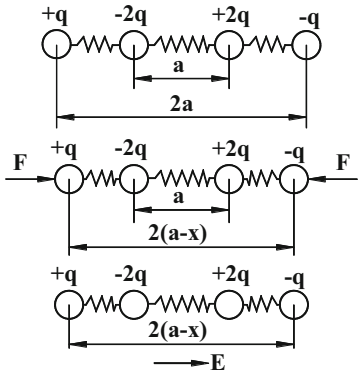

Fig. 5.1 Schematic representation of piezoelectric phenomena

reorient themselves and are aligned relative to the electric field. Such process is called poling. If the dipoles maintain their aligned orientations after cooling, the material is said to be poled and exhibits piezoelectric effect. Let four charges be in equilibrium on a straight line as shown in Fig. 5.1. Let the magnitudes of the first and the fourth charges be "$+q$" and "$-q$" while the second and the third charges be "$-2q$" and "$+2q$." The first and the fourth charges are "$2a$" apart, while the distance between the second and the third charges is "a." The locations of the charges are symmetric about the center, and thus, the charges are in equilibrium, but they are not centrosymmetric as the 180° rotation of this system of charges causes a different system of charges. The net dipole moment or the polarization of this system of charges is obviously zero. Now if the first and the fourth charges are displaced toward the center of the charges by an amount "x" due to an applied force F, this system of charges will exhibit a net polarization of amount "$2qx$." This displacement "x" is treated as the measure of mechanical deformation due to the application of mechanical energy. Thus the non-centrosymmetric system of charges exhibits electric polarization upon mechanical stimulation. On the other hand, if this system of charges is subjected to an electric field E, the charges will be displaced resulting in the conversion of the electrical energy into the mechanical energy.

5.2 Introduction to Smart Fuzzy Fiber-Reinforced Composite

In the quest for developing very lightweight high-performance flexible structures, a concept has emerged for developing the structures with self-controlling and/or self-monitoring capabilities. Expediently, utilizing the piezoelectric effects, Forward (1981) first attempted to demonstrate the feasibility of the effectiveness of the piezoelectric actuator to damp out the vibrations of a cylindrical fiber glass mast. Subsequently, Bailey and Hubbard (1985), (1987), Crawley and Luis (1987), and Im and Atluri (1989) successfully reported that the patches of piezoelectric

actuators being bonded with the host beams efficiently perform as the distributed actuators of the host beams. Miller and Hubbard (1987) first demonstrated that a layer of the piezoelectric material being integrated with a cantilever beam can act as the distributed sensor of the host cantilever beam. When these distributed sensors and actuators are coupled with the elements of the control systems such that the distributed piezoelectric actuators can be activated with a proper control voltage, the host structure attains the self-controlling and self-sensing capabilities. Such flexible host structures possessing built-in mechanism for achieving self-controlling and self-sensing capabilities are being customarily called as smart structures. Since its inception, enormous research (Baz and Poh 1988; Ha et al. 1992; Ray et al. 1994; Lin et al. 1996; Saravanos et al. 1997; Chee et al. 1999; Varadarajan et al. 2000; Ray and Pradhan 2007; Sohn et al. 2009; Ray and Faye 2009; Suresh Kumar and Ray 2012) on smart structures has been going on for developing very light weight smart flexible structures.

The performance of the smart structures depends on the magnitudes of the piezoelectric coefficients of the piezoelectric materials. The magnitudes of the piezoelectric coefficients of monolithic polymer piezoelectric materials are very low, while the monolithic piezoceramic materials are characterized with large values of the piezoelectric coefficients. But the monolithic piezoceramic materials such as **PZT5**, **PZT5H**, etc. are highly brittle and not conformable to the cylindrical surface or vibrating surface of the host structures. Hence, these smart materials find limitations in their use as distributed actuators. The conventional advanced fiber-reinforced composites are composed of brittle fibers of high stiffness. Probably this way of using high stiff brittle materials motivated the researchers to develop piezoelectric composites using brittle piezoceramic fibers. One of the commercially available piezoelectric composites (Smith and Auld 1991) is popularly known as 1–3 piezoelectric (**PZC**). In a lamina of vertically reinforced 1–3 **PZC**, the ceramic piezoelectric fibers are vertically aligned across the thickness of the lamina. Such 1–3 **PZC** provides a wide range of effective material properties not offered by the existing monolithic piezoelectric materials, renders anisotropic actuations, and is characterized by good conformability and strength. However, this 1–3 **PZC** also suffers from the drawback that its effective in-plane piezoelectric coefficient is much smaller than its transverse effective piezoelectric coefficient. The in-plane piezoelectric coefficient accounts for the performance of the piezoelectric actuator for bending control of smart structures. The performance of the distributed actuator made of such 1–3 **PZC** can be enhanced if the magnitude of its in-plane piezoelectric coefficient can be tailored to an improved value.

Since the discovery of carbon nanotubes (**CNT**s) (Iijima 1991), researchers have been carrying out extensive work (Treacy et al. 1996; Shen and Li 2004; Cheng et al. 2009) to predict their effective material properties, and it has been revealed that the **CNT**s are characterized with exceptionally high elastic properties. However, **CNT**s alone cannot be used for structural applications as they are difficult to be aligned and prone to agglomeration. To exploit the excellent elastic properties of **CNT**s, a great deal of research has been devoted to the development of high-performance nanocomposites using **CNT**s as reinforcements (Thostenson and

Chou 2003; Griebel and Hamaekers 2004; Odegard et al. 2003; Seidel and Lagoudas 2004; Jiang et al. 2009; Shadlou et al. 2011). For structural applications, recent research focuses on improving the effective properties of the existing advanced fiber-reinforced polymer composite by growing **CNT**s on the surfaces of the fiber reinforcements. Bower et al. (2000) demonstrated the growth of aligned **CNT**s on the substrate surface using microwave plasma-enhanced chemical vapor deposition. Mathur et al. (2008) experimentally investigated that the flexural strength and the modulus of the carbon fiber-reinforced composite can be improved by growing **CNT**s on the surface of the carbon fiber. Zhang et al. (2008) produced **CNT** arrays on the host aluminum silicate and the quartz fiber. Gracia et al. (2008) fabricated a hybrid laminate in which the reinforcement is a woven cloth of alumina fibers with in situ-grown **CNT**s on the surface of the fibers. They demonstrated that both the mechanical and electrical properties of such a laminate are enhanced because of **CNT**s grown on the surface of the alumina fibers. Recently, Kundalwal and Ray (2011, 2012) derived micromechanics models for estimating all the effective elastic coefficients of novel fuzzy fiber-reinforced composite (**FFRC**). Chatzigeorgiou et al. (2012) also estimated the effective mechanical properties of fuzzy fiber composite employing the composite cylinder method. Lanzara and Chang (2009) designed and fabricated the piezoelectric ceramic discs coated with vertically aligned **CNT**s. They demonstrated that the arrays of aligned **CNT**s can be normally grown on the surface of the piezoceramic (**PZT**) disc.

The paper authored by Lanzara and Chang (2009) motivated the author to presume that the **PZT** fibers may be coated with radially grown **CNT**s. Hence, in order to further improve the effective in-plane properties of the existing 1–3 **PZC**, Ray (2010) and Dhala and Ray (2015) delineated a concept of developing novel **SFFRC**. The **SFFRC** is a smart hybrid piezoelectric composite in which the piezoelectric fiber reinforcements are vertically aligned and **CNT**s are radially grown on the surfaces of these piezoelectric fibers. This chapter is concerned with the derivation of an analytical micromechanics model for estimating the effective elastic and piezoelectric properties of this novel **SFFRC**. First an analytical micromechanics model of the existing vertically reinforced 1–3 **PZC** is presented. How this model is augmented to derive the micromechanics model of **SFFRC** is presented in the subsequent sections. Numerical results are presented to demonstrate that the **CNT**s can improve the effective in-plane piezoelectric coefficient of the existing 1–3 **PZC**.

5.3 Three-Dimensional Effective Properties of 1–3 Piezoelectric Composites

Figure 5.2 schematically illustrates a lamina made of the vertically reinforced 1–3 piezoelectric composite (**PZC**). Here the pattern "1–3" refers to the connectivity pattern of the piezoelectric composite. In case of the pattern like "1–3," the first

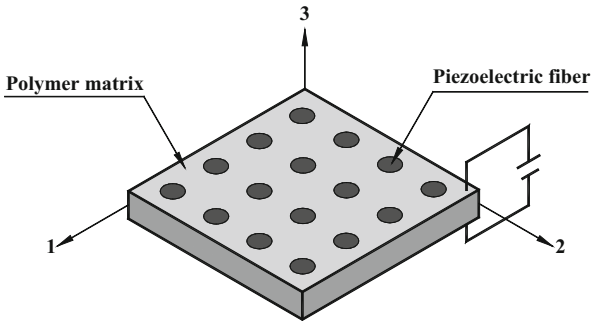

Fig. 5.2 Schematic diagram of a lamina of vertically reinforced 1–3 piezoelectric composite

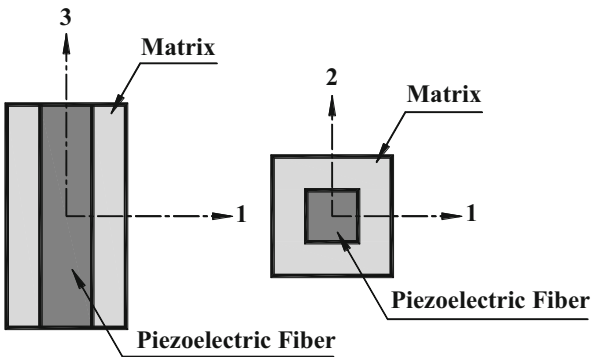

Fig. 5.3 In-plane and transverse cross sections of the RVE of the 1–3 piezoelectric composite

digit represents the number of connectivity of the fiber reinforcement along the principal material coordinate axes, while the second digit denotes the same of the matrix phase (Newnham et al. 1978). It may be observed from Fig. 5.2 that the piezoelectric fiber reinforcements are vertically aligned across the thickness of the lamina. The matrix phase is a polymer material.

The top and the bottom surfaces of the lamina are electroded such that the electric field can be applied across the thickness of the lamina. The orthogonal principal material coordinate system $(1-2-3)$ is considered in such a way that the 3-axis is aligned with the length of the fibers while 1- and 2-axes are aligned with the length and the width of the lamina, i.e., transverse to the fiber direction. The in-plane and vertical cross sections of the representative volume element (**RVE**) of this 1–3 **PZC** are illustrated in Fig. 5.3. It is considered that the lamina of the 1–3 **PZC** shown in Fig. 5.2 is subjected to the electric field along the thickness of the lamina only. Thus, the constitutive equations for the converse piezoelectric effect (Ray and Pradhan 2007), exhibited by the piezoelectric material of the fibers, are given by

$$\{\sigma^p\} = [C^p]\{\in^p\} - \{e^p\}E_3 \tag{5.1}$$

The constitutive relations for the matrix material are

$$\{\sigma^m\} = [C^m]\{\in^m\} \tag{5.2}$$

In Eqs. (5.1) and (5.2), $\{\sigma\}$, $\{\in\}$, and $[C]$ with superscript p or m represent the state of stress, the state of strain, and the elastic coefficient matrix at any point in the constituent phase, respectively, while $\{e\}$ and E_3 are the piezoelectric coefficient matrix and the electric field along the thickness (i.e., 3-axis) of the lamina of the 1–3 **PZC**, respectively. Their explicit forms are

$$\{\sigma^r\} = \begin{bmatrix} \sigma_1^r & \sigma_2^r & \sigma_3^r & \sigma_{23}^r & \sigma_{13}^r & \sigma_{12}^r \end{bmatrix}^T, \{\in^r\} = \begin{bmatrix} \in_1^r & \in_2^r & \in_3^r & \gamma_{23}^r & \gamma_{13}^r & \gamma_{12}^r \end{bmatrix}^T,$$

$$[C^r] = \begin{bmatrix} C_{11}^r & C_{12}^r & C_{13}^r & 0 & 0 & 0 \\ C_{12}^r & C_{22}^r & C_{23}^r & 0 & 0 & 0 \\ C_{13}^r & C_{23}^r & C_{33}^r & 0 & 0 & 0 \\ 0 & 0 & 0 & C_{44}^r & 0 & 0 \\ 0 & 0 & 0 & 0 & C_{55}^r & 0 \\ 0 & 0 & 0 & 0 & 0 & C_{66}^r \end{bmatrix} \text{ and } \{e^p\} = \begin{Bmatrix} e_{31}^p \\ e_{32}^p \\ e_{33}^p \\ 0 \\ 0 \\ 0 \end{Bmatrix}; r = p \text{ or } m \tag{5.3}$$

In Eq. (5.3), for the constituent phase denoted by r, σ_1^r, σ_2^r, and σ_3^r represent the normal stresses along the 1-, 2-, and 3-axes, respectively; σ_{23}^r, σ_{13}^r, and σ_{12}^r are the shear stresses; and C_{ij}^r is the elastic coefficient. Also, it may be noted that if the applied electric field is applied along the 3-direction, the in-plane piezoelectric coefficients e_{31}^p and e_{32}^p provide the measure of the in-plane actuations along the 1- and 2-directions, respectively, while the piezoelectric coefficient e_{33}^p accounts for the measure of the transverse actuation. The existence of perfect bonding between the fibers and the matrix phase in the **RVE** allows one to write the following iso-field conditions (Aboudi et al. 2013):

$$\begin{Bmatrix} \sigma_1^{pc} \\ \sigma_2^{pc} \\ \in_3^{pc} \\ \sigma_{23}^{pc} \\ \sigma_{13}^{pc} \\ \sigma_{12}^{pc} \end{Bmatrix} = \begin{Bmatrix} \sigma_1^m \\ \sigma_2^m \\ \in_3^m \\ \sigma_{23}^m \\ \sigma_{13}^m \\ \sigma_{12}^m \end{Bmatrix} = \begin{Bmatrix} \sigma_1^p \\ \sigma_2^p \\ \in_3^p \\ \sigma_{23}^p \\ \sigma_{13}^p \\ \sigma_{12}^p \end{Bmatrix} \tag{5.4}$$

The existence of perfect bonding between the fibers and matrix also requires to satisfy the following rules of mixtures (Aboudi et al. 2013):

$$\begin{aligned} &\sigma_3^{pc} = V_p\sigma_3^p + V_m\sigma_3^m,\ \in_1^{pc} = V_p \in_1^p + V_m \in_1^m,\ \in_2^{pc} = V_p \in_2^p + V_m \in_2^m, \\ &\gamma_{23}^{pc} = V_p\gamma_{23}^p + V_m\gamma_{23}^m, \gamma_{13}^{pc} = V_p\gamma_{13}^p + V_m\gamma_{13}^m, \gamma_{12}^{pc} = V_p\gamma_{12}^p + V_m\gamma_{12}^m, \end{aligned} \tag{5.5}$$

In Eq. (5.5), V_p and V_m represent the piezoelectric fiber volume fraction and the matrix volume fraction in the **RVE** of the 1–3 **PZC**, respectively. It should be noted that the field variables with superscript *pc* appearing in Eqs. (5.4) and (5.5) represent the field variables of the homogenized **RVE** of the 1–3 **PZC**. At this juncture, it must be noted that a field variable used here for the constituent phases or the homogenized **RVE** actually represents the average of the corresponding field variable in the constituent phases or the homogenized **RVE**, respectively (Aboudi et al. 2013). The state of stress $\{\sigma^{pc}\}$ and the state of strain $\{\in^{pc}\}$ in the homogenized **RVE** can be written in terms of the strains in the constituent phases as follows:

$$\{\sigma^{pc}\} = [C_1]\{\in^p\} + [C_2]\{\in^m\} - \{e_1\}\{E\} \tag{5.6}$$

$$\{\in^{pc}\} = [V_1]\{\in^p\} + [V_2]\{\in^m\} \tag{5.7}$$

in which

$$\{\sigma^{pc}\} = \begin{Bmatrix} \sigma_1^{pc} \\ \sigma_2^{pc} \\ \sigma_3^{pc} \\ \sigma_{23}^{pc} \\ \sigma_{13}^{pc} \\ \sigma_{12}^{pc} \end{Bmatrix}, \{\in^{pc}\} = \begin{Bmatrix} \in_1^{pc} \\ \in_2^{pc} \\ \in_3^{pc} \\ \gamma_{23}^{pc} \\ \gamma_{13}^{pc} \\ \gamma_{12}^{pc} \end{Bmatrix}, [C_1] = \begin{bmatrix} 0 & 0 & 0 & 0 & 0 & 0 \\ 0 & 0 & 0 & 0 & 0 & 0 \\ V_pC_{13}^p & V_pC_{23}^p & V_pC_{33}^p & 0 & 0 & 0 \\ 0 & 0 & 0 & 0 & 0 & 0 \\ 0 & 0 & 0 & 0 & 0 & 0 \\ 0 & 0 & 0 & 0 & 0 & 0 \end{bmatrix}$$

$$[C_2] = \begin{bmatrix} C_{11}^m & C_{12}^m & C_{13}^m & 0 & 0 & 0 \\ C_{12}^m & C_{22}^m & C_{23}^m & 0 & 0 & 0 \\ V_mC_{13}^m & V_mC_{23}^m & V_mC_{33}^m & 0 & 0 & 0 \\ 0 & 0 & 0 & C_{44}^m & 0 & 0 \\ 0 & 0 & 0 & 0 & C_{55}^m & 0 \\ 0 & 0 & 0 & 0 & 0 & C_{66}^m \end{bmatrix}, \{e_1\} = \begin{Bmatrix} 0 \\ 0 \\ V_pe_{33}^p \\ 0 \\ 0 \\ 0 \end{Bmatrix}$$

$$[V_1] = \begin{bmatrix} V_p & 0 & 0 & 0 & 0 & 0 \\ 0 & V_p & 0 & 0 & 0 & 0 \\ 0 & 0 & 1 & 0 & 0 & 0 \\ 0 & 0 & 0 & V_p & 0 & 0 \\ 0 & 0 & 0 & 0 & V_p & 0 \\ 0 & 0 & 0 & 0 & 0 & V_p \end{bmatrix} \text{ and } [V_2] = \begin{bmatrix} V_m & 0 & 0 & 0 & 0 & 0 \\ 0 & V_m & 0 & 0 & 0 & 0 \\ 0 & 0 & 0 & 0 & 0 & 0 \\ 0 & 0 & 0 & V_m & 0 & 0 \\ 0 & 0 & 0 & 0 & V_m & 0 \\ 0 & 0 & 0 & 0 & 0 & V_m \end{bmatrix} \tag{5.8}$$

The continuity conditions between the fiber and the matrix phase of the **RVE** of the 1–3 **PZC** given in Eq. (5.4) can be expressed in terms of the strains in the constituent phases and the electric field as follows:

$$[C_3]\{\in^p\} - [C_4]\{\in^m\} = \{e_2\}\{E\} \tag{5.9}$$

in which

$$[C_3] = \begin{bmatrix} C_{11}^p & C_{12}^p & C_{13}^p & 0 & 0 & 0 \\ C_{12}^p & C_{22}^p & C_{23}^p & 0 & 0 & 0 \\ 0 & 0 & 1 & 0 & 0 & 0 \\ 0 & 0 & 0 & C_{44}^p & 0 & 0 \\ 0 & 0 & 0 & 0 & C_{55}^p & 0 \\ 0 & 0 & 0 & 0 & 0 & C_{66}^p \end{bmatrix}, [C_4] = \begin{bmatrix} C_{11}^m & C_{12}^m & C_{13}^m & 0 & 0 & 0 \\ C_{12}^m & C_{22}^m & C_{23}^m & 0 & 0 & 0 \\ 0 & 0 & 1 & 0 & 0 & 0 \\ 0 & 0 & 0 & C_{44}^m & 0 & 0 \\ 0 & 0 & 0 & 0 & C_{55}^m & 0 \\ 0 & 0 & 0 & 0 & 0 & C_{66}^m \end{bmatrix},$$

$$\text{and } \{e_2\} = \begin{bmatrix} e_{31}^p & e_{32}^p & 0 & 0 & 0 & 0 \end{bmatrix}^T \tag{5.10}$$

Using Eqs. (5.6) and (5.8), one can derive that

$$\{\in^m\} = [V_3]^{-1}\{\in^{pc}\} - [V_3]^{-1}[V_1][C_3]^{-1}\{e_2\}E_3 \tag{5.11}$$

and

$$\{\in^p\} = [V_4]^{-1}\{\in^{pc}\} - [V_4]^{-1}[V_2][C_4]^{-1}\{e_2\}E_3 \tag{5.12}$$

in which

$[V_3] = [V_2] + [V_1][C_3]^{-1}[C_4]$ and $[V_4] = [V_1] + [V_2][C_4]^{-1}[C_3]$.

Substituting Eqs. (5.10) and (5.11) into Eq. (5.5), the following effective constitutive relation for the converse piezoelectric effect in the vertically reinforced 1–3 **PZC** can be derived:

$$\{\sigma^{pc}\} = [C^{pc}]\{\in^{pc}\} - \{e^{pc}\}E_3 \tag{5.13}$$

in which the effective elastic coefficient matrix $[C^{pc}]$ and the effective piezoelectric coefficient matrix $\{e^{pc}\}$ of the 1–3 **PZC** are given by

$$[C^{pc}] = [C_1][V_4]^{-1} + [C_2][V_3]^{-1} \tag{5.14}$$

$$\{e^{pc}\} = \{e_1\} - [C_1][V_4]^{-1}[V_2][C_4]^{-1}\{e_2\} + [C_2][V_3]^{-1}[V_1][C_3]^{-1}\{e_2\} \tag{5.15}$$

It is obvious from Eq. (5.14) that the in-plane effective piezoelectric coefficients e_{31}^{pc} and e_{32}^{pc} of the 1–3 **PZC** are $e^{pc}(1)$ and $e^{pc}(2)$, respectively, while the transverse

effective piezoelectric coefficient e_{33}^{pc} of the 1–3 **PZC** is $e^{pc}(3)$. It may be noted that the matrix $[C_4]$ contains the elastic properties of the matrix phase. Hence, it is obvious from the expression of the effective piezoelectric coefficient $\{e^{pc}\}$ given by Eq. (5.14) that for a particular piezoelectric material, the magnitude of the effective piezoelectric coefficient can be improved if the elastic properties of the matrix are improved.

5.4 Effective Properties of the SFFRC

Figure 5.4 illustrates a schematic sketch of a lamina of the **SFFRC**. The novel constructional feature of such a continuous unidirectional vertically reinforced composite is that **CNT**s of equal length are uniformly aligned in the plane of the lamina and radially grown on the surface of the piezoelectric fiber reinforcements. **CNT**s considered here are transversely isotropic (Shen and Li 2004). They are grown on the surface of the piezoelectric fibers in such a way that their axes of transverse isotropy are normal to the surface of the piezoelectric fibers. Such a resulting piezoelectric fuzzy fiber (**PFF**) is shown in Fig. 5.5. When this **PFF** is embedded into the polymer material, the gap between the **CNT**s is filled with the polymer. Therefore, the radially aligned **CNT**s reinforce the polymer matrix surrounding the piezoelectric fiber along the direction transverse to the length of the piezoelectric fiber. Consequently, the augmented **PFF** can be viewed as a circular cylindrical piezoelectric composite fuzzy fiber (**PCFF**) in which a piezoelectric fiber is embedded in the **CNT**-reinforced polymer matrix nanocomposite (**PMNC**) and the radius of the **PCFF** is equal to the sum of the radius of the piezoelectric fiber and the length of a **CNT**. The cross sections of such a **PCFF** are illustrated in Fig. 5.6. Therefore, the **RVE** of the **SFFRC** can be treated as being composed of two phases where the reinforcement is the **PCFF** and the matrix is the polymer material. The piezoelectric fiber is poled along the thickness direction, and the only electric field considered here is applied across the thickness of the lamina. Thus, the analytical micromechanics model for estimating the effective properties of the

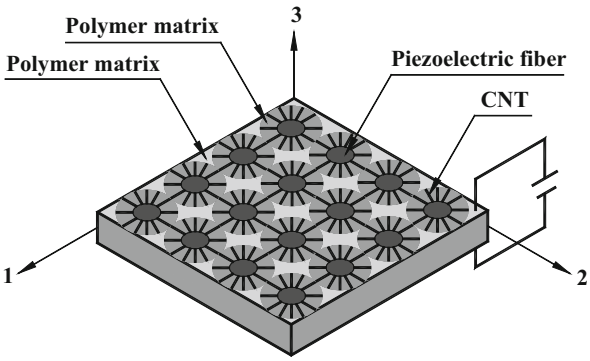

Fig. 5.4 Schematic diagram of a lamina of smart fuzzy fiber-reinforced composite (SFFRC)

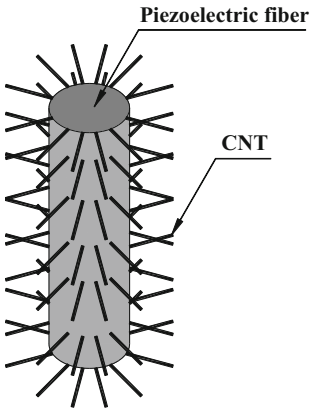

Fig. 5.5 Piezoelectric fuzzy fiber (**PFF**)

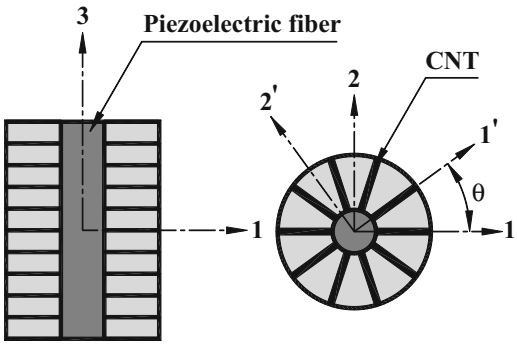

Fig. 5.6 Longitudinal and transverse cross sections

SFFRC first needs the derivation of the micromechanics model for estimating the effective elastic properties of the **PMNC** material. Subsequently, considering the **PMNC** material as the matrix phase and the piezoelectric fibers as the reinforcements, effective elastic properties and effective piezoelectric properties of the **PCFF** are to be computed. Finally, utilizing the effective properties of the **PCFF** and the polymer matrix, the effective properties of the **SFFRC** can be estimated. Also, **PCFF**s are assumed to be uniformly spaced over the volume of a lamina of the **SFFRC** in such a way that three orthogonal principal material coordinate axes (1–2–3) exist in the composite as shown in Fig. 5.4. Micromechanics models for estimating the properties of the **PMNC**, the **PCFF**, and the **SFFRC** are derived in the following sections.

5.4.1 Micromechanics Model of the PMNC

This section presents a simple micromechanics model to estimate the effective elastic properties of the **PMNC** material surrounding the piezoelectric fiber which

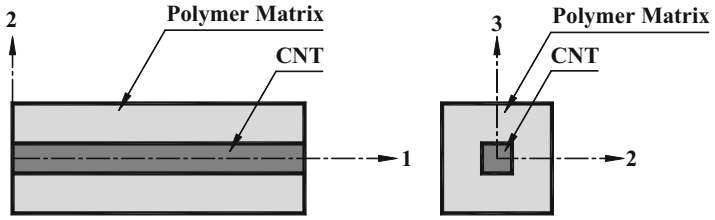

Fig. 5.7 Longitudinal and transverse section of the **RVE** of the **PMNC**

are required as inputs for the derivation of the model of the **PCFF**. Since the piezoelectric fibers are vertically aligned, the radially grown **CNT**s on the surface of the piezoelectric fibers are aligned either with the 1-axis or with the $1'$-axis as shown in Fig. 5.6. Let us first estimate the properties of an **RVE** in which the **CNT** fiber aligns with the 1-axis. The cross sections of such an **RVE** of the **PMNC** have been shown in Fig. 5.7. Assuming **CNTs** as solid fibers (Gao and Li 2005), the micromechanics model derived in Sect. 5.3 can be modified to predict the average effective elastic constants of the **PMNC** surrounding the piezoelectric fiber. Based on the principal material coordinate (1–2–3) axes shown in Fig. 5.7, the constitutive relations for the constituent phases of the **RVE** of the **PMNC** are given by

$$\{\sigma^r\} = [C^r]\{\in^r\};\ r = nt \,\text{and}\, m \tag{5.16}$$

where the stress vector, the strain vector, and the elastic coefficient matrix of the phase denoted by r are given by Eq. (5.3). In Eq. (5.14) the superscripts nt and m denote, respectively, the **CNT** fiber and the monolithic polymer matrix. It may be mentioned here that the basics of **CNT**s may be studied from some original literature (Thostenson and Chou 2003). It is assumed that **CNTs** and the polymer matrix are perfectly bonded. Therefore, the following iso-field relations and the rules of mixture (Aboudi et al. 2013) satisfying the perfect bonding conditions between the fiber and the matrix can be written as

$$\begin{Bmatrix} \sigma_2^{nc} \\ \sigma_3^{nc} \\ \in_1^{nc} \\ \sigma_{23}^{nc} \\ \sigma_{13}^{nc} \\ \sigma_{12}^{nc} \end{Bmatrix} = \begin{Bmatrix} \sigma_2^{m} \\ \sigma_3^{m} \\ \in_1^{m} \\ \sigma_{23}^{m} \\ \sigma_{13}^{m} \\ \sigma_{12}^{m} \end{Bmatrix} = \begin{Bmatrix} \sigma_2^{nt} \\ \sigma_3^{nt} \\ \in_1^{nt} \\ \sigma_{23}^{nt} \\ \sigma_{13}^{nt} \\ \sigma_{12}^{nt} \end{Bmatrix} \tag{5.17}$$

and

$$\begin{aligned} &\sigma_1^{nc} = V_{nt}\sigma_1^{nt} + V_m\sigma_1^{nt},\ \in_2^{nc} = V_{nt}\in_2^{nt} + V_m\in_2^{m},\ \in_3^{nc} = V_{nt}\in_3^{nt} + V_m\in_3^{m},\\ &\gamma_{23}^{nc} = V_{nt}\gamma_{23}^{nt} + V_m\gamma_{23}^{m},\ \gamma_{13}^{nc} = V_{nt}\gamma_{13}^{nt} + V_m\gamma_{13}^{m} \text{ and } \gamma_{12}^{nc} = V_{nt}\gamma_{12}^{nt} + V_m\gamma_{12}^{m} \end{aligned} \tag{5.18}$$

In Eqs. (5.15) and (5.17), V_{nt} is the volume fraction of the **CNT** with respect to the volume of the **RVE** of the **PMNC** and $V_m = 1 - V_{nt}$. Also, the superscript nc represents the homogenized **PMNC** material. From Eqs. (5.15) and (5.17), the stress and the strain vectors in the homogenized **PMNC** material can be expressed in terms of the strain vectors of the constituent phases as follows:

$$\{\sigma^{nc}\} = [C_5]\{\in^{nt}\} + [C_6]\{\in^{m}\} \tag{5.19}$$

$$\{\in^{nc}\} = [V_5]\{\in^{nt}\} + [V_6]\{\in^{m}\} \tag{5.20}$$

Also, using the iso-field conditions between the constituent phases given by Eq. (5.15), the relations among the strains in the constituent phases can be written as

$$[C_7]\{\in^{nt}\} = [C_8]\{\in^{m}\} \tag{5.21}$$

The various matrices appearing in Eqs. (5.16)–(5.18) are

$$[C_5] = V_{nt}\begin{bmatrix} C_{11}^{nt} & C_{12}^{nt} & C_{13}^{nt} & 0 & 0 & 0 \\ 0 & 0 & 0 & 0 & 0 & 0 \\ 0 & 0 & 0 & 0 & 0 & 0 \\ 0 & 0 & 0 & 0 & 0 & 0 \\ 0 & 0 & 0 & 0 & 0 & 0 \\ 0 & 0 & 0 & 0 & 0 & 0 \end{bmatrix}, [C_6] = \begin{bmatrix} V_m C_{11}^{m} & V_m C_{12}^{m} & V_m C_{13}^{m} & 0 & 0 & 0 \\ C_{12}^{m} & C_{22}^{m} & C_{23}^{m} & 0 & 0 & 0 \\ C_{13}^{m} & C_{23}^{m} & C_{33}^{m} & 0 & 0 & 0 \\ 0 & 0 & 0 & 0 & 0 & 0 \\ 0 & 0 & 0 & 0 & 0 & 0 \\ 0 & 0 & 0 & 0 & 0 & 0 \end{bmatrix},$$

$$[V_5] = \begin{bmatrix} 1 & 0 & 0 & 0 & 0 & 0 \\ 0 & V_{nt} & 0 & 0 & 0 & 0 \\ 0 & 0 & V_{nt} & 0 & 0 & 0 \\ 0 & 0 & 0 & V_{nt} & 0 & 0 \\ 0 & 0 & 0 & 0 & V_{nt} & 0 \\ 0 & 0 & 0 & 0 & 0 & V_{nt} \end{bmatrix}, [V_6] = \begin{bmatrix} 0 & 0 & 0 & 0 & 0 & 0 \\ 0 & V_m & 0 & 0 & 0 & 0 \\ 0 & 0 & V_m & 0 & 0 & 0 \\ 0 & 0 & 0 & V_m & 0 & 0 \\ 0 & 0 & 0 & 0 & V_m & 0 \\ 0 & 0 & 0 & 0 & 0 & V_m \end{bmatrix},$$

$$[C_7] = \begin{bmatrix} 1 & 0 & 0 & 0 & 0 & 0 \\ C_{12}^{nt} & C_{22}^{nt} & C_{23}^{nt} & 0 & 0 & 0 \\ C_{13}^{nt} & C_{23}^{nt} & C_{33}^{nt} & 0 & 0 & 0 \\ 0 & 0 & 0 & C_{44}^{nt} & 0 & 0 \\ 0 & 0 & 0 & 0 & C_{55}^{nt} & 0 \\ 0 & 0 & 0 & 0 & 0 & C_{66}^{nt} \end{bmatrix}, [C_8] = \begin{bmatrix} 1 & 0 & 0 & 0 & 0 & 0 \\ C_{12}^{m} & C_{22}^{m} & C_{23}^{m} & 0 & 0 & 0 \\ C_{13}^{m} & C_{23}^{m} & C_{33}^{m} & 0 & 0 & 0 \\ 0 & 0 & 0 & C_{44}^{m} & 0 & 0 \\ 0 & 0 & 0 & 0 & C_{55}^{m} & 0 \\ 0 & 0 & 0 & 0 & 0 & C_{66}^{m} \end{bmatrix}, \tag{5.22}$$

Using Eqs. (5.17) and (5.18), the local strain vectors $\{\in^{nt}\}$ and $\{\in^{m}\}$ can be expressed in terms of $\{\in^{nc}\}$, and subsequently, using them in Eq. (5.16), the following constitutive relation between the states of stresses and strains at any point in the homogenized **PMNC** material is obtained:

$$\{\sigma^{nc}\} = [C^{nc}]\{\in^{nc}\} \tag{5.23}$$

where the effective elastic coefficient matrix $[C^{nc}]$ of the lamina of the **PMNC** is given by

$$[C^{nc}] = [C_5][V_8]^{-1} + [C_6][V_7]^{-1} \tag{5.24}$$

in which

$$[V_7] = [V_6] + [V_5][C_7]^{-1}[C_8] \text{ and } [V_8] = [V_5] + [V_6][C_8]^{-1}[C_7] \tag{5.25}$$

It should be noted that the effective elastic coefficient matrix at a point in the portion of the **PMNC** surrounding the piezoelectric fiber where the **CNT** is aligned with the 1-axis or 1′-axis is given by $[C^{nc}]$. Thus, the matrix $[C^{nc}]$ provides the local effective elastic coefficient matrix at a point in the **PMNC** either with respect to the $1-2-3$ coordinate system or with respect to the $1^{'}-2^{'}-3$ coordinate system. But for estimating the effective properties of the **SFFRC**, the homogenized properties of the **PMNC** with respect to the $1-2-3$ coordinate system are to be estimated. For the point located in the **PMNC** where the **CNT** is oriented at an angle θ with the 1-axis of the $1-2$ plane, the effective elastic coefficient matrix $\left[\overline{C}^{nc}\right]$ at the said point with respect to the $1-2-3$ coordinate system can be obtained by the following transformations:

$$\left[\overline{C}^{nc}\right] = [T]^{T}[C^{nc}][T] \tag{5.26}$$

where

$$[T] = \begin{bmatrix} m^2 & n^2 & 0 & 0 & 0 & -2mn \\ n^2 & m^2 & 0 & 0 & 0 & 2mn \\ 0 & 0 & 1 & 0 & 0 & 0 \\ 0 & 0 & 0 & m & n & 0 \\ 0 & 0 & 0 & -n & m & 0 \\ mn & -mn & 0 & 0 & 0 & m^2 - n^2 \end{bmatrix}, m = \cos\theta \text{ and } n = \sin\theta \tag{5.27}$$

Therefore, the effective elastic properties of the **PMNC** surrounding the piezoelectric fiber with respect to the principal material coordinate axes of the **SFFRC** varies over an annular cross section of the **PMNC** phase of the **RVE** of the **PCFF**. However, without loss of generality, the volume average of these location-dependent effective

elastic properties $\left[\overline{C}^{nc}\right]$ over the volume of the **PMNC** can be treated as the effective elastic properties $[C^{\text{PMNC}}]$ of the **PMNC** material surrounding the piezoelectric fiber with respect to the 1–2–3 coordinate axes of the **SFFRC** and is given by

$$\left[C^{\text{PMNC}}\right] = \frac{1}{\pi\left(R^2 - a^2\right)} \int_0^{2\pi} \int_a^R \overline{C}^{nc} r \, dr \, d\theta \tag{5.28}$$

in which a and R are the radii of the piezoelectric fiber and the **PCFF**, respectively. Thus, the effective constitutive relations for the **PMNC** material with respect to the principal material coordinate axes of the **SFFRC** can be expressed as

$$\left\{\sigma^{\text{PMNC}}\right\} = \left[C^{\text{PMNC}}\right]\left\{\in^{\text{PMNC}}\right\} \tag{5.29}$$

5.4.2 *Effective Elastic Properties of the PCFF*

The constructional feature of the **PCFF** shown in Fig. 5.6 can be viewed as a circular cylindrical fiber which has been cut from a lamina of the vertically reinforced 1–3 **PZC**. The reinforcement phase of such 1–3 **PZC** is the piezoelectric fiber and the matrix phase is composed of the homogenized **PMNC** material with its effective elastic properties given by Eq. (5.23). Thus, following the micromechanics model derived in Sect. 5.3 for the vertically reinforced 1–3 **PZC**, the constitutive relation for the converse piezoelectric effect in the **PCFF** can be derived as follows:

$$\left\{\sigma^{\text{PCFF}}\right\} = \left[C^{\text{PCFF}}\right]\left\{\in^{\text{PCFF}}\right\} - \left\{e^{\text{PCFF}}\right\}E_3 \tag{5.30}$$

in which the effective elastic coefficient matrix $[C^{\text{PCFF}}]$ and the effective piezoelectric coefficient matrix $\{e^{\text{PCFF}}\}$ of the **PCFF** are

$$\left[C^{\text{PCFF}}\right] = [C_9][V_{12}]^{-1} + [C_{10}][V_{11}]^{-1} \tag{5.31}$$

$$\left\{e^{\text{PCFF}}\right\} = \{e_1\} - [C_9][V_{12}]^{-1}[V_{10}][C_{12}]^{-1}\{e_2\} + [C_{10}][V_{11}]^{-1}[V_9][C_{11}]^{-1}\{e_2\} \tag{5.32}$$

The various matrices appearing in Eqs. (5.26) and (5.27) are

$$[C_9] = [C_1],\ [C_{11}] = [C_3],$$

$$[C_{10}] = \begin{bmatrix} C_{11}^{\text{PMNC}} & C_{12}^{\text{PMNC}} & C_{13}^{\text{PMNC}} & 0 & 0 & 0 \\ C_{12}^{\text{PMNC}} & C_{22}^{\text{PMNC}} & C_{23}^{\text{PMNC}} & 0 & 0 & 0 \\ V_{\text{PMNC}} C_{13}^{\text{PMNC}} & V_{\text{PMNC}} C_{23}^{\text{PMNC}} & V_{\text{PMNC}} C_{33}^{\text{PMNC}} & 0 & 0 & 0 \\ 0 & 0 & 0 & C_{44}^{\text{PMNC}} & 0 & 0 \\ 0 & 0 & 0 & 0 & C_{55}^{\text{PMNC}} & 0 \\ 0 & 0 & 0 & 0 & 0 & C_{66}^{\text{PMNC}} \end{bmatrix},$$

$$[V_9] = \begin{bmatrix} \overline{V}_p & 0 & 0 & 0 & 0 & 0 \\ 0 & \overline{V}_p & 0 & 0 & 0 & 0 \\ 0 & 0 & 1 & 0 & 0 & 0 \\ 0 & 0 & 0 & \overline{V}_p & 0 & 0 \\ 0 & 0 & 0 & 0 & \overline{V}_p & 0 \\ 0 & 0 & 0 & 0 & 0 & \overline{V}_p \end{bmatrix},$$

$$[V_{10}] = \begin{bmatrix} V_{\text{PMNC}} & 0 & 0 & 0 & 0 & 0 \\ 0 & V_{\text{PMNC}} & 0 & 0 & 0 & 0 \\ 0 & 0 & 0 & 0 & 0 & 0 \\ 0 & 0 & 0 & V_{\text{PMNC}} & 0 & 0 \\ 0 & 0 & 0 & 0 & V_{\text{PMNC}} & 0 \\ 0 & 0 & 0 & 0 & 0 & V_{\text{PMNC}} \end{bmatrix},$$

$$[C_{12}] = \begin{bmatrix} C_{11}^{\text{PMNC}} & C_{12}^{\text{PMNC}} & C_{13}^{\text{PMNC}} & 0 & 0 & 0 \\ C_{12}^{\text{PMNC}} & C_{22}^{\text{PMNC}} & C_{23}^{\text{PMNC}} & 0 & 0 & 0 \\ 0 & 0 & 1 & 0 & 0 & 0 \\ 0 & 0 & 0 & C_{44}^{\text{PMNC}} & 0 & 0 \\ 0 & 0 & 0 & 0 & C_{55}^{\text{PMNC}} & 0 \\ 0 & 0 & 0 & 0 & 0 & C_{66}^{\text{PMNC}} \end{bmatrix},$$

$$V_{\text{PMNC}} = 1 - \overline{V}_p,\ [V_{11}] = [V_{10}] + [V_9][C_{11}]^{-1}[C_{12}]$$

$$\text{and}\ \ [V_{12}] = [V_9] + [V_{10}][C_{12}]^{-1}[C_{11}] \tag{5.33}$$

It should be noted that here the piezoelectric fiber volume fraction $\overline{V}_p$ is based on the volume of the **RVE** of the **PCFF**.

5.4.3 *Effective Properties of the SFFRC*

The constructional feature of the **SFFRC** can also be viewed as a vertically reinforced 1–3 **PZC** in which the **PCFF** is the piezoelectric fiber reinforcement and the monolithic polymer is the matrix phase. Thus, replacing the piezoelectric fiber by the **PCFF** in the micromechanics model of the 1–3 **PZC** derived in Sect. 5.3, the micromechanics model of the converse piezoelectric effect in the **SFFRC** can be derived as follows:

$$\{\sigma\} = [C]\{\in\} - \{e\}E_3 \tag{5.34}$$

in which the effective elastic coefficient matrix $[C]$ and the effective piezoelectric coefficient matrix $\{e\}$ of the **SFFRC** are given by

$$[C] = [C_{13}][V_{16}]^{-1} + [C_{14}][V_{15}]^{-1} \tag{5.35}$$

$$\{e\} = \{e_3\} - [C_{13}][V_{16}]^{-1}[V_{14}][C_{16}]^{-1}\{e_4\} + [C_{14}][V_{15}]^{-1}[V_{13}][C_{15}]^{-1}\{e_4\} \tag{5.36}$$

The various matrices appearing in Eqs. (5.30) and (5.31) are

$$[C_{13}] = V_{\text{PCFF}}\begin{bmatrix} 0 & 0 & 0 & 0 & 0 & 0 \\ 0 & 0 & 0 & 0 & 0 & 0 \\ C_{13}^{\text{PCFF}} & C_{23}^{\text{PCFF}} & C_{33}^{\text{PCFF}} & 0 & 0 & 0 \\ 0 & 0 & 0 & 0 & 0 & 0 \\ 0 & 0 & 0 & 0 & 0 & 0 \\ 0 & 0 & 0 & 0 & 0 & 0 \end{bmatrix}, [C_{14}] = [C_2], [V_{14}] = [V_2],$$

$$[V_{13}] = \begin{bmatrix} V_{\text{PCFF}} & 0 & 0 & 0 & 0 & 0 \\ 0 & V_{\text{PCFF}} & 0 & 0 & 0 & 0 \\ 0 & 0 & 1 & 0 & 0 & 0 \\ 0 & 0 & 0 & V_{\text{PCFF}} & 0 & 0 \\ 0 & 0 & 0 & 0 & V_{\text{PCFF}} & 0 \\ 0 & 0 & 0 & 0 & 0 & V_{\text{PCFF}} \end{bmatrix},$$

$$[V_{15}] = [V_{14}] + [V_{13}][C_{15}]^{-1}[C_{16}], [V_{16}] = [V_{13}] + [V_{14}][C_{16}]^{-1}[C_{15}],$$

$$[C_{15}] = \begin{bmatrix} C_{11}^{\text{PCFF}} & C_{12}^{\text{PCFF}} & C_{13}^{\text{PCFF}} & 0 & 0 & 0 \\ C_{12}^{\text{PCFF}} & C_{22}^{\text{PCFF}} & C_{23}^{\text{PCFF}} & 0 & 0 & 0 \\ 0 & 0 & 1 & 0 & 0 & 0 \\ 0 & 0 & 0 & C_{44}^{\text{PCFF}} & 0 & 0 \\ 0 & 0 & 0 & 0 & C_{55}^{\text{PCFF}} & 0 \\ 0 & 0 & 0 & 0 & 0 & C_{66}^{\text{PCFF}} \end{bmatrix}, [C_{16}] = [C_4],$$

$$\{e_3\} = \begin{bmatrix} 0 & 0 & V_{\text{PCFF}}e_{33}^{\text{PCFF}} & 0 & 0 & 0 \end{bmatrix}^T \text{and} \{e_4\} = \begin{bmatrix} e_{31}^{\text{PCFF}} & e_{32}^{\text{PCFF}} & 0 & 0 & 0 & 0 \end{bmatrix}^T \tag{5.37}$$

5.5 Determination of Volume Fractions

Volume fraction of **CNT**s (V_{CNT}) in the **SFFRC** depends on the **CNT** diameter, the piezoelectric fiber diameter, and the surface to surface distance of two adjacent radially aligned **CNT**s at their roots. The surface to surface distance between the two adjacent **CNT**s at their roots is considered as 1.7 nm (Jiang et al. 2009). For fibers with circular cross section, it is well known that the hexagonal array of packing is the optimal packing of fibers and the corresponding maximum fiber volume fraction is 0.9069. Hence, for computing the numerical values of the effective properties of the **SFFRC**, the hexagonal packing array of the **PCFF**s is considered as shown in Fig. 5.8. It is also to be noted that the number of **CNT**s grown on the surface of the piezoelectric fibers imposes a constraint on the maximum value of V_{CNT}. Thus, one cannot arbitrarily assume the large value of V_{CNT}. Based on the hexagonal array of packing of the **PCFF**, the transverse cross section of the **RVE** of the **SFFRC** will be an equilateral triangle. Thus, the volume (V^{SFFRC}) of the **RVE** of the **SFFRC** is given by

$$V^{\mathrm{SFFRC}} = \frac{\sqrt{3}}{4} D^2 L \tag{5.38}$$

where D is the diameter of the **PCFF** and L is the length of the **RVE**. The volume (V^p) of the piezoelectric fiber is

$$V^p = \frac{\pi}{8} d^2 L \tag{5.39}$$

where d is the diameter of the piezoelectric fiber. Thus, the piezoelectric fiber volume fraction (V_p) in the **SFFRC** can be found as

$$V_p = \frac{V^p}{V^{\mathrm{SFFRC}}} = \frac{\pi}{2\sqrt{3}} \frac{d^2}{D^2} \tag{5.40}$$

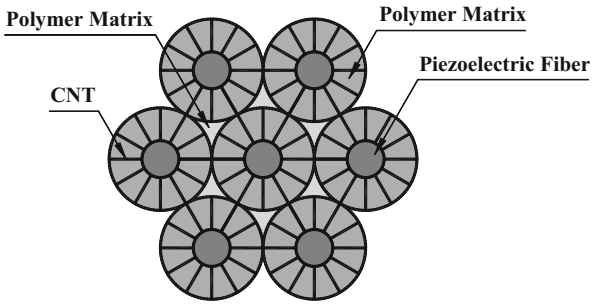

Fig. 5.8 Hexagonal array of packing for the **PCFF** fibers in **SFFRC**

Using Eqs. (5.34) and (5.35), the piezoelectric fiber volume fraction ($\overline{V}_p$) based on the volume of the **PCFF** can be determined as

$$\overline{V}_p = \frac{2\sqrt{3}}{\pi} V_p \tag{5.41}$$

Based on the surface to surface distance at the roots of the two adjacent **CNT**s and the **CNT** diameter, the maximum number of radially grown aligned **CNT**s ($N_{\text{CNT}}|_{\max}$) on the surface of the piezoelectric fiber can be determined as

$$N_{\text{CNT}}|_{\max} = \frac{\pi dL}{2\left(d_n + 1.7 \times 10^{-9}\right)^2} \tag{5.42}$$

where d_n is the diameter of **CNT**. Therefore, the volume of **CNT**s (V^{CNT}) present in the **RVE** is

$$V^{\text{CNT}} = \frac{\pi}{\pi} d_n^2 (R - a) N_{\text{CNT}}|_{\max} \tag{5.43}$$

Thus, the maximum volume fraction ($V_{\text{CNT}}|_{\max}$) of **CNT**s with respect to the volume of the **RVE** of the **SFFRC** is

$$V_{\text{CNT}}|_{\max} = \frac{V^{\text{CNT}}}{V^{\text{SFFRC}}} = \frac{\pi d_n^2}{2\left(d_n + 1.7 \times 10^{-9}\right)^2} \left(\sqrt{\frac{\pi V_p}{2\sqrt{3}}} - V_p \right) \tag{5.44}$$

Finally, the maximum volume fraction ($V_{nt}|_{\max}$) of the **CNT**s with respect to the volume of the **PMNC** can be determined as follows:

$$V_{nt}|_{\max} = \frac{V^{\text{CNT}}}{V^{\text{PMNC}}} = \frac{2\sqrt{3}}{\pi - 2\sqrt{3} V_p} V_{\text{CNT}}|_{\max} \tag{5.45}$$

5.6 Numerical Example

An example of the **SFFRC** is considered for presenting the numerical estimation of its effective properties. The **SFFRC** considered here is composed of epoxy, **PZT5** fiber, and armchair **CNT**s. The material properties of these constituent phases are listed in Table 5.1.

It is evident from Eq. (5.39) that when V_p is zero, V_{CNT} is zero. Also, when $V_p = \pi/2\sqrt{3}$, i.e., **PMNC** is absent, the value of V_{CNT} is also zero. Thus, the maximum value of V_{CNT} given by Eq. (5.39) will be maximized at a particular value of V_p. Figure 5.9 illustrates the variation of the maximum volume fraction of

Table 5.1 Material properties of the constituent phases of **SFFRC**

Material	C_{11} (GPa)	C_{12} (GPa)	C_{23} (GPa)	C_{33} (GPa)	C_{55} (GPa)	e_{31} (Cm^{-2})	e_{33} (Cm^{-2})	(nm)
CNT (5, 5) Shen and Li (2004)	2143.4	184.4	404	668	791	–	–	$d_n = 0.678$
CNT (10, 10) Shen and Li (2004)	1088.4	87.8	254		442	–	–	$d_n = 1.356$
CNT (20, 20) Shen and Li (2004)	545	43.52	134	138	227	–	–	$d_n = 2.712$
PZT5 Smith and Auld (1991)	121	75.4	75.2	111	21.1	−5.4	15.8	–
Epoxy Smith and Auld (1991)	5.3	3.1	3.1	5.3	0.64	–	–	–

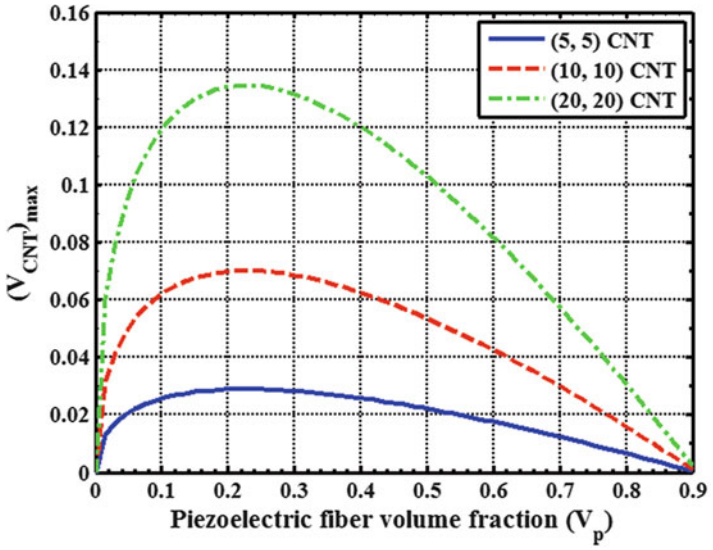

Fig. 5.9 Variation of the maximum value of **CNT** volume fraction with the piezoelectric fiber volume fraction in **SFFRC**

CNTs in the **SFFRC** with respect to V_p. It may be observed from this figure that the maximum values of V_{CNT} for different **CNT** diameters are almost independent of the **CNT** diameter and are maximized at $V_p = 0.24$. Few graphical results are presented in Figs. 5.10, 5.11, 5.12, 5.13, and 5.14. While estimating the effective properties shown in Figs. 5.10, 5.11, 5.12, 5.13, and 5.14, the maximum value of

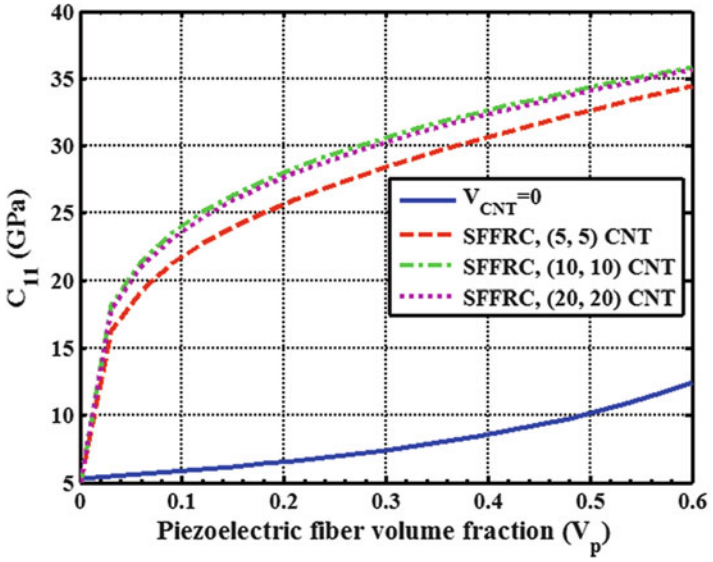

Fig. 5.10 Effective elastic coefficient C_{11} of the **SFFRC**

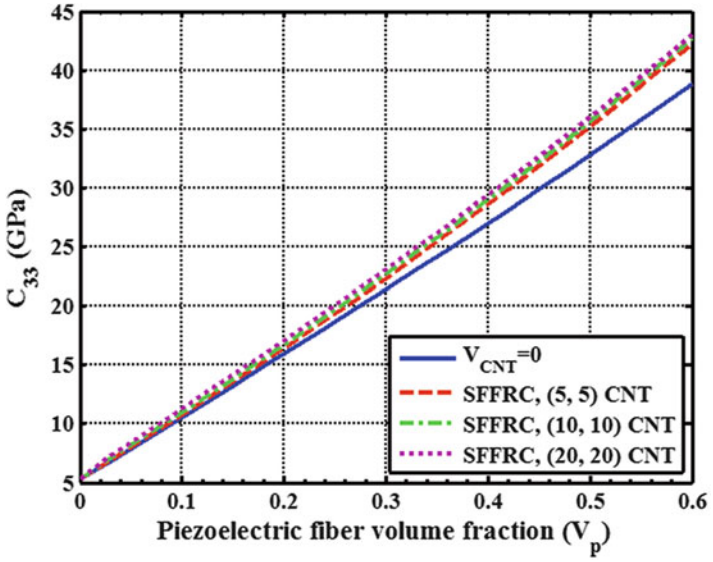

Fig. 5.11 Effective elastic coefficient C_{33} of the **SFFRC**

V_{CNT} for a particular value of V_p is used from Eq. (5.39). First the effective properties of the **PMNC** are computed using Eq. (5.23). Using the results obtained by Eq. (5.23), effective properties of the **PCFF** are evaluated from Eqs. (5.26) and

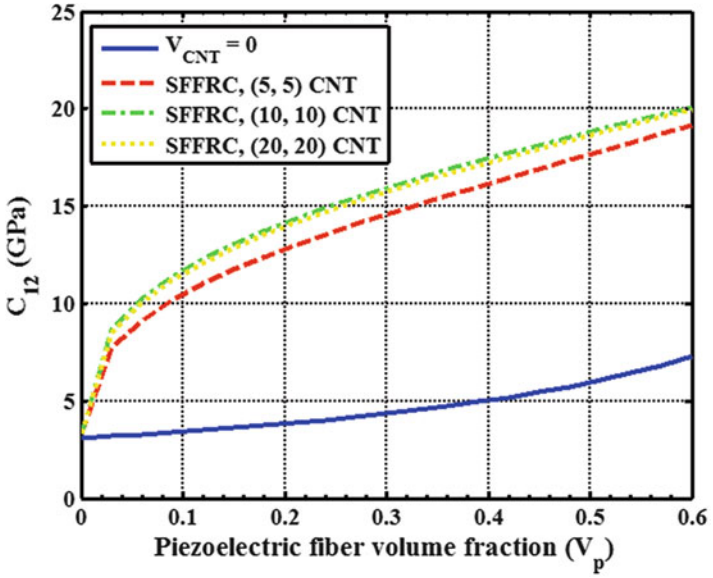

Fig. 5.12 Effective elastic coefficient C_{12} of the **PFFRC**

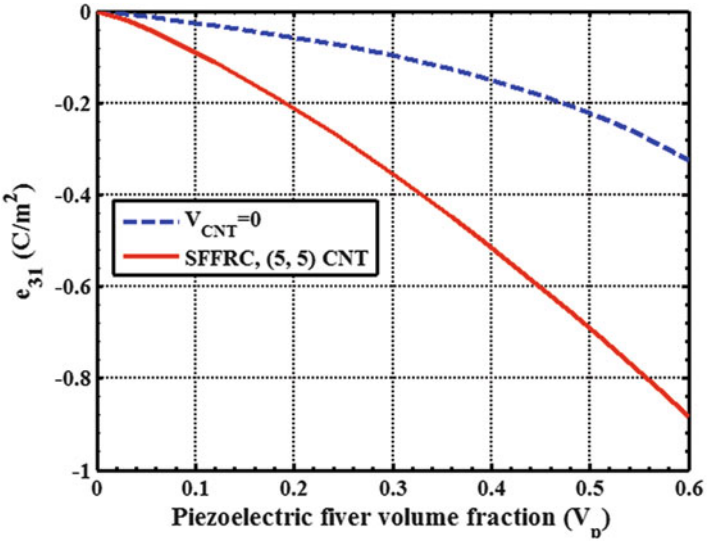

Fig. 5.13 Effective in-plane piezoelectric coefficient e_{31} of the **SFFRC**

(5.27). Finally, Eqs. (5.30) and (5.31) are used to estimate the effective properties of the **SFFRC**. Figure 5.10 illustrates the variation of the effective in-plane elastic coefficient C_{11} of the **SFFRC** with the piezoelectric fiber volume fraction V_p. It

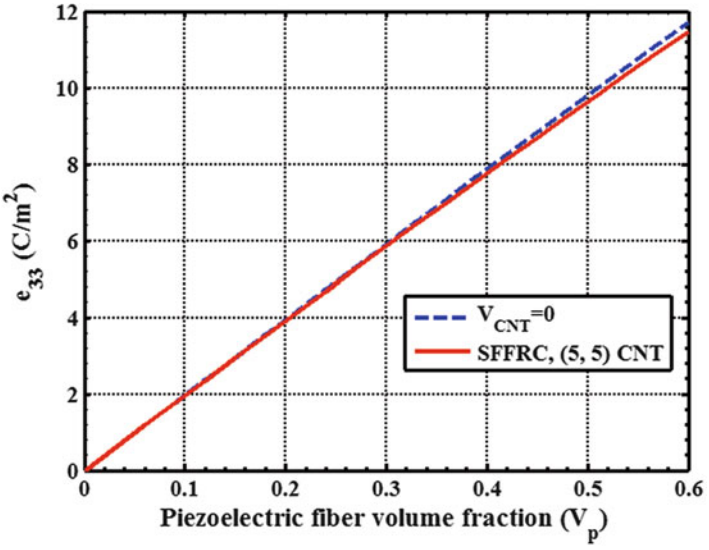

Fig. 5.14 Effective piezoelectric coefficient (e_{33}) of the **SFFRC**

may be observed from Fig. 5.10 that the effective value of C_{11} of the **PFFRC** is significantly larger than that of the existing 1–3 **PZC** without having **CNT**s.

This is attributed to the fact that the radially grown **CNT**s strengthen the matrix surrounding the piezoelectric fiber along 1- or 1′-direction. Figure 5.11 illustrates the variation of the transverse effective elastic coefficient C_{33} of the **SFFRC** with the piezoelectric fiber volume fraction V_p. It is important to note from this figure that the radially grown **CNT**s on the surface of the piezoelectric fibers do not appreciably affect the magnitude of the effective transverse elastic coefficient C_{33} when compared with that of the existing 1–3 **PZC** without **CNTs**. This is attributed to the fact that the **CNT**s are grown transverse to the piezoelectric fiber and the elastic properties of **CNT** transverse to its axis (i.e., along 3-direction) are much less than those along its axis. Radially grown **CNT**s also significantly improve the other effective elastic coefficient C_{12} of the **SFFRC** as shown in Fig. 5.12. It is also to be noted from Figs. 5.10, 5.11, and 5.12 that the **CNT** diameter marginally influences the effective elastic properties of the **SFFRC**. Figure 5.13 illustrates the variation of the effective in-plane piezoelectric coefficient e_{31} of the **SFFRC**. It can be observed from this figure that for $V_p = 0.6$, the magnitude of e_{31} of the **SFFRC** is almost three times that of the existing 1–3 **PZC** without containing **CNT**s. This enhancement of the in-plane piezoelectric coefficient is attributed to the in-plane stiffening of the polymer matrix surrounding the piezoelectric fiber by radially grown aligned **CNT**s. The other in-plane effective piezoelectric coefficient e_{32} is found to be identical to e_{31}. It is because that the **SFFRC** is transversely isotropic. Figure 5.14 illustrates the variation of the effective transverse piezoelectric coefficient e_{33} of the **SFFRC** with the piezoelectric fiber volume fraction. It is important

to note from this figure that the radially grown **CNT**s on the surface of the piezoelectric fibers negligibly affect the magnitude of the effective piezoelectric coefficient e_{33} when compared with that of the 1–3 **PZC** without **CNT**s.

References

Aboudi, J., Arnold, S.M., Bednarcyk, B.A.: Micromechanics of composite materials. Academic Press, New York (2013)

Bailey, T., Hubbard, J.E.: Distributed piezoelectric polymer active vibration control of a cantilever beam. AIAA J. Guid. Contr. **8**, 605–611 (1985)

Baz, A., Poh, S.: Performance of an active control system with piezoelectric actuators. J. Sound Vib. **126**, 327–343 (1988)

Bower, C., Zhu, W., Jin, S., Zhou, O.: Plasma-induced alignment of carbon nanotubes. Appl. Phys. Lett. **77**, 830–832 (2000)

Bruke, S.E., Hubbard, J.E.: Active vibration control of a simply supported beam using a spatially distributed actuator. IEEE Contr. Syst. Mag. **8**, 25–30 (1987)

Chatzigeorgiou, G., Seidel, G.D., Lagoudas, D.C.: Effective mechanical properties of fuzzy fiber composites. Compos. B **43**, 2577–2593 (2012)

Chee, C., Tong, L., Steven, G.P.: Piezoelectric actuator orientation optimization for static shape control of composite plates. Compos. Struct. **55**, 169–184 (1999)

Cheng, H.C., Liu, Y.L., Hsu, Y.C., Chen, W.H.: Atomistic-continuum modeling for mechanical properties of single-walled carbon nanotubes. Int. J. Solid. Struct. **46**, 1695–1704 (2009)

Crawley, E.F., Luis, J.D.: Use of piezoelectric actuators as elements of ontelligent structures. AIAA J. **27**, 1801–1807 (1987)

Dhala, S., Ray, M.C.: Micromechanics of piezoelectric fuzzy fiber-reinforced composites. Mech. Mater. **81**, 1–17 (2015)

Forward, R.L.: Electronic damping of orthogonal bending modes in a cylindrical mast-experiment. J. Spacecraft Rocket. **18**, 11–17 (1981)

Gao, X.L., Li, K.: A shear-lag model for carbon nanotube reinforced polymer composites. Int. J. Solid. Struct. **42**, 1649–1667 (2005)

Gracia, E.J., Wardle, B.L., Hart, A.J., Yamamoto, N.: Fabrication and multifunctional properties of a hybrid laminate with aligned carbon nanotubes grown in situ. Compos. Sci. Technol. **68**, 2034–2041 (2008)

Griebel, M., Hamaekers, J.: Molecular dynamics simulations of the elastic moduli of polymer–carbon nanotube composites. Comput. Meth. Appl. Mech. Eng. **193**, 1773–1788 (2004)

Ha, S.K., Keilers, C., Chang, F.K.: Finite element analysis of composite structures containing distributed piezoceramic sensors and actuators. AIAA J. **30**, 772–780 (1992)

Iijima, S.: Helical microtubules of graphitic carbon. Nature **354**, 56–58 (1991)

Im, S., Atluri, S.N.: Effects of piezoactuator on a finitely deformed beam subjected to general loading. AIAA J. **25**, 1373–1385 (1989)

Jiang, B., Liu, C., Zhang, C., Liang, R., Wang, B.: Maximum nanotube volume fraction and its effect on overall elastic properties of nanotube-reinforced composites. Composites B **40**, 212–217 (2009)

Kundalwal, S.I., Ray, M.C.: Micromechanical analysis of fuzzy fiber reinforced composites. Int. J. Mech. Mater. Des. **7**, 149–166 (2011)

Kundalwal, S.I., Ray, M.C.: Effective properties of a novel composite reinforced with short carbon fibers and radially aligned carbon nanotubes. Mech. Mater. **53**, 47–60 (2012)

Lanzara, G., Chang, F.K.: Design and characterization of a carbon-nanotube-reinforced adhesive coating for piezoelectric ceramic discs. Smart Mater. Struct. **18**, 125001 (2009)

Lin, C., Hsu, C., Huang, H.N.: Finite element analysis on deflection control of plates with piezoelectric actuators. Compos. Struct. **35**, 423–433 (1996)
Mathur, R.B., Chatterjee, S., Singh, B.P.: Growth of carbon nanotubes on carbon fiber substrates to produce hybrid/phenolic composites with improved mechanical properties. Compos. Sci. Technol. **68**, 1608–1615 (2008)
Miller, S.E., Hubbard, J.E.: Observability of a Bernoulli-Euler beam using PVF2 as a distributed sensor. MIT Draper Laboratory Report (1987)
Newnham, R.E., Shinner, D.P., Cross, L.E.: Connectivity and piezoelectric-pyroelectric composites. Mater. Res. Bull. **13**, 525–536 (1978)
Odegard, G.M., Gates, T.S., Wise, K.E., Park, C., Siochi, E.J.: Constitutive modeling of nanotube-reinforced polymer composites. Compos. Sci. Technol. **63**, 1671–1687 (2003)
Ray, M.C.: Concept of a novel hybrid smart composite reinforced with radially aligned zigzag carbon nanotubes on piezoelectric fibers. Smart Mater. Struct. **19**, 035008 (2010)
Ray, M.C., Faye, A.: Theoretical and experimental investigations on active structural-acoustic control of thin isotropic plate using vertically reinforced 1-3 piezoelectric composite. Smart Mater. Struct. **18**, 015012 (2009)
Ray, M.C., Pradhan, A.K.: On the use of vertically reinforced 1-3 piezoelectric composites for hybrid damping of laminated composite plates. Mech. Adv. Mater. Struct. **15**, 245–261 (2007)
Ray, M.C., Bhattacharyya, R., Samanta, B.: Static analysis of an intelligent structure by the finite element method. Comput. Struct. **52**, 617–631 (1994)
Saravanos, D.A., Hetliger, P.R., Hopkins, D.A.: Layerwise mechanics and finite element for the dynamic analysis of piezoelectric composite plates. Int. J. Solid. Struct. **34**, 359–378 (1997)
Seidel, G.D., Lagoudas, D.C.: Micromechanical analysis of the effective elastic properties of carbon nanotube reinforced composites. Mech. Mater. **38**, 884–907 (2004)
Shadlou, M.R., Shokrieh, S., Ayatollahi, M.M.: Multiscale modeling for mechanical properties of carbon nanotube reinforced nanocomposites subjected to different types of loading. Compos. Struct. **93**, 2250–2259 (2011)
Shen, L., Li, J.: Transversely isotropic elastic properties of single-walled carbon nanotubes. Phys. Rev. B **69**, 045414 (2004)
Smith, W.A., Auld, B.A.: Modeling 1-3 composite piezoelectrics: thickness mode oscillations. IEEE Trans. Ultrason. Ferroelectr. Freq. Control **31**, 40–47 (1991)
Sohn, J.W., Choi, S.B., Lee, C.H.: Active vibration control of smart hull structure using piezoelectric actuator. Smart Mater. Struct. **18**, 074004 (2009)
Suresh Kumar, R., Ray, M.C.: Active control of geometrically nonlinear vibrations of doubly curved smart sandwich shells using 1-3 piezoelectric composites. Compos. Struct. **105**, 173–187 (2012)
Thostenson, E.T., Chou, T.W.: On the elastic properties of carbon nanotubes based composites: modelling and characterization. J. Phys. D Appl. Phys. **36**, 573–582 (2003)
Treacy, M.M.J., Ebbessen, T.W., Gibson, J.M.: A Exceptionally high Young's modulus observed for individual carbon nanotube. Nature **381**, 678–680 (1996)
Varadarajan, S., Chandrashekhara, K., Agarwal, S.: LQG/LTR-based robust control of composite beams with piezoelectric devices. J. Vib. Control. **6**, 607–630 (2000)
Zhang, Q., Qian, W., Xiang, R., Yang, Z., Luo, G., Wang, Y., Wei, F.: In situ growth of carbon nanotubes on inorganic fibers with different surface properties. Mater. Chem. Phys. **107**, 317–321 (2008)

Chapter 6
Composite Nanowires for Room-Temperature Mechanical and Electrical Bonding

Yanbin Cui and Yang Ju

Abstract At millimeter dimension or less, the conventional bonding technology in electronic assembly relies heavily on reflow soldering and suffers from severe performance and reliability degradation. Meanwhile, the traditional high temperature bonding process (easily reach 220 °C) tends to result in undesired thermal damage and residual stress at the bonding interface. It is therefore a major challenge to find a means to preparing room-temperature connectors or fasteners with good mechanical and electrical bonding. Very recently, composite nanowires have been used to fabricate room-temperature fasteners. In this chapter, we summarize the state-of-the-art progress on the use of composite nanowires for room-temperature mechanical and electrical bonding. Using anodic aluminum oxide (AAO) and polycarbonate (PC) membrane as templates, the fabrication of Cu/parylene and Cu/polystyrene nanowires was described, while the fabrication of carbon nanotube (CNTs) array used to connect with Cu/parylene nanowires was also introduced. Finally, the performances of the composite nanowires (Cu/parylene, Cu/polystyrene, and CNT-Cu/parylene) used as surface fastener for room-temperature mechanical and electrical bonding were demonstrated.

6.1 Introduction

Surface mount devices (SMDs) relies heavily on reflow soldering and has become the cornerstone of today's electronic industry. The heating temperatures of traditional reflow soldering technique can easily reach 220 °C during reflow soldering, which may not only cause energy consumption but also thermal damage to the

Y. Cui
State Key Laboratory of Multiphase Complex System, Institute of Process Engineering, Chinese Academy of Sciences, Beijing 100190, China
e-mail: ybcui@ipe.ac.cn

Y. Ju (✉)
Department of Mechanical Science and Engineering, Nagoya University, Nagoya 464-8603, Japan
e-mail: ju@mech.nagoya-u.ac.jp

S.A. Meguid (ed.), *Advances in Nanocomposites*,
DOI 10.1007/978-3-319-31662-8_6

surface mount components. Additionally, the toxicity of traditional Sn-Pb solder has led to a trend of worldwide legislation that mandates the removal of lead from electronics. Although various types of lead-free solder have been proposed and adopted in the electronics industry, the melting points of these lead-free solders are always 5–20 °C higher than Sn-Pb solder. Moreover, the recycling of rare metals in the surface mount components and printed circuit boards is not easy due to the difficulties in detaching the components, circuit boards, and solder materials (Ju et al. 2012). On the other hand, the continuous trend toward miniaturization and functional density enhancement makes it necessary to improve the bonding technology in surface mount technology (SMT). At millimeter dimensions or less, conventional electrical connectors or fasteners tend to suffer from severe performance and reliability degradation (Cui et al. 2014a). It is therefore a major challenge to find a nontoxic and room-temperature bonding technique that afford good mechanical bonding as well as electrical contact; especially for micro/nano-electronic circuits and flexible electronic devices.

With regard to developing a room-temperature bonding technique for SMT, one possible approach is to make use of cold welding. Cold welding of thin gold films on elastomeric supports has been carried out under ambient conditions and low loads (Ferguson et al. 1991). However, only the lower limit of approximately 0.1 N/cm^2 was reported for the adhesion strength. Besides, many researchers have also succeeded in joining individual nanostructures by nanoscale-welding method (Dong et al. 2006; Jin et al. 2008; Peng et al. 2008). Although direct heating was not performed and large forces were not applied in these nanoscale-welding techniques, fine manipulation of an individual nanowire or nanotube by specific equipment was always necessary. Therefore, these nanoscale-welding techniques, in which the connection between two nanowires or nanotubes was performed, are suitable for nanoscale connection but inefficient for the mass production of SMDs.

Recently, hybrid core/shell nanowire forests have been used to fabricate electrical and chemical connectors (Ko et al. 2009; Kapadia et al. 2009). Specifically, we prepared a serial of nanowire (including metallic and hybrid core/shell nanowire arrays) and carbon nanotube (CNT) arrays, in which the nanowire and CNT arrays were used as a fastener for SMT (Cui et al. 2014a, b; Ju et al. 2012; Teshima et al. 2014; Wang et al. 2013a, b, 2015). For SMT, the fastener should ideally have both high adhesion strength and provide a good electrical connection. In this chapter, we summarize the state of the art concerning the use of composite nanowires for room-temperature mechanical and electrical bonding. First, the fabrication of anodic aluminum oxide (AAO) membrane, which used for the growing Cu nanowires, is presented. Then, using AAO and polycarbonate (PC) membrane as templates, the synthesis of copper/parylene and copper/polystyrene composite nanowires are described and discussed. While, the fabrication of carbon nanotube (CNTs) array used to connect with Cu/parylene nanowires is also introduced. Lastly, the performances of the composite nanowires used as surface fastener for room-temperature mechanical and electrical bonding are demonstrated.

6.2 Fabrication of Anodic Aluminum Oxide Membrane

Anodic aluminum oxide (AAO) nanoporous membrane is popular for its self-organized nanostructure. Due to its highly ordered porous structure, significant thermal stability, and cost-effectiveness (Woo et al. 2005; Li et al. 2005), AAO membranes are widely used for the fabrication of nanowires and nanotube arrays to be utilized as filters, sensors, catalysts, and solar cells, among others (Woo et al. 2005; Gorokh et al. 2006; Attaluri et al. 2009; Wei et al. 2008; Zhiyong et al. 2009). Since Masuda and Fukuda (1995) introduced two-step anodization, the AAO got more attention from nanotechnology community. In order to produce highly ordered nanopore structures, a significant number of studies concerned with process parameters had been carried out. By changing the anodizing parameters (such as electrolytes, anodizing voltage, anodizing time, temperature, and etching methods), the structure of AAO (such as pore size, pore depth, interpore distance, thickness of membrane, and pore geometry) can be easily controlled (Crouse et al. 2000; Gâlcă et al. 2003; Chu et al. 2005; Kasi et al. 2012). AAO templates exhibit columnar pore structure, vertical to the substrate and parallel to each other with pore diameters from several tens to hundreds nanometers and with an aspect ratio between 10 and 1000 or more (Crouse et al. 2000; Chen et al. 2003; Pu et al. 2004). By filling the pores of the AAO templates, arrays of well-aligned nanowires or other 1D nanostructures with uniform diameter and length can be obtained using electroplating or other growth methods (Yan et al. 2007).

In general, a two-step anodization method was employed to produce well-arranged porous AAO template (Masuda and Fukuda 1995). Typical fabrication processes of the AAO template are shown in Fig. 6.1. Appropriate electrolyte solution (such as oxalic acid) was used for the anodization. The pretreated

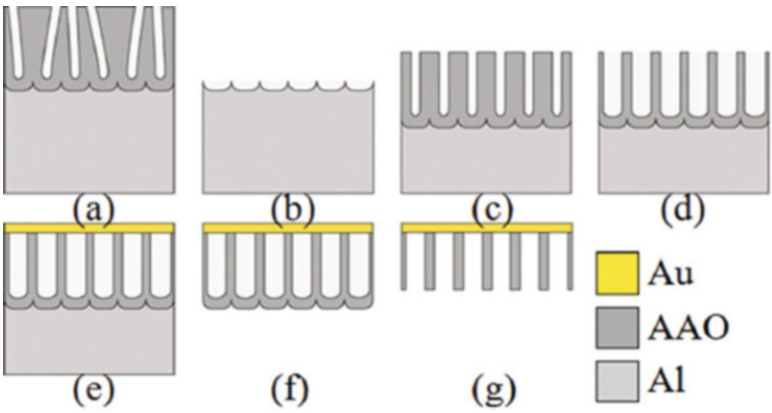

Fig. 6.1 Schematic of fabricating the AAO: (**a**) a first-step anodization, (**b**) wet etching of AAO fabricated in a first-step anodization, (**c**) a second-step anodization, (**d**) extending the pores, (**e**) sputtering Au film, (**f**) dissolving aluminum substrate, and (**g**) dissolving barrier layer and extending pores (Teshima et al. 2014)

aluminum foils were anodized in electrolyte solution under constant voltage at room temperature. At the first anodization step, the alumina layer fabricated was dissolved by wet chemical etching in a mixture of 6 wt% phosphoric acid and 1.5 wt% chromic acid solution for 30 min at 60 °C. The resulting inner aluminum foils have uniform concave nanoarray, which is crucial to achieving ordered pore size distribution (Belwalkar et al. 2008). After removal, the second anodization step was carried out at the same condition. After the two-step anodization process, the remaining aluminum on the AAO was dissolved in the solution made up of one part by volume of 0.1 mol/L $CuCl_2$ solution and four parts by volume of 10 wt% HCl (Belwalkar et al. 2008). Finally, the oxide barrier layer of the AAO was removed and the pores were enlarged by floating the sample on the surface of 0.5 mol/L phosphoric acid solution at room temperature using to the surface tension of the AAO (Cui et al. 2012).

It is well known that the value of the anodizing voltage for preparing the best nanopore order in self-ordered AAO is different for each electrolyte (Zaraska et al. 2011). For instance, in sulfuric acid, oxalic acid, and phosphoric acid, anodizing voltages were 25, 40, and 195 V, respectively. If a higher anodizing voltage is applied, then the higher current density and Joule heating generation will cause damage or lead to the collapse of the pore structure. In practice, a higher potential is beneficial in increasing the pore size. Chung et al. (2013) proposed a high-potential hybrid pulse anodization (HPA) technique to resolve this problem. In HPA technique, a period of small negative potential is applied to suppress the Joule heating effect during the AAO preparation process. The scanning electron microscope (SEM) results showed that HPA with an anodizing potential of 60 V resulted in an intact pore structure on the AAO surface (Fig. 6.2). By contrast, the AAO formed using conventional direct current anodization (DCA) with the same anodizing potential contained many small irregular pores around each original pore (Fig. 6.2a) (Chung et al. 2013). On the other hand, it is clearly seen that the reduction of the irregular small branch pores in AAO formed by HPA, as shown in Fig. 6.2b. Chung et al. (2011) also found that the HPA technique not only merits manufacturing convenience and cost reduction but also promotes pore distribution

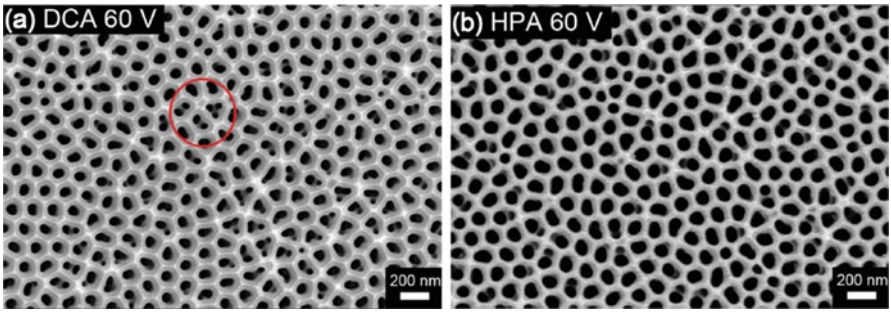

Fig. 6.2 Top-view SEM micrographs of AAO nanostructures formed by (**a**) DCA 60 V, (**b**) HPA 60 V with following pore widening for 10 min (Chung et al. 2013)

uniformity of AAO at severe conditions of low-purity Al foils and relatively high room temperature. The pore distribution uniformity can be improved by HPA compared with the DCA. Very good AAO distribution uniformity (91 %) was achieved in high-purity aluminum foil by HPA. This is because it can suppress the heating effect to diminish the dissolution reaction (Chung et al. 2011).

Controlling the size and uniformity of the pores is the key in manipulating the structure and properties of the materials confined within the pores of AAO. Kim et al. (2007) reported a new approach for preparing pretextured surface patterns on aluminum using solvent-dependent differential swelling of block copolymers. Long-range order in a hexagonal-packed monolayer was created using solvent-induced ordering of poly (styrene-b-4-vinylpyridine) (PS-b-P4VP) micellar films, followed by surface reconstruction to make nanoporous patterns. Using reactive ion etching (RIE), patterns were transferred to the Al surface. Subsequent anodization in concentrated sulfuric acid enabled the formation of channels with long-range lateral order. Highly ordered porous alumina with a hole interval of 45 nm and a hole size of 12 nm was produced (Fig. 6.3) (Kim et al. 2007).

Besides, ultrathin AAO membranes were also be used as masks for the fabrication of nanoparticle arrays on different surfaces. The AAO membranes can be formed directly on some surfaces, such as silicon and indium tin oxide. Typically, a thin layer of Al is deposited on these substrates, and nanoporous masks are fabricated by the anodization of this layer (Chu et al. 2001; Mao et al. 2009). Pastore et al. (2011) fabricated ultrathin AAO membranes by applying low anodization voltages that provide low reaction speed during AAO formation. A low anodization speed is required to obtain membrane thickness below 100 nm in a reproducible manner. With this procedure, AAO membranes with pore diameters below 20 nm and membrane thickness below 70 nm were obtained (Pastore et al. 2011).

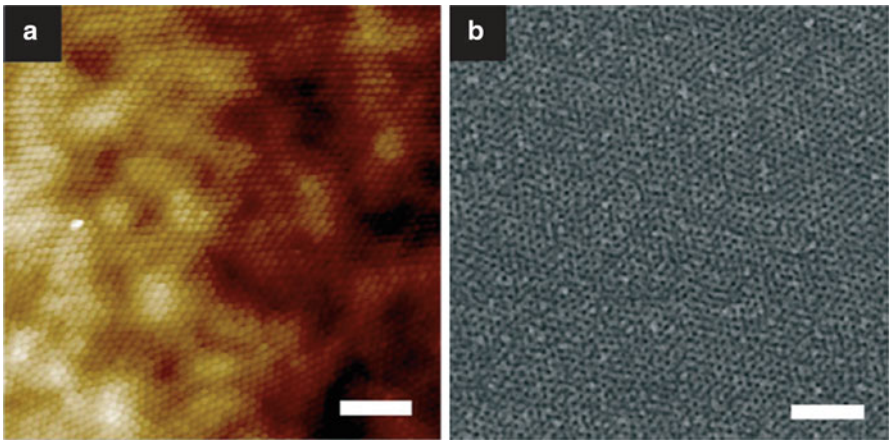

Fig. 6.3 Scanning force microscopy (SFM) image of surface view of anodized Al in 2.5 M sulfuric acid at 19 V at 48 °C for 10 min (**a**) and SEM image of anodized Al after pore widening carried out in 5 wt% phosphoric acid at 20 °C for 5 min (**b**). (Scale bar: 200 nm.) (Kim et al. 2007)

6.3 Synthesis of Copper/Parylene Composite Nanowires

Due to its ability to control nanomaterial shape, size, and uniformity, template-assisted synthesis has attracted considerable attention and proved to be a simple and versatile approach for preparing ordered nanowire, nanorod, nanoparticle, and nanodot arrays in a wide range of materials (Huczko 2000; Xu et al. 2010). Numerous nanomaterials have been prepared by utilizing hard templates such as track-etched polycarbonate (PC) membranes (Demoustier 2001), AAO templates (Ding et al. 2006; Wei et al. 2005), and soft templates such as polymers (Sumikura et al. 2008) and surfactants (Bakshi et al. 2007). On the other hand, various techniques, such as chemical vapor deposition (Venkatasubramanian et al. 2001), molecular beam epitaxy (Harman et al. 1999), vapor–liquid–solid growth process (Li et al. 2003), and hydrothermal process (Li et al. 2001), have been applied to synthesize nanowire- and/or nanotube-structured materials. Compared to those methods, electrodeposition is one the most cost-effective techniques to fabricate the nanostructured materials (Feng et al. 2008). Therefore, directional growth of nanowires/rods/pillars through PC or AAO templates via electrodeposition process is a very popular method because of its inexpensive, simple technique and ability to incorporate complex geometrical structures and easy tenability of the nanopores' dimensions (also nanowires/rods' dimension) by controlling the deposition parameters (Joo and Banerjee 2010).

Recently, Ge/parylene core/shell nanowire array was used as an electrical connector after the deposition of an Ag film with relatively high shear adhesion strength (Kapadia et al. 2009). In addition, Ni and Cu nanowire arrays have been found to have very low electrical resistance (Baek and Fearing 2009; Xu et al. 2012). Specially, nanowire surface fasteners based on gold and copper nanowire arrays were also proposed (Ju et al. 2012; Wang et al. 2013a), with relatively low electrical resistance and adhesion strengths. However, the maximum adhesion strength of the metallic nanowire surface fastener is only 8.17 N/cm^2. Therefore, it is still a challenge to achieve high adhesive strength and low electrical resistance at the same time for room-temperature surface fastener. In order to improve the performance of nanowire surface fastener, copper/parylene core/shell nanowire surface fastener was fabricated (Wang et al. 2013b). Compared with metallic nanowire surface fastener, the adhesion strength increased dramatically.

A peculiar cell (Fig. 6.4) was used to fabricate freestanding copper nanowire on the substrate directly. The introduced porous glass and porous cellulose membrane have three important functions. First, the capillary forces provided by the porous glass plate and the porous cellulose membrane help maintain a continuous electrolyte flow from the bulk of the electrolyte to PC membrane (Taberna et al. 2006). Second, the stiffness of porous glass plate ensures the contact of the substrate with PC membrane. Third, the compliance of the porous cellulose membrane offers a buffer and ensures a tight contact of the substrate with PC membrane. It is known that for flat anodes the metal is deposited preferentially at the outer border areas of the cathode (Wang et al. 2013b). This effect was avoided by using a conical copper anode, leading to a noticeably more homogeneous copper nanowire distribution

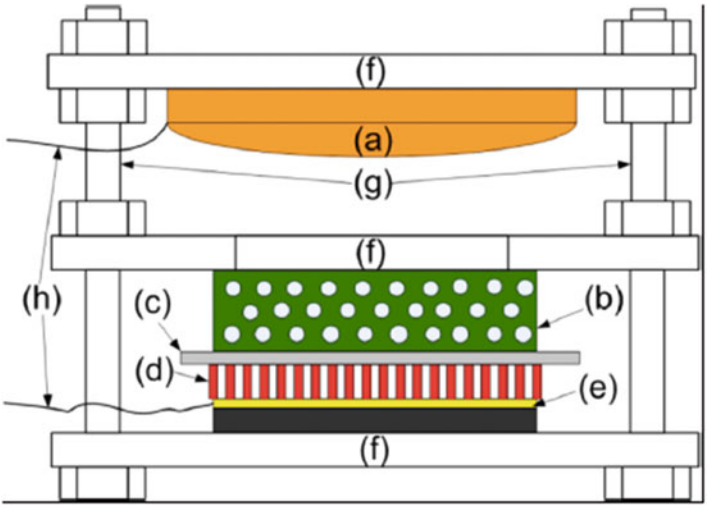

Fig. 6.4 Schematic of the cell for copper nanowire fabrication: (**a**) conical copper anode, (**b**) porous glass plate, (**c**) cellulose membrane, (**d**) polycarbonate template, (**e**) glass substrate with gold film, (**f**) isolation holder, (**g**) screw and nut, and (**h**) copper wire (Wang et al. 2013b)

over the whole cathode surface (Tomil et al. 2001). Before and after the assembly of the cell, two additional immersions were introduced to ensure an even copper ion density throughout the PC membrane (Millipore) (Wang et al. 2013b). Copper nanowire arrays were then synthesized by electrodeposition under a constant current. The electrodeposition electrolyte used was a 0.4 M $CuSO_4 \cdot 5H_2O$ solution, adjusted to pH 2 with sulfuric acid. The electrodeposition was performed at room temperature and without stir. After etching in methylene chloride to remove the PC membrane, the freestanding copper nanowire arrays on the substrate were obtained. Then, a thin film of Parylene C was deposited on copper nanowire arrays by using a DACS-LAB deposition system. The typical deposition conditions were 160 °C for the evaporation of the parylene dimer precursor, 650 °C for the pyrogenic decomposition of the dimer into monomers, and 60 mTorr for the vacuum chamber. Through controlling the amount of the loaded precursor, the corresponding thickness of parylene shell was obtained.

The fabrication procedure of the copper/parylene core/shell nanowire surface fastener is outlined in Fig. 6.5a. At first, copper nanowires were grown on glass/Cr/Au substrates by the template-assisted electrodeposition method. After etching the PC template, a thin layer of Parylene C was evenly deposited on the copper nanowires to enhance the adhesive ability of nanowire surface fastener. The SEM image of the copper nanowire arrays with an average diameter of 150 nm (Fig. 6.5b) indicates that most of the nanowires were grown vertically on the substrate, but oriented in a wide range of directions. Figure 6.5c, d show the SEM image of copper nanowires with a 100 and 200 nm parylene coating, respectively. Clearly, the grown copper nanowires sustain their high aspect ratio without aggregation, due to the high Young's modulus of the copper (110 GPa).

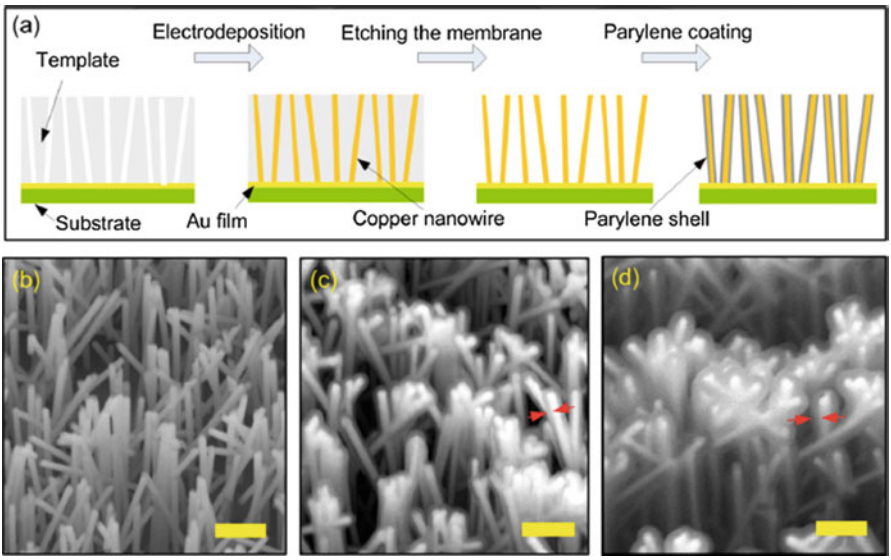

Fig. 6.5 (**a**) The fabrication process of copper/parylene core/shell nanowire. SEM images of copper nanowires (**b**) without parylene coating, (**c**) with 100 nm parylene coating, and (**d**) with 200 nm parylene coating. The *red arrows* in (**c**) and (**d**) indicate the parylene shell. The scale bar is 1 μm (Wang et al. 2013b)

6.4 Synthesis of Copper/Polystyrene Composite Nanowires

To further improve the performance of nanowire surface fastener, a copper/polystyrene core/shell nanowire surface fastener was prepared, which shows higher adhesion strength and a much lower electrical resistance than copper/parylene core/shell nanowire surface fastener (Wang et al. 2014, 2015).

The fabrication procedure of the copper/polystyrene core/shell nanowire surface fastener is shown in Fig. 6.6. The AAO membranes (Synkera Company) with a nominal pore diameter of ~80 nm and interpore distance of ~240 nm were used as templates for the synthesis of polystyrene nanotubes. These open-ended nanotubes were synthesized into the AAO template by spin-casting method (Jin et al. 2012; Wang et al. 2014). Briefly, a polymer solution (~20 μl of 2.5 wt% polystyrene solution in toluene) was directly loaded over the spinning AAO template. After 90 s of spinning, the toluene was evaporated and then the polystyrene nanotubes were formed in the template. The thickness of polystyrene nanotube can be controlled through adjusting the loaded times. After the formation of nanotubes, the copper nanowire array was fabricated into polystyrene nanotubes using template-assisted electrodeposition method (Wang et al. 2014) by setting up the stacked cell (Fig. 6.4) in a 0.4 M $CuSO_4 \cdot 5H_2O$ solution, under a constant current of 3 mA at room temperature. The pH value of the copper sulfate solution was maintained at pH 2

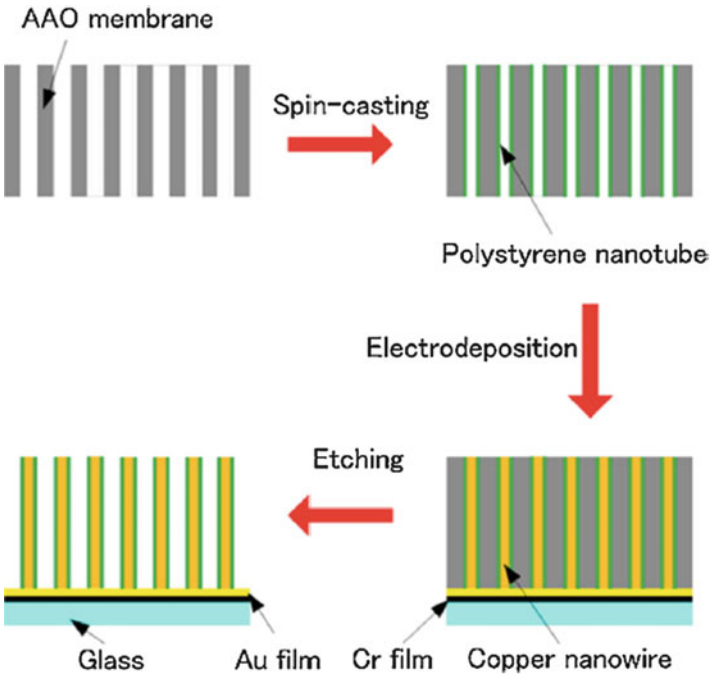

Fig. 6.6 Schematics of the fabrication process for the copper/polystyrene core/shell nanowire array (Wang et al. 2015)

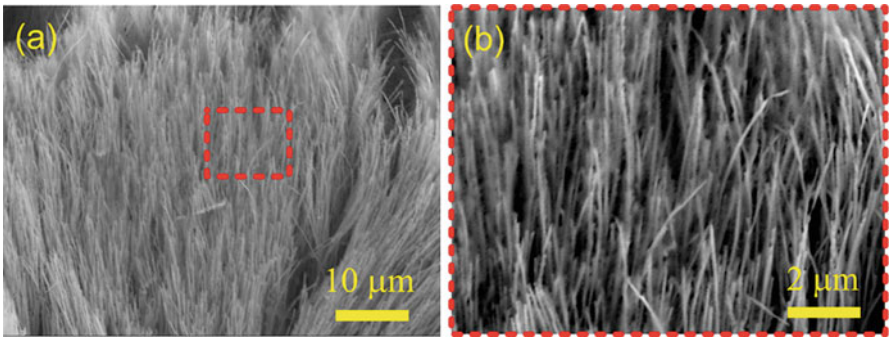

Fig. 6.7 SEM images of (**a**) a typical copper/polystyrene core/shell nanowire array and (**b**) enlarged view (Wang et al. 2015)

with sulfuric acid. Finally, the copper/polystyrene core/shell nanowire array was obtained after etching the AAO template by 3 M NaOH solution.

SEM image of a typical copper/polystyrene core/shell nanowire array is shown in Fig. 6.7, clearly indicating the mainly vertical orientation and the uniform shell thickness of the nanowires. Each of the components plays an essential role in

achieving the desired functionality of the electrical nanowire surface fasteners. The Cu core provides the following functions: (1) an electrical conductive function as the polymer shell shrinks to nanoscale (Wang et al. 2013b) and (2) preventing aggregation and/or collapse of nanowires, thereby resulting in high aspect ratio structures. The polystyrene shell enhances the surface compliance and the adhesion energy, thereby leading to an increase in the adhesion strength.

6.5 Fabrication of Carbon Nanotube Array

CNTs have been among the most scientifically studied materials for the past two decades (Gogotsi 2010). Due to their unique properties, such as extremely mechanical properties, high electrical conductivity, and thermal conductivity/stability (Chen et al. 2010; Cui et al. 2013a), CNTs have been suggested for a variety of practical applications (Cao and Rogers 2009; Cui and Zhang 2013a; Green et al. 2009; Wei and Liu 2008). The most intriguing properties of CNTs lie in their unique one-dimensional nanoscale structures that are anisotropic: properties in the longitudinal direction are drastically different from those in the azimuthal directions (Lan et al. 2011). It is highly desirable in the realization of most of the applications to control the orientation of CNTs either as a stand-alone system or in a group of many systems (Cui and Zhang 2013b).

CNT arrays typically comprise billions of CNTs per square centimeter. CNTs in a CNT array are nearly parallel to each other and have more uniform direction and length distribution than other kinds of CNTs such as tangled CNTs. CNT arrays can provide a well-defined large surface area, and they can be readily incorporated into devices with improved uniformities in mass production, greatly facilitating their integration into practical devices (Chen et al. 2010). Due to their highly ordered nature and high surface area with excellent electronic and mechanical properties (Liu et al. 2007), CNT arrays have wider applications than random bulk CNTs. These applications include field emission cathodes (Liao et al. 2010), supercapacitors (Niu et al. 1997), nanofiltration membranes (Dai 2002), and fuel cell and solar cells (Lan et al. 2011).

CNTs in CNT arrays are straight and uniformly aligned in the vertical direction, which is beneficial for fastener applications. Compared with metallic nanowires, CNTs are more bendable and have significant ability to entangle, both of which enhance side contact with fibrillary arrays. Moreover, CNTs possess good mechanical properties and high electrical conductivity, and are consequently predicted to have potential applications in electrical fasteners (Cui et al. 2014a). Therefore, CNT and Cu/parylene core/shell nanowire array was used to construct an electrical fastener. Compared with a metallic nanowire array fastener (Ju and Amano 2012; Wang et al. 2013a), the adhesion strength of the CNT-Cu/parylene nanowire array fastener is significantly greater, offering a sixfold increase that encourages their use in practical applications of room-temperature electrical fasteners (Cui et al. 2014a).

A Si wafer (<100> type, 1–10 Ω/cm) with a 600 nm SiO_2 layer was used as a substrate. A catalyst film of Fe (0.5–1.0 nm) was deposited on the Si wafer by electron beam (E-beam) evaporation (Edwards EB3 Electron Beam Evaporator). The evaporation was carried out at a pressure of about 5×10^{-7} Torr. The deposition rate of the Fe film was kept at 0.05 nm/s to achieve uniform and controllable film thickness. The thickness of the thin Fe film was monitored in situ by a quartz-crystal sensor fixed inside the E-beam evaporation chamber and calibrated ex situ by atomic force microscopy (AFM, Veeco Explorer).

The CNT arrays were synthesized in a quartz tube furnace. The reaction chamber was a quartz tube with a 3 in. diameter. The substrates were placed in the middle of the quartz tube and the quartz tube was pumped down to 5 mTorr to remove any ambient gas. The total pressure was maintained at 1 atm for all the experiments. The furnace was heated up to the growth temperature (690–780 °C) at 20 °C/min and under Ar flow. Then, C_2H_2 (99.99 %) and/or H_2 (99.99 %) were introduced into the reactor and the CNT arrays were synthesized at the growth temperature for a certain time. Lastly, the acetylene and/or hydrogen gas flow was turned off and the furnace was cooled down to room temperature with the Ar gas flow continuing (Cui et al. 2013a).

Figure 6.8 shows typical SEM images of CNT arrays on a Si substrate, grown under conditions of $C_2H_2 = 100$ sccm, $H_2 = 50$ sccm, and 750 °C. In the top layer of CNT array, it can be seen that the CNTs are entangled and not aligned (Fig. 6.8b).

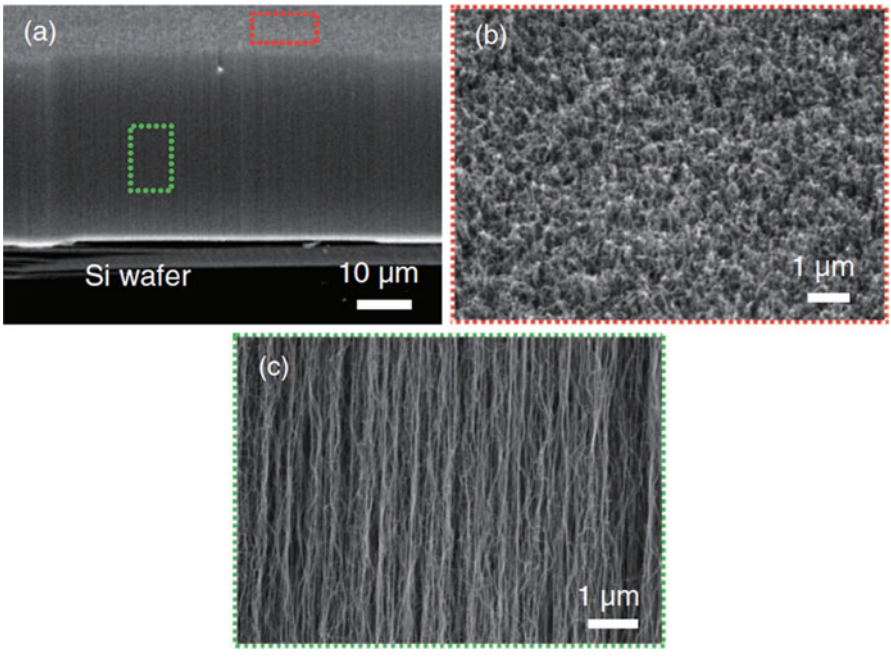

Fig. 6.8 (**a**) Cross-sectional SEM image of CNT array. (**b**) Top view of CNT array showing entanglement of CNTs at the surface. (**c**) High magnification SEM image showing the alignment of CNTs in the array side wall (Cui et al. 2014a)

It should be noted that the CNT array in this case was prepared by a normal chemical vapor deposition process, which can be easily scaled-up for the preparation of CNT arrays. The morphology of the top surface is similar to that of other CNT arrays prepared by low-pressure chemical vapor deposition methods (Qu et al. 2008). As shown in Fig. 6.8c, the CNTs in the array are well-aligned and bundled in the vertical direction, with these bundles being parallel to one another, while the waved CNTs switch between different straight CNT bundles. The curved CNTs in the top surface of the array, and the waved CNTs, can entangle and coil on the surface of Cu/parylene nanowires. This in turn increases the contact area between CNTs and Cu/parylene nanowires, which enhances the adhesion strength of the fastener (Cui et al. 2014a).

6.6 Mechanical and Electrical Performances of Nanowire Surface Fasteners

As shown in Fig. 6.9, a specific pattern for the fastener areas and printed wires (1 mm width) were designed to facilitate the testing of the mechanical bonding strength and the parasitic resistance of the electrical bonding. The diameter of each of the four fastener areas was 2 mm (Wang et al. 2013b). Au films approximately 100 nm thick were deposited onto the fastener and wire areas on Si or glass substrates with around 50 nm thick Cr adhesive layer to improve the adhesion between the substrate and the Au film. The adhesive layer and the Au film were deposited via E-beam evaporation or sputtering (Ju et al. 2012; Wang et al. 2015).

To better understand the adhesion performance of the nanowire surface fastener, we carried out macroscopic measurement of adhesion strength. The bonding strength is defined as the force acted to the nanowire surface fasteners to separate their bonding divided by the bonding area, in the normal and the shear directions. As shown in Fig. 6.10, two nanowire surface fastener samples (Fig. 6.10a), which had patterned nanowire arrays on the substrate, were brought into interconnection at a preload force (Fig. 6.10b) (Wang et al. 2013a). After the preload force was

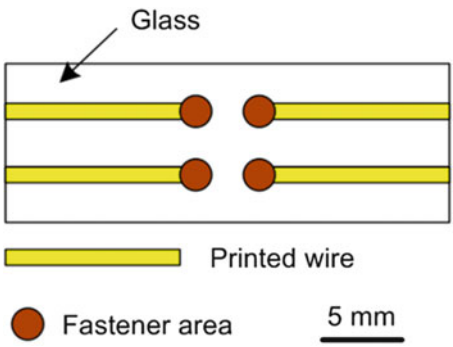

Fig. 6.9 Sketch of a sample with a specific pattern (Wang et al. 2014)

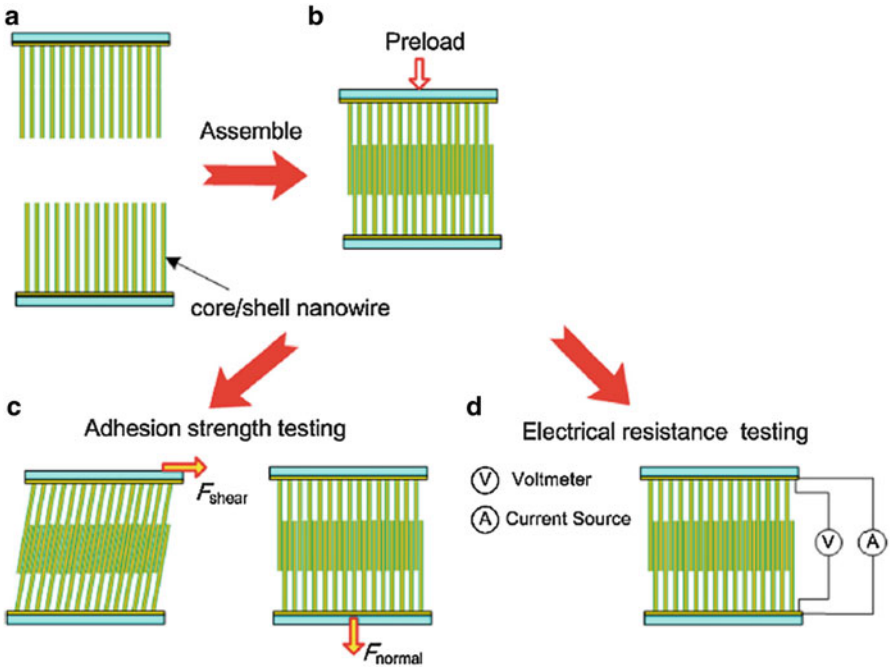

Fig. 6.10 The assembly sequence of patterned nanowire arrays as NSF together with the adhesion strength and electrical resistance test setup (Wang et al. 2015)

completely released, the weight of balance was used to measure the pull-off forces with the parallel (i.e., the shear adhesive strength) and normal (i.e., the normal adhesive strength) directions to the substrate (Fig. 6.10c) (Wang et al. 2015). To eliminate the effects of the attachment cycles and avoid the pre-alignment effect for subsequent adhesion measurements, the adhesion forces obtained from the first attachment of each sample were adopted. Adhesion tests for each reported condition were completed for four samples, and the average values were used. The four-point probe method was used to measure the electrical resistance (Fig. 6.10d). During the measurement, an electrical current in the range from 0 to 19 mA was applied using the current source and the corresponding voltage was extracted from the voltmeter (Wang et al. 2013b, 2015).

6.6.1 Performances of Copper/Parylene Nanowire Surface Fasteners

To characterize the properties of copper/parylene nanowire surface fasteners, we first measured the adhesive strength and relative electrical resistance as a function of nanowire length (5, 10, and 20 μm). All the samples in this test have a parylene

shell (100 nm thickness) and a preload of 78.02 N/cm^2. Interestingly, the Parylene C film becomes conductive due to dielectric breakdown when the thickness of it is miniaturized to nanoscale. The reason why Parylene C film in nanoscale thickness becomes conductive is mainly due to the dielectric breakdown phenomenon (Wang et al. 2013b). As can be seen in Fig. 6.11a, both shear and normal adhesion can be realized at the same time. Moreover, the adhesive strength is strongly affected by the length of the nanowires. The maximum shear and normal strengths were obtained when the length was 10 μm. When $L < 10$ μm, the nanowires sustained their high aspect ratio and the neighboring nanowires did not contact each other (Fig. 6.12a); therefore, the contact area is directly proportional to the nanowire length. However, when the nanowire length is as large as 20 μm, the nanowires tend to collapse and the neighboring nanowires contact each other (Fig. 6.12c), which leads to a reduction of the contact area of the nanowire surface fasteners. The electrical resistance is also strongly affected by the length of nanowires. Specifically, longer nanowire length results in a smaller electrical resistance (Fig. 6.11b). As can be seen in Fig. 6.12a–c, the interconnection of neighboring nanowires increases as the length of nanowires increases, and they were interconnected before the parylene coating. The interconnected neighboring nanowires connect in parallel in the electrical connection, which led to the reduction of resistance.

Besides the nanowire length, the adhesive strength and electrical resistance are also affected by the parylene thickness. The samples with the same nanowire length (10 μm) and the same preload (78.02 N/cm^2) are used in the test. As can be seen in Fig. 6.11c, the adhesive strength strongly depends on the thickness of the parylene shell. Specifically, weak adhesive strengths (~0.99 N/cm^2 in shear and ~0.57 N/cm^2 in normal directions) are obtained from the pristine copper nanowires. The adhesive strength is dramatically enhanced by the application of the parylene shell. When the thickness of the parylene shell is 150 nm, the maximum adhesive strengths (~24.97 N/cm^2 in shear and ~10.82 N/cm^2 in normal directions) are obtained. This significant enhancement in adhesion is attributed to the higher surface compliance of the parylene shell, enabling conformal contact with increased contact area between the interpenetrating nanowires (Kapadia et al. 2009). When the thickness of parylene shell further increases, the adhesive strengths decrease. This trend is attributed to the higher filling factor for thicker parylene shells (Fig. 6.5b–d). When the thickness of the parylene shell increases to 250 nm, almost no spare space exists between the neighboring nanowires (Wang et al. 2013b). Hence, the interconnected mode changes from "wire–wire" to "tip–tip" when the thickness of parylene shell increases, which results in the reduction of adhesive strengths. The electrical properties of nanowire surface fasteners are also affected by the parylene shell thickness. It can be seen from Fig. 6.11d that larger parylene shell thickness results in larger electrical resistance of the nanowire surface fasteners. This trend is attributed to the poor electrical conductivity of parylene. To examine the effect of preload on the adhesive and electrical properties of copper/parylene core/shell nanowire surface fastener, two nanowire surface fastener samples were brought into interconnection at a preload of 39.01, 78.02, and 156.04 N/cm^2. A monotonic increase in the normal adhesive strength and decrease in electrical resistance are

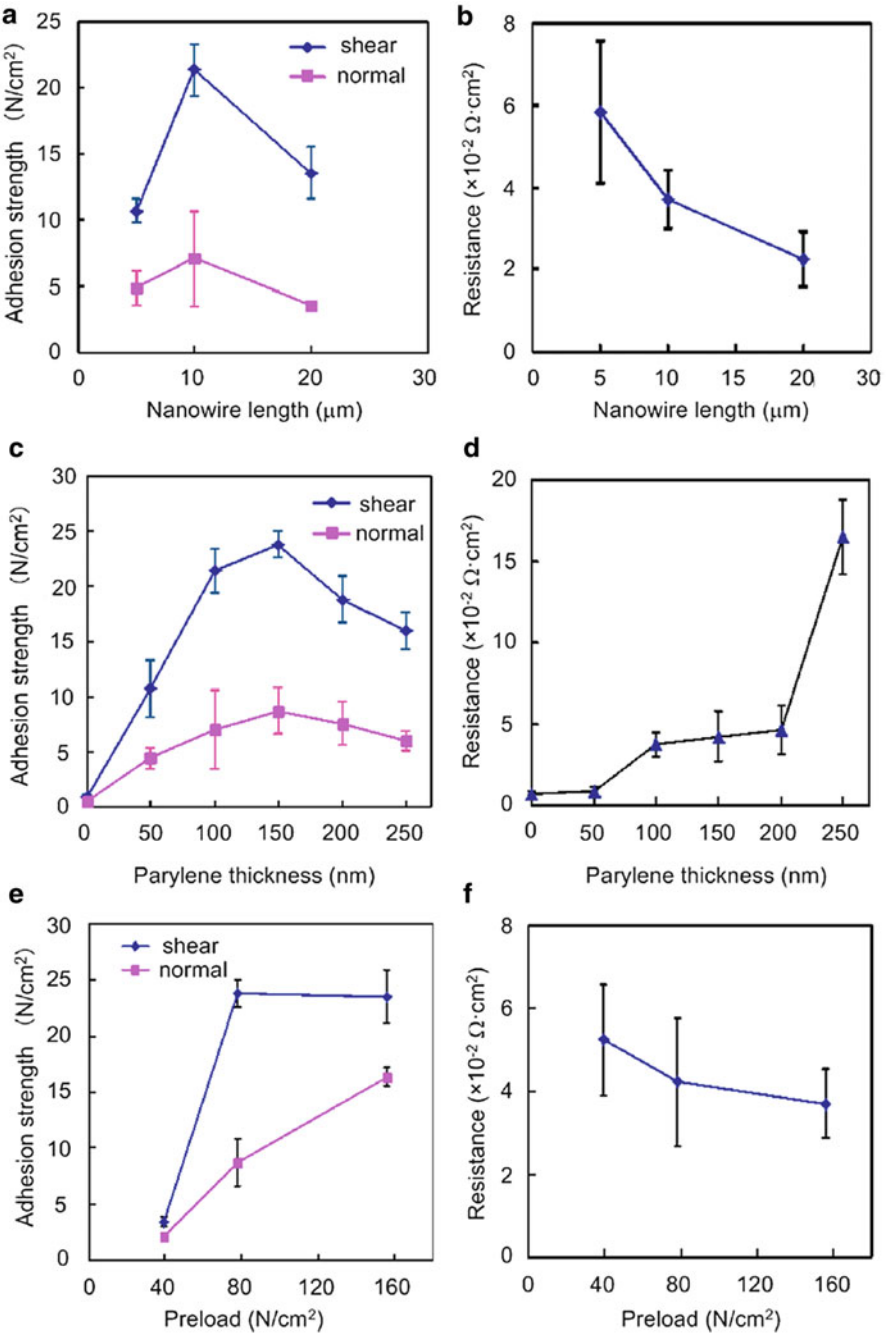

Fig. 6.11 (**a**) Adhesive strength and (**b**) electrical resistance of nanowire surface fasteners as a function of nanowire length. The preload is 78.02 N/cm^2 and the thickness of the parylene shell is 100 nm. (**c**) Adhesive strength and (**d**) electrical resistance of nanowire surface fasteners as a function of parylene thickness. The preload is 78.02 N/cm^2 and the length of the nanowire array is 10 μm. (**e**) Adhesive strength and (**f**) electrical resistance of nanowire surface fasteners as a function of preload. The thickness of parylene shell is 150 nm and the length of nanowire array is 10 μm (Wang et al. 2013b)

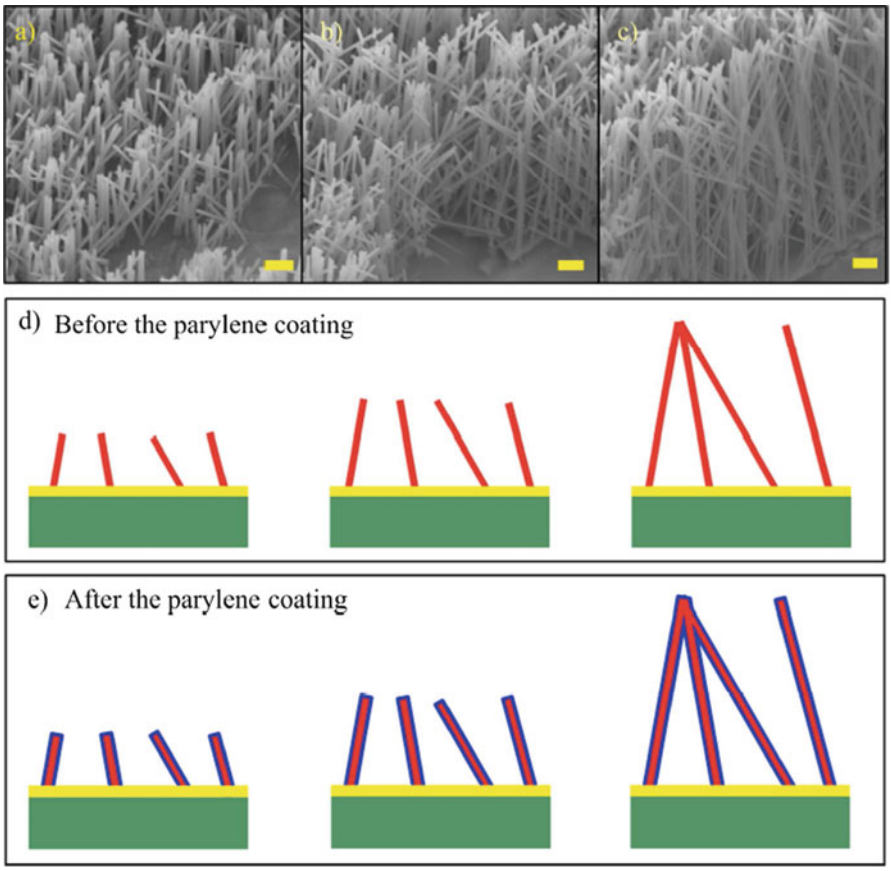

Fig. 6.12 (**a**–**c**) Side-view SEM images of copper nanowire arrays before parylene coating with lengths of 5, 10, and 20 μm. (**d**) Illustration of nanowire arrays before the parylene coating with the length of 5, 10, and 20 μm. (**e**) Illustration of nanowire arrays after the parylene coating with lengths of 5, 10, and 20 μm. The scale bar is 1 μm (Wang et al. 2013b)

observed with the increase of preload force (Fig. 6.11e, f). This phenomenon is just as expected because the higher preload force leads to a larger contact area between the nanowires. However, no increase in the shear adhesion was observed when the preload increases from 78.02 to 156.04 N/cm^2. This phenomenon is attributed to the poor adhesion of electrodeposited copper nanowires on the Au seed layer (Wang et al. 2013b).

Figure 6.13a shows a schematic of copper/parylene core/shell nanowire surface fasteners. An example of the strong bonding achieved is shown in Fig. 6.13b in which the copper/parylene core/shell nanowire surface fasteners with a surface area of ~3.14×4 mm^2 enables 300 g of weight to be hung without failure in the shear direction. As shown in Fig. 6.13c, the red light from the light-emitting diode shows that the core/shell nanowire surface fasteners are conductive.

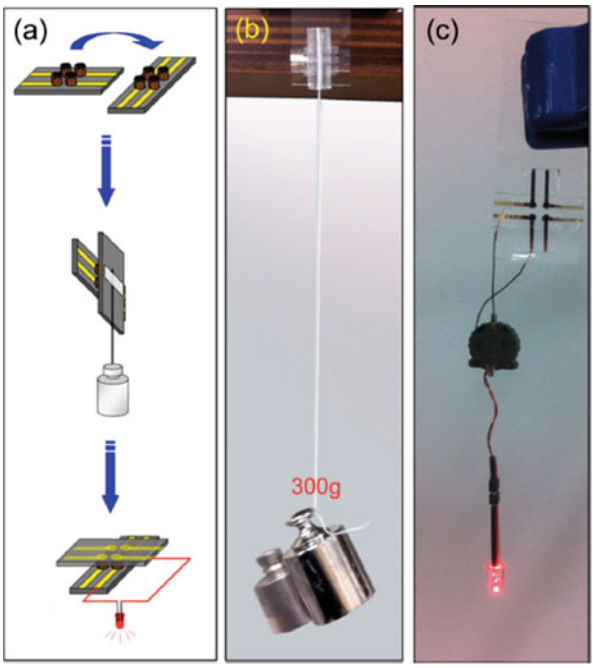

Fig. 6.13 (**a**) Schematic of this room-temperature electrical bonding technique. (**b**) Photo showing a weight of 300 g hanging on the interconnected copper nanowire surface fasteners. (**c**) Light-emitting diode suspended by the nanowire surface fasteners to show electrical conductivity (Wang et al. 2013b)

6.6.2 *Performances of Copper/Polystyrene Nanowire Surface Fasteners*

To demonstrate the importance of the polystyrene shell, we systematically studied the adhesion strength as a function of polystyrene thickness. The samples with the same nanowire length (40 μm) and the same preload (9.8 N) are used in the test. As can be seen in Fig. 6.14a, the adhesive properties strongly depend on the thickness of the polystyrene shell. Specifically, weak adhesion strengths (1.25 N/cm^2 in shear and 0.76 N/cm^2 in normal directions) are obtained from the pristine copper nanowires. The adhesion strength is dramatically enhanced by the application of polystyrene shell. When the thickness of the polystyrene shell is 18 nm, the maximum adhesion strengths (44.42 N/cm^2 in shear and 21.43 N/cm^2 in normal) are obtained. This drastic enhancement of the adhesion strength with polystyrene shell thickness can be explained by an increase in contact width between the engaged nanowire arrays (Kapadia et al. 2009). A decrease in adhesion strength is observed for the thickness of the polystyrene shell that is larger than 18 nm. This trend is attributed to decrease the density of Cu core because of thicker polystyrene shells. When the thickness of the polystyrene shell increases to 24 nm, the polystyrene nanotube becomes more hydrophobic which prevents the electrolyte getting into the polystyrene nanotube and then decreasing the density of Cu core (Jin et al. 2005). The electrical properties of copper/polystyrene core/shell nanowire

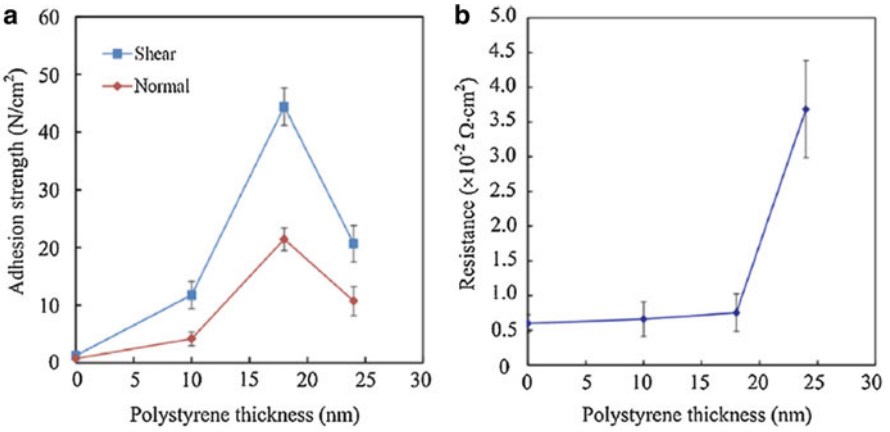

Fig. 6.14 (**a**) Adhesion strength and (**b**) electrical resistance of nanowire surface fastener as a function of polystyrene thickness. The preload is 9.8 N and the length of nanowire array is ~40 μm (Wang et al. 2015)

surface fastener are also affected by the polystyrene shell thickness. It can be seen from Fig. 6.14b that larger polystyrene shell thickness results in larger electrical resistance of the nanowire surface fastener. This trend is attributed to the poor electrical conductivity of polystyrene (Wang et al. 2015).

Besides the polystyrene shell thickness, the adhesion strength is also affected by the molecular weight of polystyrene shell. The samples with the same shell thickness (18 nm) and the same preload (9.8 N) are used in the test. As can be seen in Fig. 6.15a, a monotonic increase in the adhesion strength is observed with the molecular weight of polystyrene. Specifically, the shear adhesion strength increases from 4.64 to 44.42 N/cm^2 as the molecular weight of polystyrene is increased from 35,000 to 350,000 g/mol. The adhesion energy of polystyrene increases with an increase in the molecular weight, thus enhancing the adhesion forces between the core/shell nanowires (Lau and Burns 1974). On the other hand, the changes of the electrical resistance for the nanowire surface fastener were rather small when the molecular weight of polystyrene varied (Fig. 6.15b). The reason is due to that polystyrene shells reach dielectric breakdown and become conductive at this thickness, which is no relationship with the molecular weight of polystyrene shells (Wang et al. 2015).

Compared with the copper/parylene core/shell nanowire surface fastener (Wang et al. 2013b), the copper/polystyrene core/shell nanowire surface fastener tends to achieve higher adhesion strength. Different with parylene, polystyrene is a kind of solvent-welding plastic. Plastic solvent-welding is a technique which uses a solvent to partially liquefy plastic along the joint and allows the joint to solidify, causing a permanent chemical weld. Besides the van der Waals force, the chemical force has a big contribution to the adhesion strength. That is the reason that polystyrene shell has a better performance than parylene shell for nanowire surface fastener. Moreover, the polymer shell thickness of copper/polystyrene core/shell nanowire surface

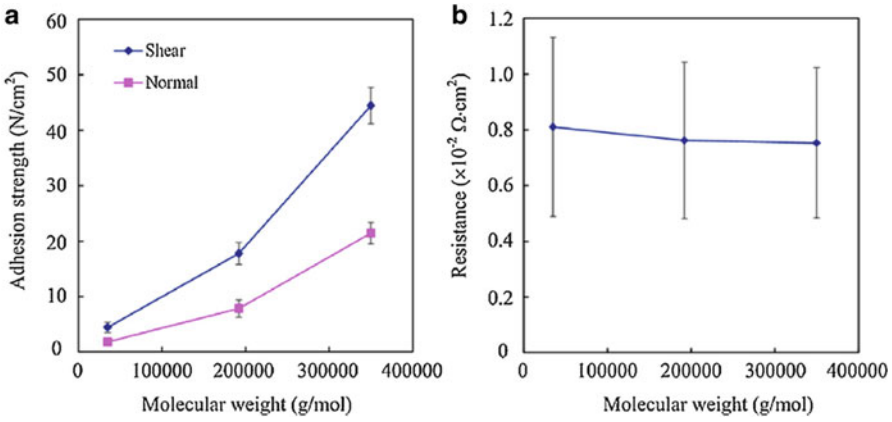

Fig. 6.15 (**a**) Adhesion strength and (**b**) electrical resistance of nanowire surface fastener as a function of the molecular weight of polystyrene. The preload is 9.8 N and the thickness of polystyrene shell is ~18 nm (Wang et al. 2015)

fastener is much thinner than that of copper/parylene core/shell nanowire surface fastener (Wang et al. 2013b), which leads to a good electrical conductivity of copper/polystyrene core/shell nanowire surface fastener. On the other hand, the copper/polystyrene core/shell nanowire surface fastener was fabricated by synthesizing copper nanowires into polystyrene nanotubes, which may easily form homogeneous polymer shell along the whole length of copper nanowires by comparing with copper/parylene core/shell nanowire surface fastener which was formed by coating parylene shell on core copper nanowires (Wang et al. 2015).

6.6.3 *Performances of CNT-Copper/Parylene Nanowire Surface Fasteners*

To characterize the performance of a CNT-Cu/parylene nanowire array fastener, we systematically measured the macroscopic shear and normal adhesion strength as a function of the CNT array length (Fig. 6.16a). This revealed that the adhesion strength of a CNT-Cu/parylene nanowire array fastener steadily increases with the increase in the length of the CNT array. For example, the adhesive shear strength increases almost linearly from 20.29 to 50.72 N/cm^2 when the length of the CNT array increases from 35 to 120 μm. The maximum adhesive shear strength obtained of 50.72 N/cm^2 is comparable to that achievable with CNT-based adhesives (Qu et al. 2008; Qu and Dai 2007) and is six times higher than that of a metallic nanowire fastener (Ju et al. 2012; Ko et al. 2009; Wang et al. 2013a). The corresponding normal adhesion strength also increases from 14.82 to 28.48 N/cm^2 over the same range of CNT lengths, which is approximately five times higher than that of a metallic nanowire fastener (Ju et al. 2012; Wang et al. 2013a). Unlike

gecko adhesives, the CNT-Cu/parylene nanowire array fastener produces both high shear and normal adhesion strengths simultaneously, which is important for the practical application of electrical fasteners.

Besides the length of the CNT array, the adhesion strength of CNT-Cu/parylene nanowire array fasteners is also affected by the preload applied to engage the fastener. As shown in Fig. 6.16b, the adhesion strength of a CNT-Cu/parylene nanowire array fastener increases with the applied preload. Specifically, it increases from 7.02 to 20.29 N/cm^2 as the preload is increased from 4.9 to 19.6 N. The interpenetration depth between CNTs and Cu/parylene nanowires increases with an increase in the applied preload force, thus enhancing the contact area and van der Waals interactions between the CNTs and Cu/parylene nanowires (Hyunhyub et al. 2010; Chen et al. 2012).

As shown in Fig. 6.17a, the electrical resistance of the CNT-Cu/parylene nanowire array fastener was investigated. The solid lines in the figure are obtained through linear fitting of the measured values. The resistance of the fastener was extracted from the *I*–*V* curves (Fig. 6.17b) (Kapadia et al. 2009). As shown in Fig. 6.17a, the fastener exhibits ohmic behavior over the entire range of measurement; however, the resistance of the fastener decreases with an increase in the preload force. For example, the resistance decreases from 142.3 to 45.4 Ω when the preload force is increased from 0 to 19.6 N as shown in Fig. 6.17b, which indicates that the CNT-Cu/parylene nanowire array fastener has good electrical conductivity. Since an increase in preload force increases the interpenetration depth and connection between CNTs and Cu/parylene nanowires, the electrical performance of the fastener is also improved (Cui et al. 2014a). It should also be noted that the resistance of the CNT-Cu/parylene nanowire array fastener was almost constant for the first 20 cycles of attachment–detachment tests.

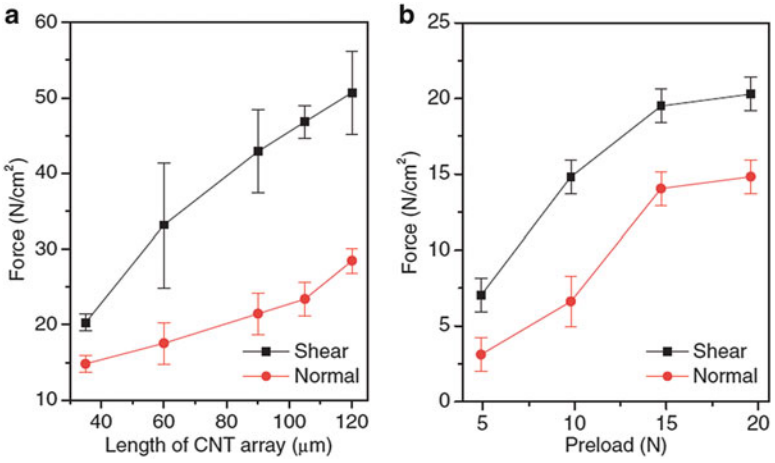

Fig. 6.16 (**a**) Shear and normal adhesion force of a CNT-Cu/parylene nanowire array fastener as a function of the CNT array length. The preload used to engage the fastener was 19.6 N. (**b**) Preload force-dependent adhesion force of a CNT-Cu/parylene nanowire array fastener. The errors represent standard errors calculated from four measurements (Cui et al. 2014a)

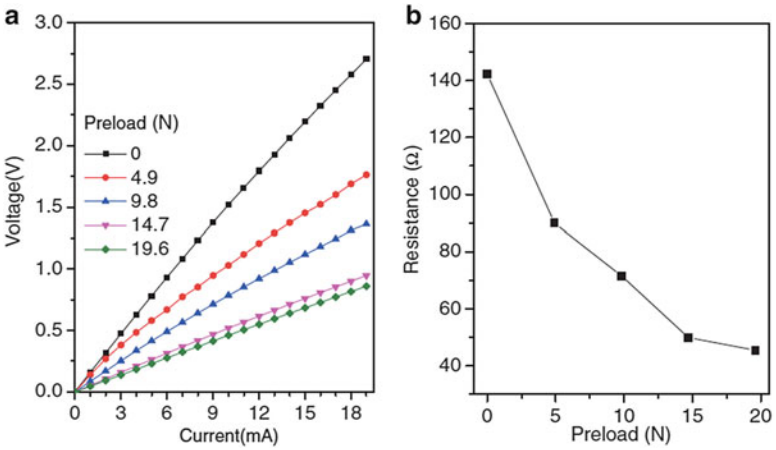

Fig. 6.17 (**a**) *I–V* curves of CNT-Cu/parylene array fastener under different preload forces. (**b**) Measured resistance as a function of preload force (Cui et al. 2014a)

6.7 Conclusions

In this chapter, we outlined the progress made in the use of composite nanowires for room-temperature mechanical and electrical bonding. The fabrication of Cu/parylene and Cu/polystyrene nanowires using AAO and PC membrane as templates was described. While, the fabrication of carbon nanotube (CNTs) array used to connect with Cu/parylene nanowires was also discussed. For copper/parylene core/shell nanowire array, both strong bonding and small electrical resistance were achieved at room temperature. It is important to note that this electrical surface fastener exhibits high macroscopic adhesion strength (25 N/cm^2) and low electrical resistance (4.22×10^{-2} Ω cm^2). We also developed an electrical surface fastener with strong adhesion based on copper/polystyrene core/shell nanowire arrays. The adhesion strength of this surface fastener could be mediated by the shell thickness and the molecular weight of polystyrene. Uniquely, this electrical surface fastener exhibits high macroscopic adhesion strength (44.42 N/cm^2) and low electrical resistance (~0.75×10^{-2} Ω cm^2), indicative that the copper/polystyrene core/shell nanowire surface fastener exhibits a higher adhesion strength and a lower electrical resistance than the copper/parylene core/shell nanowire surface fastener. Besides, copper/parylene nanowires and a CNT array were also chosen to construct a room-temperature electrical fastener. The adhesion strength of this fastener was found to increase with an increase in the length of the CNT arrays. The shear adhesion strength (50.72 N/cm^2) of the CNT-Cu/parylene nanowire array fastener is shown to be six times higher than that of a metallic nanowire fastener. The resistance of the fastener was measured as 45.4 Ω, which indicates that it has good electrical conductivity. In comparison with conventional reflow soldering method, the present cold bonding technique can be performed at room temperature,

which could improve the process compatibility and component reliability. Furthermore, a type of surface fastener without solder enables easier detachment of the surface mount component from the circuit board, by which recycling and sustainability of rare metals becomes significantly more convenient.

References

Attaluri, A.C., Huang, Z., Belwalkar, A., Van, G.W., Gao, D., Misiolek, W.: Evaluation of nanoporous alumina membranes for hemodialysis application. ASAIO J. **55**, 217–223 (2009)

Baek, S.S., Fearing, R.S.: Reducing contact resistance using compliant nickel nanowire arrays. IEEE T. Compon. Pack. T. **31**, 859–868 (2009)

Bakshi, M.S., Poonam, S., Banipal, T.S.: Au and Au-Ag bimetallic nanoparticles synthesized by using 12-3-12 cationic Gemini surfactant as template. Mater. Lett. **61**, 5004–5009 (2007)

Belwalkar, A., Grasing, E., Geertruyden, W.V., Huang, Z., Misiolek, W.Z.: Effect of processing parameters on pore structure and thickness of anodic aluminum oxide (AAO) tubular membranes. J. Memb Sci. **319**, 192–198 (2008)

Cao, Q., Rogers, J.A.: Ultrathin films of single-walled carbon nanotubes for electronics and sensors: a review of fundamental and applied. Adv. Mater. **21**, 29–53 (2009)

Chen, B., Goldberg Oppenheimer, P., Shean, T.A.V., Wirth, C.T., Hofmann, S., Robertson, J.: Adhesive properties of gecko-inspired mimetic via micropatterned carbon nanotube forests. J. Phys. Chem. C **116**, 20047–20053 (2012)

Chen, H., Roy, A., Baek, J.B., Zhu, L., Qu, J., Dai, L.: Controlled growth and modification of vertically-aligned carbon nanotubes for multifunctional applications. Mat. Sci. Eng. R. **70**, 63–91 (2010)

Chen, P.L., Kuo, C.T., Tsai, T.G., Wu, B.W., Hsu, C.C., Pan, F.M.: Self-organized titanium oxide nanodot arrays by electrochemical anodization. Appl. Phys. Lett. **83**, 2796–2798 (2003)

Chung, C.K., Chang, W.T., Liao, M.W., Chang, H.C., Lee, C.T.: Fabrication of enhanced anodic aluminum oxide performance at room temperatures using hybrid pulse anodization with effective cooling. Electrochim Acta **56**, 6489–6497 (2011)

Chung, C.K., Liao, M.W., Khor, O.K.: Fabrication of porous anodic aluminum oxide by hybrid pulse anodization at relatively high potential. Microsyst. Technol. **20**, 1827–1832 (2013)

Chu, S.Z., Todoroki, S., Wada, K., Inoue, S.: Formation and microstructures of anodic alumina films from aluminum sputtered on glass substrate. J. Electrochem. Soc. **149**, B321–B327 (2001)

Chu, S.Z., Wada, K., Inoue, S., Isogai, M., Yasumori, A.: Fabrication of ideally ordered nanoporous alumina films and integrated alumina nanotubule arrays by high-field anodization. Adv. Mater. **17**, 2115–2119 (2005)

Crouse, D., Lo, Y.H., Miller, A.E., Crouse, M.: Self-ordered pore structure of anodized aluminum on silicon and pattern transfer. Appl. Phys. Lett. **76**, 49–51 (2000)

Cui, J., Wu, Y., Wang, Y., Zheng, H., Xu, G., Zhang, X.: A facile and efficient approach for pore-opening detection of anodic aluminum oxide membranes. Appl. Surf. Sci. **258**, 5305–5311 (2012)

Cui, Y., Ju, Y., Wang, P., Xu, B., Kojima, N., Ichioka, K., Hosoi, A.: Carbon nanotube–Cu/parylene nanowire array electrical fasteners with high adhesion strength. Appl. Phys. Express **7**, 015012 (2014a)

Cui, Y., Ju, Y., Xu, B., Wang, P., Kojima, N., Ichioka, K., Hosoi, A.: Mimicking a gecko's foot with strong adhesive strength based on a spinnable vertically aligned carbon nanotube array. RSC Adv. **4**, 9056 (2014b)

Cui, Y., Wang, B., Zhang, M.: Optimizing reaction condition for synthesizing spinnable carbon nanotube arrays by chemical vapor deposition. J. Mater. Sci. **48**, 7749–7756 (2013)

Cui, Y., Zhang, M.: Cross-links in carbon nanotube assembly introduced by using polyacrylonitrile as precursor. ACS Appl. Mater. Inter. **16**, 8173–8178 (2013a)
Cui, Y., Zhang, M.: Fabrication of cross-linked carbon nanotube foam using polymethylmethacrylate microspheres as templates. J. Mater. Chem. **1**, 13984–13988 (2013b)
Dai, H.: Carbon nanotubes: synthesis, integration, and properties. Acc. Chem. Res. **35**, 1035–1044 (2002)
Demoustier, S.: Preparation of polymeric and metallic nanostructures using a template-based deposition method. Mater. Sci. Eng. C **15**, 269–271 (2001)
Ding, G.Q., Shen, W.Z., Zheng, M.J., Fan, D.H.: Synthesis of ordered large-scale ZnO nanopore arrays. Appl. Phys. Lett. **88**, 103106 (2006)
Dong, L., Tao, X., Zhang, L., Zhang, X., Nelson, B.J.: Nanorobotic spot welding: controlled metal deposition with attogram precision from copper-filled carbon nanotubes. Nano Lett. **7**, 58–63 (2006)
Feng, X., Hangarter, C., Yoo, B., Rheem, Y., Lee, K.H., Myung, N.V.: Recent progress in electrodeposition of thermoelectric thin films and nanostructures. Electrochim. Acta **53**, 8103–8117 (2008)
Ferguson, G.S., Chaudhury, M.K., Sigal, G.B., Whitesides, G.M.: Contact adhesion of thin gold films on elastomeric supports: cold welding under ambient conditions. Science **253**, 776–778 (1991)
Gâlcă, A.C., Kooij, E.S., Wormeester, S., Salm, C., Leca, V., Rector, J.H., Poelsema, B.: Structural and optical characterization of porous anodic aluminum oxide. J. Appl. Phys. **94**, 4296–4305 (2003)
Gogotsi, Y.: High-temperature rubber made from carbon nanotubes. Science **330**, 1332–1333 (2010)
Gorokh, G., Mozalev, A., Solovei, D., Khatko, V., Llobet, E., Correig, X.: Anodic formation of low-aspect-ratio porous alumina films for metal-oxide sensor application. Electrochim. Acta **52**, 1771–1780 (2006)
Green, M.J., Behabtu, N., Pasquali, M., Adams, W.W.: Nanotubes as polymers. Polymer **50**, 4979–4997 (2009)
Harman, T.C., Taylor, P.J., Spears, D.L., Walsh, M.P.: Thermoelectric quantum-dot superlattices with high ZT. J. Electron. Mater. **29**, L1–L2 (1999)
Huczko, A.: Template-based synthesis of nanomaterials. Appl. Phys. A **70**, 365–376 (2000)
Hyunhyub, K., Zhang, Z., Ho, J.C., Kuniharu, T., Rehan, K., Yu-Lun, C., Weizhen, C., Brett, A.C., Ali, J.: Flexible carbon-nanofiber connectors with anisotropic adhesion properties. Small **6**, 22–26 (2010)
Jin, C., Suenaga, K., Iijima, S.: Plumbing carbon nanotubes. Nat. Nanotechnol. **7**, 17–21 (2008)
Jin, M., Feng, X., Feng, L., Sun, T., Zhai, J., Li, T., Jiang, L.: Superhydrophobic aligned polystyrene nanotube films with high adhesive force. Adv. Mater. **17**, 1977–1981 (2005)
Jin, S., Lee, Y., Jeon, S.M., Sohn, B.H., Chae, W.S., Lee, J.K.: Simple fabrication of single-and multi-layer polymer nanotubes by spin-casting method within anodized aluminum oxide (AAO) templates. J. Mater. Chem. **22**, 23368–23373 (2012)
Joo, S.W., Banerjee, A.N.: FESEM studies of densely packed aligned nickel nanopillars on silicon substrate by electrochemical deposition through porous alumina membrane. Mater. Sci. Eng. B **175**, 36–40 (2010)
Ju, Y., Amano, M., Chen, M.: Mechanical and electrical cold bonding based on metallic nanowire surface fasteners. Nanotechnology **23**, 365202 (2012)
Kasi, A.K., Kasi, J.K., Afzulpurkar, N., Bohez, E., Tuantranont, A.: Continuous Voltage Detachment and Etching (CVDE) technique for fabrication of nano-porous anodic aluminum oxide (AAO) tubular membrane. Nanosci. Nanotech. Lett. **4**, 530–536 (2012)
Kapadia, R., Ko, H., Chueh, Y.L., Ho, J.C.: Hybrid core-multishell nanowire forests for electrical connector applications. Appl. Phys. Lett. **94**, 263110 (2009)
Kim, B., Park, S., McCarthy, T.J., Russell, T.P.: Fabrication of ordered anodic aluminum oxide using a solvent-induced array of block-copolymer micelles. Small **3**, 1869–1872 (2007)
Ko, H., Lee, J., Schubert, B.E., Chueh, Y.L., Leu, P.W., Fearing, R.S., Javey, A.: Hybrid core-shell nanowire forests as self-selective chemical connectors. Nano Lett. **9**, 2054–2058 (2009)

Lan, Y., Wang, Y., Ren, Z.F.: Physics and applications of aligned carbon nanotubes. Adv. Phys. **60**, 553–678 (2011)

Lau, W.W.Y., Burns, C.M.: Effect of temperature and molecular weight on the rate of spreading of polystyrene melts on plane soda lime glass surfaces. J. Polym. Sci. Pol. Phys. **12**, 431–439 (1974)

Liao, Q., Yang, Y., Qi, J., Zhang, Y., Huang, Y., Xia, L., Liu, L.: High intensity, plasma-induced electron emission from large area carbon nanotube array cathodes. Appl. Phys. Lett. **96**, 073109 (2010)

Li, D., Wu, Y., Fan, R., Yang, P., Majumdar, A.: Thermal conductivity of Si/SiGe superlattice nanowires. Appl. Phys. Lett. **83**, 3186–3188 (2003)

Li, H., Xu, C.L., Zhao, G.Y., Li, H.L.: Effects of annealing temperature on magnetic property and structure of amorphous Co49Pt51 alloy nanowire arrays prepared by direct-current electrodeposition. J. Phys. Chem. B **109**, 3759–3763 (2005)

Liu, K., Jiang, K., Wei, Y., Ge, S., Liu, P., Fan, S.: Controlled termination of the growth of vertically aligned carbon nanotube arrays. Adv. Mater. **19**, 975–978 (2007)

Li, Y., Wang, J., Deng, Z., Wu, Y., Sun, X., Yu, D., Yang, D.: Bismuth nanotubes: a rational low-temperature synthetic route. J. Am. Chem. Soc. **123**, 9904–9905 (2001)

Mao, R.W., Lin, S.K., Tsai, C.S.: In situ preparation of an ultra-thin nanomask on a silicon wafer. Nanotechnology **20**, 685–688 (2009)

Masuda, H., Fukuda, K.: Ordered metal nanohole arrays made by a two-step replication of honeycomb structures of anodic alumina. Science **268**, 1466–1468 (1995)

Niu, C., Sichel, E.K., Hoch, R., Moy, D., Tennent, H.: High power electrochemical capacitors based on carbon nanotube electrodes. Appl. Phys. Lett. **70**, 1480–1482 (1997)

Pastore, I., Poplausks, R., Apsite, I., Pastare, I., Lombardi, F., Erts, D.: Fabrication of ultra thin anodic aluminium oxide membranes by low anodization voltages. IOP Conf. Ser. Mater. Sci. Eng. **23**, 012025 (2011)

Peng, Y., Cullis, Y., Inkson, B.: Bottom-up nanoconstruction by the welding of individual metallic nanoobjects using nanoscale solder. Nano Lett. **9**, 91–96 (2008)

Pu, L., Shi, Y., Zhu, J.M., Bao, X.M., Zhang, R., Zheng, Y.D.: Electrochemical lithography: fabrication of nanoscale Si tips by porous anodization of Al/Si wafer. Chem. Commun. **8**, 942–943 (2004)

Qu, L., Dai, L.: Gecko-foot-mimetic aligned single-walled carbon nanotube dry adhesives with unique electrical and thermal properties. Adv. Mater. **19**, 3844–3849 (2007)

Qu, L., Dai, L., Stone, M., Xia, Z., Wang, Z.L.: Carbon nanotube arrays with strong shear binding-on and easy normal lifting-off. Science **322**, 238–242 (2008)

Sumikura, S., Mori, S., Shimizu, S., Usami, H., Suzuki, E.: Syntheses of NiO nanoporous films using nonionic triblock co-polymer templates and their application to photo-cathodes of p-type dye-sensitized solar cells. J. Photochem. Photobiol. A Chem **199**, 1–7 (2008)

Taberna, P.L., Mitra, S., Poizot, P., Simon, P., J-M, T.: High rate capabilities Fe_3O_4-based Cu nano-architectured electrodes for lithium-ion battery applications. Nat. Mater. **5**, 567–573 (2006)

Teshima, H., Kojima, K., Ju, Y.: Fabrication of anodic aluminum oxide template and copper nanowire surface fastener. J. Electron. Packaging **136**, 044501 (2014)

Tomil, M.M.E., Buschmann, V., Dobrev, D., Neumann, R., Scholz, R., Schuchert, I.U., Vetter, J.: Single-crystalline copper nanowires produced by electrochemical deposition in polymeric ion track membranes. Adv. Mater. **13**, 62–65 (2001)

Venkatasubramanian, R., Siivola, E., Colpitts, T., O'Quinn, B.: Thin-film thermoelectric devices with high room-temperature figures of merit. Nature **413**, 597–602 (2001)

Wang, P., Ju, Y., Chen, M., Hosoi, A., Song, Y., Iwasaki, Y.: Room-temperature bonding technique based on copper nanowire surface fastener. Appl. Phys. Express **6**, 035001 (2013a)

Wang, P., Ju, Y., Cui, Y., Hosoi, A.: Copper/parylene core/shell nanowire surface fastener used for room-temperature electrical bonding. Langmuir **29**, 13909–13916 (2013b)

Wang, P., Ju, Y., Hosoi, A.: Core-shell nanowire based electrical surface fastener used for room-temperature electronic packaging bonding. Electron. Mater. Lett. **10**, 503–507 (2014)

Wang, P., Ju, Y., Chen, M.: Room-temperature electrical bonding technique based on copper/polystyrene core/shell nanowire surface fastener. Appl. Surf. Sci. **349**, 774–779 (2015)

Wei, D., Liu, Y.: The intramolecular junctions of carbon nanotubes. Adv. Mater. **20**, 2815–2841 (2008)

Wei, S., Shen, Y., Ge, D., Xue, M., Cao, H., Huang, S., Wang, J.X., Zhang, G.L., Zhang, F.B.: Functionalized anodic aluminum oxide (AAO) membranes for affinity protein separation. J. Membr. Sci. **325**, 801–808 (2008)

Wei, W.X., Guang, T.F., Jinm, X.X., Zhen, J., De, Z.L.: Size-dependent orientation growth of large-area ordered Ni nanowire arrays. J. Phys. Chem. B **109**, 24326 (2005)

Woo, L., Roland, S., Kornelius, N., Ulrich, G.S.: A template-based electrochemical method for the synthesis of multisegmented metallic nanotubes. Angew. Chem. Int. Ed. Engl. **44**, 6050–6054 (2005)

Xu, J., Cheng, G., Zheng, R.: Controllable synthesis of highly ordered Ag nanorod arrays by chemical deposition method. Appl. Surf. Sci. **256**, 5006–5010 (2010)

Xu, J., Razeeb, K. M., Sitaraman, S. K., Mathewson, A.: The fabrication of ultra long metal nanowire bumps and their application as interconnects. Nanotechnology. IEEE C Nano 12th, pp. 1–6 (2012)

Yan, B., Pham, H.T.M., Ma, Y., Zhuang, Y., Sarro, P.M.: Fabrication of in situ ultrathin anodic aluminum oxide layers for nanostructuring on silicon substrate. Appl. Phys. Lett. **91**, 053117 (2007)

Zaraska, L., Sulka, G.D., Jaskula, M.: Anodic alumina membranes with defined pore diameters and thicknesses obtained by adjusting the anodizing duration and pore opening/widening time. J. Solid State Electr. **15**, 2427–2436 (2011)

Zhiyong, F., Haleh, R., Jae-won, D., Aimee, M., Onur, E., Yu-Lun, C., Paul, W.L., Johnny, C.H., Toshitake, T., Lothar, A.R., Steven, N., Kyoungsik, Y., Ming, W., Joel, W.A., Ali, J.: Three-dimensional nanopillar-array photovoltaics on low-cost and flexible substrates. Nat. Mater. **8**, 648–653 (2009)

Chapter 7
Recent Developments in Multiscale Thermomechanical Analysis of Nanocomposites

J.N. Reddy, V.U. Unnikrishnan, and G.U. Unnikrishnan

Abstract Multifunctional nanocomposite materials have been used extensively in aerospace, mechanical, civil engineering industries, and other engineering applications. This is mainly due to the enhanced mechanical characteristics such as high strength-to-weight ratio and the unique thermal and physiochemical properties of these nanostructures. It has been reported that there are significant improvements in the thermal conductivity of composite structures with the addition of low volume fractions of graphene. To understand and develop efficient composite systems with desired thermal characteristics, it is necessary to develop accurate thermal transport models of these advanced composite systems. In this chapter, the authors discuss some of the recent developments in multiscale modeling of the thermal and mechanical properties of advanced nanocomposite systems. To enhance the theoretical model development discussed in this chapter, the authors have also included some relevant works from the literature.

7.1 Introduction

Carbon nanotubes are excellent alternatives to conventional materials used in modern electronic devices (Ezawa 2008; Geim and MacDonald 2007) and are considered to be the most important material used in modern industrial age, especially for thermal applications. Conductive nanostructures (such as carbon nanotubes and graphene) embedded in polymers or other high-strain alloys (the matrix phase), with appropriate network morphology and interface junctions

J.N. Reddy (✉) • G.U. Unnikrishnan
Department of Mechanical Engineering, Texas A&M University, College Station, TX 77843, USA
e-mail: jnreddy@tamu.edu; ginuuk@gmail.com

V.U. Unnikrishnan
Department of Aerospace Engineering & Mechanics, The University of Alabama, Tuscaloosa, AL 35487, USA
e-mail: vunnikrishnan@ua.edu

S.A. Meguid (ed.), *Advances in Nanocomposites*,
DOI 10.1007/978-3-319-31662-8_7

between the nano-constituents, are being studied for bridging material conductivity (electrical and thermal). However, commercial applications of these nanostructures remain limited due to the lack of understanding of the thermal flux change and dissipation characteristics of the nanocomposite materials. This difficulty can be overcome by developing multiscale computational models that consider the influence of materials at the nano- and macroscales. There has been tremendous effort to characterize the high thermal conductance properties of nanocomposites. Thermal interfacial effects are one of the most challenging properties to measure particularly at the nano- and microlevels (Pulavarthy and Haque 2015; Li et al. 2015). The effect of interfacial properties of the nanoparticles can significantly affect the overall effective behavior of composite system (Torquato and Rintoul 1995; Chapelle et al. 2009), especially the debonding characteristics and contact resistance at the interface, which can significantly affect the overall effective behavior of the composite. Thus, in this chapter, we focus on the recent developments in the theoretical formulations and associated computational procedures in the thermomechanical characterization of nanocomposite systems. Specifically, attention is devoted to examining the effect of the size of nanoparticles on the overall effective properties of composite systems. These formulations, which are multiphysical and multiscale in nature, can ascertain the thermal dissipation characteristics of composites (Brey and Fertig 2006; Stauber et al. 2007).

The estimation of thermal properties of the nanomaterials has been carried out by considering the effect of the "size" of the nanoparticle, excluding the geometry and material property. The size effect is considered as a resistance to the flow of thermal energy. There have been numerous attempts in the literature to characterize the size and interfacial property from an atomistic level to a continuum level using mean field theories (Nan et al. 1997, 2003; Unnikrishnan et al. 2008a, b; Duan and Karihaloo 2007; Shenogin et al. 2004; Bryning et al. 2005; Dunn and Taya 1993). The effect of the size of the nanoparticles on the thermal properties was developed by Duan and Karihaloo (2007). The effect of the size of the nanoparticles on the thermal properties of nanocomposite systems was studied using atomistic simulations of the interfacial thermal resistance (Unnikrishnan et al. 2008a, b, 2009). This was further extended to the study of the size parameter for different types of nanotube composite systems (Unnikrishnan 2015).

Following this brief "Introduction," the remainder of the chapter is organized as follows: estimation of interfacial thermal resistance of atomistic systems is discussed next, followed by a discussion on the study of the size of nanoparticles and their orientations. The chapter also presents some of the significant numerical results on the estimation of the overall effective thermal conductivities for pristine and defective nanotube-based composite systems. The chapter concludes with some results and discussion.

7.2 Atomistic Thermomechanical Properties of Nanostructures

Carbon nanotubes can be idealized as those formed by folding a (graphene) sheet made of graphene ring units into hollow cylinders, each of the carbon atoms having three nearest neighboring bonds. In a fully relaxed system, the angles between these bonds depend on the radius of the cylinder as well as on their orientation. The fundamental CNT structure can be classified into three categories in terms of their helicity: armchair, zigzag, and chiral. The properties of these atomistic systems at various configurations of the nanostructures can be studied more accurately using atomistic simulations when compared to experimental investigations. The experimental investigation is extremely difficult to conduct as it is difficult to obtain high-quality defect-free CNTs of sufficient length and purity. These physical processes (e.g., thermal) that occur at different spatial and temporal scales can be studied using atomistic simulations that can establish the mechanical properties as well as the thermal dissipation characteristics (Brey and Fertig 2006; Stauber et al. 2007) of the nanocomposite material.

The properties of nanomaterials estimated from these atomistic simulations are often found to be higher than the bulk properties of the same material (Clancy and Gates 2006). This is due to the degradation of higher-scale properties from the microscale imperfections in the bulk material. The accurate characterization of molecular interactions is not always straightforward as predicting the material properties like strength, thermal characteristics, and so on from principles of continuum mechanics (Reddy 2006, 2013).

Multiscale modeling of nano-reinforced polymeric systems, therefore, seeks an understanding of the atomistic- and macroscopic-level interactions. The mechanical properties of nanocomposite systems are often estimated using molecular dynamics (MD) simulations. A typical computational model of the carbon nanotube-based composite is shown in Fig. 7.1. In MD simulations, the motion of particles in an atomistic system is governed by the Hamiltonian and the Hamiltonian equations of motion. The variation of the potential energy with respect to the spatial distance gives the elastic constants for nanoparticles (Unnikrishnan and Reddy 2005; Blonski et al. 1994). The elastic moduli tensor components can be expressed as

$$C_{\alpha\beta\gamma\delta} = \frac{1}{2N\Omega_a}\sum_{j\neq i}\left[\left(\frac{\mathrm{d}^2U}{\mathrm{d}r_{ij}^2} - \frac{1}{r_{ij}}\frac{\mathrm{d}U}{\mathrm{d}r_{ij}}\right)a_{ij}^{\alpha}a_{ij}^{\beta}a_{ij}^{\gamma}a_{ij}^{\delta} + \delta_{\beta\delta}\underbrace{\frac{1}{r_{ij}}\frac{\mathrm{d}U}{\mathrm{d}r_{ij}}a_{ij}^{\alpha}a_{ij}^{\gamma}}_{A_{\alpha\gamma}=0}\right] \tag{7.1}$$

where $C_{\alpha\beta\gamma\delta}$ are the elastic moduli; $U = U\left(r_{ij}\right)$ is the strain energy as a function of interatomic distance r_{ij}; $A_{\alpha\gamma}$ is internal stress tensor, which at equilibrium is equal to zero; Ω_a is the average volume of an atom; N is the number of atoms; $\delta_{\alpha\beta}$ is the

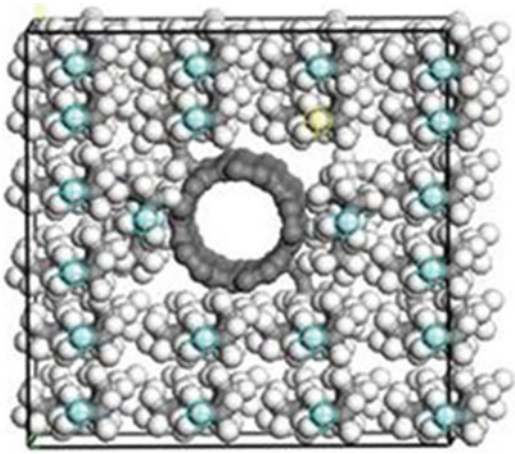

Fig. 7.1 Computational model of a nanotube embedded in polymer matrix

Kronecker delta symbol (i.e., components of identity tensor); a_{ij} is the undeformed value of r_{ij}, $u_{ij} = r_{ij} - a_{ij}$ with $u_{ij}^{\beta} = a_{ij}^{\alpha}\varepsilon_{\alpha\beta}$; $\varepsilon_{\alpha\beta}$ is the infinitesimal strain tensor between atoms i, j; and $\alpha, \beta, \gamma, \delta$ are the indices taking the values of the spatial dimensions.

Apart from the material deformation response characterization, the determination of thermal properties of nanomaterials has also received considerable attention lately, and this is primarily due to the different physical processes that play a role in an atomistic regime. Thermal transport properties of nanotubes can be estimated using MD simulations, which are conducted in equilibrium conditions under constant energy, temperature, atomic number, volume, or pressure. Increasingly, non-equilibrium MD method (NEMD) is also used to calculate the thermal properties of atomistic systems. In NEMD, a constant temperature difference or a heat flux is applied on the computational domain to simulate a heat source and sink. The thermal energy transport between these regions gives a direct indication of the thermal properties of the nano-systems (Feng et al. 2015; Mohebbi 2012; Mortazavi et al. 2012; Salaway and Zhigilei 2014).

Most of the experimental studies have shown that nanomaterials enhance the thermal properties of the ensuing composite; however, there is a large discrepancy in the accepted values, and there is a lack of understanding of the processes that depends on the *size*, which becomes highly significant as we go down the length scales. The interfacial thermal barrier resistance ($1/h_c$), also known as the Kapitza resistance, offers resistance to heat flow and reduces the effective conductivity of a fiber in a composite medium. This interfacial resistance is dependent on the time constant τ of temperature decay of a nanotube with the surrounding matrix depending on the nanotube heat capacity (C_T) and the thermal resistance of the nanotube-matrix interface R_k (see Fig. 7.2):

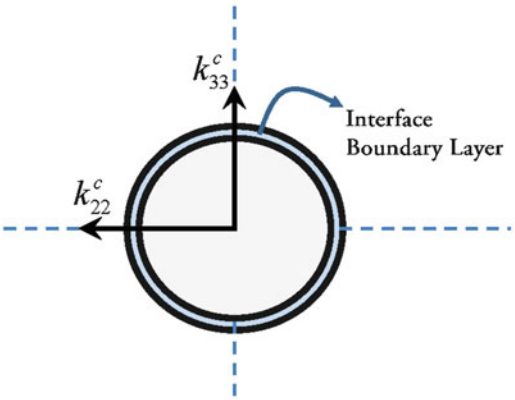

Fig. 7.2 Composite unit cell of a nanostructure with a thin interfacial thermal barrier layer

$$\tau = R_{\mathrm{k}}\left(\frac{1}{A_{\mathrm{T}}/C_{\mathrm{T}}}\right) \tag{7.2}$$

A_{T} is the area of the nanotube and $\frac{C_{\mathrm{T}}}{A_{\mathrm{T}}}$ is the heat capacity per unit area of the nanostructure which is usually taken as 5.6×10^{-4} J/m^2 K for carbon nanotubes. Let us consider a composite material having a dilute dispersion phase with thermal conductivity (κ_{p}) and interfacial thermal conductance h_{c} and embedded in a matrix having thermal conductivity κ_{m}. The effective transverse thermal conductivity of flat plates with half thickness $a/2$ with n dispersions per unit volume can be obtained using the modified *Maxwell-Raleigh theory* (see Hasselman and Johnson (1987)) as in Eq. (7.3):

$$\kappa_{\mathrm{e}} = \frac{\kappa_{\mathrm{p}}}{\left[\left(1 - \frac{\kappa_{\mathrm{p}}}{\kappa_{\mathrm{m}}} + \frac{2\kappa_{\mathrm{p}}}{ah_{\mathrm{c}}}\right)v_{\mathrm{p}} + \frac{\kappa_{\mathrm{p}}}{\kappa_{\mathrm{m}}}\right]} \tag{7.3}$$

At the interface, the normal component of heat flux is continuous (i.e., balanced) with $q_i^{(1)} n_i = q_i^{(2)} n_i$, where n_i are the direction cosines of the unit vector normal to the interfacial surface, while the temperature field is discontinuous (Benveniste 1987). The volume-averaged intensity ($\overline{\mathbf{H}}_i$) and flux fields $\overline{\mathbf{q}}_i$ over the interfacial surface are given by

$$\overline{\mathbf{H}}_i = -\frac{1}{V}\int_s \phi n_i \mathrm{d}S \tag{7.4}$$

$$\overline{\mathbf{q}}_i = -\frac{1}{V}\int_s q_i n_j x_i \mathrm{d}S \tag{7.5}$$

For a two-phase material with dilute dispersion phase consisting of a nanoparticle with thermal conductivity k_p and interfacial thermal conductance h_c and embedded in a matrix with thermal conductivity k_m, the effective thermal transport behavior is given by the averaged response of the two material phases having volume fraction ϕ. Thus, the averaged heat flux and temperature gradient under steady-state conditions without the heat source is given by

$$\langle \mathbf{q} \rangle_\mathrm{c} = \phi \langle \mathbf{q} \rangle_\mathrm{p} + (1-\phi)\langle \mathbf{q} \rangle_\mathrm{m} \tag{7.6}$$

$$\langle \mathbf{H} \rangle_\mathrm{c} = \phi \Big[\langle \mathbf{H} \rangle_\mathrm{p} + \mathbf{J} \Big] + (1-\phi)\langle H \rangle_\mathrm{m} \tag{7.7}$$

The average heat flux involves only the two terms for the matrix and the particle phase since the normal component of the heat flux is continuous across the interface between the nanoparticle and the matrix. The discontinuous temperature jump between the particle and matrix phase is indicated by $\mathbf{J}$ (Benveniste 1987), and the temperature jump is proportional to the normal heat flux across the interface as given by $\Delta T = -R_\mathrm{k}\mathbf{q}^n$. The particle with the interfacial thermal resistance is replaced by an equivalent particle having a perfect thermal interface in a self-consistent method, and the averaged heat flux is solved for a particle embedded in an unbounded matrix under uniform far-field heat flux (Yin et al. 2008), as given in Eq. (7.8). The average heat flux and temperature gradient are given by

$$\langle q_i \rangle_\Omega = \frac{1}{V^\Omega} \int_\Omega q_i(x) \ \mathrm{d}x \tag{7.8}$$

$$\langle H_i \rangle_\Omega = \frac{1}{V^\Omega} \left[\int_\Omega H_i(x) \ \mathrm{d}x + \int_{\partial\Omega} \Delta T(x) n_j \ \mathrm{d}S \right] \tag{7.9}$$

where $\langle q_i \rangle$, for example, is the jump in heat flux at the interface along the surface having an outward normal n_j (Unnikrishnan 2015). Thus, for a spherical nanoparticle with radius α, the effective thermal conductivity $\overline{k}_\mathrm{p}$ of the nanoparticle becomes (Yin et al. 2008) $\overline{k}_\mathrm{p} = \frac{k_\mathrm{p}}{1+\frac{R_\mathrm{k} k_\mathrm{p}}{\alpha}}$, where k_p is the original thermal conductivity of the particle.

Next, consider an ellipsoidal particle with an imperfect interface embedded in a matrix. The imperfect interface may be considered as a having thermal conductivity k_s and thickness δ. From the multiple scattering approach of Nan (1993), the equivalent thermal conductivity K^c_{ii} of the composite system along the symmetric axis of the unit cell is given by

$$K^\mathrm{c}_{ii} = K_\mathrm{s} \frac{K_\mathrm{s} + L_{ii}\big(K_\mathrm{p} - K_\mathrm{s}\big)(1-\nu) + \nu\big(K_\mathrm{p} - K_\mathrm{s}\big)}{K_\mathrm{s} + L_{ii}\big(K_\mathrm{p} - K_\mathrm{s}\big)(1-\nu)} \tag{7.10}$$

where $\nu = \frac{a_1^2 a_3}{(a_1+\delta)^2(a_3+\delta)}$ and K_p is the thermal conductivity of the ellipsoidal particle; a_1 and a_3 denote the major and the minor radii of the ellipsoidal particle, respectively, and L_{ii} is the geometrical parameter that depends on the particle size and shape as given by

$$L_{11} = L_{22} = \left\{ \begin{array}{ll} \dfrac{p^2}{2(p^2-1)} - \dfrac{p}{2(p^2-1)^{3/2}} \cosh^{-1} p, & \text{for} \quad p > 1 \\ \dfrac{p^2}{2(p^2-1)} - \dfrac{p}{2(1-p^2)^{3/2}} \cos^{-1} p, & \text{for} \quad p < 1 \end{array} \right\} \tag{7.11}$$

$$L_{33} = 1 - 2L_{11} \tag{7.12}$$

Here $p = \frac{a_3}{a_1}$ denotes the aspect ratio of the ellipsoid, and $p > 1$ and $p < 1$ are for a prolate (particle with $a_1 = a_2 < a_3$) and oblate (particle with $a_1 = a_2 > a_3$) ellipsoidal inclusion.

The interfacial thermal resistance R_k that offers resistance to heat flow reduces the effective conductivity of the nanoparticle in a composite medium (Jiajun and Xiao-Su 2004). This interfacial thermal resistance is dependent on the time constant τ of temperature decay of nanoparticle with the surrounding matrix, and it depends on the heat capacity C_τ and thermal resistance of the nanoparticle-matrix interface R_k (Shenogin et al. 2004; Clancy and Gates 2006; Huxtable et al. 2003). The effective thermal conductivity of the nanoparticle reinforced composite system using the self-consistent method is given by (see Yin et al. (2008) for details)

$$k^* = \frac{k_m}{\left(1 - 3\phi \frac{\overline{k}_p - k_m}{\overline{k}_p + 2k^*}\right)} \tag{7.13}$$

Similarly, the thermal conductivity of an equivalent ellipsoidal inclusion was obtained by Duan and Karihaloo (2007) for low conducting interfaces, and the effective thermal conductivity of this ellipsoidal inclusion was given in Eq. (7.14). Thus, the effective transverse thermal conductivity of the composite for aligned cylindrical fibers is given by

$$\overline{k}_p = \frac{k_p}{1 + R_k K_p S_{ir}\left(\frac{1}{a_r} + \frac{1}{b_r} + \frac{1}{c_r}\right)} \tag{7.14}$$

$$k_t^* = k_m + k_m \frac{\phi \xi_t}{\left(1 - \frac{\phi \xi_t}{2}\right)} \tag{7.15}$$

where $\xi_t = 2 \ \frac{\overline{k}_p^t - k_m}{\overline{k}_p^t + k_m}$ for cylindrical inclusions.

7.3 Results and Discussion

Consider a nanotube embedded in a polymer layer, as shown in Fig. 7.1, and heated to a required temperature. The general-purpose universal force field (UFF) of Cerius2 (version 4.6, Accelrys, Inc.) was used in the MD simulations with direct velocity scaling of the atoms of pristine nanotubes. Analyses were also carried out on defective nanotubes with one and two Stone-Wales defect (Pan et al. 2012; Ebrahimi 2015). The temperature of the individual atoms was prescribed to predefined temperatures (Clancy and Gates 2006; Yao and Lordi 1998). Once the central nanotube was brought to the required temperature, the entire ensemble was allowed to cool. From the cooling profile, the difference in temperature with time is shown for pristine nanotube in Fig. 7.3 and for nanotubes with defects at single and double locations in Figs. 7.4 and 7.5, respectively. A monotonic decay of the temperature, which follows an exponential order, is observed in these simulations. The interfacial thermal resistance value is estimated for single-walled nanotube embedded in LDPE as $5.05 \times 10^{-8} \mathrm{m}^2\mathrm{K/W}$ (Unnikrishnan et al. 2008a, 2009). The effect of the defects in single-walled nanotubes is found to decrease the interfacial thermal resistance values to 3.85×10^{-8} m^2 K/W and 4.42×10^{-8} m^2 K/W for one and two defects, respectively (Unnikrishnan et al. 2008a, 2009).

The nanotube can now be considered as a homogeneous material, which helps in expressing the heat transfer from the central nanotube to the surrounding polymer using various thermal measures, namely, the interfacial thermal resistance, the

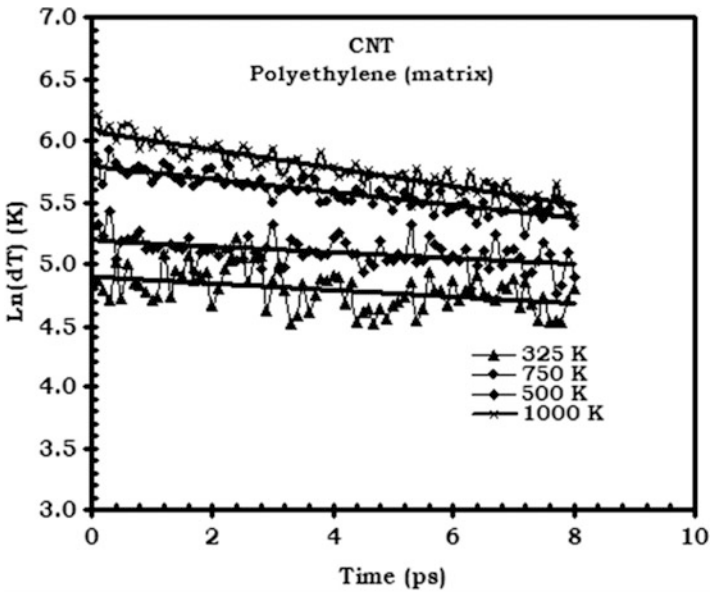

Fig. 7.3 Cooling profiles of pristine single-walled nanotube in LDPE

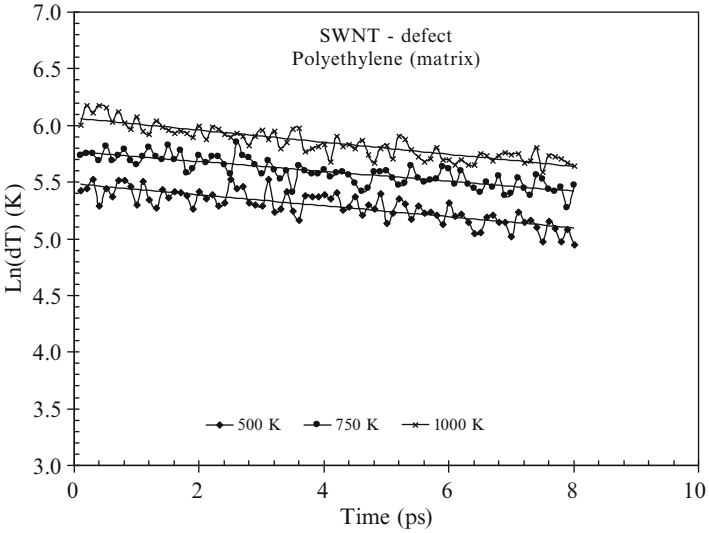

Fig. 7.4 Cooling profiles of single-walled nanotube in LDPE with a single Stone-Wales defect

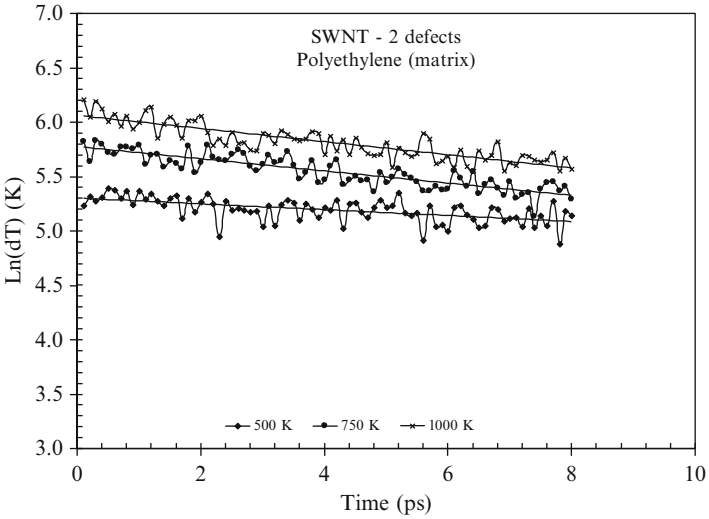

Fig. 7.5 Cooling profiles of single-walled nanotube in LDPE with a double Stone-Wales defect

thermal conductivity, and the size of the nanoparticle (Unnikrishnan et al. 2008a, 2009). It should be noted that, because of the interfacial boundary resistance, there exists a strong anisotropy in the thermal behavior of the nanomaterials. In the simulations, the thermal conductivity of the nanoparticle is taken as 6000 W/mK and for the matrix polyethylene (LDPE) is taken as 0.33 W/mK (Nan et al. 2004),

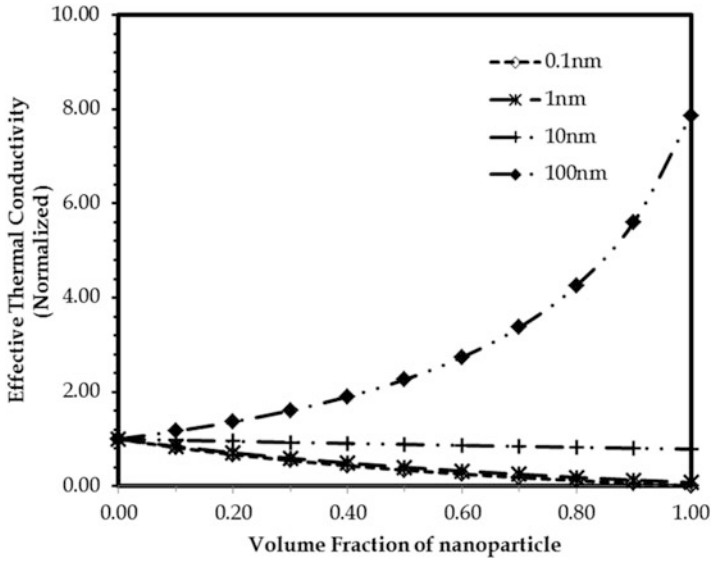

Fig. 7.6 Effective thermal conductivity of nanocomposite with aligned defective nanotube for varying radius of nanoparticle

and the variation of the effective thermal conductivity of the composite is calculated for various sizes of the nanoparticles with interfacial thermal resistance value of $3.5 \times 10^{-8} \mathrm{m^2K/W}$ using the self-consistent method.

The variation of the effective thermal conductivity of the composite was calculated for various sizes of the pristine and defective aligned nanotubes, as shown in Fig. 7.6. It is seen that the effect of larger sized nanoparticles increases the effective thermal conductivity of the composite while smaller scaled nanoparticles reduces the effective conductivity due to the predominance of the interfacial thermal resistance effects. The simulations also indicate that the thermal conductivity increased with decrease in the interfacial thermal resistance values as was expected.

7.4 Conclusions

Carbon nanotube and nanographene-based nanostructures have generated great interest, and they hold promise to be the next-generation materials for use in a variety of applications. This is attributed primarily to their high strength-to-weight ratio and unique thermal and physiochemical properties. In this work, recent developments in the thermal-mechanical analysis of carbon nanostructure with specific emphasis on the interfacial thermal characteristics have been discussed.

The thermomechanical analysis is carried out from the atomistic level using MD simulations, and the properties of interest are scaled to the macroscale using homogenization techniques to develop the overall thermal conductivity of the nanocomposite system.

Acknowledgments The authors would like to acknowledge the support of the Oscar S. Wyatt Endowed Chair, and they are also grateful to the Texas A&M University's Supercomputing Facility for providing the computational support and the Laboratory for Molecular Simulation in the Department of Chemistry at Texas A&M University for the software support. The second author would also like to acknowledge the support of the faculty start-up funds from The University of Alabama. The authors are also grateful to Professor Shaker Meguid for his invitation to prepare the manuscript and for his constructive comments on the manuscript.

References

Benveniste, Y.: Effective thermal conductivity of composites with a thermal contact resistance between the constituents: nondilute case. J. Appl. Phys. **61**, 2840–2843 (1987)

Blonski, S., Brostow, W., Kuba't, J.: Molecular-dynamics simulations of stress relaxation in metals and polymers. Phys. Rev. B **49**, 6494–6500 (1994)

Brey, L., Fertig, H.A.: Electronic states of graphene nanoribbons studied with the Dirac equation. Phys. Rev. B **73**, 235411 (2006)

Bryning, M.B., Milkie, D.E., Islam, M.F., Kikkawa, J.M., Yodh, A.G.: Thermal conductivity and interfacial resistance in single-wall carbon nanotube epoxy composites. Appl. Phys. Lett. **87**, 161909 (2005)

Chapelle, E., Garnier, B., Bourouga, B.: Interfacial thermal resistance measurement between metallic wire and polymer in polymer matrix composites. Int. J. Therm. Sci. **48**, 2221–2227 (2009)

Clancy, T.C., Gates, T.S.: Modeling of interfacial modification effects on thermal conductivity of carbon nanotube composites. Polymer **47**, 5990–5996 (2006)

Duan, H.L., Karihaloo, B.L.: Effective thermal conductivities of heterogeneous media containing multiple imperfectly bonded inclusions. Phys. Rev. B **75**, 064206 (2007)

Dunn, M.L., Taya, M.: The effective thermal conductivity of composites with coated reinforcement and the application to imperfect interfaces. J. Appl. Phys. **73**, 1711–1722 (1993)

Ebrahimi, S.: Influence of Stone–Wales defects orientations on stability of graphene nanoribbons under a uniaxial compression strain. Solid State Commun. **220**, 17–20 (2015)

Ezawa, M.: Graphene nanoribbon and graphene nanodisk. Phys. E. **40**, 1421–1423 (2008)

Feng, Y., Zhu, J., Tang, D.-W.: Molecular dynamics study on heat transport from single-walled carbon nanotubes to Si substrate. Phys. Lett. A **379**, 382–388 (2015)

Geim, A.K., MacDonald, A.H.: Graphene: exploring carbon flatland. Phys. Today **60**, 35–41 (2007)

Hasselman, D.P.H., Johnson, L.F.: Effective thermal conductivity of composites with interfacial thermal barrier resistance. J. Compos. Mater. **21**, 508–515 (1987)

Huxtable, S.T., Cahill, D.G., Shenogin, S., Xue, L., Ozisik, R., Barone, P., et al.: Interfacial heat flow in carbon nanotube suspensions. Nat. Mater. **2**, 731–734 (2003)

Jiajun, W., Xiao-Su, Y.: Effects of interfacial thermal barrier resistance and particle shape and size on the thermal conductivity of AlN/PI composites. Compos. Sci. Technol. **64**, 1623–1628 (2004)

Li, J., Wang, X., Qiao, Y., Zhang, Y., He, Z., Zhang, H.: High thermal conductivity through interfacial layer optimization in diamond particles dispersed Zr-alloyed Cu matrix composites. Scr. Mater. **109**, 72–75 (2015)

Mohebbi, A.: Prediction of specific heat and thermal conductivity of nanofluids by a combined equilibrium and non-equilibrium molecular dynamics simulation. J. Mol. Liq. **175**, 51–58 (2012)

Mortazavi, B., Rajabpour, A., Ahzi, S., Rémond, Y., Mehdi Vaez Allaei, S.: Nitrogen doping and curvature effects on thermal conductivity of graphene: a non-equilibrium molecular dynamics study. Solid State Commun. **152**, 261–264 (2012)

Nan, C.-W.: Physics of inhomogeneous inorganic materials. Prog. Mater. Sci. **37**, 1–116 (1993)

Nan, C.-W., Birringer, R., Clarke, D.R., Gleiter, H.: Effective thermal conductivity of particulate composites with interfacial thermal resistance. J. Appl. Phys. **81**, 6692–6699 (1997)

Nan, C.W., Shi, Z., Lin, Y.: A simple model for thermal conductivity of carbon nanotube-based composites. Chem. Phys. Lett. **375**, 666–669 (2003)

Nan, C.-W., Liu, G., Lin, Y., Li, M.: Interface effect on thermal conductivity of carbon nanotube composites. Appl. Phys. Lett. **85**, 3549–3551 (2004)

Pan, L., Shen, Z., Jia, Y., Dai, X.: First-principles study of electronic and elastic properties of Stone–Wales defective zigzag carbon nanotubes. Phys. B Condens. Matter **407**, 2763–2767 (2012)

Pulavarthy, R.A., Haque, M.A.: A novel technique for Interfacial Thermal Resistance measurement for nanoscale thin films. Int. J. Heat Mass Transf. **89**, 743–748 (2015)

Reddy, J.N.: An introduction to the finite element method, 3rd edn. McGraw-Hill, New York (2006)

Reddy, J.N.: An introduction to continuum mechanics, 2nd edn. Cambridge University Press, New York, NY (2013)

Salaway, R.N., Zhigilei, L.V.: Molecular dynamics simulations of thermal conductivity of carbon nanotubes: resolving the effects of computational parameters. Int. J. Heat Mass Transf. **70**, 954–964 (2014)

Shenogin, S., Xue, L., Ozisik, R., Keblinski, P., Cahill, D.G.: Role of thermal boundary resistance on the heat flow in carbon-nanotube composites. J. Appl. Phys. **95**, 8136–8144 (2004)

Stauber, T., Peres, N.M.R., Guinea, F.: Electronic transport in graphene: a semiclassical approach including midgap states. Phys. Rev. B **76**, 205423 (2007)

Torquato, S., Rintoul, M.D.: Effect of the interface on the properties of composite media. Phys. Rev. Lett. **75**, 4067–4070 (1995)

Unnikrishnan, V.U.: Interfacial thermal properties and size-effect in thermo-mechanical characterisation of nanocomposites. Nanomater. Energy **4**, 39–44 (2015)

Unnikrishnan, V.U., Reddy, J.N.: Characteristics of silicon doped carbon nanotube reinforced nanocomposites. Int. J. Multiscale Comput. Eng. **3**, 437–450 (2005)

Unnikrishnan, V.U., Banerjee, D., Reddy, J.N.: Atomistic-mesoscale interfacial resistance based thermal analysis of carbon nanotube systems. Int. J. Therm. Sci. **47**, 1602–1609 (2008a)

Unnikrishnan, V.U., Reddy, J.N., Banerjee, D., Rostam-Abadi, F.: Thermal characteristics of defective carbon nanotube-polymer nanocomposites. Interact. Multiscale Mech. **1**, 397–409 (2008b)

Unnikrishnan, V.U., Unnikrishnan, G.U., Reddy, J.N.: Multiscale nonlocal thermo-elastic analysis of graphene nanoribbons. J. Therm. Stresses **32**, 1087–1100 (2009)

Yao, N., Lordi, V.: Young's modulus of single-walled carbon nanotubes. J. Appl. Phys. **84**, 1939–1943 (1998)

Yin, H.M., Paulino, G.H., Buttlar, W.G., Sun, L.Z.: Effective thermal conductivity of functionally graded particulate nanocomposites with interfacial thermal resistance. J. Appl. Mech. **75**, 051113 (2008)

Chapter 8
Magnetoelectric Coupling and Overall Properties of a Class of Multiferroic Composites

Yang Wang and George J. Weng

Abstract In this chapter we present a widely useful composite model for the calculation of magnetoelectric coupling and all other properties of a two-phase multiferroic composite consisting of aligned piezomagnetic (or piezoelectric) spheroidal inclusions in a piezoelectric (or piezomagnetic) matrix. Both perfect and imperfect interface conditions are considered. Among the many features of the properties reported is the intriguing magnetoelectric coupling that signifies the "$0 + 0 \rightarrow 1$" product effect of the multiferroic composite. It is also reported that, due to the piezoelectric-piezomagnetic interaction, the elastic C_{44} of the composite can be substantially higher than that of either of the two phases. We have used the theory to calculate the 17 independent material constants: 5 elastic, 3 piezoelectric, 3 piezomagnetic, 2 dielectric, 2 magnetic, and 2 magnetoelectric coefficients of a transversely isotropic $BaTiO_3$-$CoFe_2O_4$ composite, and show how these magneto-electro-elastic constants depend on the volume concentration, aspect ratio of inclusions, and the interface condition. We conclude by pointing out that a weak interface model is often required to capture the experimentally measured data of a bulk multiferroic composite.

8.1 Introduction

A multiferroic composite generally refers to a two-phase composite involving two ferroic phases. Most notable among them is the piezoelectric-piezomagnetic composite. The piezoelectric phase, such as barium titanate ($BaTiO_3$, or BTO), lead zirconium titanate (PZT), and lead magnesium titanate-lead titanate (PMT-PT), is generally transversely isotropic, and so is the piezomagnetic phase, such as cobalt ferrite ($CoFe_2O_4$, or CFO), Terfenol-D, lanthanum strontium manganite (LSMO), and nickel ferrite (NFO). In such composites, strong coupling tends to develop

Y. Wang • G.J. Weng (✉)
Department of Mechanical and Aerospace Engineering, Rutgers University, New Brunswick, NJ 08903, USA
e-mail: yang.wang@rutgers.edu; weng@jove.rutgers.edu

S.A. Meguid (ed.), *Advances in Nanocomposites*,
DOI 10.1007/978-3-319-31662-8_8

among the elastic, piezoelectric, dielectric, piezomagnetic, and magnetic properties of the constituent phases. These coupling effects can lead to some unique overall properties for the composite. Among the most intriguing features of the coupled effects is the generation of the magnetoelectric coupling coefficients, α_{33} and α_{11}, which are absent in either the piezoelectric or the piezomagnetic phase alone. This property enables the composite to exhibit magnetization under an electric field, and electric polarization under a magnetic field. It is the so-called "$0 + 0 \rightarrow 1$" product effect that makes this class of composite so appealing. For instance, in information storage this coupling allows the data to be written electronically and read magnetically; it does not require the generation of a strong local magnetic field to write. In addition, the strong coupling can also make the elastic constant, C_{44}, of the composite greater than that of either phase. The unique and strong properties generated in multiferroic composites due to the magneto-electro-elastic coupling make them highly attractive for applications that require the exchange and interaction of mechanical, electrical, and magnetic energies. They are also useful as sensors, actuators, transducers, and high-frequency devices whose properties need to be tuned electrically or magnetically.

These potential applications and the desire to understand the underlying mechanism of magneto-electro-elastic coupling were what motivated us to undertake this study. In this work, we will consider a two-phase composite consisting of aligned spheroidal piezomagnetic (or piezoelectric) inclusions embedded in a piezoelectric (or piezomagnetic) matrix, as depicted in the general sketch of Fig. 8.1a, to develop the theory and examine the overall characteristics of the multiferroic composite. Here the aspect ratio (length-to-diameter ratio) of the inclusions can be 1, ∞, or 0 that respectively represents the particulate, fibrous, and multilayered composites. These three types are also shown in Fig. 8.1b–d that display the commonly referred 0-3, 1-3, and 2-2 connectivities. The inclusion shape in the intermediate state can be oblate or prolate that, as the particulate one, also belongs to 0-3 connectivity. In addition, the interface between the two phases may or may not be perfect. Both phases will be taken to be transversely isotropic, with direction 3 representing the symmetric axis and plane 1-2 isotropic. In such a system the composite as a whole is also transversely isotropic. It has 17 independent material constants, whereas the piezoelectric or the piezomagnetic phase each has 12. The objective of this study is to find all these 17 independent magneto-electro-elastic constants of the multiferroic composite in terms of the 12 independent constants of each phase, and the volume concentration, c_1, and aspect ratio, α, of the inclusions under both perfect and imperfect interface conditions.

We will first introduce a homogenization theory for its overall property under both perfect and imperfect interface conditions, and then use the properties of $BaTiO_3$ (or BTO) and $CoFe_2O_4$ (or CFO) to represent the piezoelectric and the piezomagnetic phase, respectively, to calculate and illustrate the general characteristics of the 17 overall constants for both CFO-in-BTO and BTO-in-CFO composites. Then the results with a weak interface are discussed. In this way we will be able to make a direct comparison between the two systems to draw the conclusion whether CFO-in-BTO will perform better than BTO-in-CFO in terms of the

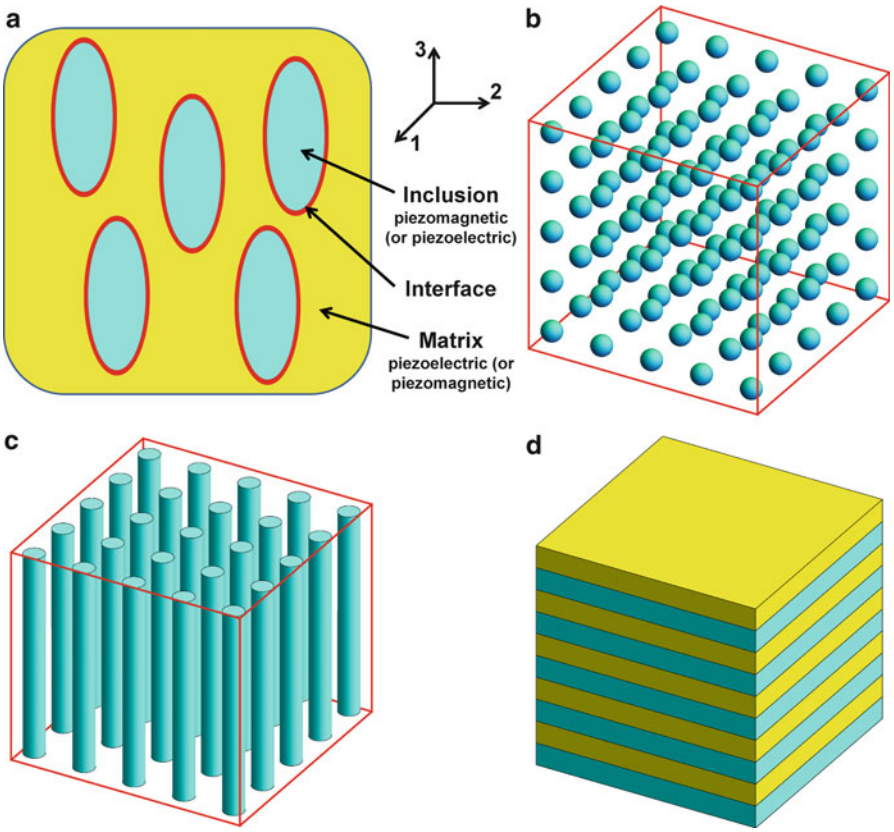

Fig. 8.1 Schematics of the piezoelectric/piezomagnetic multiferroic composite with an interface: (**a**) general aligned spheroidal inclusions, (**b**) particulate composite with 0-3 connectivity ($\alpha = 1$), (**c**) fibrous composite with 1-3 connectivity ($\alpha - \infty$), and (**d**) multilayers with 2-2 connectivity ($\alpha \to 0$). In calculations $BaTiO_3$ (or BTO) and $CoFe_2O_4$ (or CFO) are taken as the piezoelectric and piezomagnetic phases, respectively

generated magnetoelectric coupling coefficients and other magneto-electro-elastic constants at the same volume concentration of the piezomagnetic or piezoelectric phase. We will also be able to see to what extent an imperfect interface, that is, a weak interface, could adversely affect the generated magnetoelectric coupling coefficients and other constants.

In retrospect, the magnificent feature of "$0 + 0 \to 1$" product effect was long reported (van Suchtelen 1972), but it was not until the Green's function formulation put forward by Nan (1994) that a sound theoretical treatment was given. Nan also used the properties of CFO and BTO as the model constituents to compute the aspect-ratio dependence of the magnetoelectric coupling coefficients, α_{33} and α_{11}. On a more restricted basis a square block model was earlier adopted by

Harshé et al. (1993) and a multilayer model considered by Avellaneda and Harshé (1994). Soon after, Benveniste (1995) also presented a theory in a spirit related to Hill (1964) and Milgrom and Shtrikman (1989) to determine the magnetoelectric coupling of a fibrous piezoelectric-piezomagnetic composite. The explicit expressions of the coupling coefficient, α_{33}, of the fibrous composite given by Nan (1994) and Benveniste (1995) are particularly enlightening, as the expressions vividly show how the elastic, piezoelectric, and piezomagnetic constants of the constituent phases jointly contribute to this magnetoelectric coupling coefficient. It is often said that magnetoelectric coupling of a piezoelectric phase and a piezomagnetic phase is created by the compatibility of their elastic strains, but these explicit results have made it clear that it is not just the elastic constants, but also the piezoelectric and the piezomagnetic constants, that jointly play the role for the transmission from electric to magnetic field, or from magnetic to electric field, to create the magnetoelectric coupling of a multiferroic fibrous composite.

A critical issue in Nan's Green's function approach was the evaluation of Eshelby's S-tensor (1957) of an ellipsoidal inclusion in the context of piezoelectric (or piezomagnetic) response. This issue was not directly confronted within Nan's paper, as the study of Green's function in a transversely isotropic piezoelectric (or piezomagnetic) medium was still in its infant stage in the early 1990s. To this writer's recollection, the first paper to analyze the Green's function of a 3-D piezoelectric material was published by Wang (1992), but immediately also by Chen (1993a, b, 1997), Dunn and Taya (1993a), and Dunn and Wienecke (1996). During this period, the explicit components of the S-tensor for the fibrous and the lamellar inclusion began to emerge, as reported by Dunn and Taya (1993b), Dunn (1994), Huang and Yu (1994), Huang (1998), Huang et al. (1998), Li and Dunn (1998a), and Mikata (2000, 2001). But so far no explicit expressions have been derived for the spherical inclusion in a transversely isotropic piezoelectric (or piezomagnetic) matrix, or for the general ellipsoid. This issue remains a challenge at present.

The progress in the formulation of Green's function and Eshelby's S-tensor has made it possible for the study of effective properties of transversely isotropic piezoelectric composites containing spheroidal inclusions. Most notably among them are the works of Huang and Kuo (1997), Li and Dunn (1998b), and Srinivas et al. (2006), in addition to Nan's seminal work. The availability of explicit formulae for the S-tensor of a flat lamina and long circular cylinder has also greatly facilitated the study of piezoelectric multilayered structures and fibrous systems. For details one may refer to Kuo et al. (2010), Bichurin et al. (2003), Wang et al. (2012), Liu and Kuo (2012), Kuo and Bhattacharya (2013), Chen et al. (2014), and Liu et al. (2014), among others.

Nevertheless, all of these works were concerned with the perfect interface case. In contrast there have been very few studies on the magnetoelectric coupling of multiferroic composites with an imperfect interface. It appears that the first one to undertake such a study was by Wang and Pan (2007) for the case of a fibrous composite. They conducted a 2-D study under the transverse electric and magnetic fields and longitudinal axial shear loading. The imperfect interface was modeled by

the jump conditions of axial displacement and electric and magnetic potentials across the fiber-matrix interface. Then, a complex variable approach was adopted to find the 2-D average field, and, finally, the Mori-Tanaka method was employed to calculate the overall property of the imperfectly bonded fibrous composite. Later Dinzart and Sabar (2012), Kuo (2013), and Yue and Xu (2013) have also considered a similar issue for the fibrous composites. The approach of Dinzart and Sabar (2012) was very similar to that of Wang and Pan (2007). On the other hand, Kuo (2013) has extended Rayleigh's analysis of periodic conditions to the coupled, imperfectly bonded interface, while Yue and Xu (2013) have instead used Taylor's expansion to solve the fields in the interphase. These few works have all pointed to the significance of interface conditions in magnetoelectric coupling, but so far the focus of interface effects has been limited to the fibrous composites.

We now return to the composite model depicted in Fig. 8.1. To address the stated problem the constitutive equations of the constituent phases and the multiferroic composite will be recalled first, in Sect. 8.2. A homogenization theory with a perfect interface will be provided in Sect. 8.3, and another one with an imperfect interface given in Sect. 8.4. The 17 constants of the multiferroic composite will be calculated and discussed in Sect. 8.5, where the importance of the imperfect interface model will also be highlighted. We will conclude in Sect. 8.6, and add several useful information in the Appendix.

8.2 The Coupled Magneto-Electro-Elastic Constitutive Equations

The piezoelectric or the piezomagnetic phase has its usual electroelastic or magnetoelastic coupling, but neither has the magnetoelectric coupling. The multiferroic composite, however, has them all. The coupled linear relations involve six physical quantities: mechanical stress σ and strain ε, electric displacement D and electric field E, and magnetic flux density B and magnetic field H, all in tensors or vectors. As shown in Appendix 1, there are eight different ways to write the constitutive equations. But here we choose σ, D, and B as one pair and ε, E, and H as the other. This choice has the virtue that the quantities of the former group all satisfy the divergence-free condition whereas the latter can all be derived from the appropriate potentials. In indicial notations they satisfy

$$\sigma_{ij,j} = 0, \qquad D_{i,i} = 0, \qquad B_{i,i} = 0. \tag{8.1}$$

$$\varepsilon_{ij} = \frac{1}{2}\left(u_{i,j} + u_{j,i}\right), \qquad E_i = -\phi_{,i}, \qquad H_i = -\varphi_{,i}, \tag{8.2}$$

where u_i is the displacement vector, and ϕ and φ are the electric and magnetic potentials, respectively. The first equation in Eq. (8.1) is the mechanical equilibrium in the absence of body force and the remaining two are the quasi-static form of

Maxwell's equations in the absence of free charges. The coupled constitutive equations can be written as

$$\begin{aligned} \sigma &= \mathbf{C}_{\varepsilon} - \mathbf{e}^{\mathrm{T}} E - \mathbf{q}^{\mathrm{T}} H, \\ D &= \mathbf{e}\varepsilon + \kappa E + \alpha H, \\ B &= \mathbf{q}\varepsilon + \alpha E + \mu H, \end{aligned} \tag{8.3}$$

where the diagonal terms $\mathbf{C}$, $\boldsymbol{\kappa}$, and $\boldsymbol{\mu}$ are the elastic stiffness tensor (measured at constant electric and magnetic fields), electric permittivity tensor (measured at constant strain and magnetic field), and magnetic permeability tensor (measured at constant strain and electric field), respectively. The off-diagonal $\mathbf{e}$ and $\mathbf{q}$ are the piezoelectric and piezomagnetic constant tensors, and the off-diagonal $\boldsymbol{\alpha}$ is the magnetoelectric coupling coefficient tensor. The superscript T stands for the transpose (note that $\boldsymbol{\alpha}$ in bold face is a tensor, with the components, α_{33} and α_{11} $(= \alpha_{22})$, but α in scalar is the aspect ratio of inclusions).

This set of constitutive equations can be cast in a unified notation in matrix form, as

$$\mathbf{X}_i = \mathbf{L}_{ij}\mathbf{Y}_j, \qquad i,j = 1 \sim 12, \tag{8.4}$$

where

$$\begin{aligned} \mathbf{X} &= [\sigma,\ D,\ B]^{\mathrm{T}} = [\sigma_1\ \sigma_2\ \sigma_3\ \sigma_4\ \sigma_5\ \sigma_6\ D_1\ D_2\ D_3\ B_1\ B_2\ B_3]^{T}, \\ \mathbf{Y} &= [\varepsilon,\ -E,\ -H]^{\mathrm{T}} = [\varepsilon_1\ \varepsilon_2\ \varepsilon_3\ \varepsilon_4\ \varepsilon_5\ \varepsilon_6\ -E_1\ -E_2\ -E_3\ -H_1\ -H_2\ -H_3]^{T}, \end{aligned} \tag{8.5}$$

and

$$\mathbf{L} = \begin{bmatrix} \mathbf{C} & \mathbf{e}^{\mathrm{T}} & \mathbf{q}^{\mathrm{T}} \\ \mathbf{e} & -\kappa & -\alpha \\ \mathbf{q} & -\alpha & -\mu \end{bmatrix}. \tag{8.6}$$

Both $\mathbf{X}$ and $\mathbf{Y}$ are 12-dimensional vectors, and $\mathbf{L}$ is a 12×12 matrix, which includes $\mathbf{C}$ as a 6×6, $\mathbf{e}$ and $\mathbf{q}$ as a 3×6, and $\boldsymbol{\kappa}$, $\boldsymbol{\alpha}$, and $\boldsymbol{\mu}$ as a 3×3 matrix. The matrix $\mathbf{L}$ is the magneto-electro-elastic moduli matrix. If $\mathbf{L}$ is transversely isotropic along direction-3 as is the case in the present study, it can be simplified to

$$\mathbf{L}=\begin{bmatrix} C_{11} & C_{12} & C_{13} & 0 & 0 & 0 & 0 & 0 & e_{31} & 0 & 0 & q_{31} \\ C_{12} & C_{11} & C_{13} & 0 & 0 & 0 & 0 & 0 & e_{31} & 0 & 0 & q_{31} \\ C_{13} & C_{13} & C_{33} & 0 & 0 & 0 & 0 & 0 & e_{33} & 0 & 0 & q_{33} \\ 0 & 0 & 0 & C_{44} & 0 & 0 & 0 & e_{15} & 0 & 0 & q_{15} & 0 \\ 0 & 0 & 0 & 0 & C_{44} & 0 & e_{15} & 0 & 0 & q_{15} & 0 & 0 \\ 0 & 0 & 0 & 0 & 0 & C_{66} & 0 & 0 & 0 & 0 & 0 & 0 \\ 0 & 0 & 0 & 0 & e_{15} & 0 & -\kappa_{11} & 0 & 0 & -\alpha_{11} & 0 & 0 \\ 0 & 0 & 0 & e_{15} & 0 & 0 & 0 & -\kappa_{11} & 0 & 0 & -\alpha_{11} & 0 \\ e_{31} & e_{31} & e_{33} & 0 & 0 & 0 & 0 & 0 & -\kappa_{33} & 0 & 0 & -\alpha_{33} \\ 0 & 0 & 0 & 0 & q_{15} & 0 & -\alpha_{11} & 0 & 0 & -\mu_{11} & 0 & 0 \\ 0 & 0 & 0 & q_{15} & 0 & 0 & 0 & -\alpha_{11} & 0 & 0 & -\mu_{11} & 0 \\ q_{31} & q_{31} & q_{33} & 0 & 0 & 0 & 0 & 0 & -\alpha_{33} & 0 & 0 & -\mu_{33} \end{bmatrix}. \tag{8.7}$$

This matrix involves 17 independent material constants (note: $C_{66}=(C_{11}-C_{12})/2$): five elastic ones, C_{11}, C_{12}, C_{13}, C_{33}, C_{44}; two dielectric ones, κ_{33} and κ_{11}; two magnetic ones, μ_{33} and μ_{11}; three piezoelectric ones, e_{31}, e_{33}, and e_{15}; three piezomagnetic ones, q_{31}, q_{33}, and q_{15}; and two magnetoelectric ones, α_{33} and α_{11}, for the multiferroic composite. But for the piezoelectric phase the piezomagnetic q-components and the magnetoelectric α-components are all zero, and for the piezomagnetic phase the piezoelectric e-components and the magnetoelectric α-components are also zero. This makes the constituent piezoelectric and piezomagnetic phases have 12 independent constants each. It is the determination of these 17 independent constants of the multiferroic composite that is the objective of this study.

In this formulation we have chosen the negative $-E_i$ and $-H_i$ as the input variables so that matrix $\mathbf{L}$ can be diagonally symmetric. Such a diagonal symmetry for the constituent phases will ensure its product with Eshelby's S-tensor—which is not diagonally symmetric for a general spheroid—to recover the diagonal symmetry for the effective $\mathbf{L}$ of the composite. This occurs in Eq. (8.8) below for the $\mathbf{S}\mathbf{L}_0{}^{-1}$-term.

8.3 The Effective Magneto-Electro-Elastic Tensor, L, of the Composite with a Perfect Interface

With the inclusion-matrix microgeometry shown in Fig. 8.1, the Mori-Tanaka method is the most convenient one to apply. In the elastic context this approach has been extensively discussed by Weng (1984, 1990) and Benveniste (1987). Its extension to this coupled problem is direct with the proper choice of the field

quantities. By taking the inclusions as phase 1 and matrix as phase 0, and then denoting their respective volume concentrations as c_1 and c_0, and phase moduli as $\mathbf{L}_1$ and $\mathbf{L}_0$, respectively, the effective magneto-electro-elastic moduli tensor of the composite can be written analogously as (Weng 1984)

$$\mathbf{L} = \mathbf{L}_0 + c_1(\mathbf{L}_1 - \mathbf{L}_0)\left[\mathbf{I} + c_0\mathbf{S}\mathbf{L}_0{}^{-1}(\mathbf{L}_1 - \mathbf{L}_0)\right]^{-1}, \tag{8.8}$$

where $\mathbf{S}$ is Eshelby's S-tensor of the ellipsoidal inclusion in the matrix phase which can be piezoelectric or piezomagnetic. With the exception of a fibrous composite (1-3 connectivity) or a multilayered structure (2-2 connectivity), its components cannot be written explicitly but can be evaluated numerically. We have adopted a Gaussian quadrature procedure to calculate these components. It is outlined in Appendix 2, where the explicit components of S-tensor for both fibrous and multilayered composites are also given in Eq. (8.22).

Equation (8.8) enables us to determine the needed 17 constants of $\mathbf{L}$ from $\mathbf{L}_1$ and $\mathbf{L}_0$, at a given volume concentration, c_1, and aspect ratio, α, of inclusions. This moduli tensor also has the virtue that it always stays on or within the Willis bounds (1977); it will never violate the bounds (see Weng 1992).

8.4 The Influence of an Imperfect Interface on L

To treat the effect of an imperfect interface as shown in Fig. 8.1, we assume that there exists a very thin layer of interphase. This thin layer is taken to be on the surface of the inclusion which could be piezomagnetic or piezoelectric. Together they form a thinly coated inclusion. The volume concentration of the interphase in the coated inclusion is denoted as c_{int}, and that of the remaining inclusion as $(1 - c_{\text{m}})$. Due to the amorphous nature of the interphase, its property will be assumed to be isotropic, with no piezoelectric, piezomagnetic, or magneto-electric coupling. So there are only four independent constants for the interphase moduli, $\mathbf{L}_{\text{int}}$; that is, $\mathbf{L}_{\text{int}} = \left(C_{11}^{\text{int}},\ C_{44}^{\text{int}},\ \kappa^{\text{int}},\ \mu^{\text{int}}\right)$ and its form is given in Appendix 2. But tensor $\mathbf{L}_1$ of the inclusion remains transversely isotropic as before. By treating the interphase as the matrix phase in this thinly coated inclusion, the effective moduli tensor of this coated inclusion, denoted by $\mathbf{L}_{\text{coat}}$, follows analogously from Eq. (8.8), as

$$\mathbf{L}_{\text{coat}} = \mathbf{L}_{\text{int}} + (1 - c_{\text{int}})(\mathbf{L}_1 - \mathbf{L}_{\text{int}})\left[\mathbf{I} + c_{\text{int}}\mathbf{S}_{\text{int}}\mathbf{L}_{\text{int}}{}^{-1}(\mathbf{L}_1 - \mathbf{L}_{\text{int}})\right]^{-1}. \tag{8.9}$$

This S-tensor, denoted as $\mathbf{S}_{\text{int}}$, implies that its components are evaluated with the property of the isotropic $\mathbf{L}_{\text{int}}$. These components are known explicitly; we have also listed them in Eq. (8.22) of Appendix 2.

The overall property, $\mathbf{L}$, of the multiferroic composite with an imperfect interface can be evaluated from Eq. (8.8) again by replacing $\mathbf{L}_1$ there by $\mathbf{L}_{\text{coat}}$. This

two-step procedure will give rise to a reduced **L** due to the reduction of field transfer from the matrix to the inclusion across the interface.

Both Eqs. (8.8) and (8.9) are explicit, but their simplicity can be deceiving, as Eq. (8.8) involves some heavy computations during the evaluation of S-tensor of the transversely isotropic spheroidal piezoelectric (or piezomagnetic) inclusion. The general spheroidal shape of the inclusion and the anisotropic piezoelectric (or piezomagnetic) matrix property are what make it complicated, but for the α_{33} and α_{11} of 1-3 and 2-2 composites, we have worked out a set of explicit formulae under both perfect and imperfect interface conditions. Due to the importance of these two quantities, we have added an Appendix 3 to provide the explicit forms of α_{33} and α_{11} under both perfect and imperfect interface conditions.

8.5 Results and Discussion

The established theory allows us to calculate all the 17 independent components of the effective magneto-electro-elastic moduli tensor, **L**, for the piezoelectric-piezomagnetic multiferroic composite. We now use the property of $BaTiO_3$ (BTO) as the piezoelectric phase and that of $CoFe_2O_4$ (CFO) as the piezomagnetic phase to present the calculated results. BTO and CFO are two widely considered piezoelectric and piezomagnetic materials. Even though the CFO-BTO composite systems have been considered before, very few covered the entire range of aspect ratio, and none addressed the issue of an imperfect interface of spheroidal inclusions. So the results reported here could have benchmark value. Their properties are also listed in Table 8.1.

With this set of phase properties, the two magnetoelectric α_{ij}, two dielectric κ_{ij}, two magnetic μ_{ij}, three piezoelectric e_{ij}, three piezomagnetic q_{ij}, and five elastic C_{ij} of tensor **L** under a perfect interface can be calculated from Eq. (8.8). To calculate the properties under the imperfect interface condition, the following interphase properties—taken from Wang et al. (2015)—will be adopted:

$$\begin{aligned} &C_{11}^{\text{int}} = 3 \times 10^9 \text{Pa}, \quad C_{44}^{\text{int}} = 1 \times 10^9 \text{Pa}; \\ &\kappa^{\text{int}} = 2\varepsilon_0, \qquad \varepsilon_0 = 8.854 \times 10^{-22} \text{F/m}, \text{vacuum permittivity}; \\ &\mu^{\text{int}} = 2\mu_0, \qquad \mu_0 = 1.257 \times 10^{-6} \text{H/m}, \text{vacuum permeability}. \end{aligned} \tag{8.10}$$

Initially the interphase volume concentration, c_{int}, is taken to be 0.01 (1 % of the coated inclusion), but to guarantee it to reduce to zero as c_1 reaches 1, we take it to depend on c_1 as

$$c_{\text{int}} = 0.01 \times [1 - F(c_1; 20, 1)], \tag{8.11}$$

where F is the cumulative distribution function of the Bata distribution. The nature of this c_{int} is plotted in Fig. 8.2 along with the $c_{\text{int}} = 0.01$ used in Wang et al. (2015)

Table 8.1 Material constants used in numerical calculations

Source	Huang and Kuo (1997) and Li and Dunn (1998a, b)		Harshé et al. (1993)	
Matrix phase	BTO	CFO	BTO	CFO
C_{11} GPa	166	286	283	284
C_{12} GPa	77	173	186	171
C_{13} GPa	78	170	142	168
C_{33} GPa	162	269.5	178	268
C_{44} GPa	43	45.3	43	45.3
e_{31} C/m^2	−4.4	0	−9.69	0
e_{33} C/m^2	18.6	0	11.7	0
e_{15} C/m^2	11.6	0	11.6	0
q_{31} N/(A·m)	0	550	0	574
q_{33} N/(A·m)	0	580.3	0	695
q_{15} N/(A·m)	0	699.7	0	550
κ_{11} C^2/(N·m^2)	11.2×10^{-9}	0.08×10^{-9}	11.2×10^{-9}	0.08×10^{-9}
κ_{33} C^2/(N·m^2)	12.6×10^{-9}	0.093×10^{-9}	8.2×10^{-9}	0.089×10^{-9}
μ_{11} N/A^2	5×10^{-6}	590×10^{-6}	5×10^{-6}	590×10^{-6}
μ_{33} N/A^2	10×10^{-6}	157×10^{-6}	10×10^{-6}	157×10^{-6}

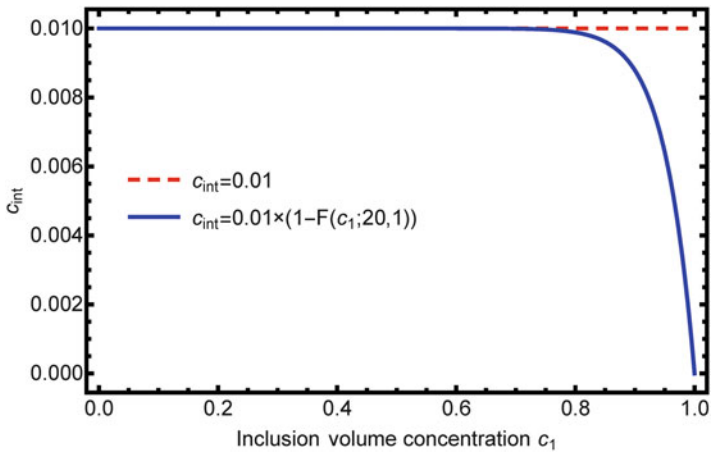

Fig. 8.2 Variation of volume concentration of interphase c_{int} as c_1 increases

in the evaluation of α_{33} and α_{11}. It can be seen that there is little difference between the two when $c_1 < 0.8$, but this new interface model has the virtue that the interface will disappear as $c_1 \to 1$, whereas the former still retains a finite $c_{\text{int}} = 0.01$. While this is not a critical issue for the calculation of α_{33} and α_{11} because the interphase possesses no α_{33} or α_{11}, it becomes a problem for the evaluation of other constants, such as C_{ij}, κ_{ij}, and μ_{ij}, where the different values of these constants in the

interphase will not bring the composite property back to that of inclusions as $c_1 \to 1$. Since all the 17 material constants are to be evaluated here, this new interphase function is deemed to be more appropriate.

In what follows, the results for the perfect interface will be given first, followed by those with an imperfect interface. To make a direct comparison between the CFO-in-BTO and BTO-in-CFO composites, we will present their results in parallel, in (a) and (b), for each figure.

8.5.1 Effective Properties of CFO-in-BTO and BTO-in-CFO Composites with a Perfect Interface

8.5.1.1 The Magnetoelectric Coupling Coefficients, α_{33} and α_{11}

This set of properties is often referred to as the figure of merits in a multiferroic composite. It is the true expression of the "$0 + 0 \to 1$" product effect. The magnitude—especially its maximum—signifies its potential for applications in many electronic devices.

For α_{33}, its c_1-dependences at five aspect ratios of inclusions, $\alpha = 0$, 0.5, 1, 10, and ∞, are displayed in Fig. 8.3a for the CFO-in-BTO composite, and in Fig. 8.3b for BTO-in-CFO. This quantity represents the induced axial magnetization, B_3, under a unit axial electric field, E_3, or conversely, the induced axial electric displacement, D_3, under a unit axial magnetic field, H_3, of the composite. From both figures it can be observed that, in this axial direction, fibrous composite always provides the strongest magnetoelectric coupling. Its 1-3 connectivity is strongly favored over other microstructures, including the particle-type 0-3 connectivity of all aspect ratios, such as $\alpha = 0.5$, 1, and 10, and the 2-2 multilayers with $\alpha \to 0$. For CFO-in-BTO, the maximum coupling occurs at around $c_1 = 0.56$, with a magnitude of about $30 \times 10^{-10}\mathrm{C}/(\mathrm{A} \cdot \mathrm{m})$. The maximum value steadily decreases as the aspect ratio of inclusions decreases, down to almost zero with the lamellar structure. The data for BTO-in-CFO in Fig. 8.3b show a similar trend. The maximum of the

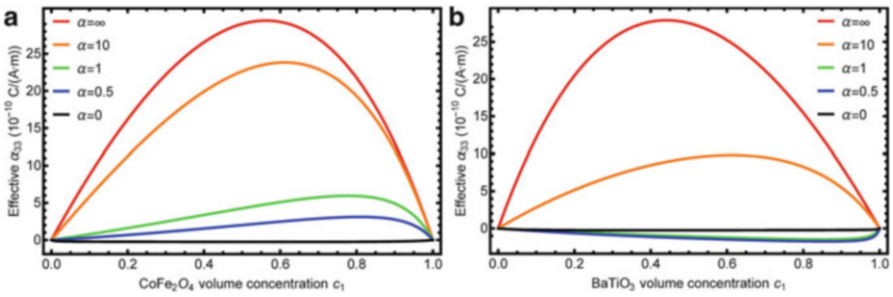

Fig. 8.3 The c_1 dependence of the magnetoelectric coefficient α_{33}: (**a**) CFO-in-BTO and (**b**) BTO-in-CFO

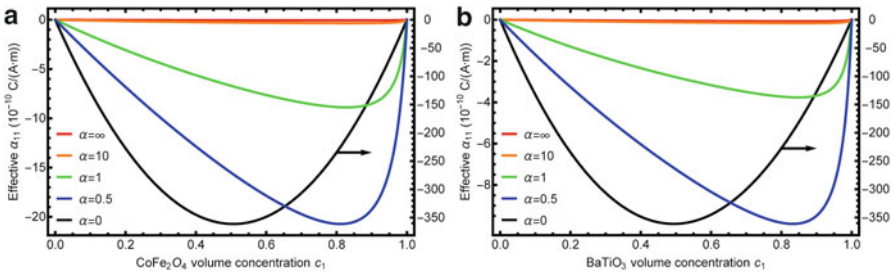

Fig. 8.4 The c_1 dependence of the magnetoelectric coefficient α_{11}: (**a**) CFO-in-BTO and (**b**) BTO-in-CFO

fibrous composite occurs at around $c_1 = 0.44$, which is 0.56 in terms of the volume concentration of CFO, as in Fig. 8.3a, but its value at $28 \times 10^{-10}\mathrm{C}/(\mathrm{A} \cdot \mathrm{m})$ is lower. The multilayered structure is also the least effective for α_{33}, virtually remaining at 0. But with other aspect ratios, such as $\alpha = 10$, 1, and 0.5, it is observed that the differences in the maximum values for these two composite configurations are significant. In general the maximum values for CFO-in-BTO are notably higher than those for BTO-in-CFO. This indicates that, in terms of the α_{33}-coupling, the CFO-in-BTO composite system is superior to BTO-in-CFO.

The calculated results for α_{11} are shown in Fig. 8.4a, b. In this transverse direction the superiority of multilayers becomes apparent. The negative values of this quantity imply that a positive E_1 will generate a negative B_1, or conversely a positive H_1 will generate a negative D_1. The difference between α_{33} and α_{11} for each aspect ratio in Figs. 8.3 and 8.4 signifies the transverse anisotropy of the composite. In both CFO-in-BTO and BTO-in-CFO, the multilayered structure is seen to generate the strongest magnetoelectric coupling for α_{11}, while the fibrous composite gives virtually no coupling effect. This is in direct contrast to the α_{33} characteristics. The multilayered curves in Fig. 8.4a, b are symmetric, for in this case there is no distinction between inclusions and matrix. The maximum occurs at $c_1 = 0.5$, with an absolute value of $350 \times 10^{-10}\mathrm{C}/(\mathrm{A} \cdot \mathrm{m})$. This is one order of magnitude higher than the $30 \times 10^{-10}\mathrm{C}/(\mathrm{A} \cdot \mathrm{m})$ generated for α_{33} by the fibrous CFO-in-BTO composite. For oblate inclusions with aspect ratio $\alpha = 0.5$, CFO-in-BTO is again superior to BTO-in-CFO, with the maxima of $20 \times 10^{-10}\mathrm{C}/(\mathrm{A} \cdot \mathrm{m})$ and $10 \times 10^{-10}\mathrm{C}/(\mathrm{A} \cdot \mathrm{m})$, respectively, for α_{11}. This level of difference is also observed with spherical inclusions. When the inclusion shape turns into a prolate one, the magnitudes of α_{11} are all negligible. This is similar to the oblate shapes in their effect on α_{33}, which further suggests the sharp contrast between the inclusion-shape dependence of α_{33} and α_{11}. Comparison between Figs. 8.3 and 8.4 for both CFO-in-BTO and BTO-in-CFO also reflects the strong anisotropy of the coupled behavior in an aligned multiferroic composite for each chosen inclusion shape.

8.5.1.2 The Piezoelectric Constants, e_{31}, e_{33}, and e_{15}

The piezoelectric constants e_{ij} connect the applied electric field E_j to the induced mechanical stress σ_i, or conversely the applied mechanical strain ε_j to the induced electric displacement D_i, as indicated in Eq. (8.3). The variations of these constants as a function of inclusion concentration, c_1, at the five selected aspect ratios are shown in Figs. 8.5, 8.6, and 8.7. As CFO possesses no piezoelectric effect, the

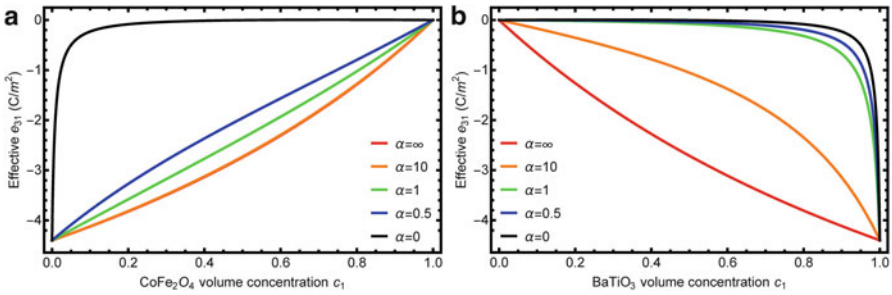

Fig. 8.5 The c_1 dependence of the piezoelectric constant e_{31}: (**a**) CFO-in-BTO and (**b**) BTO-in-CFO

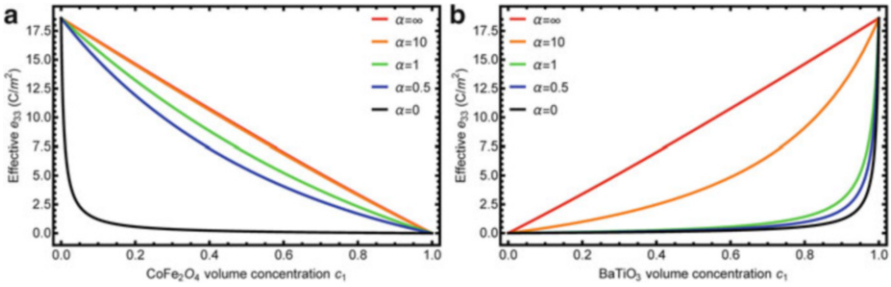

Fig. 8.6 The c_1 dependence of the piezoelectric constant e_{33}: (**a**) CFO-in-BTO and (**b**)BTO-in-CFO

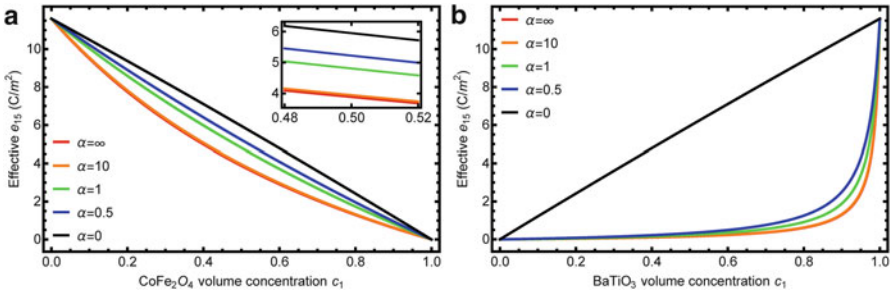

Fig. 8.7 The c_1 dependence of the piezoelectric constant e_{15}: (**a**) CFO-in-BTO and (**b**) BTO-in-CFO

magnitudes of these quantities all vary from those of BTO to zero of CFO as c_1 varies between 0 and 1. Since e_{31} is negative for BTO, this value is also negative for the composite. However, the values of e_{33} and e_{15} are all positive. Their c_1- and α-dependence as shown here all display strong sensitivity of inclusion shape on the piezoelectric constants.

8.5.1.3 The Piezomagnetic Constants, q_{31}, q_{33}, and q_{15}

The piezomagnetic constants q_{ij} are strong in the ferromagnetic CFO, but zero in the piezoelectric BTO, so the values of the composite all vary between zero on the BTO end to those of CFO as c_1 varies from 0 to 1. The calculated results are shown in Figs. 8.8, 8.9, and 8.10, for q_{31}, q_{33}, and q_{15}, in turn. For q_{31}, which signifies the induced magnetic flux density B_3 in the axial direction by the tensile strain ε_1 in the transverse direction, or the induced transverse stress σ_1 by the axial magnetic field, H_3, the fibrous composite $(\alpha = \infty)$ is seen to provide the strongest coupling effect. This is also the case for q_{33} that reflects the magneto-elastic interaction solely along the axial direction. For q_{15} which reflects the induced axial shear stress σ_5 (or σ_4) by

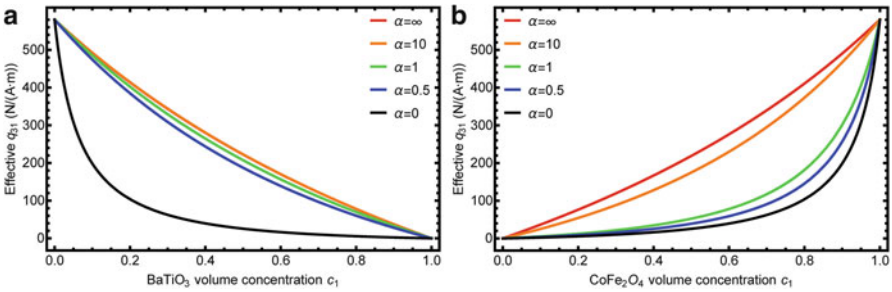

Fig. 8.8 The c_1 dependence of the piezomagnetic constant q_{31}: (**a**) CFO-in-BTO and (**b**) BTO-in-CFO

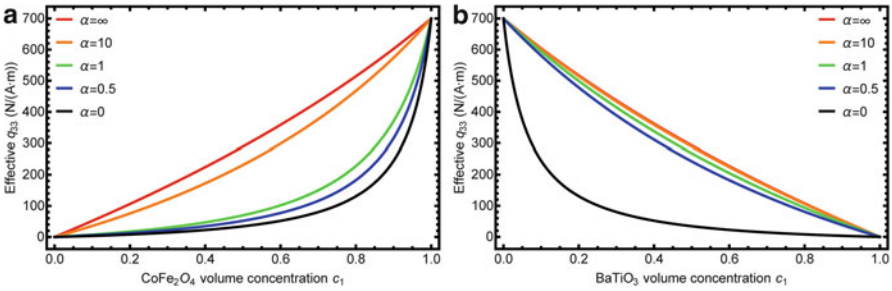

Fig. 8.9 The c_1 dependence of the piezomagnetic constant q_{33}: (**a**) CFO-in-BTO and (**b**) BTO-in-CFO

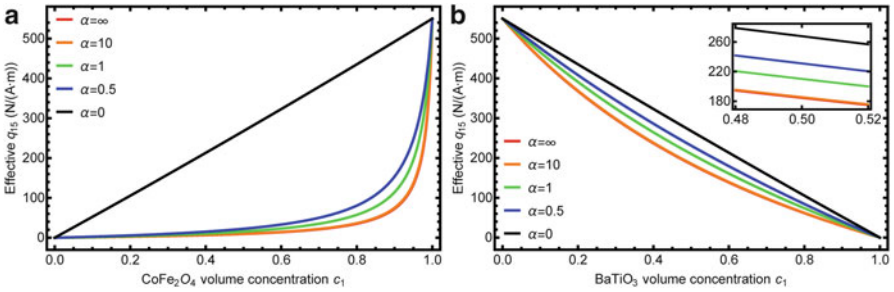

Fig. 8.10 The c_1 dependence of the piezomagnetic constant q_{15}: (**a**) CFO-in-BTO and (**b**) BTO-in-CFO

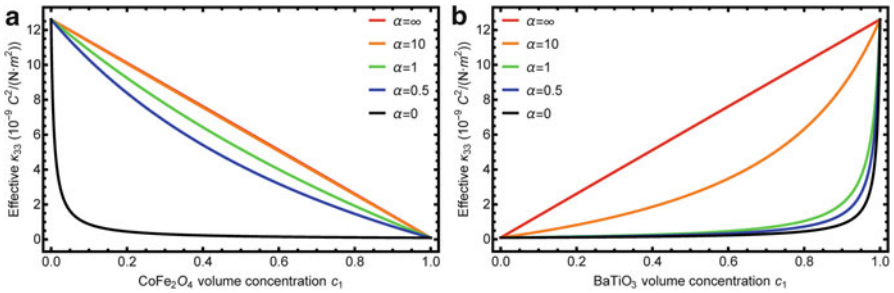

Fig. 8.11 The c_1 dependence of the permittivity κ_{33}: (**a**) CFO-in-BTO and (**b**) BTO-in-CFO

the transverse magnetic field H_1 (or H_2), as well as the induced transverse magnetic flux B_1 (or B_2) by the axial shear strain ε_5 (or ε_4), the multilayer ($\alpha = 0$) is the most effective microstructure.

8.5.1.4 The Electric Permittivity, κ_{33} and κ_{11}

The variations of electric permittivity κ_{33} are shown in Fig. 8.11, and κ_{11} in Fig. 8.12. The constant κ_{33} defines the induced electric displacement, B_3 in the axial direction by the axial electric field E_3, whereas κ_{11} provides the connection in the transverse direction 1 (and 2). As the electric permittivity is strong in BTO and very low in CFO, the trends are quite similar to those displayed for the piezoelectric constants above. The variations of these two quantities also exhibit similar characteristics as e_{33} and e_{15}, while the trends of κ_{33} are also similar to e_{33} and those of κ_{11} similar to e_{15}. For κ_{33}, it is the strongest with the fibrous composite, with a c_1-dependence that is almost linear. It is the weakest with the multilayers. For κ_{11}, the trend is exactly reversed. In the transverse direction the multilayers always represent the most effective microstructure. One may also observe the symmetric version of the multilayers by comparing (a) to (b) in each figure.

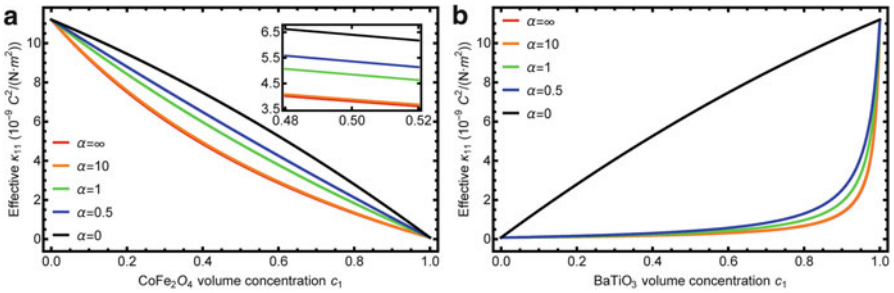

Fig. 8.12 The c_1 dependence of the permittivity κ_{11}: (**a**) CFO-in-BTO and (**b**) BTO-in-CFO

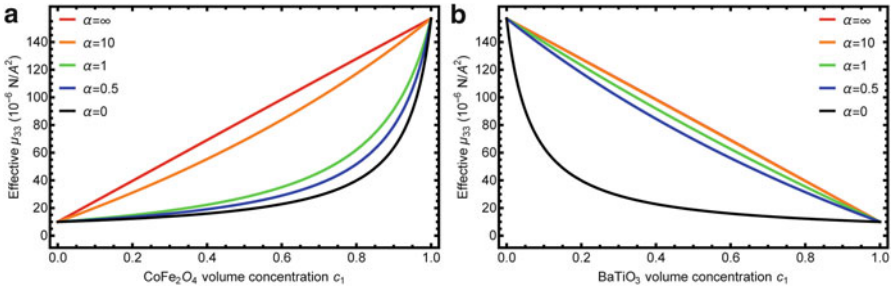

Fig. 8.13 The c_1 dependence of the permeability μ_{33}: (**a**) CFO-in-BTO and (**b**) BTO-in-CFO

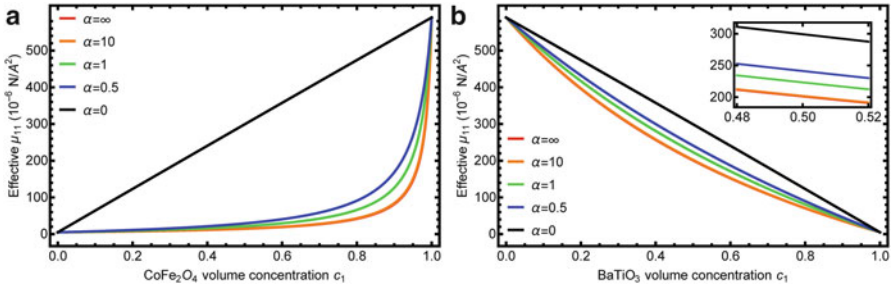

Fig. 8.14 The c_1 dependence of the permeability μ_{11}: (**a**) CFO-in-BTO and (**b**) BTO-in-CFO

8.5.1.5 The Magnetic Permeability, μ_{33} and μ_{11}

The overall permeability of the multiferroic composite, μ_{33} and μ_{11}, is shown in Figs. 8.13 and 8.14, respectively. In contrast to the permittivity, the permeability of CFO is very high whereas that of BTO is very weak. But the linear nature of the curves associated with fibrous composites for μ_{33} remains unchanged, and so is its highly nonlinear variation associated with multilayers. For μ_{11}, the trends are

reversed, with multilayers displaying a more linear increase. These results again point to the superiority of 1-3 connectivity for the direction-3 properties such as κ_{33} and μ_{33}, and that of 2-2 connectivity for the transverse properties such as κ_{11} and μ_{11}.

8.5.1.6 The Five Elastic Constants, C_{11}, C_{12}, C_{13}, C_{33}, and C_{44}

The five independent elastic constants, C_{11}, C_{12}, C_{13}, C_{33}, and C_{44}, are shown in Figs. 8.15, 8.16, 8.17, 8.18, and 8.19. As the elastic properties of CFO are stiffer than those of BTO, there is an increasing trend for CFO-in-BTO, as shown in figure (a) of each set, and a decreasing trend for BTO-in-CFO in figure (b). It can also be observed that, for C_{11}, C_{12}, and C_{13}, there is virtually no aspect-ratio dependence, and for C_{33} its dependence is visible, but very weak. So for these four constants the main factor is their c_1-dependence. In reading these figures it is useful to keep in mind that direction 3 is the axial, symmetric direction while plane 1-2 is isotropic.

But for C_{44} in Fig. 8.19, the axial shear modulus of the composite, it is highly aspect-ratio dependent. Moreover, there is a remarkable feature that its magnitude can be higher than either of the constituent phases. This feature is not to be commonly found in ordinary elastic composites. This is seen to occur in CFO-in-BTO as well as

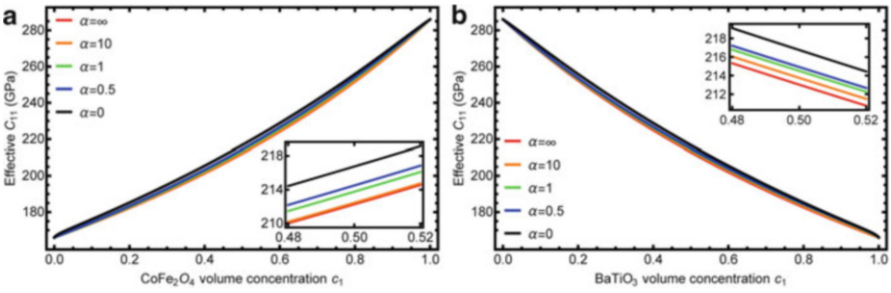

Fig. 8.15 The c_1 dependence of the elastic constant C_{11}: (**a**) CFO-in-BTO and (**b**) BTO-in-CFO

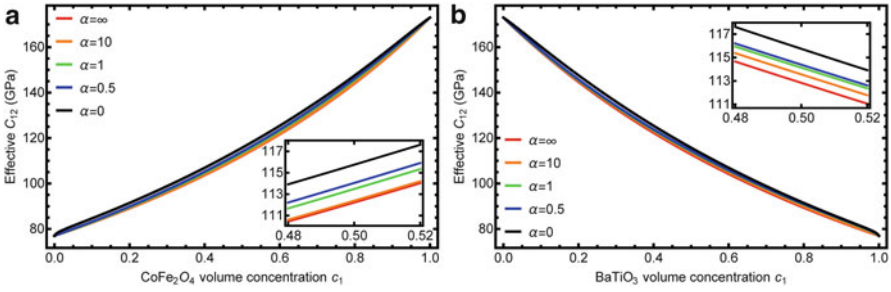

Fig. 8.16 The c_1 dependence of the elastic constant C_{12}: (**a**) CFO-in-BTO and (**b**) BTO-in-CFO

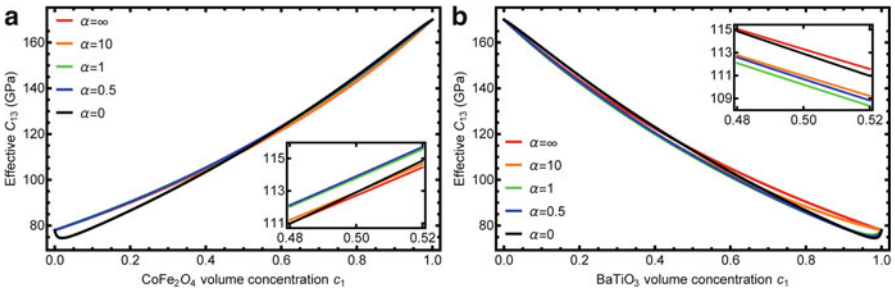

Fig. 8.17 The c_1 dependence of the elastic constant C_{13}: (**a**) CFO-in-BTO and (**b**) BTO-in-CFO

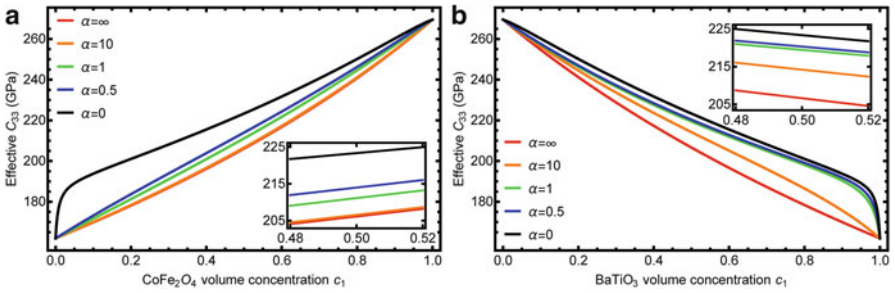

Fig. 8.18 The c_1 dependence of the elastic constant C_{33}: (**a**) CFO-in-BTO and (**b**) BTO-in-CFO

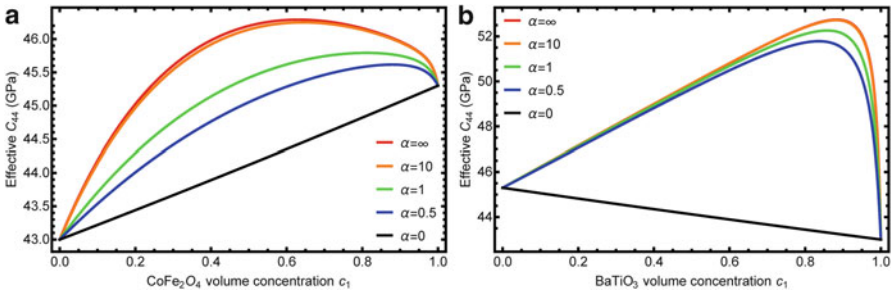

Fig. 8.19 The c_1 dependence of the elastic constant C_{44}: (**a**) CFO-in-BTO and (**b**) BTO-in-CFO

in BTO-in-CFO. This outcome is a consequence of the piezoelectric-piezomagnetic interactions in the multiferroic composite. To demonstrate that it is a unique property of the multiferroics, we have made another round of calculations using solely the elastic constants of CFO and BTO, without any piezoelectric, piezomagnetic, dielectric, or magnetic constants. The calculated C_{44} with the same five aspect ratios are shown in Fig. 8.20a, b. They all become very linear. It is clear that no such synergistic feature is present in the purely elastic composites. To make this finding more

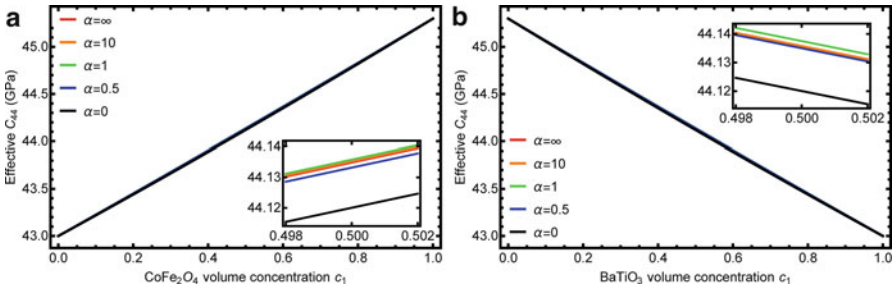

Fig. 8.20 The c_1 dependence of the elastic constant C_{44} in a purely elastic composite with the elastic properties of BTO and CFO: (**a**) CFO-in-BTO and (**b**) BTO-in-CFO

accessible, we have derived an explicit form of C_{44} for the fibrous multiferroic composite and the purely elastic composites. The results are given in Eq. (8.56) of Appendix 4, where one can see that C_{44}^{M} of the multiferroic composite is always higher than C_{44}^{E} of the purely elastic one.

8.5.2 *Properties of CFO-in-BTO and BTO-in-CFO Composites with an Imperfect Interface*

With the interphase property and volume concentration in the coated inclusion given in Eqs. (8.10) and (8.11), respectively, we have applied Eqs. (8.8) and (8.9) to compute the 17 effective magneto-electro-elastic constants of the imperfectly bonded multiferroic composite. Here we present the calculated results in the same order as in the preceding section for ready comparison. It will become evident that, due to the presence of a weak interface, many quantities are reduced.

8.5.2.1 The Magnetoelectric Coupling Coefficients, α_{33} and α_{11}, with an Imperfect Interface

The magnetoelectric coupling coefficient in the axial direction, α_{33}, is shown in Fig. 8.21a, b, for CFO-in-BTO and BTO-in-CFO, respectively. This set of data is to be compared with Fig. 8.3a, b. It is evident that the maximum with an imperfect interface is lower in each case. For instance with the fibrous composite the maximum is now only $21 \times 10^{-10}\mathrm{C}/(\mathrm{A}\cdot\mathrm{m})$ for CFO-in-BTO, whereas it was about $30 \times 10^{-10}\mathrm{C}/(\mathrm{A}\cdot\mathrm{m})$. With the aspect ratio of $\alpha = 10$, the maximum decreases from $23 \times 10^{-10}\mathrm{C}/(\mathrm{A}\cdot\mathrm{m})$ to about $16 \times 10^{-10}\mathrm{C}/(\mathrm{A}\cdot\mathrm{m})$. The values for BTO-in-CFO also have notable reductions for all aspect ratios of inclusions. For α_{11}, the results are shown in Fig. 8.22a, b. In this direction the multilayered composite gives

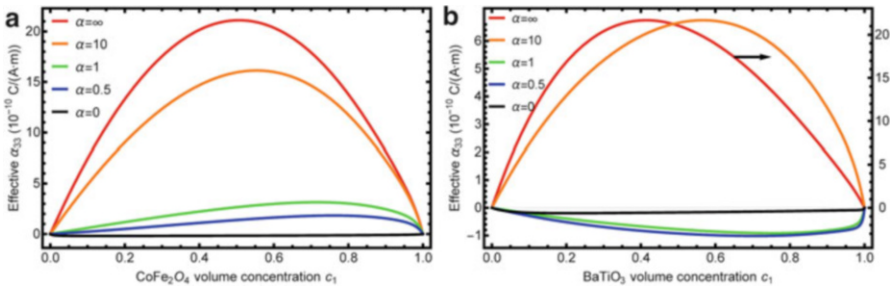

Fig. 8.21 The magnetoelectric coefficient α_{33} with an imperfect interface: (**a**) CFO-in-BTO and (**b**) BTO-in-CFO

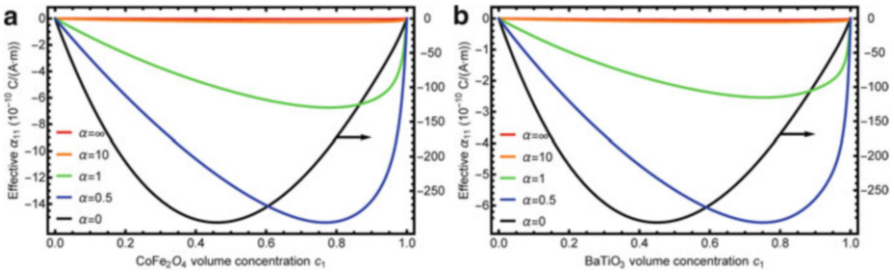

Fig. 8.22 The magnetoelectric coefficients α_{11} with an imperfect interface: (**a**) CFO-in-BTO and (**b**) BTO-in-CFO

the highest coupling, but with an imperfect interface, its maximum magnitude has decreased to about $300 \times 10^{-10}\mathrm{C}/(\mathrm{A} \cdot \mathrm{m})$ from about $360 \times 10^{-10}\mathrm{C}/(\mathrm{A} \cdot \mathrm{m})$ in Fig. 8.4.

8.5.2.2 The Piezoelectric Constants, e_{31}, e_{33}, and e_{15}, with an Imperfect Interface

The piezoelectric constants of the multiferroic composite with an imperfect interface are shown in Figs. 8.23, 8.24, and 8.25, for e_{31}, e_{33}, and e_{15}, respectively. As compared to Figs. 8.5, 8.6, and 8.7, we also see notable reductions. For instance, with $\alpha = 0.5$, the magnitude of e_{31} for CFO-in-BTO is now about -2 C/m^2 at $c_1 = 0.4$, whereas it was about -2.5 C/m^2 with a perfect interface. For BTO-in-CFO, the reduction with $\alpha \to 8$ was from -2.3 to -1.6 C/m^2 at $c_1 = 0.4$. But we notice that the reduction for e_{33} does not appear to be significant in comparison with Fig. 8.6, and so is for e_{15} in the case of CFO-in-BTO, but for BTO-in-CFO it is notable with the multilayer structure.

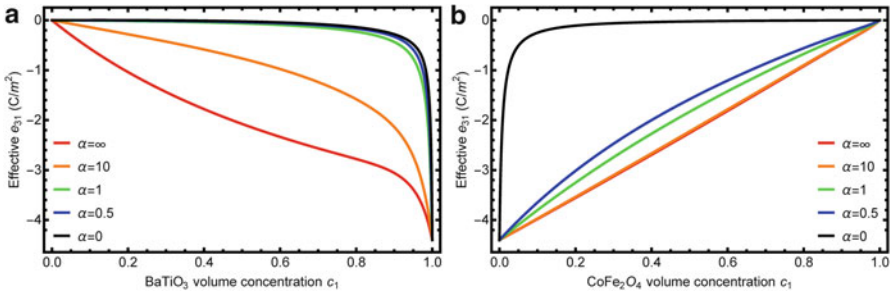

Fig. 8.23 The piezoelectric constant e_{31} with an imperfect interface: (**a**) CFO-in-BTO and (**b**) BTO-in-CFO

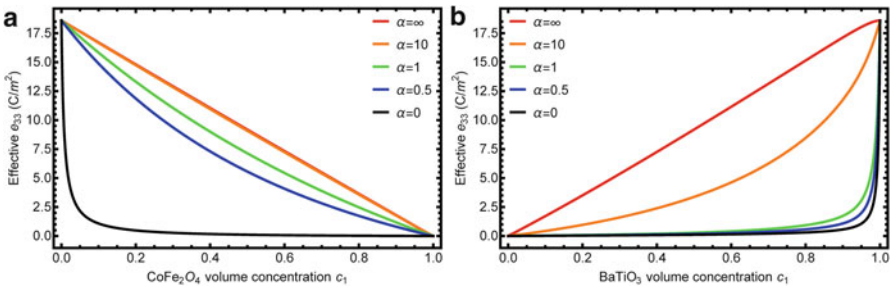

Fig. 8.24 The piezoelectric constant e_{33} with an imperfect interface: (**a**) CFO-in-BTO and (**b**) BTO-in-CFO

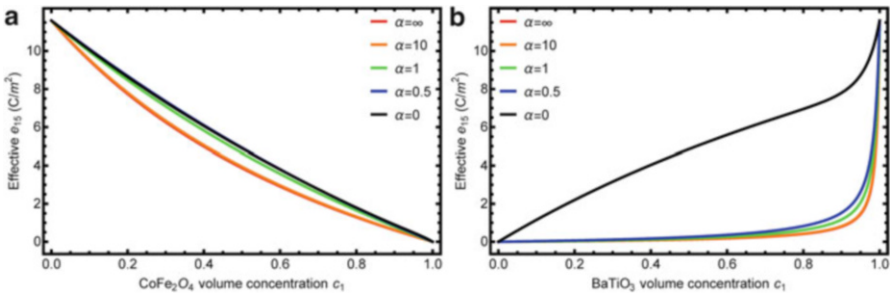

Fig. 8.25 The piezoelectric constant e_{15} with an imperfect interface: (**a**) CFO-in-BTO and (**b**) BTO-in-CFO

8.5.2.3 The Piezomagnetic Constants, q_{31}, q_{33}, and q_{15}, with an Imperfect Interface

With the interface effect, these three constants are shown in Figs. 8.26, 8.27, and 8.28. Since CFO is strongly piezomagnetic but BTO has no such effect, these two end conditions must be met in all plots as c_1 varies from 0 to 1. For q_{31} and q_{33},

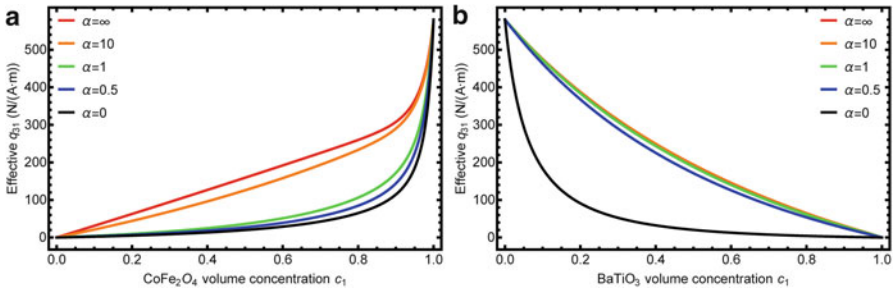

Fig. 8.26 The piezomagnetic constant q_{31} with an imperfect interface: (**a**) CFO-in-BTO and (**b**) BTO-in-CFO

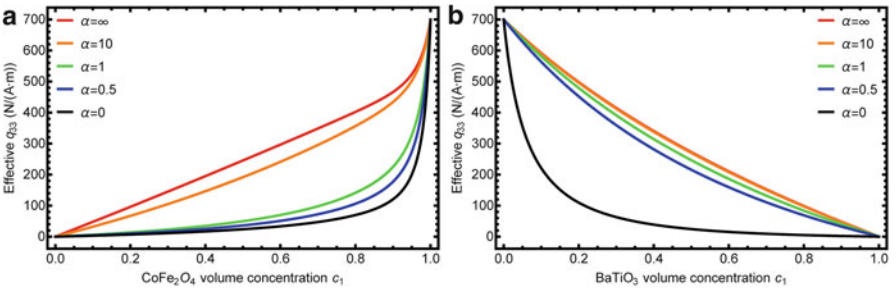

Fig. 8.27 The piezomagnetic constant q_{33} with an imperfect interface: (**a**) CFO-in-BTO and (**b**) BTO-in-CFO

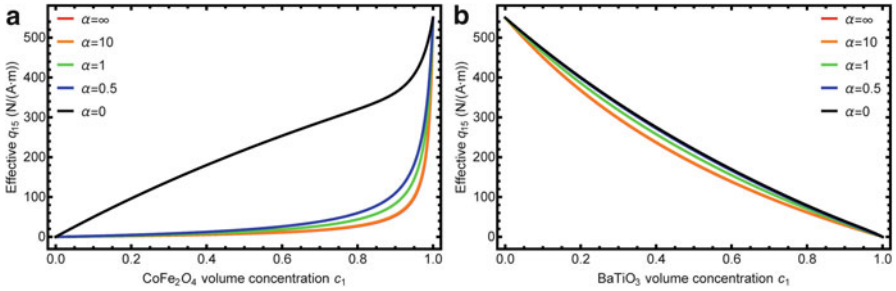

Fig. 8.28 The piezomagnetic constant q_{15} with an imperfect interface: (**a**) CFO-in-BTO and (**b**) BTO-in-CFO

which are associated with the axial magnetic loading, H_3, the fibrous composite with 1-3 connectivity represents the most favored microstructure. Their magnitudes steadily decrease as the aspect ratio of inclusions decreases. But for q_{15}, which involves the transverse magnetic loading of H_1 or H_2, multilayered structure is the most favored one. The magnitude of this constant tends to decrease with the increase of aspect ratio. In essence, the aspect-ratio dependence of these three quantities are similar to the trend displayed in the three piezoelectric constants, except that the end conditions are reversed. From these results, we can conclude that, under the axial electric or magnetic loading, 1-3 connectivity should be chosen, but under the transverse electric or magnetic loading, 2-2 connectivity should be selected, regardless of the interface condition.

8.5.2.4 The Electric Permittivity, κ_{33} and κ_{11}, with an Imperfect Interface

The influence of an imperfect interface on the dielectric permittivity, κ_{33} and κ_{11}, is shown in Figs. 8.29 and 8.30, respectively. This is to be compared with Figs. 8.11 and 8.12 with a perfect interface for the extent of reduction. With the prescribed

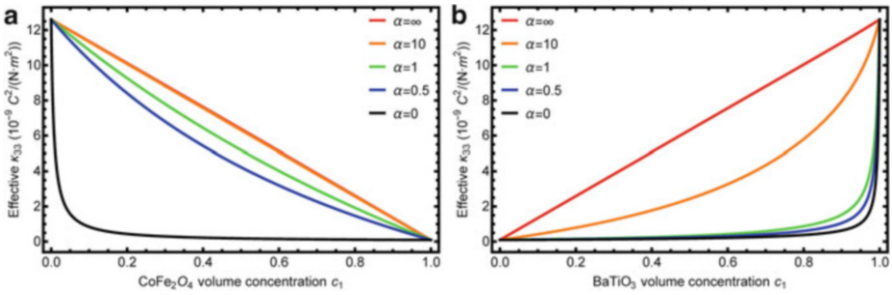

Fig. 8.29 The permittivity κ_{33} with an imperfect interface: (**a**) CFO-in-BTO and (**b**) BTO-in-CFO

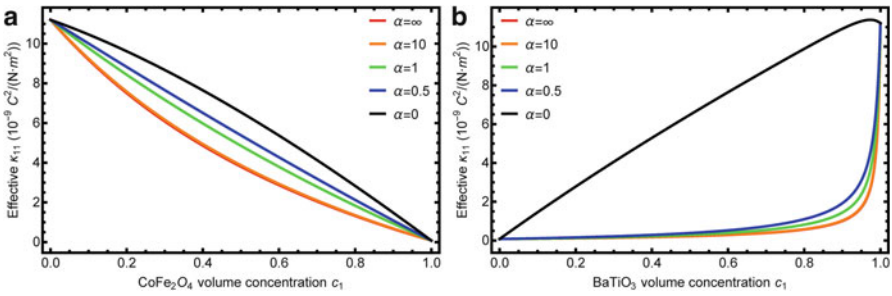

Fig. 8.30 The permittivity κ_{11} with an imperfect interface: (**a**) CFO-in-BTO and (**b**) BTO-in-CFO

interphase property and volume concentration, the reductions for both constants do not appear to be particularly significant for all aspect ratios, regardless of CFO-in-BTO or BTO-in-CFO. Direct comparison between these two composite configurations indicates that they are almost identical. The possible reason for this outcome is likely to be due to the small volume concentration of the interphase, c_{int}, that its effect on the overall permittivity is not sufficiently significant to be visible. We have double-checked the calculations for the imperfect interface; no errors were detected.

8.5.2.5 The Magnetic Permeability, μ_{33} and μ_{11}, with an Imperfect Interface

The results with the imperfect interface for μ_{33} and μ_{11} are shown in Figs. 8.31 and 8.32. In comparison with Figs. 8.13 and 8.14 for the perfect interface, the reductions in the magnitude of magnetic permeability are also found to be small. Indeed the influence of an imperfect interface here is essentially the same as that displayed in κ_{33} and κ_{11}. It turns out that, in addition to these two constants, the piezoelectric constant, e_{33}, with a perfect interface in Fig. 8.6 and an imperfect interface in

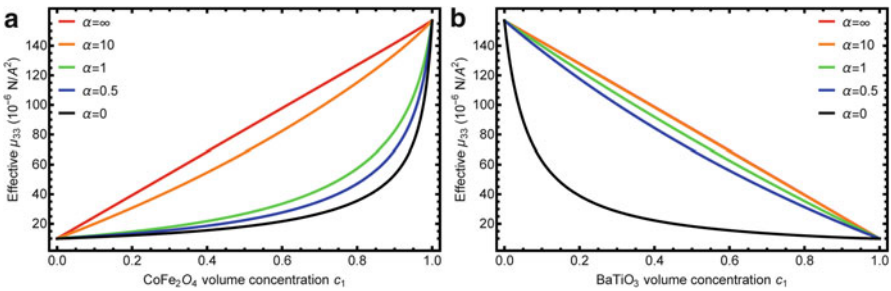

Fig. 8.31 The permeability μ_{33} with an imperfect interface: (**a**) CFO-in-BTO and (**b**) BTO-in-CFO

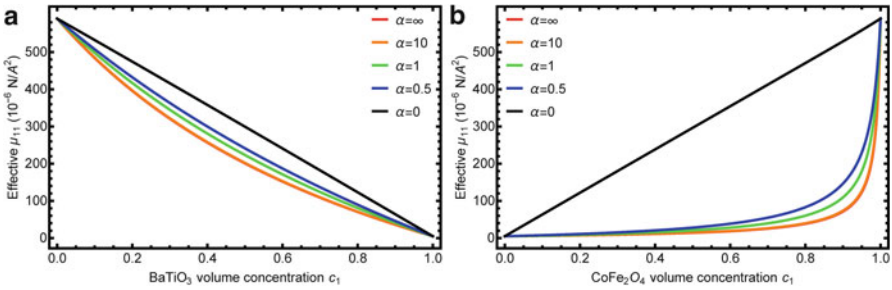

Fig. 8.32 The permeability μ_{11} with an imperfect interface: (**a**) CFO-in-BTO and (**b**) BTO-in-CFO

Fig. 8.24, is found to be another one that shows little interface effect. This is also the case for the q_{33} of BTO-in-CFO in Figs. 8.9b and 8.27b, but for the same q_{33} of CFO-in-BTO in Figs. 8.9a and 8.27a, interface effect is visible.

8.5.2.6 The Five Elastic Constants, C_{11}, C_{12}, C_{13}, C_{33}, and C_{44}, with an Imperfect Interface

The five independent elastic constants are shown in Figs. 8.33, 8.34, 8.35, 8.36, and 8.37. Unlike the prevailing cases the reductions here are significant for each quantity. Previously the transverse stiffness C_{11} in Fig. 8.15 under the perfect interface condition was virtually aspect-ratio independent, but here this quantity is highly dependent upon the aspect ratio of inclusions. For CFO-in-BTO, the multilayered structure is found to be the most significantly affected because along the planar direction 1, the weak interface can drastically lower the effective stiffness. In the case of BTO-in-CFO, its value can be lower than that of the BTO as inclusion concentration, c_1, is approaching 1. The reduction in C_{12} is very similar

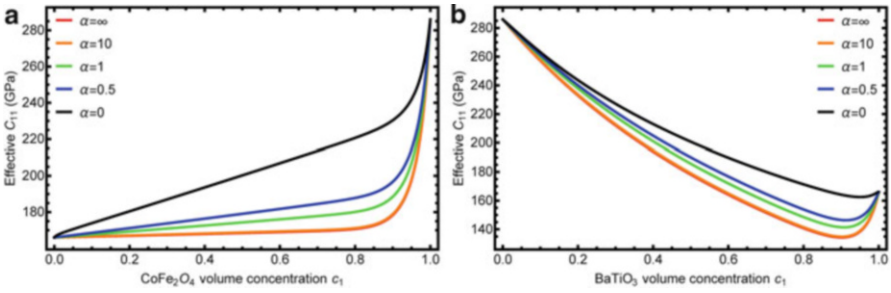

Fig. 8.33 The elastic constant C_{11} with an imperfect interface: (**a**) CFO-in-BTO and (**b**) BTO-in-CFO

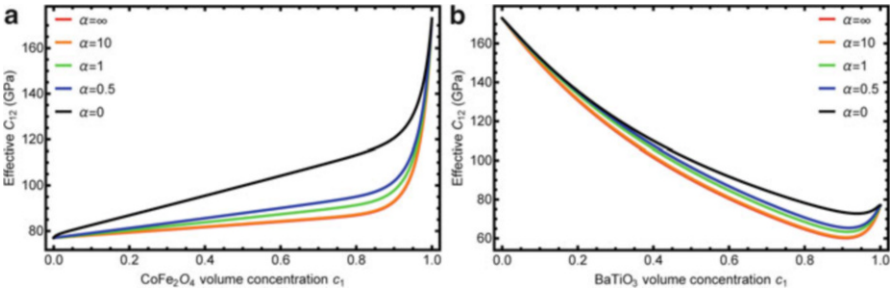

Fig. 8.34 The elastic constant C_{12} with an imperfect interface: (**a**) CFO-in-BTO and (**b**) BTO-in-CFO

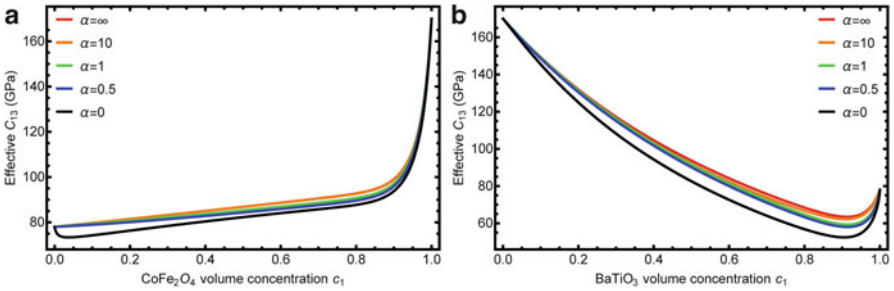

Fig. 8.35 The elastic constant C_{13} with an imperfect interface: (**a**) CFO-in-BTO and (**b**) BTO-in-CFO

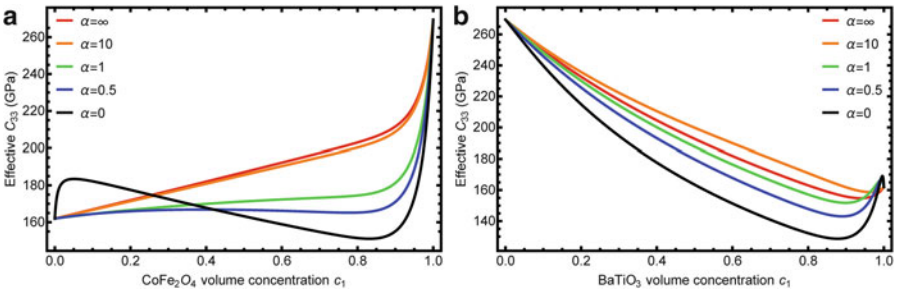

Fig. 8.36 The elastic constant C_{33} with an imperfect interface: (**a**) CFO-in-BTO and (**b**) BTO-in-CFO

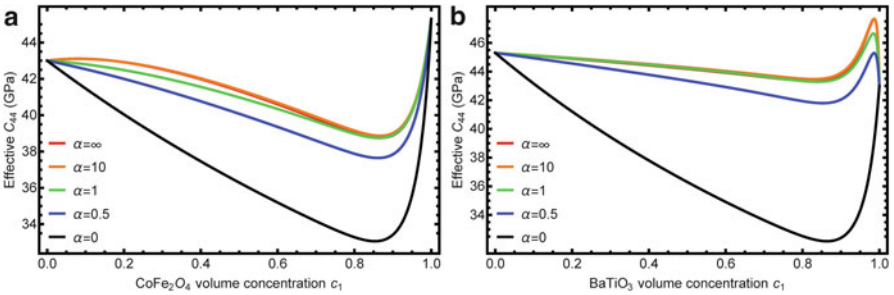

Fig. 8.37 The elastic constant C_{44} with an imperfect interface: (**a**) CFO-in-BTO and (**b**) BTO-in-CFO

to that in C_{11}. Comparing Figs. 8.17, 8.18, 8.19, 8.20, 8.21, 8.22, 8.23, 8.24, 8.25, 8.26, 8.27, 8.28, 8.29, 8.30, 8.31, 8.32, 8.33, 8.34, and 8.35 for C_{13}, a uniform reduction is found for CFO-in-BTO over the range of c_1 from 0 to 0.9, while for BTO-in-CFO, the reduction becomes more severe when the BTO inclusion concentration is near 0.9. For C_{33} and C_{44}, the influence of the interphase with the

multilayered composite is extremely sensitive. With C_{33}, it also increases monotonically at low c_1, but afterward it can cause this elastic constant to decrease with increasing c_1 over the range between $c_1 = 0.1$ and $c_1 = 0.9$. With the constant C_{44}, the value with an imperfect interface is found to be lower than that of either CFO or BTO. This is an opposite synergistic effect as C_{44} in the perfect interface case due to the simultaneous interactions of piezoelectric, piezomagnetic, and interphase effects.

8.5.3 Why Is the Imperfect Interface Model Needed?

We have taken great length to study the impact of an imperfect interface on the 17 multiferroic constants. Some are found to be very sensitive to the interface condition whereas others are less so. But the most important reason for the introduction of the imperfect interface is to be able to model the property of the real material system, as the interface of most bulk multiferroic composites is not perfect. This is also observed in carbon nanotube-based polymer nanocomposites (Wang et al. 2014). We now demonstrate that, without an imperfect interface model, the experimentally measured data cannot be adequately predicted.

Even though there are not many experimental data reported in the literature, Harshé et al. (1993) did report their measured magnetoelectric voltage coefficient, α_{E33}, of a CFO-in-BTO multiferroic composite. The voltage coefficient is related to the magnetoelectric coupling coefficient, α_{33}, through $\alpha_{E33} = \alpha_{33}/\kappa_{33}$, where κ_{33} is the electric permittivity of the multiferroic composite in direction 3. They provided the data of α_{E33} at two volume concentrations of CFO, one at 11 % and the other at 22 %. Their results are reproduced in Fig. 8.38, with the range of data indicated by the black error bar. They also provided the material constants of BTO and CFO. As the constants were given under a stress-controlled boundary condition, the values needed to be translated into the strain-controlled boundary conditions as described in Eq. (8.14) in Appendix 1. The newly calculated constants are also listed in the right column of Table 8.1. To make the comparison, we have first applied the perfect interface model to calculate α_{E33}; the result is also shown in Fig. 8.38, in red curve. It is evident that the perfect interface model has substantially overestimated the measured data, and that an imperfect interface model is needed.

We then adopt the imperfect interface model to calculate this quantity. The constants used are $c_{\text{int}} = 0.02 \times [1 - F(c_1; 20, 1)]$, and

$$\begin{gathered} C_{11}^{\text{int}} = 2 \times 10^9 \text{Pa}, \qquad C_{44}^{\text{int}} = 1 \times 10^9 \text{Pa}; \\ \kappa^{\text{int}} = 2\varepsilon_0, \qquad \varepsilon_0 = 8.854 \times 10^{-12} \text{F/m}, \text{vacuum permittivity}; \\ \mu_{\text{int}} = 2\mu_0, \qquad \mu_0 = 1.257 \times 10^{-6} \text{H/m}, \text{vacuum permeability}. \end{gathered} \tag{8.12}$$

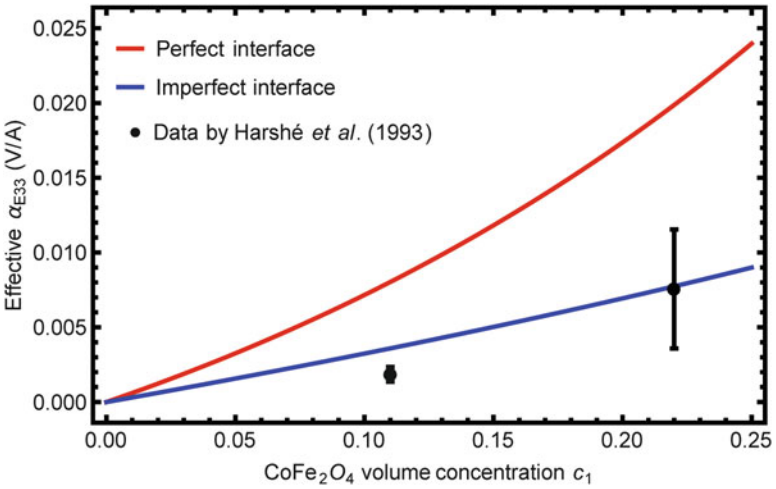

Fig. 8.38 Comparison between experiment and theory based on a perfect and an imperfect interface models for the magnetoelectric voltage coefficient α_{E33} of a CFO-in-BTO composite

The calculated results are also shown in Fig. 8.38, in blue. It is seen that the experimental data now can be captured with this weak interface model. This comparison speaks for the need of the imperfect interface model in modeling a real system.

8.6 Conclusions

In this chapter we have presented a composite model to calculate the magnetoelectric coupling coefficients and overall magneto-electro-elastic properties of a class of multiferroic composites. This class of composites is represented by aligned spheroidal inclusions which can be piezomagnetic or piezoelectric, embedded in a homogeneous piezoelectric or piezomagnetic matrix with an interface which can be perfect or imperfect. The aspect ratio of inclusions can be from 0 to ∞ that covers the entire range from multilayered structures to fibrous composites. Between these limiting cases lies the general spheroidal shape whose aspect ratio can be less than, equal to, or greater than 1. This microgeometry includes the three most widely considered microstructures that are commonly referred to as 2-2, 0-3, and 1-3 connectivities. This class of composites has 17 independent material constants whereas the piezoelectric or the piezomagnetic phase each has only 12. The determination of these 17 constants for the multiferroic composite over the entire range of inclusion concentration and aspect ratio has been the major objective of this investigation.

We have used this theory to determine these 17 material constants, first under the perfect and then under the imperfect interface condition. The case with a perfect

interface can be readily addressed by the Mori-Tanaka method. To address the influence of an imperfect interface, we have introduced a thinly coated inclusion model that consists of the original inclusion and an interphase to address the effect of interface. The coated inclusion is then embedded into the matrix to study the influence of the interface on the overall properties of the multiferroic composite. This two-step procedure renders the Mori-Tanaka approach useful in the study of multiferroic composites under either a perfect or an imperfect interface condition. One of the most challenging steps in the process of computation is the determination of the components of Eshelby's S-tensor for either the transversely isotropic spheroidal piezoelectric or piezomagnetic inclusion. While its components are explicitly known for 2-2 and 1-3 connectivity, they are not so with a general spheroid. For this purpose a Gaussian quadrature numerical procedure to evaluate its components is presented in Appendix 2.

Among the 17 material constants that are present in the multiferroic composite, the two most intriguing ones are the magnetoelectric coupling coefficients, α_{33} and α_{11}. These constants are absent in either the piezoelectric or the piezomagnetic phase, but is present in the composite. It represents the signature product effect of the multiferroic composite. These two quantities have been determined over the entire range of inclusion volume concentration and aspect ratio, under both perfect and imperfect interface conditions, for both CFO-in-BTO and BTO-in-CFO composites. It is shown that, for α_{33}, the fibrous composite represents the most favorable connectivity whereas for α_{11} it is the multilayered structure that gives the most optimal result. Due to the importance of α_{33} and α_{11} for both 1-3 and 2-2 connectivity, we have listed their explicit results under both perfect and imperfect interface conditions in Appendix 3.

We have further demonstrated how the three piezoelectric constants, e_{31}, e_{33}, and e_{15}; the three piezomagnetic constants, q_{31}, q_{33}, and q_{15}; the two dielectric permittivity, κ_{33} and κ_{11}; the two magnetic permeability, μ_{33} and μ_{11}; and the five elastic constants, C_{11}, C_{12}, C_{13}, C_{33}, and C_{44}, depend on the volume concentration and aspect ratio of inclusions, for both CFO-in-BTO and BTO-in-CFO, under both perfect and imperfect interface conditions. One of the intriguing features of these constants is the unusually high magnitude of C_{44} under the perfect interface that can far exceed the C_{44} of either the piezoelectric or the piezomagnetic phase. Such an exceptional feature is found to exist solely in a multiferroic composite but not in a purely elastic composite. An explicit expression for C_{44} of the fibrous multiferroic and elastic composites is also given in Appendix 4. It is further emphasized that, in order to capture the magnetoelectric coupling of real bulk multiferroic composites, a weak interface model is often required. As CFO-in-BTO and BTO-in-CFO are two of the most widely considered multiferroic composites, the wide range of results reported here could serve as a benchmark for future comparison.

We conclude by saying that single-phase multiferroics are rare, and that among the existing ones their magnetoelectric coupling is generally weak. It takes a multiferroic composite to generate strong magnetoelectric coupling. The present study is strongly motivated by this observation. The field of magnetoelectric coupling in multiferroic composites is a very challenging one that offers plenty of

opportunities for future research. This chapter covers only the linear coupling of piezoelectric-piezomagnetic composites; it does not include the nonlinear coupling of ferroelectric-ferromagnetic composites. The study of such nonlinear behavior would allow us to understand more deeply how the electric polarization can be switched under a magnetic field and magnetization vector can be rotated under an electric field inside each constituent phase. This will require the examination of internal magneto-electro-elastic fields by a micromechanics approach such as the one developed in Li and Weng (1999) and Weng and Wong (2009) in the study of domain switch in piezoelectric crystals. Such a nonlinear, micromechanics study will offer an expanded scope of the coupled behavior, and is much needed. In that context the present linear theory can serve as the starting point for the development of such micromechanics-based nonlinear ones.

Acknowledgements This work was supported by the US National Science Foundation, Mechanics of Materials Program, under grant CMMI-1162431.

Appendix 1: The Eight Variants of the Coupled Constitutive Equations

Eight different types of thermodynamic potentials can be developed based on different choices of the (σ, ε),, (D, E), and (B, H) pairs. This leads to eight different variants of the magneto-electro-elastic constitutive equations. Following Soh and Liu (2005), we write

Type	Independent variables	Constitutive equations
1	$\varepsilon,\ E,\ H$	$\sigma = \mathbf{C}_{E,H}\varepsilon - \mathbf{e}_H^{\mathrm{T}}E - \mathbf{q}_E^{\mathrm{T}}H$ $D = \mathbf{e}_H\varepsilon + k_{\varepsilon,H}E + \alpha_\varepsilon H$ $B = \mathbf{q}_E\varepsilon + \boldsymbol{\alpha}_\varepsilon E + \boldsymbol{\mu}_{\varepsilon,E}H$
2	$\sigma,\ D,\ B$	$\varepsilon = \mathbf{S}_{D,B}\sigma + \mathbf{g}_B^{\mathrm{T}}D + \mathbf{m}_D^{\mathrm{T}}B$ $E = -\mathbf{g}_B\sigma + \beta_{\sigma,B}D - \lambda_\sigma B$ $H = -\mathbf{m}_D\sigma - \boldsymbol{\lambda}_\sigma D + \boldsymbol{\upsilon}_{\sigma,D}B$
3	$\varepsilon,\ D,\ H$	$\sigma = \mathbf{C}_{D,H}\varepsilon - \mathbf{h}_H^{\mathrm{T}}D - \mathbf{q}_D^{\mathrm{T}}H$ $E = -\mathbf{h}_H\varepsilon + \boldsymbol{\beta}_{\varepsilon,H}D - \varsigma_\varepsilon H$ $B = \mathbf{q}_D\varepsilon + \varsigma_\varepsilon D + \boldsymbol{\mu}_{\varepsilon,D}H$
4	$\sigma,\ E,\ B$	$\varepsilon = \mathbf{S}_{E,B}\sigma + \mathbf{d}_B^{\mathrm{T}}E + \mathbf{m}_E^{\mathrm{T}}B$ $D = \mathbf{d}_B\sigma + k_{\sigma,B}E + \eta_\sigma B$ $H = -\mathbf{m}_E\sigma - \boldsymbol{\eta}_\sigma E + \boldsymbol{\upsilon}_{\sigma,E}B$
5	$\varepsilon,\ E,\ B$	$\sigma = \mathbf{C}_{E,B}\varepsilon - \mathbf{e}_B^{\mathrm{T}}E - \mathbf{n}_E^{\mathrm{T}}B$ $D = \mathbf{e}_B\varepsilon + k_{\varepsilon,B}E + \eta_\varepsilon B$ $H = -\mathbf{n}_E\varepsilon - \boldsymbol{\eta}_\varepsilon E + \boldsymbol{\upsilon}_{\varepsilon,E}B$

(continued)

6	$\sigma,\ D,\ H$	$\varepsilon = \mathbf{S}_{D,H}\sigma + \mathbf{g}_H^{\mathrm{T}} D + \mathbf{p}_D^{\mathrm{T}} H$ $E = -\mathbf{g}_H\sigma + \beta_{\sigma,H} D - \varsigma_\sigma H$ $B = \mathbf{p}_D\sigma + \varsigma_\sigma D + \boldsymbol{\mu}_{\sigma,D} H$
7	$\varepsilon,\ D,\ B$	$\sigma = \mathbf{C}_{D,B}\varepsilon - \mathbf{h}_B^{\mathrm{T}} D - \mathbf{n}_D^{\mathrm{T}} B$ $E = -\mathbf{h}_B\varepsilon + \boldsymbol{\beta}_{\varepsilon,B} D - \lambda_\varepsilon B$ $H = -\mathbf{n}_D\varepsilon - \boldsymbol{\lambda}_\varepsilon D + \boldsymbol{\upsilon}_{\varepsilon,D} B$
8	$\sigma,\ E,\ H$	$\varepsilon = \mathbf{S}_{E,H}\sigma + \mathbf{d}_H^{\mathrm{T}} E + \mathbf{p}_E^{\mathrm{T}} H$ $D = \mathbf{d}_H\sigma + \kappa_{\sigma,H} E + \alpha_\sigma H$ $B = \mathbf{p}_E\sigma + \boldsymbol{\alpha}_\sigma E + \boldsymbol{\mu}_{\sigma,E} H$

In the above constitutive equations, each subscript denotes that the corresponding tensor is measured under which kind of constant field. For instance, $\mathbf{C}_{E,H}$ means this elastic stiffness tensor is measured under constant electric and magnetic field, so it is different from $\mathbf{C}_{E,B}$. However the coefficients of one pair are dependent upon the coefficients of another. From any given pair we can derive the rest seven pairs. They can be converted from each other, as below:

1. When all the independent variables are to be reversed, a direct inversion of the matrix is sufficient. For instance, given the matrix for independent variables $(\varepsilon, E,\ H)$, we can find that for $(\sigma,\ D,\ B)$ through

$$\begin{bmatrix} \mathbf{S}_{D,B} & \mathbf{g}_B^T & \mathbf{m}_D^T \\ -\mathbf{g}_B & \beta_{\sigma,B} & -\lambda_\sigma \\ -\mathbf{m}_D & -\lambda_\sigma & \upsilon_{\sigma,D} \end{bmatrix} = \begin{bmatrix} \mathbf{C}_{E,H} & -\mathbf{e}_H^T & -\mathbf{q}_E^T \\ \mathbf{e}_H & \kappa_{\varepsilon,H} & \alpha_\varepsilon \\ \mathbf{q}_E & \alpha_\varepsilon & \mu_{\varepsilon,E} \end{bmatrix}^{-1}. \tag{8.13}$$

2. But when only one or two independent variables are to be changed, a sequential conversion is needed. For example, given the matrix for $(\varepsilon,\ E,\ H)$, we can find that for $(\sigma,\ E,\ H)$ by

$$\begin{bmatrix} \mathbf{S}_{E,H} & \mathbf{d}_H^T & \mathbf{p}_E^T \\ \mathbf{d}_H & \kappa_{\sigma,H} & \alpha_\sigma \\ \mathbf{p}_E & \alpha_\sigma & \mu_{\sigma,E} \end{bmatrix} = \begin{bmatrix} \mathbf{S}_{D,B} & \mathbf{g}_B^T & \mathbf{m}_D^T \\ \mathbf{0} & \mathbf{I} & \mathbf{0} \\ \mathbf{0} & \mathbf{0} & \mathbf{I} \end{bmatrix} \begin{bmatrix} \mathbf{C}_{E,H} & -\mathbf{e}_H^T & -\mathbf{q}_E^T \\ \mathbf{e}_H & \kappa_{\varepsilon,H} & \alpha_\varepsilon \\ \mathbf{q}_E & \alpha_\varepsilon & \mu_{\varepsilon,E} \end{bmatrix} \begin{bmatrix} \mathbf{C}_{E,H} & -\mathbf{e}_H^T & -\mathbf{q}_E^T \\ \mathbf{0} & \mathbf{I} & \mathbf{0} \\ \mathbf{0} & \mathbf{0} & \mathbf{I} \end{bmatrix}^{-1}. \tag{8.14}$$

Appendix 2: The Determination of the Magneto-Electro-Elastic S-Tensor

The magneto-electro-elastic S-tensor has been studied by Li and Dunn (1998a, b), Huang et al. (1998), and several others. Here we briefly summarize the method for calculating this S-tensor with the notations used here.

First, we define a material constant "tensor" (which is not a real tensor by rigorous definition) $\mathbf{L}_{iJMn}$ for the matrix phase of multiferroic composites, with subscript $i,n = 1 \sim 3$ and $J,M = 1 \sim 5$:

$$\mathbf{L}_{iJMn} = \begin{cases} \mathbf{C}_{iJMn}, & J,M = 1,2,3, \\ \mathbf{e}_{niJ}, & J = 1,2,3, M = 4, \\ \mathbf{q}_{niJ}, & J = 1,2,3, M = 5, \\ \mathbf{e}_{iMn}, & J = 4, M = 1,2,3, \\ \mathbf{q}_{iMn}, & J = 5, M = 1,2,3, \\ -\kappa_{in}, & J = 4, \ M = 4, \\ -\alpha_{in}, & J = 4, \ M = 5 \ \ \& \ \ J = 5, \ M = 4, \\ -\mu_{in}, & J = 5, \ M = 5. \end{cases} \tag{8.15}$$

With $\mathbf{L}_{iJMn}$, we introduce a 5×5 matrix $\mathbf{K}_{MJ}$,

$$\mathbf{K}_{MJ} = \mathbf{L}_{iJMn} x_i x_n, \tag{8.16}$$

where $x_i = [x_1, \ x_2, \ x_3]^{\mathrm{T}}$. Then we define another pseudo tensor $\mathbf{J}_{inMJ}$,

$$\mathbf{J}_{inMJ}(x_1, \ x_2, \ x_3) = x_i x_n \mathbf{K}_{MJ}^{-1}, \tag{8.17}$$

so that it is a function of x_1, x_2, and x_3. Next we integrate $\mathbf{J}_{inMJ}$ over the volume of an ellipsoid inclusion $\Omega: \ x_1^2/a_1^2 + x_2^2/a_2^2 + x_3^2/a_3^2 \leq 1$. When this inclusion is spheroidal and symmetric about three-direction, it satisfies $a_1 = a_2$ and $\alpha = \alpha_3/a_1$, where α is the aspect ratio of inclusions used in the text. Hence the volume integral of $\mathbf{J}_{inMJ}$ can be written as

$$\begin{aligned} \mathbf{H}_{inMJ} &= \int_{\Omega} \mathbf{J}_{inMJ}(x_1/a_1, \ x_2/a_2, \ x_3/a_3) \mathrm{d}V = \int_{\Omega} \mathbf{J}_{inMJ}(x_1, \ x_2, \ x_3/\alpha) \mathrm{d}V, \\ &= \int_{-1}^{1} \mathrm{d}\tau \int_{0}^{2\pi} \mathbf{J}_{inMJ}(y_1, \ y_2, \ y_3/\alpha) \mathrm{d}\theta, \end{aligned} \tag{8.18}$$

where the second equality is based on the fact that $\mathbf{J}_{inMJ}$ is a homogeneous function of order zero; thus multiplying all the variables by a_1 will not affect the integration. The third equality is given by applying a change of variables from x_1, x_2, and x_3 to

$$y_1 = \sqrt{1-\tau^2}\cos\theta, \qquad y_1 = \sqrt{1-\tau^2}\sin\theta, \qquad y_3 = \tau, \tag{8.19}$$

with $\tau \in [-1,\ \ 1]$ and $\theta \in [0,\ \ 2\pi]$. Finally the S-tensor is determined by

$$\mathbf{S}_{MnAb} = \begin{cases} \dfrac{1}{8\pi}\mathbf{L}_{iJAb}(\mathbf{H}_{inMJ} + \mathbf{H}_{iMnJ}), & M = 1 \sim 3, \\ \dfrac{1}{4\pi}\mathbf{L}_{iJAb}\mathbf{H}_{in4J}, & M = 4, \\ \dfrac{1}{4\pi}\mathbf{L}_{iJAb}\mathbf{H}_{in5J}, & M = 5. \end{cases} \tag{8.20}$$

Still $\mathbf{S}_{MnAb}$ is a pseudo tensor. For the convenience of calculation we now convert it into a 12×12 matrix $\mathbf{S}$ by the Voigt-Nye contract notations.

For a general spheroid, evaluation of the integral in Eq. (8.18) can be carried out by the Gaussian quadrature method. It turns the definite integral into a weighted sum of function values at specified points within the domain of integration. Then it can be rewritten as

$$\mathbf{H}_{inMJ} = \int_{-1}^{1} \mathrm{d}\tau \int_{0}^{2\pi} \mathbf{J}_{inMJ}(y_1,\ \ y_2,\ \ y_3/\alpha)\mathrm{d}\theta \approx \sum_{i=1}^{n} w_i f(\tau_i), \tag{8.21}$$

where $f(\tau) = \int_{0}^{2\pi} \mathbf{J}_{inMJ}(y_1,\ \ y_2,\ \ y_3/\alpha)\mathrm{d}\theta$, n is the total number of specified points (usually $n = 20$ or more will provide enough accuracy), and w_i is the weight at each specified point which can be constructed by different kinds of weight function. Up to this point the calculation of S-tensor is completed. In general, S-tensor is not symmetric, while $\mathbf{S}\mathbf{L}_0^{-1}$ must always be symmetric, as $\mathbf{L}_0$ (the material constant for matrix phase) written in Eq. (8.8) is symmetric. This can be used as a criterion to check if the calculated components of S-tensor are correct.

Explicit forms of the S-tensor are available for 1-3 fibrous composite ($\alpha \to \infty$) and 2-2 multilayered structure ($\alpha \to 0$). These two connectivities represent the most widely used microstructures and are frequently adopted in experiments. Due to the transverse isotropy of the phase, its derivation is quite involved. Keeping in mind that direction 3 is symmetric and plane 1-2 isotropic, its components can be summarized as below:

Type	Piezoelectric matrix	Piezomagnetic matrix
1-3	$S_{11}=S_{22}=\frac{5C_{11}+C_{12}}{8C_{11}}$, $S_{12}=S_{21}=-\frac{1}{8}+\frac{3C_{12}}{8C_{11}}$, $S_{13}=S_{23}=\frac{C_{13}}{2C_{11}}$, $S_{19}=S_{29}=\frac{e_{31}}{2C_{11}}$, $S_{66}=\frac{3}{4}-\frac{C_{12}}{4C_{11}}$, $S_{44}=S_{55}=S_{77}=S_{88}=S_{10,10}=S_{11,11}=\frac{1}{2}$, all the other components are zero.	$S_{11}=S_{22}=\frac{5C_{11}+C_{12}}{8C_{11}}$, $S_{12}=S_{21}=-\frac{1}{8}+\frac{3C_{12}}{8C_{11}}$, $S_{13}=S_{23}=\frac{C_{13}}{2C_{11}}$, $S_{1,12}=S_{2,12}=\frac{q_{31}}{2C_{11}}$, $S_{66}=\frac{3}{4}-\frac{C_{12}}{4C_{11}}$, $S_{44}=S_{55}=S_{77}=S_{88}=S_{10,10}=S_{11,11}=\frac{1}{2}$, all the other components are zero.
2-2	$S_{31}=S_{32}=\frac{e_{31}e_{33}+C_{13}\kappa_{33}}{{e_{33}}^2+C_{33}\kappa_{33}}$, $S_{57}=S_{48}=\frac{e_{15}}{C_{44}}$, $S_{91}=S_{92}=\frac{-C_{33}e_{31}+C_{13}e_{33}}{{e_{33}}^2+C_{33}\kappa_{33}}$, $S_{33}=S_{44}=S_{55}=S_{99}=S_{12,12}=1$, all the other components are zero.	$S_{31}=S_{32}=\frac{q_{31}q_{33}+C_{13}\mu_{33}}{{q_{33}}^2+C_{33}\mu_{33}}$, $S_{5,10}=S_{4,11}=\frac{q_{15}}{C_{44}}$, $S_{12,1}=S_{12,2}=\frac{-C_{33}q_{31}+C_{13}q_{33}}{{q_{33}}^2+C_{33}\mu_{33}}$, $S_{33}=S_{44}=S_{55}=S_{99}=S_{12,12}=1$, all the other components are zero.

(8.22)

For the S-tensor of the interphase, which is isotropic, its components are

$$
\begin{aligned}
S_{11}^{\text{int}} &= S_{22}^{\text{int}} = \frac{3}{8(1-\nu_0)}\frac{\alpha^2}{\alpha^2-1} + \frac{1}{4(1-\nu_0)}\left[1-2\nu_0-\frac{9}{4(\alpha^2-1)}\right]g(g\alpha),\\
S_{33}^{\text{int}} &= \frac{1}{2(1-\nu_0)}\left\{1-2\nu_0+\frac{3\alpha^2-1}{\alpha^2-1}-\left[1-2\nu_0+\frac{3\alpha^2}{\alpha^2-1}\right]g(\alpha)\right\},\\
S_{12}^{\text{int}} &= S_{21}^{\text{int}} = \frac{1}{4(1-\nu_0)}\left\{\frac{\alpha^2}{2(\alpha^2-1)}-\left[1-2\nu_0+\frac{3}{4(\alpha^2-1)}\right]g(\alpha)\right\},\\
S_{13}^{\text{int}} &= S_{23}^{\text{int}} = -\frac{1}{2(1-\nu_0)}\frac{\alpha^2}{\alpha^2-1} + \frac{1}{4(1-\nu_0)}\left\{\frac{3\alpha^2}{\alpha^2-1}-(1-2\nu_0)\right\}g(\alpha),\\
S_{31}^{\text{int}} &= S_{32}^{\text{int}} = -\frac{1}{2(1-\nu_0)}\left[1-2\nu_0+\frac{1}{\alpha^2-1}\right] + \frac{1}{2(1-\nu_0)}\left[1-2\nu_0+\frac{3}{2(\alpha^2-1)}\right]g(\alpha),
\end{aligned}
\tag{8.23}
$$

$$
S_{44}^{\text{int}} = S_{55}^{\text{int}} = \frac{1}{2(1-\nu_0)}\left\{1-2\nu_0-\frac{\alpha^2+1}{\alpha^2-1}-\frac{1}{2}\left[1-2\nu_0-\frac{3(\alpha^2+1)}{\alpha^2-1}\right]g(\alpha)\right\},
$$

$$S_{66}^{\text{int}} = \frac{1}{2(1-\nu_0)}\left\{\frac{\alpha^2}{2(\alpha^2-1)} + \left[1 - 2\nu_0 - \frac{3}{4(\alpha^2-1)}\right]g(\alpha)\right\},$$
$$S_{77}^{\text{int}} = S_{88}^{\text{int}} = S_{10,10}^{\text{int}} = S_{11,11}^{\text{int}} = \frac{1}{2}g(\alpha),$$
$$S_{99}^{\text{int}} = S_{12,12}^{\text{int}} = 1 - g(\alpha),$$

and all the other components are zero. Here $\nu_0 = \left(C_{11}^{\text{int}} - 2C_{44}^{\text{int}}\right)/2\left(C_{11}^{\text{int}} - C_{44}^{\text{int}}\right)$ is Poisson's ratio of the interphase, and function $g(\alpha)$ depends on the aspect ratio, as

$$g(\alpha) = \begin{cases} \dfrac{\alpha}{(1-\alpha^2)^{\frac{3}{2}}}\left[\cos^{-1}\alpha - \alpha\left(1-\alpha^2\right)^{\frac{1}{2}}\right], & \alpha < 1, \\ \dfrac{\alpha}{(\alpha^2-1)^{\frac{3}{2}}}\left[\alpha\left(\alpha^2-1\right)^{\frac{1}{2}} - \cosh^{-1}\alpha\right], & \alpha \geq 1. \end{cases} \tag{8.24}$$

This set of S-tensor can reduce to the commonly used S-tensor for the uncoupled elastic, dielectric, magnetic, electrical, or thermal conduction problem.

Finally the matrix form for the isotropic magneto-electro-elastic tensor of the interphase $\mathbf{L}_{\text{int}}$ is

$$\mathbf{L}_{\text{int}} = \begin{bmatrix} C_{11}^{\text{int}} & C_{12}^{\text{int}} & C_{12}^{\text{int}} & 0 & 0 & 0 & 0 & 0 & 0 & 0 & 0 & 0 \\ C_{12}^{\text{int}} & C_{11}^{\text{int}} & C_{12}^{\text{int}} & 0 & 0 & 0 & 0 & 0 & 0 & 0 & 0 & 0 \\ C_{12}^{\text{int}} & C_{12}^{\text{int}} & C_{11}^{\text{int}} & 0 & 0 & 0 & 0 & 0 & 0 & 0 & 0 & 0 \\ 0 & 0 & 0 & C_{44}^{\text{int}} & 0 & 0 & 0 & 0 & 0 & 0 & 0 & 0 \\ 0 & 0 & 0 & 0 & C_{44}^{\text{int}} & 0 & 0 & 0 & 0 & 0 & 0 & 0 \\ 0 & 0 & 0 & 0 & 0 & C_{44}^{\text{int}} & 0 & 0 & 0 & 0 & 0 & 0 \\ 0 & 0 & 0 & 0 & 0 & 0 & -\kappa^{\text{int}} & 0 & 0 & 0 & 0 & 0 \\ 0 & 0 & 0 & 0 & 0 & 0 & 0 & -\kappa^{\text{int}} & 0 & 0 & 0 & 0 \\ 0 & 0 & 0 & 0 & 0 & 0 & 0 & 0 & -\kappa^{\text{int}} & 0 & 0 & 0 \\ 0 & 0 & 0 & 0 & 0 & 0 & 0 & 0 & 0 & -\mu^{\text{int}} & 0 & 0 \\ 0 & 0 & 0 & 0 & 0 & 0 & 0 & 0 & 0 & 0 & -\mu^{\text{int}} & 0 \\ 0 & 0 & 0 & 0 & 0 & 0 & 0 & 0 & 0 & 0 & 0 & -\mu^{\text{int}} \end{bmatrix}, \tag{8.25}$$

where $C_{12}^{\text{int}} = C_{11}^{\text{int}} - 2C_{44}^{\text{int}}$.

Appendix 3: Explicit Results for α_{33} and α_{11} of the 1-3 and 2-2 Multiferroic Composites with a Perfect and an Imperfect Interface

For fibrous composites and multilayers, explicit formulae for the components of S-tensor are listed in the Appendix 2. With it and the theory given in Eq. (8.8) for the perfect interface, and Eq. (8.9) together with Eq. (8.8) for the imperfect interface, we have obtained the explicit expressions for the magnetoelectric coupling coefficients, α_{33} and α_{11}. As the 1-3 and 2-2 composites are widely used, we give the results here for ready reference.

In reading the following expressions, care must be exercised that superscript "e" always refers to the properties of $BaTiO_3$ regardless whether BTO exists as the matrix or inclusions, and superscript "m" always refers to the properties of $CoFe_2O_4$, also regardless whether it exists as inclusion or matrix. Superscript "int" on the other hand refers to the properties of the interface. In addition, for 1-3 composites, c_1 and c_0 denote the volume concentrations of the inclusions and matrix, respectively, which could be CFO or BTO. c_{int} denotes the volume concentration of interface in the thinly coated inclusion. While for 2-2 composites, c_0, c_1, and c_{int} denote the volume concentrations of BTO, CFO, and interface in the whole composite, so that $c_0 + c_1 + c_{\text{int}} = 1$.

The 1-3 Multiferroic Fibrous Composites with a Perfect Interface

With $CoFe_2O_4$ as inclusions and $BaTiO_3$ as the matrix, we find

$$\alpha_{33} = -\frac{2c_0c_1e_{31}^{(e)}q_{31}^{(m)}}{C_{11}^{(e)} + C_{11}^{(m)} - c_0\left(C_{12}^{(e)} - C_{12}^{(m)}\right) + c_1\left(C_{11}^{(e)} - C_{11}^{(m)}\right)}, \tag{8.26}$$

$$\alpha_{11} = -\frac{4c_0c_1e_{12}^{(e)}q_{15}^{(m)}\kappa_{11}^{(m)}\mu_{11}^{(e)}}{D_{\alpha 11}^{\text{BTO}}}, \tag{8.27}$$

where denominator $D_{\alpha 11}^{\text{BTO}}$ is

$$\begin{aligned} D_{\alpha 11}^{\text{BTO}} = {} & c_0^2 q_{15}^{(m)2}\left[\kappa_{11}^{(e)} + \kappa_{11}^{(m)} + c_1\left(\kappa_{11}^{(e)} - \kappa_{11}^{(m)}\right)\right] + \left\{(1+c_1)^2 e_{15}^{(e)}2\right. \\ & + \left[C_{44}^{(e)} + C_{44}^{(m)} + c_1\left(C_{44}^{(e)} - C_{44}^{(m)}\right)\right] \\ & \left.\times\left[\kappa_{11}^{(e)} + \kappa_{11}^{(m)} + c_1\left(\kappa_{11}^{(e)} - \kappa_{11}^{(m)}\right)\right]\right\}\left[\mu_{11}^{(e)} + \mu_{11}^{(m)} + c_1\left(\mu_{11}^{(e)} - \mu_{11}^{(m)}\right)\right]. \end{aligned} \tag{8.28}$$

On the other hand with $BaTiO_3$ as inclusion phase, we have

$$\alpha_{33} = -\frac{2c_0c_1e_{31}^{(e)}q_{31}^{(m)}}{C_{11}^{(e)} + C_{11}^{(m)} + c_0\left(C_{12}^{(e)} - C_{12}^{(m)}\right) - c_1\left(C_{11}^{(e)} - C_{11}^{(m)}\right)}, \tag{8.29}$$

$$\alpha_{11} = \frac{4c_0c_1e_{15}^{(e)}q_{15}^{(m)}\kappa_{11}^{(m)}\mu_{11}^{(e)}}{D_{\alpha 11}^{\mathrm{CFO}}}, \tag{8.30}$$

where

$$\begin{aligned} D_{\alpha 11}^{\mathrm{CFO}} = {} & c_0^2 e_{15}^{(e)2}\left[\mu_{11}^{(m)} + \mu_{11}^{(e)} + c_1\left(\mu_{11}^{(m)} - \mu_{11}^{(e)}\right)\right] + \left\{1(+c_1)^2 q_{15}^{(m)} 2\right. \\ & + \left[C_{44}^{(m)} + C_{44}^{(e)} + c_1\left(C_{44}^{(m)} - C_{44}^{(e)}\right)\right] \\ & \left.\times \left[\mu_{11}^{(m)} + \mu_{11}^{(e)} + c_1\left(\kappa_{11}^{(m)} - \kappa_{11}^{(e)}\right)\right]\right\}\left[\kappa_{11}^{(m)} + \kappa_{11}^{(e)} + c_1\left(\kappa_{11}^{(m)} - \kappa_{11}^{(e)}\right)\right]. \end{aligned} \tag{8.31}$$

The 1-3 Multiferroic Fibrous Composites with an Imperfect Interface

In order to obtain the effective magnetoelectric coefficients of 1-3 multiferroic composites with imperfect interface, we first obtain the relevant properties of coated inclusion from Eq. (8.9). This in turn can be used for the properties of the inclusion phase in Eq. (8.8) for the overall composite.

For the coated $CoFe_2O_4$ inclusion—with a prime added to superscript m—we obtain from Eq. (8.9)

$$\begin{aligned} C_{11}^{(m')} = {} & \frac{C_{11}^{(\mathrm{int})}\left(C_{11}^{(m)} + C_{12}^{(m)} + 2C_{44}^{(\mathrm{int})}\right)}{2C_{11}^{(\mathrm{int})} + c_{\mathrm{int}}\left(C_{11}^{(m)} + C_{12}^{(m)} - 2C_{11}^{(\mathrm{int})} + 2C_{44}^{(\mathrm{int})}\right)} \\ & + \frac{2(1-c_{\mathrm{int}})C_{11}^{(\mathrm{int})}C_{44}^{(\mathrm{int})}\left(C_{11}^{(m)} - C_{12}^{(m)} - 2C_{44}^{(\mathrm{int})}\right)}{4C_{11}^{(\mathrm{int})}C_{44}^{(\mathrm{int})} + c_{\mathrm{int}}\left(C_{11}^{(\mathrm{int})} + C_{44}^{(\mathrm{int})}\right)\left(C_{11}^{(m)} - C_{12}^{(m)} - 2C_{44}^{(\mathrm{int})}\right)}, \end{aligned} \tag{8.32}$$

$$C_{12}^{(m')} = \frac{C_{11}^{(\mathrm{int})}\left(C_{11}^{(m)} + C_{12}^{(m)} + 2C_{44}^{(\mathrm{int})}\right)}{2C_{11}^{(\mathrm{int})} + c_{\mathrm{int}}\left(C_{11}^{(m)} + C_{12}^{(m)} - 2C_{11}^{(\mathrm{int})} + 2C_{44}^{(\mathrm{int})}\right)} - \frac{2C_{44}^{(\mathrm{int})}\left[C_{11}^{(\mathrm{int})}\left(C_{11}^{(m)} - C_{12}^{(m)} + 2C_{44}^{(\mathrm{int})}\right) + c_{\mathrm{int}}C_{44}^{(\mathrm{int})}\left(C_{11}^{(m)} - C_{12}^{(m)} - 2C_{44}^{(\mathrm{int})}\right)\right]}{4C_{11}^{(\mathrm{int})}C_{44}^{(\mathrm{int})} + c_{\mathrm{int}}\left(C_{11}^{(\mathrm{int})} + C_{44}^{(\mathrm{int})}\right)\left(C_{11}^{(m)} - C_{12}^{(m)} - 2C_{44}^{(\mathrm{int})}\right)}, \tag{8.33}$$

$$C_{44}^{(m')} = C_{44}^{(\mathrm{int})} \times \frac{4C_{44}^{(m)}\mu^{(\mathrm{int})} + 2c_{\mathrm{int}}\left[q_{15}^{(m)2} + C_{44}^{(m)}\left(\mu_{11}^{(m)} - \mu^{(\mathrm{int})}\right) - \mu^{\mathrm{int}}\left(C_{44}^{(m)} - C_{44}^{(\mathrm{int})}\right)\right] - c_{\mathrm{int}}{}^2\left[q_{15}^{(m)2} + \left(C_{44}^{(m)} - C_{44}^{(\mathrm{int})}\right)\left(\mu_{11}^{(m)} - \mu^{(\mathrm{int})}\right)\right]}{4C_{44}^{(\mathrm{int})}\mu^{(\mathrm{int})} + 2c_{\mathrm{int}}\left[C_{44}^{(\mathrm{int})}\left(\mu_{11}^{(m)} - \mu^{(\mathrm{int})}\right) + \mu^{(\mathrm{int})}\left(C_{44}^{(m)} - C_{44}^{(\mathrm{int})}\right)\right] + c_{\mathrm{int}}{}^2\left[q_{15}^{(m)2} + \left(C_{44}^{(m)} - C_{44}^{(\mathrm{int})}\right)\left(\mu_{11}^{(m)} - \mu^{(\mathrm{int})}\right)\right]}, \tag{8.34}$$

$$q_{31}^{(m')} = \kappa^{(\mathrm{int})}\frac{2\kappa_{11}^{(m)} - c_{\mathrm{int}}\left(\kappa_{11}^{(m)} - \kappa^{(\mathrm{int})}\right)}{2\kappa^{(\mathrm{int})} + c_{\mathrm{int}}\left(\kappa_{11}^{(m)} - \kappa^{(\mathrm{int})}\right)}, \tag{8.35}$$

$$q_{15}^{(m')} = \frac{4(1 - c_{\mathrm{int}})q_{15}^{(m)}C_{44}^{(\mathrm{int})}\mu^{(\mathrm{int})}}{4C_{44}^{(\mathrm{int})}\mu^{(\mathrm{int})} + 2c_{\mathrm{int}}\left[C_{44}^{(\mathrm{int})}\left(\mu_{11}^{(m)} - \mu^{(\mathrm{int})}\right) + \mu^{(\mathrm{int})}\left(C_{44}^{(m)} - C_{44}^{(\mathrm{int})}\right)\right] + c_{\mathrm{int}}{}^2\left[q_{15}^{(m)2} + \left(C_{44}^{(m)} - C_{44}^{(\mathrm{int})}\right)\left(\mu_{11}^{(m)} - \mu^{(\mathrm{int})}\right)\right]}, \tag{8.36}$$

$$\kappa_{11}^{(m')} = \kappa^{(\mathrm{int})}\frac{2\kappa_{11}^{(m)} - c_{\mathrm{int}}\left(\kappa_{11}^{(m)} - \kappa^{(\mathrm{int})}\right)}{2\kappa^{(\mathrm{int})} + c_{\mathrm{int}}\left(\kappa_{11}^{(m)} - \kappa^{(\mathrm{int})}\right)}, \tag{8.37}$$

$$\mu_{11}^{(m')} = \mu^{(\mathrm{int})} \times \frac{4\mu_{11}^{(m)}C_{44}^{(\mathrm{int})} + 2c_{\mathrm{int}}\left[q_{15}^{(m)2} + \mu_{11}^{(m)}\left(C_{44}^{(m)} - C_{44}^{(\mathrm{int})}\right) - C_{44}^{(\mathrm{int})}\left(\mu_{11}^{(m)} - \mu^{(\mathrm{int})}\right)\right] - c_{\mathrm{int}}{}^2\left[q_{15}^{(m)2} + \left(C_{44}^{(m)} - C_{44}^{(\mathrm{int})}\right)\left(\mu_{11}^{(m)} - \mu^{(\mathrm{int})}\right)\right]}{4\mu^{(\mathrm{int})}C_{44}^{(\mathrm{int})} + 2c_{\mathrm{int}}\left[\mu^{(\mathrm{int})}\left(C_{44}^{(m)} - C_{44}^{(\mathrm{int})}\right) + C_{44}^{(\mathrm{int})}\left(\mu_{11}^{(m)} - \mu^{(\mathrm{int})}\right)\right] + c_{\mathrm{int}}{}^2\left[q_{15}^{(m)2} + \left(C_{44}^{(m)} - C_{44}^{(\mathrm{int})}\right)\left(\mu_{11}^{(m)} - \mu^{(\mathrm{int})}\right)\right]}. \tag{8.38}$$

This set can be used to replace the properties of CFO in Eqs. (8.25)–(8.27) to obtain α_{33} and α_{11} of the CFO-in-BTO composite with an imperfect interface.

Likewise for the coated $BaTiO_3$ inclusion—also with a prime added to e—we have

$$C_{11}^{(e')} = \frac{c_{11}^{(\mathrm{int})}\left(c_{11}^{(e)} + c_{12}^{(e)} + 2C_{44}^{(\mathrm{int})}\right)}{2C_{11}^{(\mathrm{int})} + c_{\mathrm{int}}\left(C_{11}^{(e)} + C_{12}^{(e)} - 2C_{11}^{(\mathrm{int})} + 2C_{44}^{(\mathrm{int})}\right)} + \frac{2(1-c_{\mathrm{int}})C_{11}^{(\mathrm{int})}C_{44}^{(\mathrm{int})}\left(C_{11}^{(e)} - C_{12}^{(e)} - 2C_{44}^{(\mathrm{int})}\right)}{4C_{11}^{(\mathrm{int})}C_{44}^{(\mathrm{int})} + c_{\mathrm{int}}\left(C_{11}^{(\mathrm{int})} + C_{44}^{(\mathrm{int})}\right)\left(C_{11}^{(e)} - C_{12}^{(e)} - 2C_{44}^{(\mathrm{int})}\right)}, \tag{8.39}$$

$$C_{12}^{(e')} = \frac{c_{11}^{(\mathrm{int})}\left(c_{11}^{(e)} + c_{12}^{(e)} + 2C_{44}^{(\mathrm{int})}\right)}{2C_{11}^{(\mathrm{int})} + c_{\mathrm{int}}\left(C_{11}^{(e)} + C_{12}^{(e)} - 2C_{11}^{(\mathrm{int})} + 2C_{44}^{(\mathrm{int})}\right)} - \frac{2C_{44}^{(\mathrm{int})}\left[C_{11}^{(\mathrm{int})}\left(C_{11}^{(e)} - C_{12}^{(e)} + 2C_{44}^{(\mathrm{int})}\right) + c_{\mathrm{int}}C_{44}^{(\mathrm{int})}\left(C_{11}^{(e)} - C_{12}^{(e)} - 2C_{44}^{(\mathrm{int})}\right)\right]}{4C_{11}^{(\mathrm{int})}C_{44}^{(\mathrm{int})} + c_{\mathrm{int}}\left(C_{11}^{(\mathrm{int})} + C_{44}^{(\mathrm{int})}\right)\left(C_{11}^{(e)} - C_{12}^{(e)} - 2C_{44}^{(\mathrm{int})}\right)}, \tag{8.40}$$

$$C_{44}^{(e')} = C_{44}^{(\mathrm{int})} \times \frac{4C_{44}^{(e)}\kappa^{(\mathrm{int})} + 2c_{\mathrm{int}}\left[e_{15}^{(e)2} + C_{44}^{(e)}\left(\kappa_{11}^{(e)} - \kappa^{(\mathrm{int})}\right) - \kappa^{\mathrm{int}}\left(C_{44}^{(e)} - C_{44}^{(\mathrm{int})}\right)\right] - c_{\mathrm{int}}{}^2\left[e_{15}^{(e)2} + \left(C_{44}^{(e)} - C_{44}^{(\mathrm{int})}\right)\left(\kappa_{11}^{(e)} - \kappa^{(\mathrm{int})}\right)\right]}{4C_{44}^{(\mathrm{int})}\kappa^{(\mathrm{int})} + 2c_{\mathrm{int}}\left[C_{44}^{(\mathrm{int})}\left(\kappa_{11}^{(e)} - \kappa^{(\mathrm{int})}\right) + \kappa^{(\mathrm{int})}\left(C_{44}^{(e)} - C_{44}^{(\mathrm{int})}\right)\right] + c_{\mathrm{int}}{}^2\left[e_{15}^{(e)2} + \left(C_{44}^{(e)} - C_{44}^{(\mathrm{int})}\right)\left(\kappa_{11}^{(e)} - \kappa^{(\mathrm{int})}\right)\right]}, \tag{8.41}$$

$$e_{31}^{(e')} = \frac{2(1-c_{\mathrm{int}})e_{31}^{(e)}C_{11}^{(\mathrm{int})}}{c_{\mathrm{int}}\left(C_{11}^{(e)} + C_{12}^{(e)} - 2C_{11}^{(\mathrm{int})} + 2C_{44}^{(\mathrm{int})}\right) + 2C_{11}^{(\mathrm{int})}}, \tag{8.42}$$

$$e_{15}^{(e')} = \frac{4(1-c_{\mathrm{int}})e_{15}^{(e)}C_{44}^{(\mathrm{int})}\kappa^{(\mathrm{int})}}{4C_{44}^{(\mathrm{int})}\kappa^{(\mathrm{int})} + 2c_{\mathrm{int}}\left[C_{44}^{(\mathrm{int})}\left(\kappa_{11}^{(e)} - \kappa^{(\mathrm{int})}\right) + \kappa^{(\mathrm{int})}\left(C_{44}^{(e)} - C_{44}^{(\mathrm{int})}\right)\right] + c_{\mathrm{int}}{}^2\left[e_{15}^{(e)2} + \left(C_{44}^{(e)} - C_{44}^{(\mathrm{int})}\right)\left(\kappa_{11}^{(e)} - \kappa^{(\mathrm{int})}\right)\right]}, \tag{8.43}$$

$$\kappa_{11}^{(e')} = \kappa^{(\mathrm{int})} \times \frac{\begin{array}{l} 4\kappa_{11}^{(e)} C_{44}^{(\mathrm{int})} + 2c_{\mathrm{int}}\left[e_{15}^{(e)2} + \kappa_{11}^{(e)}\left(C_{44}^{(e)} - C_{44}^{(\mathrm{int})}\right) - C_{44}^{(\mathrm{int})}\left(\kappa_{11}^{(e)} - \kappa^{(\mathrm{int})}\right)\right] \\ - {c_{\mathrm{int}}}^2\left[e_{15}^{(e)2} + \left(C_{44}^{(e)} - C_{44}^{(\mathrm{int})}\right)\left(\kappa_{11}^{(e)} - \kappa^{(\mathrm{int})}\right)\right] \end{array}}{\begin{array}{l} 4\kappa^{(\mathrm{int})} C_{44}^{(\mathrm{int})} + 2c_{\mathrm{int}}\left[\kappa^{(\mathrm{int})}\left(C_{44}^{(e)} - C_{44}^{(\mathrm{int})}\right) + C_{44}^{(\mathrm{int})}\left(\kappa_{11}^{(e)} - \kappa^{(\mathrm{int})}\right)\right] \\ + {c_{\mathrm{int}}}^2\left[e_{15}^{(e)2} + \left(C_{44}^{(e)} - C_{44}^{(\mathrm{int})}\right)\left(\kappa_{11}^{(e)} - \kappa^{(\mathrm{int})}\right)\right] \end{array}}, \tag{8.44}$$

$$\mu_{11}^{(e')} = \mu^{(\mathrm{int})} \frac{2\mu_{11}^{(e)} - c_{\mathrm{int}}\left(\mu_{11}^{(e)} - \mu^{(\mathrm{int})}\right)}{2\mu^{(\mathrm{int})} + c_{\mathrm{int}}\left(\mu_{11}^{(e)} - \mu^{(\mathrm{int})}\right)}. \tag{8.45}$$

This set can be used to replace the properties of BTO in Eqs. (8.28)–(8.30) to obtain α_{33} and α_{11} of the BTO-in-CFO composite with an imperfect interface.

The 2-2 Multiferroic Multilayers with a Perfect Interface

For the 2-2 multiferroic composites with a perfect interface, we find

$$\alpha_{33} = -\frac{c_0 c_1 e_{33}^{(e)} q_{33}^{(m)} \kappa_{33}^{(m)} \mu_{33}^{(e)}}{D_{\alpha 33}}, \tag{8.46}$$

$$\alpha_{11} = -\frac{c_0 c_1 e_{15}^{(e)} q_{15}^{(m)}}{c_0 C_{44}^{(m)} + c_1 C_{44}^{(e)}}, \tag{8.47}$$

where the denominator $D_{\alpha 33}$ is

$$\begin{aligned} D_{\alpha 33} = {} & {c_0}^2\left(c_0\kappa_{33}^{(m)} + c_1\kappa_{33}^{(e)}\right)\left(q_{33}^{(m)2} + C_{33}^{(m)}\mu_{33}^{(m)}\right) + c_0 c_1\left[\left(c_0\kappa_{33}^{(m)} + c_1\kappa_{33}^{(e)}\right)C_{33}^{(m)}\mu_{33}^{(e)}\right. \\ & \left. + \left(c_0\mu_{33}^{(m)} + c_1\mu_{33}^{(e)}\right)C_{33}^{(e)}\kappa_{33}^{(m)}\right] + {c_1}^2\left(c_0\mu_{33}^{(m)} + c_1\mu_{33}^{(e)}\right)\left(e_{33}^{(e)2} + C_{33}^{(e)}\kappa_{33}^{(e)}\right), \end{aligned} \tag{8.48}$$

where c_0 is for BTO and c_1 for CFO.

The 2-2 Multiferroic Multilayers with an Imperfect Interface

With an imperfect interface, we have

$$\alpha_{33} = -\frac{c_0 c_1 e_{33}^{(e)} q_{33}^{(m)} \kappa_{33}^{(m)} \mu_{33}^{(e)} C_{11}^{(\mathrm{int})} \kappa^{\mathrm{int}} \mu^{\mathrm{int}}}{D_{\alpha 33}}, \tag{8.49}$$

$$\alpha_{11} = -\frac{c_0 c_1 e_{15}^{(e)} q_{15}^{(m)} C_{44}^{(\mathrm{int})}}{c_0 C_{44}^{(m)} C_{44}^{(\mathrm{int})} + c_1 C_{44}^{(e)} C_{44}^{(\mathrm{int})} + c_{\mathrm{int}} C_{44}^{(e)} C_{44}^{(m)}}, \tag{8.50}$$

where

$$D_{\alpha 33} = \lambda_1 {c_0}^3 + \lambda_2 {c_1}^3 + \lambda_3 {c_{\mathrm{int}}}^3 + \lambda_4 {c_0}^2 c_1 + \lambda_5 {c_0}^2 c_{\mathrm{int}} + \lambda_6 {c_1}^2 c_0 + \lambda_7 {c_1}^2 c_{\mathrm{int}} + \lambda_8 {c_{\mathrm{int}}}^2 c_0 + \lambda_9 {c_{\mathrm{int}}}^2 c_1 + \lambda_{10} c_0 c_1 c_{\mathrm{int}}. \tag{8.51}$$

The coefficients λ_1 to λ_{10} are given by

$$\lambda_1 = \kappa_{33}^{(m)} \left({q_{33}^{(m)}}^2 + C_{33}^{(m)} \mu_{33}^{(m)} \right) C_{11}^{(\mathrm{int})} \kappa^{\mathrm{int}} \mu^{\mathrm{int}},$$

$$\lambda_2 = \mu_{33}^{(e)} \left({e_{33}^{(e)}}^2 + C_{33}^{(e)} \kappa_{33}^{(e)} \right) C_{11}^{(\mathrm{int})} \kappa^{\mathrm{int}} \mu^{\mathrm{int}},$$

$$\lambda_3 = \mu_{33}^{(e)} \left({e_{33}^{(e)}}^2 + C_{33}^{(e)} \kappa_{33}^{(e)} \right) {C_{11}}^{(\mathrm{int})} \kappa^{\mathrm{int}} \mu^{\mathrm{int}},$$

$$\lambda_4 = C_{11}^{(\mathrm{int})} \kappa^{\mathrm{int}} \mu^{\mathrm{int}} \left[\kappa_{33}^{(e)} \left({q_{33}^{(m)}}^2 + C_{33}^{(m)} \mu_{33}^{(m)} \right) + \kappa_{33}^{(m)} \left(C_{33}^{(e)} \mu_{33}^{(m)} + C_{33}^{(m)} \mu_{33}^{(e)} \right) \right],$$

$$\lambda_5 = \kappa_{33}^{(m)} \left({q_{33}^{(m)}}^2 + C_{33}^{(m)} \mu_{33}^{(m)} \right) \left[C_{33}^{(e)} \kappa^{\mathrm{int}} \mu^{\mathrm{int}} + C_{11}^{(\mathrm{int})} \left(\kappa^{\mathrm{int}} \mu_{33}^{(e)} + \kappa_{33}^{(e)} \mu^{\mathrm{int}} \right) \right],$$

$$\lambda_6 = C_{11}^{(\mathrm{int})} \kappa^{\mathrm{int}} \mu^{\mathrm{int}} \left[\mu_{33}^{(m)} \left({e_{33}^{(e)}}^2 + C_{33}^{(e)} \kappa_{33}^{(e)} \right) + \mu_{33}^{(e)} \left(C_{33}^{(e)} \kappa_{33}^{(m)} + C_{33}^{(m)} \kappa_{33}^{(e)} \right) \right],$$

$$\lambda_7 = \mu_{33}^{(e)} \left({e_{33}^{(e)}}^2 + C_{33}^{(e)} \kappa_{33}^{(e)} \right) \left[C_{33}^{(m)} \kappa^{\mathrm{int}} \mu^{\mathrm{int}} + C_{11}^{(\mathrm{int})} \left(\kappa^{\mathrm{int}} \mu_{33}^{(m)} + \kappa_{33}^{(m)} \mu^{\mathrm{int}} \right) \right],$$

$$\lambda_8 = \kappa_{33}^{(m)} \left({q_{33}^{(m)}}^2 + C_{33}^{(m)} \mu_{33}^{(m)} \right) \left[\mu^{\mathrm{int}} \left({e_{33}^{(e)}}^2 + C_{33}^{(e)} \kappa_{33}^{(e)} \right) + \mu_{33}^{(e)} \left(C_{33}^{(e)} \kappa^{\mathrm{int}} + C_{11}^{(\mathrm{int})} \kappa_{33}^{(e)} \right) \right],$$

$$\lambda_9 = \mu_{33}^{(m)} \left({q_{33}^{(m)}}^2 + C_{33}^{(m)} \mu_{33}^{(m)} \right) \left[\kappa^{\mathrm{int}} \left({q_{33}^{(m)}}^2 + C_{33}^{(m)} \mu_{33}^{(m)} \right) + \mu_{33}^{(m)} \left(C_{33}^{(m)} \mu^{\mathrm{int}} + C_{11}^{(\mathrm{int})} \kappa_{33}^{(m)} \right) \right],$$

$$\lambda_{10} = C_{11}^{(\mathrm{int})} \left[\kappa_{33}^{(m)} \mu_{33}^{(m)} \mu \left({e_{33}^{(e)}}^2 + C_{33}^{(e)} \kappa_{33}^{(e)} \right) + \kappa_{33}^{(e)} \mu_{33}^{(e)} \kappa^{\mathrm{int}} \left({q_{33}^{(m)}}^2 + C_{33}^{(m)} \mu_{33}^{(m)} \right) + \kappa_{33}^{(m)} \mu_{33}^{(e)} \left(C_{33}^{(e)} \mu_{33}^{(m)} \kappa^{\mathrm{int}} + C_{33}^{(m)} \kappa_{33}^{(e)} \mu^{\mathrm{int}} \right) \right] + \kappa^{\mathrm{int}} \mu^{\mathrm{int}} \left({e_{33}^{(e)}}^2 + C_{33}^{(e)} \kappa_{33}^{(e)} \right) \left({q_{33}^{(m)}}^2 + C_{33}^{(m)} \mu_{33}^{(m)} \right). \tag{8.52}$$

Most of Appendix 2 and 3 can also be found in Wang et al. (2015).

Appendix 4: The Elastic C_{44} of the Fibrous Multiferroic Composite and the Purely Elastic Composite

We have seen the extraordinary value of C_{44} of the multiferroic composite in Fig. 8.19, and that its value can be higher than the individual value of the constituent phases. But this is not the case with the purely elastic composite shown in Fig. 8.20. This extraordinary value is an outcome of the piezoelectric and piezomagnetic interactions. To make such a difference more apparent, we give the explicit form of C_{44} with 1-3 connectivity.

Here we use the superscript (e) to denote the piezoelectric phase such as BTO, and the superscript (m) to denote the piezomagnetic phase such as CFO. We further use C_{44}^{E} to denote the C_{44} value of the purely elastic composite, and C_{44}^{M} to denote the C_{44} of the multiferroic composite. After making use of the explicit form of S-tensor for a circular cylinder, we have used Eq. (8.8) to derive the effective C_{44} in both cases.

First with the piezoelectric BTO as the matrix, we have found that, for the elastic composite,

$$C_{44}^{\mathrm{E}} = \frac{C_{44}^{(e)}\left[\left(C_{44}^{(e)} + C_{44}^{(m)}\right) - c_1\left(C_{44}^{(e)} - C_{44}^{(m)}\right)\right]}{\left(C_{44}^{(e)} + C_{44}^{(m)}\right) + c_1\left(C_{44}^{(e)} - C_{44}^{(m)}\right)}, \tag{8.53}$$

and for the multiferroic composite, we have

$$C_{44}^{\mathrm{M}} = C_{44}^{\mathrm{E}} + \frac{4c_1(1-c_1)\left(C_{44}^{(e)2} q_{15}^{(m)} 2\widetilde{\kappa}_{11}^{(e)} + C_{44}^{(e)2} e_{15}^{(e)2} \widetilde{\mu}_{11}^{(e)} + e_{15}^{(e)2} q_{15}^{(e)2} \widetilde{C}_{44}^{(e)}\right)}{\widetilde{C}_{44}^{(e)}\left[\widetilde{C}_{44}^{(e)}\widetilde{\kappa}_{11}^{(e)}\widetilde{\mu}_{11}^{(e)} + (1+c_1)^2 e_{15}^{(e)2}\widetilde{\mu}_{11}^{(e)} + (1-c_1)^2 q_{15}^{(e)2}\widetilde{\mu}_{11}^{(e)}\right]}, \tag{8.54}$$

where

$$\begin{aligned}
\widetilde{C}_{44}^{(e)} &= C_{44}^{(e)} + C_{44}^{(m)} + c_1\left(C_{44}^{(e)} - C_{44}^{(m)}\right), \\
\widetilde{\kappa}_{11}^{(e)} &= \kappa_{11}^{(e)} + \kappa_{11}^{(m)} + c_1\left(\kappa_{11}^{(e)} - \kappa_{11}^{(m)}\right), \\
\widetilde{\mu}_{11}^{(e)} &= \mu_{11}^{(e)} + \mu_{11}^{(m)} + c_1\left(\mu_{11}^{(e)} - \mu_{11}^{(m)}\right).
\end{aligned} \tag{8.55}$$

On the other hand with the piezomagnetic CFO as the matrix, we have

$$C_{44}^{\mathrm{E}} = \frac{C_{44}^{(m)}\left[\left(C_{44}^{(m)} + C_{44}^{(e)}\right) - c_1\left(C_{44}^{(m)} - C_{44}^{(e)}\right)\right]}{\left(C_{44}^{(m)} + C_{44}^{(e)}\right) + c_1\left(C_{44}^{(m)} - C_{44}^{(e)}\right)}, \tag{8.56}$$

and for the multiferroic composite, we find

$$C_{44}^{\mathrm{M}} = C_{44}^{E} + \frac{4c_1(1-c_1)\left(C_{44}^{(e)2} q_{15}^{(e)2} \widetilde{\kappa}_{11}^{(m)} + C_{44}^{(e)2} e_{15}^{(e)2} \widetilde{\mu}_{11}^{(m)} + e_{15}^{(e)2} q_{15}^{(m)2} \widetilde{C}_{44}^{(m)}\right)}{\widetilde{C}_{44}^{(m)}\left[\widetilde{C}_{44}^{(m)} \widetilde{\kappa}_{11}^{(m)} \widetilde{\mu}_{11}^{(m)} + (1+c_1)^2 q_{15}^{(m)2} \widetilde{\kappa}_{11}^{(m)} + (1-c_1)^2 e_{15}^{(e)2} \widetilde{\mu}_{11}^{(m)}\right]}, \tag{8.57}$$

where

$$\begin{aligned} \widetilde{C}_{44}^{(m)} &= C_{44}^{(m)} + C_{44}^{(e)} + c_1\left(C_{44}^{(m)} - C_{44}^{(e)}\right), \\ \widetilde{\kappa}_{11}^{(m)} &= \kappa_{11}^{(m)} + \kappa_{11}^{(e)} + c_1\left(\kappa_{11}^{(m)} - \kappa_{11}^{(e)}\right), \\ \widetilde{\mu}_{11}^{(m)} &= \mu_{11}^{(m)} + \mu_{11}^{(e)} + c_1\left(\mu_{11}^{(m)} - \mu_{11}^{(e)}\right). \end{aligned} \tag{8.58}$$

This set of results also gives rise to the outcome of $C_{44}^{\mathrm{M}} \geq C_{44}^{\mathrm{E}}$, regardless of the particular phase serving as the matrix.

References

Avellaneda, M., Harshé, G.: Magnetoelectric effect in piezoelectric/magnetostrictive multilayer (2-2) composites. J. Intell. Mater. Syst. Struct. **5**, 501–513 (1994)

Benveniste, Y.: A new approach to the application of Mori-Tanaka's theory in composite materials. Mech. Mater. **6**, 147–157 (1987)

Benveniste, Y.: Magnetoelectric effect in fibrous composites with piezoelectric and piezomagnetic phases. Phys. Rev. B **51**, 16424–16427 (1995)

Bichurin, M.I., Petrov, V.M., Srinivasan, G.: Theory of low-frequency magnetoelectric coupling in magnetostrictive-piezoelectric bilayers. Phys. Rev. B **68**, 054402 (2003)

Chen, T.: Green's functions and the non-uniform transformation problem in a piezo electric medium. Mech. Res. Commun. **20**, 271–278 (1993a)

Chen, T.: Piezoelectric properties of multipase fibrous composites: some theoretical results. J. Mech. Phys. Solids **41**, 1781–1794 (1993b)

Chen, T.: Exact moduli and bounds of two-phase composites with coupled multifield linear responses. J. Mech. Phys. Solids **45**, 385–398 (1997)

Chen, Z., Su, Y., Meguid, S.A.: The effect of field-orientation on the magnetoelectric coupling in Terfenol-D/PZT/Terfenol-D laminated structure. J. Appl. Phys. **116**, 173910 (2014)

Dinzart, F., Sabar, H.: Magnetoelectric effect in coated fibrous magnetic–piezoelectric composites. J. Intell. Mater. Syst. Struct. **23**, 1249–1261 (2012)

Dunn, M.L.: Electroelastic Green's functions for transversely isotropic piezoelectric media and their application to the solution of inclusion and inhomogeneity problems. Int. J. Eng. Sci. **32**, 119–131 (1994)

Dunn, M.L., Taya, M.: An analysis of piezoelectric composite materials containing ellipsoidal inhomogeneities. Proc. R. Soc. Lond. A **443**, 265–287 (1993a)

Dunn, M.L., Taya, M.: Micromechanics predictions of the effective electroelastic moduli of piezoelectric composites. Int. J. Solids Struct. **30**, 161–175 (1993b)

Dunn, M.L., Wienecke, H.A.: Green's functions for transversely isotropic piezoelectric solids. Int. J. Solids Struct. **33**, 4571–4581 (1996)
Eshelby, J.D.: The determination of the elastic field of an ellipsoidal inclusion, and related problems. Proc. R. Soc. Lond. A **241**, 376–396 (1957)
Harshé, G., Dougherty, J.P., Newnham, R.E.: Theoretical modelling of 3-0/0-3 magnetoelectric composites. Int. J. Appl. Elec. Mech. **4**, 161–171 (1993)
Hill, R.: Theory of mechanical properties of fibre-strengthened materials: I. Elastic behaviour. J. Mech. Phys. Solids **12**, 199–212 (1964)
Huang, J.H.: Analytical predictions for the magnetoelectric coupling in piezomagnetic materials reinforced by piezoelectric ellipsoidal inclusions. Phys. Rev. B **58**, 12–15 (1998)
Huang, J.H., Chiu, Y.-H., Liu, H.-K.: Magneto-electro-elastic Eshelby tensors for a piezoelectric-piezomagnetic composite reinforced by ellipsoidal inclusions. J. Appl. Phys. **83**, 5364–5370 (1998)
Huang, J.H., Kuo, W.-S.: The analysis of piezoelectric/piezomagnetic composite materials containing ellipsoidal inclusions. J. Appl. Phys. **81**, 1378–1386 (1997)
Huang, J.H., Yu, J.S.: Electroelastic Eshelby tensors for an ellipsoidal piezoelectric inclusion. Compos. Eng. **4**, 1169–1182 (1994)
Kuo, H.-Y.: Effective property of multiferroic fibrous composites with imperfect interfaces. Smart Mater. Struct. **22**, 105005 (2013)
Kuo, H.-Y., Bhattacharya, K.: Fibrous composites of piezoelectric and piezomagnetic phases. Mech. Mater. **60**, 159–170 (2013)
Kuo, H.-Y., Slinger, A., Bhattacharya, K.: Optimization of magnetoelectricity in piezoelectric–magnetostrictive bilayers. Smart Mater. Struct. **19**, 125010 (2010)
Li, J., Weng, G.J.: A theory of domain switch for the nonlinear behavior of ferroelectrics. Proc. R. Soc. Lond. A **455**, 3493–3511 (1999)
Li, J.Y., Dunn, M.L.: Anisotropic coupled-field inclusion and inhomogeneity problems. Phil. Mag. A **77**, 1341–1350 (1998a)
Li, J.Y., Dunn, M.L.: Micromechanics of magnetoelectroelastic composite materials: average fields and effective behavior. J. Intell. Mater. Syst. Struct. **9**, 404–416 (1998b)
Liu, G., Zhang, C., Dong, S.: Magnetoelectric effect in magnetostrictive/piezoelectric laminated composite operating in shear-shear mode. J. Appl. Phys. **116**, 074104 (2014)
Liu, L.P., Kuo, H.-Y.: Closed-form solutions to the effective properties of fibrous magnetoelectric composites and their applications. Int. J. Solids Struct. **49**, 3055–3062 (2012)
Mikata, Y.: Determination of piezoelectric Eshelby tensor in transversely isotropic piezoelectric solids. Int. J. Eng. Sci. **38**, 605–641 (2000)
Mikata, Y.: Explicit determination of piezoelectric Eshelby tensors for a spheroidal inclusion. Int. J. Solids Struct. **38**, 7045–7063 (2001)
Milgrom, M., Shtrikman, S.: Linear response of two-phase composites with cross moduli: exact universal relations. Phys. Rev. A **40**, 1568–1575 (1989)
Nan, C.-W.: Magnetoelectric effect in composites of piezoelectric and piezomagnetic phases. Phys. Rev. B **50**, 6082–6088 (1994)
Soh, A.K., Liu, J.X.: On the constitutive equations of magnetoelectroelastic solids. J. Intell. Mater. Syst. Struct. **16**, 597–602 (2005)
Srinivas, S., Li, J.Y., Zhou, Y.C., Soh, A.K.: The effective magnetoelectroelastic moduli of matrix-based multiferroic composites. J. Appl. Phys. **99**, 043905 (2006)
van Suchtelen, J.: Product properties: a new application of composite materials. Philips Res. Rep. **27**, 28–37 (1972)
Wang, B.: Three dimensional analysis of an ellipsoidal inclusion in a piezoelectric material. Int. J. Solids Struct. **29**, 298–303 (1992)
Wang, X., Pan, E.: Magnetoelectric effects in multiferroic fibrous composite with imperfect interface. Phys. Rev. B **76**, 214107 (2007)

Wang, Y., Hasanyan, D., Li, M., Gao, J., Li, J., Viehland, D., Luo, H.: Theoretical model for geometry-dependent magnetoelectric effect in magnetostrictive/piezoelectric composites. J. Appl. Phys. **111**, 124513 (2012)

Wang, Y., Su, Y., Li, J., Weng, G.J.: A theory of magnetoelectric coupling with interface effects and aspect-ratio dependence in piezoelectric-piezomagnetic composites. J. Appl. Phys. **117**, 164106 (2015)

Wang, Y., Weng, G.J., Meguid, S.A., Hamouda, A.M.: A continuum model with a percolation threshold and tunneling-assisted interfacial conductivity for carbon nanotube-based nanocomposites. J. Appl. Phys. **115**, 193706 (2014)

Weng, G.J.: Some elastic properties of reinforced solids, with special reference to isotropic ones containing spherical inclusions. Int. J. Eng. Sci. **22**, 845–856 (1984)

Weng, G.J.: The theoretical connection between Mori-Tanaka's theory and the Hashin-Shtrikman-Walpole bounds. Int. J. Eng. Sci. **28**, 1111–1120 (1990)

Weng, G.J.: Explicit evaluation of Willis' bounds with ellipsoidal inclusions. Int. J. Eng. Sci. **30**, 83–92 (1992)

Weng, G.J., Wong, D.T.: Thermodynamic driving force in ferroelectric crystals with a rank-2 laminated domain pattern, and a study of enhanced electrostriction. J. Mech. Phys. Solids **57**, 571–597 (2009)

Willis, J.R.: Bounds and self-consistent estimates for the overall properties of anisotropic composites. J. Mech. Phys. Solids **25**, 185–202 (1977)

Yue, Y.M., Xu, K.Y.: Influence of thin interphase on magnetoelectric effect of coated cylindrical fibrous multiferroic composites. J. Appl. Phys. **113**, 224101 (2013)

Chapter 9
Snap-Through Buckling of Micro/ Nanobeams in Bistable Micro/ Nanoelectromechanical Systems

Xue Chen and Shaker A. Meguid

Abstract In this chapter, we investigate the instability behavior of an initially curved micro/nanobeam subject to an electrostatic force. The general governing equations of the curved beam are developed using Euler-Bernoulli beam theory and are solved using the Galerkin decomposition method. Firstly, the size effect on the symmetric snap-through buckling of the microbeam is studied. The size effect is accounted for in the beam model using the modified couple stress theory. The fringing field effect and the intermolecular effects, such as van der Waals and Casimir forces, are also included in the snap-through formulations. The model simulations reveal the significant effect of the beam size, and to a much lesser extent the effect of fringing field and intermolecular forces, upon the snap-through criterion for the curved microbeam. Secondly, the surface effects on the asymmetric bifurcation of the nanobeam are studied. The surface effects, including the surface elasticity and the residual surface tension, are accounted for in the model formulation. The results reveal the significant size effect due to the surface elasticity and the residual surface tension on the symmetry-breaking criterion for the considered nanobeam.

9.1 Introduction

Micro/nano-electro-mechanical systems (MEMS/NEMS) have aroused great interest for their unique advantages such as small size, high precision, and low power consumption. One benchmark of MEMS/NEMS is the initially straight micro/nanobeam system driven by electrostatic force, whose static and dynamic behaviors have been largely investigated in the literature (Carr et al. 1999; Dequesnes et al. 2002; Jia et al. 2011; Ke et al. 2005; Kinaret et al., 2003; Li et al., 2013; Ruzziconi et al., 2013; Tilmans and Legtenberg, 1994; Verbridge et al., 2007

X. Chen • S.A. Meguid (✉)
Mechanics and Aerospace Design Laboratory, Department of Mechanical and Industrial Engineering, University of Toronto, 5 King's College Road, Toronto, ON, Canada, M5S 3G8
e-mail: xchen@mie.utoronto.ca; meguid@mie.utoronto.ca

S.A. Meguid (ed.), *Advances in Nanocomposites*,
DOI 10.1007/978-3-319-31662-8_9

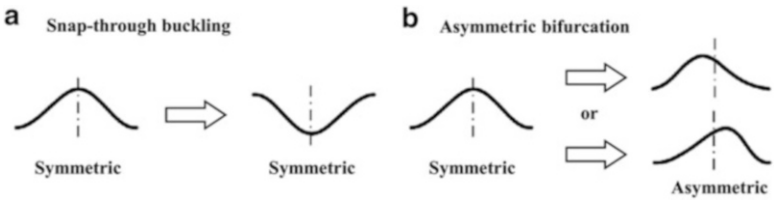

Fig. 9.1 Schematics of instability behaviors of arch under transverse force

among many others). Recently, the bistable MEMS/NEMS based on initially curved micro/nanobeams have drawn more and more attention from the scientific community for their various potential applications such as optical switches, microvalves, and non-volatile memories (Charlot et al., 2008; Goll et al., 1996; Intaraprasonk and Fan (2011); Roodenburg et al., 2009).

The initially curved beam (arch) under transverse forces may exhibit two main instabilities: symmetric snap-through buckling and asymmetric bifurcation. The symmetric snap-through buckling is the transition between two stable states (Medina et al. 2012). After the snap-though, the arch shape is symmetric, as depicted in Fig. 9.1a. However, for the asymmetric bifurcation, the arch may exhibit one of the asymmetric deformations shown in Fig. 9.1b.

The existence of snap-through buckling and asymmetric bifurcation depends on various factors, e.g., initial arch rise and beam thickness. Pippard (1990) conducted experiments to develop a phase diagram of instability in terms of the arch span and the initial angle at the clamped ends. This work was followed by Patricio et al. (1998) in which they developed theoretical model simulations to derive a similar phase diagram. As a result of the earlier experiments and model simulations, Krylov et al. (2008) revealed that the symmetric snap-through buckling occurs at large initial deflections. Pane and Asano (2008) conducted energy analysis and further found that the existence of bistable states in an initially curved beam depends on the ratio of its initial deflection to its thickness. Park and Hah (2008) conducted theoretical investigations and showed that the existence of bistable states also depends on the residual axial stress in the beam. Das and Batra (2009a) developed a finite element model to study the transient snap-through behavior of the initially curved beam, and found that at high loading rates (i.e., voltage is applied at a high rate), the snap-through buckling is suppressed. Moghimi Zand (2012) also developed a finite element model and found the significant inertia effect on the dynamic snap-through behavior. Medina et al. (2012, 2014a) examined the symmetric snap-through buckling and the asymmetric bifurcation of an electrostatically actuated mircobeam with/without residual stress. They derived the criteria of symmetric snap-through and symmetry breaking for quasi-static loading conditions.

Careful literature review indicates that many studies consider a uniform mechanical force as the applied load. However, the electrostatic force applied on the curved micro/nanobeam is highly nonuniform and strongly depends on the beam deflection. Several studies consider the electrostatic force, but they fail to examine the

fringing field effect and/or the influence of the intermolecular forces such as Casimir and van der Waals forces. Furthermore, the size effect at the microscale and the surface effects at the nanoscale are neglected in almost all the existing studies.

For the microstructures, the size effect on deformation behaviors has already been observed experimentally (Fleck et al. 1994; Lam et al. 2003; Ma and Clarke 1995; McFarland and Colton 2005), and such size dependency is attributed to the non-local effects, which cannot be described by the classical continuum theories of local character. Various nonclassical continuum theories with additional material length scale parameters have been proposed (Eringen 1983; Fleck and Hutchinson 2001; Lam et al. 2003; Mindlin 1965; Toupin 1962; Yang et al. 2002). Among them, the modified couple stress theory developed by Yang et al. (2002) with a length scale parameter is one of the most used. Determining the microstructure-dependent length scale parameters is difficult, so it is desirable to use the theories with only one length scale parameter (Reddy 2011). Based on the nonclassical continuum theories, the size effect on various behaviors of microbeams has been theoretically studied, including bending, buckling, free vibration, and pull-in instability (Belardinelli et al. 2014; Farokhi et al. 2013; Kong 2013; Ma et al. 2008).

For the nanostructures, experiments have shown that their elastic properties are size dependent (Cuenot et al. 2004; Jing et al. 2006; Li et al. 2003; Poncharal et al. 1999; Sadeghian et al. 2009; Salvetat et al. 1999; Shin et al. 2006), and such size dependency can be explained by the associated surface effects (Cuenot et al. 2004; Dingreville et al. 2005; Jing et al. 2006; Miller and Shenoy 2000; Sadeghian et al. 2011; Zhu 2010). The surface elasticity theory of Gurtin and Murdoch (1975, 1978) can predict the size-dependent effective elastic properties of the nanostructures, which has been extensively validated by experiments (Asthana et al. 2011; Fu et al. 2010; He and Lilley 2008; Xu et al. 2010). Based on this theory, the surface effects on various deformation behaviors of nanobeams have been investigated, such as bending, buckling, free vibration, and pull-in instability (Fu and Zhang 2011; He and Lilley 2008; Wang and Feng 2007, 2009).

In this chapter, we extend the earlier studies to investigate the size effect and the surface effects on the instability behaviors of the initially curved micro- and nanobeams under electrostatic force. Section 9.2 is devoted to the size effect on the symmetric snap-through buckling of microbeam. The beam model is developed considering the modified couple stress theory (Yang et al. 2002). The fringing field effect is taken into account by Meijs-Fokkema formula (van der Meijs and Fokkema 1984), and the influence of the intermolecular forces is also examined. In Sect. 9.3, the surface effects on the asymmetric bifurcation of nanobeam are studied. The surface elasticity and the residual surface tension are accounted for in the beam model by using the surface elasticity theory of Gurtin and Murdoch (1975, 1978) and the generalized Young–Laplace equation (Chen et al. 2006; Gurtin et al. 1998). Based on the models and simulation results, the criteria for the existence of snap-through buckling and asymmetric bifurcation are derived, which can be used for the design of the bistable MEMS/NEMS.

9.2 Size Effect on Symmetric Snap-Through Buckling of Microbeam

9.2.1 Formulation

9.2.1.1 Governing Equations

Consider an initially curved rectangular microbeam of span L, width b, and thickness h undergoing in-plane bending ($x-z$ plane in Fig. 9.2). The respective displacements u_x, u_y, and u_z along x-, y-, and z-coordinates are assumed to be dependent only on x and z. u_y is further assumed to be 0. For a thin beam ($h << L$), the Euler-Bernoulli beam theory is applied:

$$u_x(x,z) = u(x) - zw'(x) \tag{9.1a}$$

$$u_z(x,z) = w(x) \tag{9.1b}$$

where $u(x)$ and $w(x)$ are, respectively, the axial (along x-coordinate) and transverse (along z) displacements of a point on the midplane of the beam; a superimposed apostrophe denotes a derivative with respect to x. During the snap-through buckling, the midplane stretching can be important. To consider this effect, the von Karman nonlinear strain is used. With the aid of Eq. (9.1a, b), the nonzero strain component (i.e., axial strain ε^*_{xx}) can be obtained as (Reddy 2011)

$$\varepsilon^*_{xx} = u' - zw'' + \frac{1}{2}\left(w'\right)^2 \tag{9.2}$$

Considering the initial strain ε^0_{xx} related to the initial deflection $w_0(x)$ by $\varepsilon^0_{xx} = -zw''_0 + \left(w'_0\right)^2/2$, we calculate the axial strain change ε_{xx} from Eq. (9.2) as

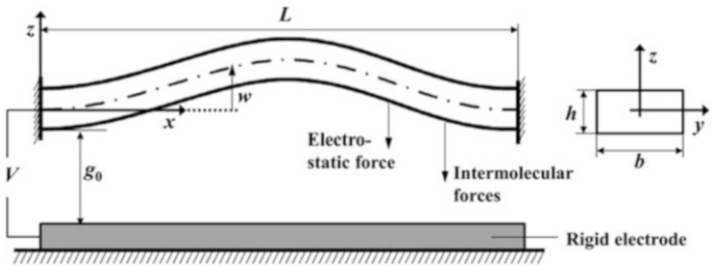

Fig. 9.2 Initially curved double-clamped micro/nanobeam under electrostatic force. The directions of electrostatic and intermolecular forces are indicated by *arrows*

$$\varepsilon_{xx} = \varepsilon_{xx}^{*} - \varepsilon_{xx}^{0} = u^{'} - z\left(w^{''} - w_0^{''}\right) + \frac{1}{2}\left(\left(w^{'}\right)^2 - \left(w_0^{'}\right)^2\right) \tag{9.3}$$

The symmetric curvature tensor $\underline{\underline{\chi}}$ conjugated to the deviatoric couple stress tensor $\underline{\underline{\psi}}$ in the modified couple stress theory is (Yang et al. 2002)

$$\underline{\underline{\chi}} = \frac{1}{2}\left(\nabla\underline{\omega} + (\nabla\underline{\omega})^{\mathrm{T}}\right) \tag{9.4}$$

where $\underline{\omega}\left(= (\nabla \times \underline{u})/2\right)$ is the rotation vector, with $\underline{u}\left(= \left(u_x, u_y, u_z\right)^{\mathrm{T}}\right)$ being the displacement vector; the superimposed T denotes the transpose of the matrix. With the aid of Eq. (9.1a, b), the nonzero curvature components in Eq. (9.4) are calculated as

$$\chi_{xy}^{*} = \chi_{yx}^{*} = -\frac{1}{2}w^{''} \tag{9.5}$$

Considering the initial nonzero curvature $\chi_{xy}^{0} = \chi_{yx}^{0} = -w_0^{''}/2$ due to the initial deflection w_0, we obtain the curvature change χ_{xy} and χ_{yx} from Eq. (9.5) as

$$\chi_{xy} = \chi_{yx} = \chi_{xy}^{*} - \chi_{xy}^{0} = -\frac{1}{2}\left(w^{''} - w_0^{''}\right) \tag{9.6}$$

To derive the governing equations, the theorem of minimum potential energy is used:

$$\delta U_{\mathrm{elas}} - \delta W_{\mathrm{ext}} = 0 \tag{9.7}$$

where δU_{elas} and δW_{ext} are, respectively, the variations of the elastic strain energy, and the work done by the external forces. Considering the nonzero strain component ε_{xx} and the nonzero curvature components χ_{xy} and χ_{yx}, we can calculate δU_{elas} as (Yang et al. 2002)

$$\delta U_{\mathrm{elas}} = \int_0^L \int_S \left(\underline{\underline{\sigma}} : \delta\underline{\underline{\varepsilon}} + \underline{\underline{\psi}} : \delta\underline{\underline{\chi}}\right)\mathrm{d}s\,\mathrm{d}x = \int_0^L \int_S \left(\sigma_{xx}\delta\varepsilon_{xx} + 2\psi_{xy}\delta\chi_{xy}\right)\mathrm{d}s\,\mathrm{d}x \tag{9.8}$$

where $\int_S \mathrm{d}s$ is the integral over the cross section (y–z plane in Fig. 9.2). Introduce Eqs. (9.3) and (9.6) into Eq. (9.8), integrate the resulting equation by parts with respect to x, and we obtain

$$\begin{aligned}\delta U_{\text{elas}} = &-\int_0^L N^{'}\delta u\mathrm{d}x - \int_0^L \left(M^{''} + C^{''} + \left(Nw^{'}\right)^{'}\right)\delta w\mathrm{d}x \\ &- N(0)\delta u(0) + N(L)\delta u(L) - (M^{'}(0) + C^{'}(0) + N(0)w^{'}(0))\delta w(0) \\ &+ (M^{'}(L) + C^{'}(L) + N(L)w^{'}(L))\delta w(L) + (M(0) + C(0))\delta w^{'}(0) \\ &- (M(L) + C(L))\delta w^{'}(L)\end{aligned} \tag{9.9}$$

where the stress resultants N, M, and C are defined as

$$N = \int_S \sigma_{xx}\,\mathrm{d}s \tag{9.10a}$$

$$M = \int_S z\sigma_{xx}\,\mathrm{d}s \tag{9.10b}$$

$$C = \int_S \psi_{xy}\,\mathrm{d}s \tag{9.10c}$$

Neglecting the gravity, we can calculate the variation δW_{ext} of the work done by the external forces as

$$\delta W_{\text{ext}} = \int_0^L f_z(x)\delta w\,\mathrm{d}x \tag{9.11}$$

where the distributed transverse load f_z is composed of

$$f_z = f_{\text{elec}} + f_{\text{casi}} + f_{\text{VDW}} \tag{9.12}$$

f_{elec}, f_{casi}, and f_{VDW} are, respectively, the electrostatic force, Casimir force, and van der Waals force per unit length.

The electrostatic force f_{elec} per unit length can be calculated using (Batra et al. 2006; Dequesnes et al. 2002)

$$f_{\text{elec}} = \frac{1}{2}V^2\frac{\mathrm{d}C_{\text{cap}}}{\mathrm{d}g} \tag{9.13}$$

where the sign of the force depends on the coordinate system, V is the applied voltage between the beam and the rigid electrode, C_{cap} is the capacitance per unit length of the capacitor composed of the beam and the electrode, and g is the gap between the beam and the electrode as being

$$g(x) = g_0 + w(x) \tag{9.14}$$

with g_0 being the initial gap (i.e., distance between the clamped beam ends and the rigid electrode (see Fig. 9.2)). For a small gap g ($<<$ beam length), the beam with

the electrode can be regarded as a parallel-plate capacitor. To further take into account the fringing fields at the edges of the microbeam, the capacitance C_{cap} is estimated using the Meijs-Fokkema formula (van der Meijs and Fokkema 1984):

$$C(g) = \varepsilon_0 \left(\frac{b}{g} + 0.77 + 1.06 \left(\frac{b}{g} \right)^{0.25} + 1.06 \left(\frac{h}{g} \right)^{0.5} \right) \tag{9.15}$$

where ε_0 is the vacuum permittivity. It is noted that the error of the estimated capacitance using Eq. (9.15) is within 6 % for the microbeam systems satisfying beam-width-to-gap ratio (b/g) larger than 0.3 and beam-thickness-to-gap ratio (h/g) smaller than 10 (van der Meijs and Fokkema 1984). So to ensure the proper application of Eq. (9.15), this chapter only studies the microbeam systems with the width-to-initial-gap ratio (b/g_0) larger than 0.5 (considering $w_{\max} = 0.5\, g_0$ in Eq. (9.14)) and the thickness-to-initial-gap ratio (h/g_0) smaller than 5 (considering $w_{\min} = -0.5\, g_0$). Introduce Eqs. (9.14) and (9.15) into Eq. (9.13), and after several calculations we obtain (Krylov et al. 2008)

$$f_{\text{elec}} = -\frac{1}{2} \frac{\varepsilon_0 b V^2}{(g_0 + w)^2} \left(1 + 0.265 \left(\frac{b}{h} \right)^{-0.75} \left(\frac{g_0 + w}{h} \right)^{0.75} + 0.53 \left(\frac{b}{h} \right)^{-1} \left(\frac{g_0 + w}{h} \right)^{0.5} \right) \tag{9.16}$$

The intermolecular forces can be described by Casimir and van der Waals forces. The former force is attributed to the attraction between two closely spaced conducting surfaces, and the latter one is due to the electrostatic interactions among dipoles at the atomic scale (Batra et al. 2007; Lifshitz 1956). For a small gap (<< beam length), the parallel-plate approximation is applied (Casimir 1948; Israelachvili 2011):

$$f_{\text{casi}} = -\frac{\pi^2 \hbar c b}{240 (g_0 + w)^4} \tag{9.17a}$$

$$f_{\text{VDM}} = -\frac{A b}{6\pi (g_0 + w)^3} \tag{9.17b}$$

where $\hbar$ is the reduced Planck constant; c is the speed of light; A is the Hamaker constant.

Introducing Eqs. (9.9) and (9.11) into Eq. (9.7), we arrive at

$$\begin{aligned} &\int_0^L N' \delta u \mathrm{d}x + \int_0^L \left(M'' + C'' + \left(N w' \right)' + f_z \right) \delta w \mathrm{d}x + N(0) \delta u(0) - N(L) \delta u(L) \\ &+ (M'(0) + C'(0) + N(0) w'(0)) \delta w(0) - (M'(L) + C'(L) + N(L) w'(L)) \delta w(L) \\ &- (M(0) + C(0)) \delta w'(0) + (M(L) + C(L)) \delta w'(L) = 0 \end{aligned} \tag{9.18}$$

To satisfy Eq. (9.18) with arbitrary variations of displacements δu and δw, we obtain the following governing equations:

$$\delta u: \quad N' = 0 \tag{9.19a}$$

$$\delta w: \quad M'' + C'' + \left(Nw'\right)' + f_z = 0 \tag{9.19b}$$

With Eq. (9.19a), Eq. (9.19b) can be reduced to

$$M'' + C'' + Nw'' + f_z = 0 \tag{9.20}$$

Suppose the beam material is elastically isotropic with Young's modulus E and Poisson's ratio ν. For an Euler-Bernoulli beam undergoing in-plane bending, the 1D constitutive relation is

$$\sigma_{xx} = E\varepsilon_{xx} \tag{9.21}$$

The deviatoric couple stress ψ_{xy} is related to the symmetric curvature χ_{xy} by (Yang et al. 2002):

$$\psi_{xy} = \frac{El^2}{(1+\nu)}\chi_{xy} \tag{9.22}$$

where l is a length scale parameter. With Eqs. (9.3), (9.6), (9.21), and (9.22), Eq. (9.10a, b, c) is changed to

$$N(x) = ES\left(u' + \frac{1}{2}\left(w'\right)^2 - \frac{1}{2}\left(w_0'\right)^2\right) \tag{9.23a}$$

$$M(x) = -EI\left(w'' - w_0''\right) \tag{9.23b}$$

$$C(x) = -\frac{ESl^2}{2(1+\nu)}\left(w'' - w_0''\right) \tag{9.23c}$$

where S ($=bh$) is the cross-sectional area (y–z plane in Fig. 9.2); I ($=bh^3/12$) is the second moment of area. Introduce Eq. (9.23a, b, c) into Eq. (9.20), and we have

$$\begin{aligned} &EI\left(1 + \frac{6}{(1+\nu)}\left(\frac{l}{h}\right)^2\right)\left(w'''' - w_0''''\right) \\ &- ES\left(\left(u' + \frac{1}{2}\left(w'\right)^2 - \frac{1}{2}\left(w_0'\right)^2\right)w'\right)' - f_z = 0 \end{aligned} \tag{9.24}$$

Equation (9.19a) shows that the axial force N is constant. So N can be estimated as the average value calculated from Eq. (9.23a):

$\frac{ES}{L}\left(\int_0^L\left(u'+\frac{1}{2}\left(w'\right)^2-\frac{1}{2}\left(w_0'\right)^2\right)\mathrm{d}x\right)$. In Eq. (9.24), replace N with the average value, consider the boundary conditions of double-clamped beam, and we obtain

$$\begin{aligned}&EI\left(1+\frac{6}{(1+\nu)}\left(\frac{l}{h}\right)^2\right)\left(w''''-w_0''''\right)\\&-\frac{ES}{2L}\left(\int_0^L\left(\left(w'\right)^2-\left(w_0'\right)^2\right)\mathrm{d}x\right)w''-f_z=0\end{aligned}\tag{9.25}$$

Introducing Eqs. (9.12), (9.16), and (9.17a, b) into Eq. (9.25), and we have

$$\begin{aligned}&EI\left(1+\frac{6}{(1+\nu)}\left(\frac{l}{h}\right)^2\right)\left(w''''-w_0''''\right)-\frac{ES}{2L}\left(\int_0^L\left(\left(w'\right)^2-\left(w_0'\right)^2\right)\mathrm{d}x\right)w''\\&+\frac{1}{2}\frac{\varepsilon_0 bV^2}{(g_0+w)^2}\left(1+0.265\left(\frac{b}{h}\right)^{-0.75}\left(\frac{g_0+w}{h}\right)^{0.75}+0.53\left(\frac{b}{h}\right)^{-1}\left(\frac{g_0+w}{h}\right)^{0.5}\right)\\&+\frac{\pi^2\hbar cb}{240(g_0+w)^4}+\frac{Ab}{6\pi(g_0+w)^3}=0\end{aligned}\tag{9.26}$$

It is seen from Eq. (9.26) that the length scale parameter l has the effect of increasing the effective Young's modulus $(E)_{\text{eff}}$ for bending, being

$$(E)_{\text{eff}}=E\left(1+\frac{6}{(1+\nu)}\left(\frac{l}{h}\right)^2\right)\tag{9.27}$$

For thin beams (beam thickness h close to l), the effective Young's modulus for bending can be as large as $\left(1+\frac{6}{(1+\nu)}\right)$ ($\approx$5.7 at $\nu=0.27$) times the conventional Young's modulus (E), while for thick beams ($h\gg l$) the effective Young's modulus is nearly equal to the conventional one, indicating that the size effect is negligible.

Rewrite Eq. (9.26) in the following non-dimensional form:

$$\begin{aligned}&\left(\overline{w}''''-\overline{w_0}''''\right)-\alpha\left(\int_0^1\left(\left(\overline{w}'\right)^2-\left(\overline{w_0}'\right)^2\right)\mathrm{d}\overline{x}\right)\overline{w}''+\lambda_{\text{VDW}}\frac{1}{(1+\overline{w})^3}+\lambda_{\text{casi}}\frac{1}{(1+\overline{w})^4}\\&=-\frac{\beta_v}{(1+\overline{w})^2}\left(1+0.265\left(\frac{b}{h}\right)^{-0.75}\left(\frac{1+\overline{w}}{\overline{h}}\right)^{0.75}+0.53\left(\frac{b}{h}\right)^{-1}\left(\frac{1+\overline{w}}{\overline{h}}\right)^{0.5}\right)\end{aligned}\tag{9.28}$$

where the non-dimensional quantities are defined in Table 9.1; a superimposed apostrophe in the non-dimensional equations denotes a derivative with respect to

Table 9.1 Non-dimensional quantities adopted in this chapter

Quantity	Expression	Meaning
$\overline{h}$	h/g_0	Dimensionless thickness
q_0	r/g_0	Dimensionless initial arch rise
$\overline{w}$	w/g_0	Dimensionless deflection
$\overline{w_0}$	w_0/g_0	Dimensionless initial deflection
$\overline{x}$	x/L	Normalized coordinate
α	$6/\left(\frac{h}{g_0}\right)^2/\left(1+\frac{6}{(1+\nu)}\left(\frac{l}{h}\right)^2\right)$	Stretching parameter (size effect considered)
α^*	$6\left(1+2\frac{E^s}{E^*}\frac{1}{h}\right)/\left(\frac{h}{g_0}\right)^2/\left(1+6\frac{E^s}{E^*}\frac{1}{h}\right)$	Stretching parameter (surface effects considered)
β_v	$\varepsilon_0 bL^4V^2/(2EIg_0^3)/\left(1+\frac{6}{(1+\nu)}\left(\frac{l}{h}\right)^2\right)$	Voltage parameter (size effect considered)
β_v^*	$\varepsilon_0 bL^4V^2/(2E^*Ig_0^3)/\left(1+6\frac{E^s}{E^*}\frac{1}{h}\right)$	Voltage parameter (surface effects considered)
λ_{casi}	$\pi^2\hbar cbL^4/(240EIg_0^5)/\left(1+\frac{6}{(1+\nu)}\left(\frac{l}{h}\right)^2\right)$	Casimir force parameter
λ_{s}	$2bL^2\tau^0/E^*I/\left(1+6\frac{E^s}{E^*}\frac{1}{h}\right)$	Dimensionless residual surface tension
λ_{VDW}	$AbL^4/(6\pi EIg_0^4)/\left(1+\frac{6}{(1+\nu)}\left(\frac{l}{h}\right)^2\right)$	van der Waals force parameter

the normalized coordinate $\overline{x}$. The non-dimensional boundary conditions of double-clamped beam are

$$\delta\overline{w}: \quad \overline{w}(0)=0, \quad \overline{w}(1)=0 \tag{9.29a}$$

$$\delta\overline{w}': \quad \overline{w}'(0)=0, \quad \overline{w}'(1)=0 \tag{9.29b}$$

9.2.1.2 Influence of Intermolecular Forces

In the non-dimensional governing equation (Eq. (9.28)), we can identify the dimensionless van der Waals force $\overline{f_{\text{VDW}}}$, Casimir force $\overline{f_{\text{casi}}}$, and electrostatic force $\overline{f_{\text{elec}}}$ as

$$\overline{f_{\text{VDW}}} = -\lambda_{\text{VDW}}\frac{1}{(1+\overline{w})^3} \tag{9.30a}$$

$$\overline{f_{\text{casi}}} = -\lambda_{\text{casi}}\frac{1}{(1+\overline{w})^4} \tag{9.30b}$$

$$\overline{f_{\text{elec}}} = -\frac{\beta_v}{(1+\overline{w})^2}\left(1+0.265\left(\frac{b}{h}\right)^{-0.75}\left(\frac{1+\overline{w}}{\overline{h}}\right)^{0.75}+0.53\left(\frac{b}{h}\right)^{-1}\left(\frac{1+\overline{w}}{\overline{h}}\right)^{0.5}\right) \tag{9.30c}$$

Table 9.2 Values of constants

Constant	Meaning	Value
A	Hamaker constant	10^{-19} J (Hamaker constants of condensed phases are about 10^{-19} J for interactions in vacuum (Israelachvili 2011))
c	Speed of light	3×10^8 m $\cdot$ s^{-1}
$\hbar$	Reduced Planck constant	1.0546×10^{-34} J $\cdot$ s
ε_0	Vacuum permittivity	8.8542×10^{-12} F $\cdot$ m^{-1}

where λ_{VDW}, λ_{casi}, and β_v are, respectively, the van der Waals force parameter, the Casimir force parameter, and the voltage parameter. With the aid of Table 9.1, we can compare λ_{VDW} and λ_{casi} with β_v as follows:

$$\frac{\lambda_{\text{VDW}}}{\beta_v} = \frac{A}{3\pi\varepsilon_0}\frac{1}{g_0 V^2} \tag{9.31a}$$

$$\frac{\lambda_{\text{casi}}}{\beta_v} = \frac{\pi^2\hbar c}{120\varepsilon_0}\frac{1}{g_0^2 V^2} \tag{9.31b}$$

Consider $g_0 \approx 10^{-6}$m for the microscale systems and $V \approx 10^1$V for the order of applied voltage, and with the values of the constants in Table 9.2 we calculate Eq. (9.31a, b) as

$$\frac{\lambda_{\text{VDW}}}{\beta_v} \approx 10^{-5} \tag{9.32a}$$

$$\frac{\lambda_{\text{casi}}}{\beta_v} \approx 3 \times 10^{-6} \tag{9.32b}$$

With Eqs. (9.30a, b, c) and (9.32a, b), the force ratios can be estimated as

$$\left|\overline{f_{\text{VDW}}}/\overline{f_{\text{elec}}}\right| < 10^{-5}\frac{1}{1+\overline{w}} \tag{9.33a}$$

$$\left|\overline{f_{\text{casi}}}/\overline{f_{\text{elec}}}\right| < 3 \times 10^{-6}\frac{1}{(1+\overline{w})^2} \tag{9.33b}$$

The maximum force ratios are determined by the minimum stable deflection, i.e., deflection at pull-in instability, which is roughly half gap ($\overline{w} = -0.5$) (Ballestra et al. 2010; Dequesnes et al. 2002; Hu et al. 2004). Then Eq. (9.33a, b) leads to

$$\max\left|\overline{f_{\text{VDW}}}/\overline{f_{\text{elec}}}\right| \approx 2 \times 10^{-5} \tag{9.34a}$$

$$\max\left|\overline{f_{\text{casi}}}/\overline{f_{\text{elec}}}\right| \approx 1 \times 10^{-5} \tag{9.34b}$$

Equation (9.34a, b) shows that the intermolecular forces (van der Waals and Casimir forces) are negligible with respect to the electrostatic force when studying the snap-through buckling of microbeams.

9.2.1.3 One Degree of Freedom Reduced-Order Model

In the previous subsection, we have proved that the intermolecular forces can be neglected in the study of snap-through buckling of microbeams. So the governing equation (Eq. (9.28)) can be further reduced to

$$\begin{aligned}&(\overline{w}'''' - \overline{w_0}'''') - \alpha\left(\int_0^1 \left((\overline{w}')^2 - (\overline{w_0}')^2\right)\mathrm{d}\overline{x}\right)\overline{w}'' \\ &= -\frac{\beta_v}{(1+\overline{w})^2}\left(1 + 0.265\left(\frac{b}{h}\right)^{-0.75}\left(\frac{1+\overline{w}}{\overline{h}}\right)^{0.75} + 0.53\left(\frac{b}{h}\right)^{-1}\left(\frac{1+\overline{w}}{\overline{h}}\right)^{0.5}\right)\end{aligned} \tag{9.35}$$

Equation (9.35) with the boundary conditions expressed in Eq. (9.29a, b) can be solved using the Galerkin decomposition of the dimensionless deflection $\overline{w}(\overline{x})$ (Das and Batra 2009b; Krylov et al. 2008; Medina et al. 2012):

$$\overline{w}(\overline{x}) \approx \sum_{k=1}^{n} q_k \phi_k(\overline{x}) \tag{9.36}$$

where ϕ_k ($k = 1, 2, \ldots, n$) is the kth eigenmode of the straight beam, and q_k is its generalized coordinate. The buckling eigenmodes are taken here, which have been found more suitable for the studies on the buckling behaviors (Medina et al. 2014a, b):

$$\phi_k(\overline{x}) = A_k\left(\frac{\cos(\lambda_k) - 1}{\sin(\lambda_k) - \lambda_k}\sin(\lambda_k\overline{x}) - \cos(\lambda_k\overline{x}) - \lambda_k\frac{\cos(\lambda_k) - 1}{\sin(\lambda_k) - \lambda_k}\overline{x} + 1\right) \tag{9.37}$$

where A_k is a constant satisfying $\max_{\overline{x}\in[0,1]} |\phi_k(\overline{x})| = 1$, and λ_k is the eigenvalue satisfying $\lambda_k \sin(\lambda_k) + 2\cos(\lambda_k) = 2$.

It is shown by Das and Batra (2009b) that the numerical simulations using $n \geq 6$ in Eq. (9.36) are indistinguishable from each other. They also found that a reasonably accurate prediction of the symmetric snap-through behavior can be given by considering only the first mode, which indicates that the first mode approximation of the deflection can capture the characteristics of the symmetric snap-through

behavior. So in order to simplify our study for an analytical snap-through criterion, we decided to make the first mode approximation here. Suppose that the dimensionless initial deflection $\overline{w_0}(\bar{x})$ is also in the first mode, then we have

$$\overline{w}(\bar{x}) = q_1\phi_1(\bar{x}) \tag{9.38a}$$

$$\overline{w_0}(\bar{x}) = q_0\phi_1(\bar{x}) \tag{9.38b}$$

where q_1 is the dimensionless midpoint deflection; q_0 ($= r/g_0$) is the dimensionless initial arch rise, with r being the initial arch rise (i.e., initial deflection at the midpoint). Introduce Eq. (9.38a, b) into Eq. (9.35), multiply the result by ϕ_1, and then integrate over the domain [0, 1]. Further integrate by parts with respect to $\bar{x}$ and consider the boundary conditions (Eq. (9.29a, b)); we obtain the following reduced-order model with one degree of freedom:

$$\beta_v = -\frac{\alpha s_{11}^2}{I_1(q_1)}q_1^3 - \frac{b_{11} - \alpha s_{11}^2 q_0^2}{I_1(q_1)}q_1 + \frac{b_{11}q_0}{I_1(q_1)} \tag{9.39}$$

where the values of b_{11} and s_{11} are given in Table 9.3, and the expression of I_1 is

$$I_1(q_1) = \int_0^1 \frac{\phi_1}{(1+q_1\phi_1)^2}\left(1 + 0.265\left(\frac{b}{h}\right)^{-0.75}\left(\frac{1+q_1\phi_1}{\overline{h}}\right)^{0.75} + 0.53\left(\frac{b}{h}\right)^{-1}\left(\frac{1+q_1\phi_1}{\overline{h}}\right)^{0.5}\right)\mathrm{d}\bar{x} \tag{9.40}$$

Table 9.3 Values of coefficients related to first and second buckling eigenmodes

Coefficient	Expression	Value
b_{11}	$\int_0^1 (\phi_1'')^2 \mathrm{d}\bar{x}$	194.8182
b_{22}	$\int_0^1 (\phi_2'')^2 \mathrm{d}\bar{x}$	1667.9624
f_1	$\int_0^1 \phi_1 \mathrm{d}\bar{x}$	0.5000
m_{11}	$\int_0^1 \phi_1^2 \mathrm{d}\bar{x}$	0.3750
m_{22}	$\int_0^1 \phi_2^2 \mathrm{d}\bar{x}$	0.4262
s_{11}	$\int_0^1 (\phi_1')^2 \mathrm{d}\bar{x}$	4.9348
s_{22}	$\int_0^1 (\phi_2')^2 \mathrm{d}\bar{x}$	20.6529

Table 9.4 Dimensional quantities of electrostatically actuated microbeam system obtained from Krylov et al. (2008) and Zhang et al. (2007)

Quantity	Meaning	Value
b	Beam width	30 μm
E	Young's modulus of silicon	160 GPa
g_0	Gap between beam ends and rigid electrode	10 μm
h	Beam thickness	2.5 μm
L	Span of arch	1000 μm
r	Initial arch rise	0–5 μm
V	Applied voltage	0–120 V
ν	Poisson's ratio of silicon	0.27

9.2.2 *Results and Discussions*

9.2.2.1 Influence of Initial Arch Rise on Snap-Through Behavior

Let us consider an electrostatically actuated microbeam system described by the dimensional quantities in Table 9.4, which is obtained from Krylov et al. (2008) for the experiments, and Zhang et al. (2007) for the material properties. Taking the material length scale parameter $l = 10^{-1}$ μm for silicon (Rokni et al. 2013), and with the aid of Tables 9.1 and 9.4, we calculate the corresponding dimensionless quantities, and introduce them into Eq. (9.39). The obtained equation is plotted in Fig. 9.3 at different levels of q_0 ($0 \sim 0.5$). The experimental results from Krylov et al. (2008) are also shown. It is seen that the model (Eq. (9.39)) can approximately describe the snap-through behavior observed from the experiments. The difference in the critical voltages (i.e., voltage parameters at the extreme points) is possibly due to the non-ideal clamping conditions, residual stresses, initial imperfections in the beam shape, and variations of beam geometry due to the low fabrication tolerances (Krylov et al. 2008).

Figure 9.3 shows that the existence of the snap-through buckling depends on the level of the dimensionless initial arch rise q_0. For very small q_0 (e.g., $q_0 = 0$ in Fig. 9.3a), there is only one extreme point q_p on the $\beta_v - q_1$ curve. With the increase of the voltage (β_v increases), the microbeam bends towards the rigid electrode due to the electrostatic force. The equilibrium position of the beam can be determined by the balance of the elastic and electrostatic forces. Therefore, the beam deflection decreases gradually (see the loading path $A \rightarrow q_p$ in Fig. 9.3a). When the critical point q_p is reached, the microbeam becomes unstable (i.e., the elastic force can no longer resist the electrostatic force), so it collapses onto the rigid electrode ($q_p \rightarrow B$). This behavior is called pull-in instability.

For a larger value of q_0 (e.g., 0.35 in Fig. 9.3b), two more extreme points q_s and q_r appear, which correspond, respectively, to the snap-through buckling and the release (snap-back). With the increase of β_v, the beam deflection decreases gradually ($C \rightarrow q_s$ in Fig. 9.3b) until reaching the critical point q_s where two stable states (q_s and D) coexist. A slight increase in β_v makes the state at q_s unstable, which

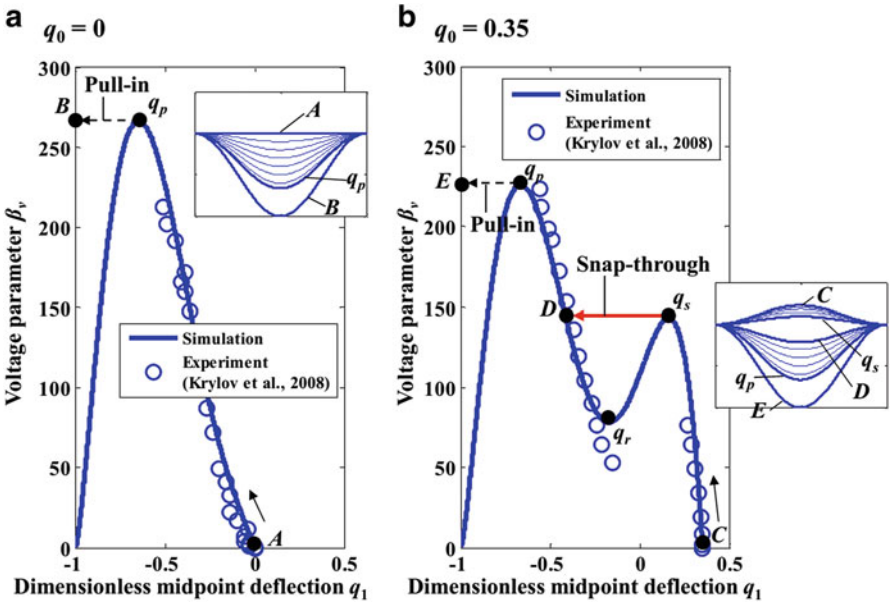

Fig. 9.3 Evolution of voltage parameter β_v with dimensionless midpoint deflection q_1 at different levels of dimensionless initial arch rise q_0. The extreme points q_s, q_r, and q_p correspond, respectively, to the critical points of the snap-through buckling, the release (snap-back), and the pull-in instability. The *insets* show the evolutions of the deformed beam

results in a sudden transition from q_s to the second stable state D. Such transition is called snap-through buckling. After the snap-through buckling, the beam deflection continues to decrease gradually with β_v ($D \rightarrow q_p$) until reaching the pull-in instability where the beam collapses onto the rigid electrode ($q_p \rightarrow E$).

9.2.2.2 Size and Fringing Field Effects on Necessary Snap-Through Criterion

The extreme points q_s, q_r, and q_p on $\beta_v - q_1$ curve (refer to Fig. 9.3) can be obtained by solving the following equation with the aid of Eq. (9.39):

$$\begin{aligned}&\frac{d\beta_v}{dq_1} = 0\\ &\quad\Rightarrow \alpha s_{11}^2 I_2 q_1^3 - 3\alpha s_{11}^2 I_1 q_1^2 + I_2\left(b_{11} - \alpha s_{11}^2 q_0^2\right)q_1 - \left(b_{11} - \alpha s_{11}^2 q_0^2\right)I_1\\ &\qquad - b_{11} I_2 q_0\\ &\quad = 0\end{aligned} \tag{9.41}$$

where I_2 is calculated from Eq. (9.40) as

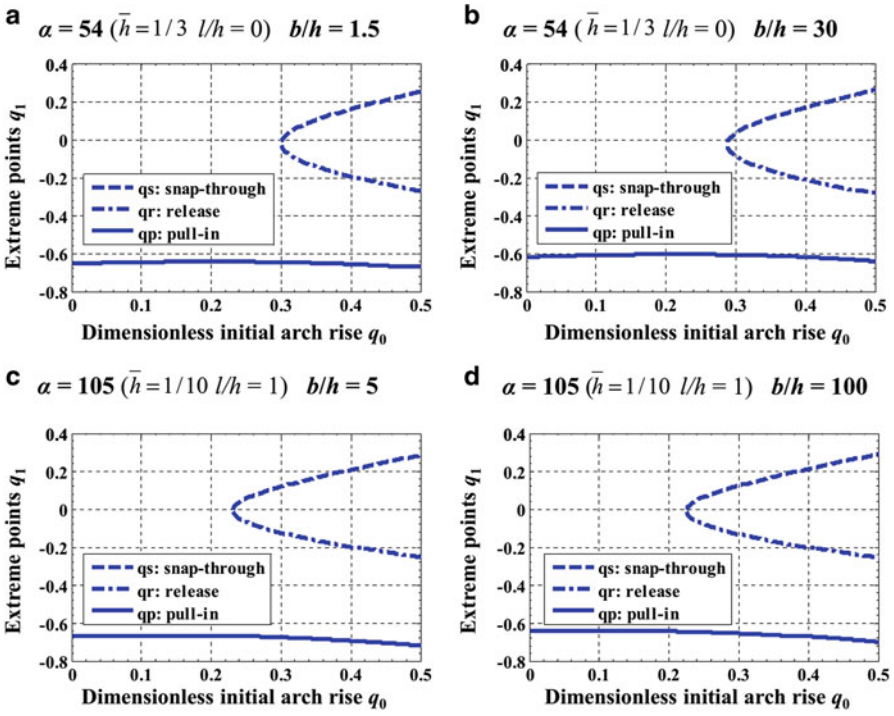

Fig. 9.4 Evolutions of the extreme points (q_s, q_r, q_p) with the dimensionless initial arch rise q_0 at different levels of stretching parameter α and width-to-thickness ratio b/h

$$I_2 = \frac{\mathrm{d}I_1}{\mathrm{d}q_1} = \int_0^1 \frac{-2\phi_1^2}{(1+q_1\phi_1)^3}\left(1+0.165625\left(\frac{b}{h}\right)^{-0.75}\left(\frac{1+q_1\phi_1}{\overline{h}}\right)^{0.75} +0.3975\left(\frac{b}{h}\right)^{-1}\left(\frac{1+q_1\phi_1}{\overline{h}}\right)^{0.5}\right)\mathrm{d}\overline{x} \tag{9.42}$$

Equation (9.41) containing integrals (I_1, I_2) cannot be solved analytically. So we solve the equation numerically, and show the typical results in Fig. 9.4. It is seen that q_0 must be larger than a critical value $q_0^{\min}$ for the existence of the snap-through points q_s and q_r. At $q_0 = q_0^{\min}$, both q_s and q_r are near 0. So for a first approximation, we take $q_1 = 0$ in Eq. (9.41) and find

$$q_0^{\min} = \sqrt{\frac{b_{11}}{\alpha s_{11}^2} + \left(\frac{b_{11}m_{11}^*}{\alpha s_{11}^2 f_1^*}\right)^2} - \frac{b_{11}m_{11}^*}{\alpha s_{11}^2 f_1^*} \tag{9.43}$$

where the values of b_{11} and s_{11} are given in Table 9.3; f_1^* and m_{11}^* are

$$f_1^* = \left(1 + 0.265\left(\frac{b}{h}\right)^{-0.75}\left(\overline{h}\right)^{-0.75} + 0.53\left(\frac{b}{h}\right)^{-1}\left(\overline{h}\right)^{-0.5}\right)\int_0^1 \phi_1 \mathrm{d}\overline{x} \tag{9.44a}$$

$$m_{11}^* = \left(1 + 0.165625\left(\frac{b}{h}\right)^{-0.75}\left(\overline{h}\right)^{-0.75} + 0.3975\left(\frac{b}{h}\right)^{-1}\left(\overline{h}\right)^{-0.5}\right)\int_0^1 \phi_1^2 \mathrm{d}\overline{x} \tag{9.44b}$$

Introducing Eq. (9.44a, b) into Eq. (9.43) and replacing the non-dimensional quantities (α, q_0) with the expressions in Table 9.1, we obtain the following necessary criterion for the existence of snap-through buckling:

$$\left(\frac{r}{h}\right)_{\min} = \sqrt{\frac{b_{11}}{6s_{11}^2}\left(1+\frac{6}{(1+\nu)}\left(\frac{l}{h}\right)^2\right) + \left(\frac{b_{11}m_{11}}{6s_{11}^2 f_1}\overline{h}\right)^2\left(1+\frac{6}{(1+\nu)}\left(\frac{l}{h}\right)^2\right)^2\left(\frac{1+0.165625\left(\frac{b}{h}\right)^{-0.75}\left(\overline{h}\right)^{-0.75}+0.3975\left(\frac{b}{h}\right)^{-1}\left(\overline{h}\right)^{-0.5}}{1+0.265\left(\frac{b}{h}\right)^{-0.75}\left(\overline{h}\right)^{-0.75}+0.53\left(\frac{b}{h}\right)^{-1}\left(\overline{h}\right)^{-0.5}}\right)^2} - \frac{b_{11}m_{11}}{6s_{11}^2 f_1}\overline{h}\left(1+\frac{6}{(1+\nu)}\left(\frac{l}{h}\right)^2\right)\left(\frac{1+0.165625\left(\frac{b}{h}\right)^{-0.75}\left(\overline{h}\right)^{-0.75}+0.3975\left(\frac{b}{h}\right)^{-1}\left(\overline{h}\right)^{-0.5}}{1+0.265\left(\frac{b}{h}\right)^{-0.75}\left(\overline{h}\right)^{-0.75}+0.53\left(\frac{b}{h}\right)^{-1}\left(\overline{h}\right)^{-0.5}}\right) \tag{9.45}$$

where the values of b_{11}, s_{11}, f_1, and m_{11} are given in Table 9.3. Eq. (9.45) is plotted in Fig. 9.5 to show the size effect (by introducing the length scale parameter l, normalized as l/h) and the fringing field effect (considering the finite beam width b, normalized as b/h) on the minimum allowable ratio $(r/h)_{\min}$. It is seen that both effects increase $(r/h)_{\min}$ and the size effect is much more significant. Eq. (9.27) shows that the size effect (l/h) increases the effective Young's modulus for bending, so the microbeam becomes stiffer and more difficult to exhibit snap-through buckling. As a result, the minimum allowable ratio $(r/h)_{\min}$ increases.

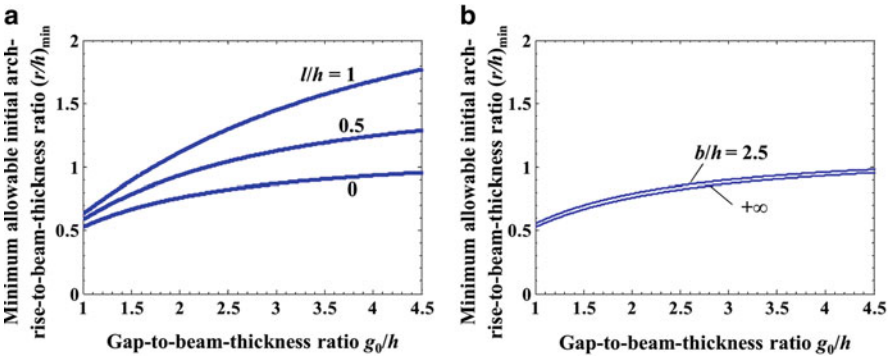

Fig. 9.5 (**a**) Size effect (l/h) on the minimum allowable ratio $(r/h)_{\min}$ at $b/h = +\infty$. No size effect at $l/h = 0$ (i.e., beam thickness $h \gg l$). (**b**) Fringing field effect (b/h) on the minimum allowable ratio $(r/h)_{\min}$ at $l/h = 0$. No fringing field effect at $b/h = +\infty$ (infinitely wide beam)

9.3 Surface Effects on Asymmetric Bifurcation of Nanobeam

9.3.1 Formulation

9.3.1.1 Surface Effects

In the surface elasticity theory of Gurtin and Murdoch (1975, 1978), the surface layer is regarded as a thin film of negligible thickness. In the surface layer, there exists a surface stress $\underline{\underline{\sigma}}^{s}(\mathrm{N/m})$, which is related to the surface energy density γ ($\mathrm{J/m^2}$) by (Cammarata 1994)

$$\underline{\underline{\sigma}}^{s} = \gamma \underline{\underline{\delta}} + \frac{\partial \gamma}{\partial \underline{\underline{\varepsilon}}^{s}} \tag{9.46}$$

where $\underline{\underline{\delta}}$ is the Kronecker delta; $\underline{\underline{\varepsilon}}^{s}$ is the strain tensor in the surface layer. Assuming an elastic surface, we can derive a linear constitutive equation from Eq. (9.46) as (Miller and Shenoy 2000)

$$\underline{\underline{\sigma}}^{s} = \underline{\underline{\tau}}^{0} + \underline{\underline{\underline{\underline{C}}}}^{s} : \underline{\underline{\varepsilon}}^{s} \tag{9.47}$$

where $\underline{\underline{\tau}}^{0}$ is the residual surface stress tensor; $\underline{\underline{\underline{\underline{C}}}}^{s}$ (N/m) is the surface elasticity tensor. Both $\underline{\underline{\tau}}^{0}$ and $\underline{\underline{\underline{\underline{C}}}}^{s}$ can be calculated by atomistic simulations, and they can be either positive or negative depending on the crystallographic structures of the materials (Miller and Shenoy 2000; Wang and Feng 2009). We only consider the axial stress here. Then Eq. (9.47) can be reduced to the following 1D form (He and Lilley 2008; Wang and Feng 2009):

$$\sigma^{s} = \tau^{0} + E^{s}\varepsilon^{s} \tag{9.48}$$

where τ^{0} is the residual surface tension; E^{s} (N/m) is the surface elastic modulus, which is related to the surface Lame constants μ^{s} and λ^{s} by $E^{s} = 2\mu^{s} + \lambda^{s}$ in 1D condition.

It is seen from Eq. (9.48) that there are two contributions to the surface effects: the residual surface tension (τ^{0}) and the surface elasticity (E^{s}). The surface elasticity (E^{s}) introduces an additional axial elastic stress σ^{*} being

$$\sigma^{*} = E^{s}\varepsilon^{s} \tag{9.49}$$

And the residual surface tension τ^{0} results in a distributed transverse load f^{s}, which can be determined by the generalized Laplace-Young equation (Chen et al. 2006;

Gurtin et al. 1998). This equation relates the stress jump $[\underline{\underline{\sigma}}]$ across an interface to the curvature $\underline{\underline{\kappa}}$ and the surface stress $\underline{\underline{\sigma}}^{\mathrm{s}}$ of that interface, from which we have (Chen et al. 2006; Miller and Shenoy 2000; Wang and Feng 2007)

$$\underline{n} : \underline{\underline{\sigma}} : \underline{n} = \underline{\underline{\sigma}}^{\mathrm{s}} : \underline{\underline{\kappa}} \tag{9.50}$$

where $\underline{n}$ is the interface unit normal. By only considering the axial stress, we can simplify the right-hand side of Eq. (9.50) to $\sigma^{\mathrm{s}}\kappa$, where κ is the beam curvature. Suppose that the slope of the beam is small compared with the unity; then κ can be approximated as w'', with w being the beam deflection (transverse displacement). Considering a rectangular beam of width b, we can obtain the distributed transverse load f^{s} from Eq. (9.50) as (He and Lilley 2008; Wang and Feng 2007, 2009)

$$f^{\mathrm{s}} = 2\tau^0 b w'' \tag{9.51}$$

9.3.1.2 Governing Equations

Consider an initially curved rectangular nanobeam subjected to an electrostatic force (Fig. 9.2). For a thin beam ($h \ll L$), the axial strain change ε_{xx} is given in Eq. (9.3). Then the variation δU_{elas} of the elastic strain energy including the surface elasticity can be calculated as

$$\begin{aligned}
\delta U_{\mathrm{elas}} &= \int_0^L \left(\int_S \sigma_{xx} \delta \varepsilon_{xx} ds + \int_{\partial S} \sigma^* \delta \varepsilon_{xx} \mathrm{d}l \right) \mathrm{d}x \\
&= -\int_0^L N' \delta u \mathrm{d}x - \int_0^L (M'' + (N w')') \delta w \mathrm{d}x \\
&\quad - N(0)\delta u(0) + N(L)\delta u(L) - (M'(0) + N(0)w'(0))\delta w(0) \\
&\quad + (M'(L) + N(L)w'(L))\delta w(L) + M(0)\delta w'(0) - M(L)\delta w'(L)
\end{aligned} \tag{9.52}$$

where stress resultants N and M are defined as

$$N = \int_S \sigma_{xx} \mathrm{d}s + \int_{\partial S} \sigma^* \mathrm{d}l \tag{9.53a}$$

$$M = \int_S z\sigma_{xx} \mathrm{d}s + \int_{\partial S} z\sigma^* \mathrm{d}l \tag{9.53b}$$

σ^* is the additional axial stress from surface elasticity (Eq. (9.49)), and $\int_{\partial S} \mathrm{d}l$ is the integral over the boundary of the cross section. Neglecting the gravity and the intermolecular forces, we can calculate the variation δW_{ext} of the work done by the external forces as

$$\delta W_{\text{ext}} = \int_0^L (f_{\text{elec}} + f^{\text{s}}) \delta w \mathrm{d}x \tag{9.54}$$

where f^{s} is the distributed load due to the residual surface tension (Eq. (9.51)); f_{elec} is the distributed electrostatic force. Suppose that the beam is infinitely wide (width $b \gg$ thickness h); then the fringing field can be neglected, and Eq. (9.16) can be reduced to

$$f_{\text{elec}} = -\frac{1}{2} \frac{\varepsilon_0 b V^2}{(g_0 + w)^2} \tag{9.55}$$

Introducing Eqs. (9.52) and (9.54) into the theorem of minimum potential energy given in Eq. (9.7), we obtain the following governing equations:

$$\delta u: \quad N' = 0 \tag{9.56a}$$

$$\delta w: \quad M'' + (Nw')' + f_{\text{elec}} + f^{\text{s}} = 0 \tag{9.56b}$$

With Eq. (9.56a), Eq. (9.56b) can be rewritten as

$$M'' + Nw'' + f_{\text{elec}} + f^{\text{s}} = 0 \tag{9.57}$$

Suppose that the beam material is elastically isotropic with Young's modulus E and Poisson's ratio ν. Then the 1D constitutive equation for an infinitely wide beam becomes

$$\sigma_{xx} = E^* \varepsilon_{xx} \tag{9.58}$$

where the effective elastic modulus E^* is

$$E^* = \frac{E}{1 - \nu^2} \tag{9.59}$$

Introduce Eqs. (9.3), (9.49), and (9.58) into Eq. (9.53a, b), and consider $b \gg h$; we have

$$N(x) = E^* S\left(1 + 2\frac{E^s}{E^*}\frac{1}{h}\right)\left(u' + \frac{1}{2}\left(w'\right)^2 - \frac{1}{2}\left(w_0'\right)^2\right) \tag{9.60a}$$

$$M(x) = -E^* I\left(1 + 6\frac{E^s}{E^*}\frac{1}{h}\right)\left(w'' - w_0''\right) \tag{9.60b}$$

The effective axial stiffness $(ES)_{\text{eff}}$ can be derived from Eq. (9.60a) as

$$(ES)_{\text{eff}} = E^* bh + 2E^s b \tag{9.61}$$

And the effective Young's modulus $(E)_{\text{eff}}$ for bending can be derived from Eq. (9.60b) as

$$(E)_{\text{eff}} = E^*\left(1 + 6\frac{E^s}{E^*}\frac{1}{h}\right) \tag{9.62}$$

It is seen that the surface elasticity (E^s) has the effect of increasing or decreasing $(E)_{\text{eff}}$, depending on the sign of E^s.

Introduce Eqs. (9.51), (9.55), and (9.60b) into Eq. (9.57), replace the axial force by the average value calculated from Eq. (9.60a), and we obtain the following governing equation:

$$E^* I\left(1 + 6\frac{E^s}{E^*}\frac{1}{h}\right)\left(w'''' - w_0''''\right) - \frac{E^* S}{2L}\left(1 + 2\frac{E^s}{E^*}\frac{1}{h}\right)\left(\int_0^L \left((w')^2 - (w_0')^2\right)\mathrm{d}x\right) \cdot w'' - 2\tau^0 b w'' = -\frac{1}{2}\frac{\varepsilon_0 b V^2}{(g_0 + w)^2} \tag{9.63}$$

Rewrite Eq. (9.63) in the non-dimensional form as

$$\left(w'''' - w_0''''\right) - \left(\lambda_s + \alpha^*\left(\int_0^1 \left((w')^2 - (w_0')^2\right)\mathrm{d}x\right)\right)w'' = -\frac{\beta_v^*}{(1+w)^2} \tag{9.64}$$

with the non-dimensional quantities given in Table 9.1, and the non-dimensional boundary conditions given in Eq. (9.29a, b).

9.3.1.3 Two Degrees of Freedom Reduced-Order Model

Equations (9.64) and (9.29a, b) can be solved using the Galerkin decomposition method (see Eq. (9.36)). For the asymmetric deformations, the participation of the second mode is more than that of the fourth and sixth modes (Das and Batra 2009b).

So we decided to focus on the first two modes (i.e., $n=2$ in Eq. (9.36)). The dimensionless initial deflection $\overline{w_0}(\bar{x})$ is assumed to be in the first mode state; then we have

$$\overline{w}(\bar{x}) = q_1\phi_1(\bar{x}) + q_2\phi_2(\bar{x}) \tag{9.65a}$$

$$\overline{w_0}(\bar{x}) = q_0\phi_1(\bar{x}) \tag{9.65b}$$

where q_1 is the dimensionless midpoint deflection (since $\phi_1(0.5) = 1, \phi_2(0.5) = 0$); q_0 $(= r/g_0)$ is the dimensionless initial arch rise, with r being the initial arch rise (deflection at the midpoint). Introduce Eq. (9.65a, b) into Eq. (9.64), multiply the result by ϕ_1 and ϕ_2, respectively, and then integrate over the domain [0, 1]. Further integrate by parts and take into account the orthogonality of ϕ_1 and ϕ_2; we obtain the reduced-order model with two degrees of freedom:

$$\phi_1: \ \alpha^* s_{11}^2 q_1^3 + \left(b_{11} - \alpha^* s_{11}^2 q_0^2 + \lambda_s s_{11}\right) q_1 + \alpha^* s_{11} s_{22} q_1 q_2^2 - b_{11} q_0 = -\beta_v^* I_1^*(q_1, q_2) \tag{9.66a}$$

$$\phi_2: \ \alpha^* s_{22}^2 q_2^3 + \left(b_{22} - \alpha^* s_{11} s_{22} q_0^2 + \lambda_s s_{22}\right) q_2 + \alpha^* s_{11} s_{22} q_1^2 q_2 = -\beta_v^* I_2^*(q_1, q_2) \tag{9.66b}$$

where b_{11}, b_{22}, s_{11}, s_{22}, and f_1 are given in Table 9.3; the integrals I_1^* and I_2^* are given below:

$$I_1^*(q_1, q_2) = \int_0^1 \frac{\phi_1}{\left(1 + q_1\phi_1 + q_2\phi_2\right)^2} \, \mathrm{d}\bar{x} \tag{9.67a}$$

$$I_2^*(q_1, q_2) = \int_0^1 \frac{\phi_2}{\left(1 + q_1\phi_1 + q_2\phi_2\right)^2} \, \mathrm{d}\bar{x} \tag{9.67b}$$

9.3.2 *Results and Discussions*

9.3.2.1 Influence of Initial Arch Rise on Asymmetric Bifurcation Behavior

Introducing $\alpha^* = 600$ and $\lambda_s = 2$ into Eq. (9.66a, b), we plot the obtained equation in Fig. 9.6 at different levels of the dimensionless initial arch rise q_0. The dimensionless residual surface tension λ_s is calculated using the expression in Table 9.1 with the surface parameters $\tau^0 = 0.6056\ \mathrm{N \cdot m^{-1}}$ and $E^s = -10.036\ \mathrm{N \cdot m^{-1}}$ from Miller and Shenoy (2000), and the beam dimensions and bulk material properties $L = 15\ \mu\mathrm{m}$, $b = 400\ \mathrm{nm}$, $h = 200\ \mathrm{nm}$, $E = 185\ \mathrm{GPa}$, and $\nu = 0.28$ from Intaraprasonk and Fan (2011).

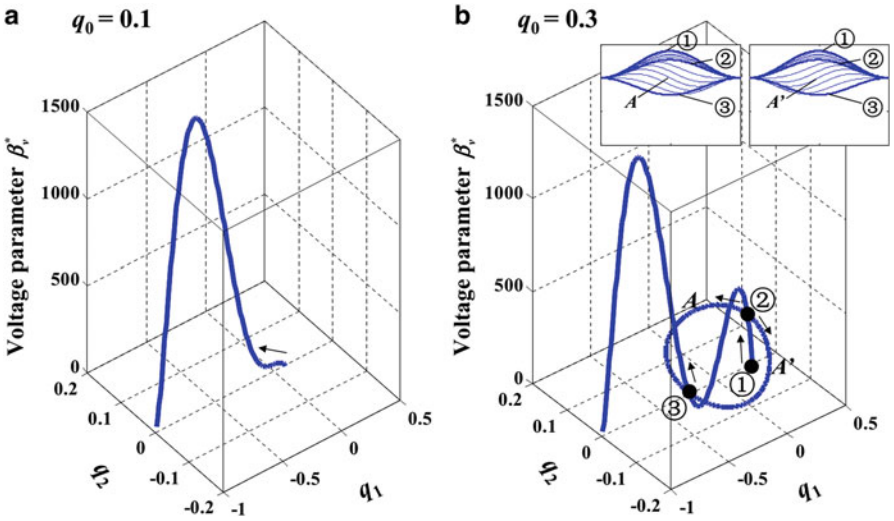

Fig. 9.6 Bifurcation diagram of nanobeam actuated by electrostatic force. ② and ③ are bifurcation points. The *insets* show the evolutions of the deformed beam

It is seen from Fig. 9.6 that when q_0 is small (e.g., 0.1 in Fig. 9.6a), the solution of the asymmetric deformation doesn't exist (i.e., $q_2 \equiv 0$), so the beam always deforms symmetrically. When q_0 is large enough (0.3 in Fig. 9.6b), the solution of the asymmetric deformation exists. With the decrease of the midpoint deflection (q_1 decreases), the beam deforms symmetrically (① → ② in Fig. 9.6b) until reaching the bifurcation point ② where there are two asymmetric deformations given by Eq. (9.66a, b). By following one of the asymmetric deformations, the beam deforms asymmetrically (② → ③) until reaching another bifurcation point ③. After ③, the beam returns to deform symmetrically with the decrease of the midpoint deflection.

9.3.2.2 Surface Effects on Necessary Symmetry-Breaking Criterion

Near the asymmetric bifurcation points (② and ③ in Fig. 9.6b), q_2 is about 0. So we linearize the governing equations (Eq. (9.66a, b)) around $q_2 = 0$ as (Medina et al. 2014a)

$$\phi_1 : \ \alpha^* s_{11}^2 q_1^3 + \left(b_{11} - \alpha^* s_{11}^2 q_0^2 + \lambda_s s_{11}\right) q_1 - b_{11} q_0 = -\beta_v^* I_1^*(q_1, 0) \tag{9.68a}$$

$$\phi_2 : \ \left(b_{22} - \alpha^* s_{11} s_{22} q_0^2 + \lambda_s s_{22} + \alpha^* s_{11} s_{22} q_1^2\right) q_2 = 2\beta_v I_3^*(q_1) q_2 \tag{9.68b}$$

with I_3^* being

$$I_3^*(q_1) = \int_0^1 \frac{\phi_2^2}{(1+q_1\phi_1)^3}\,\mathrm{d}\bar{x} \tag{9.69}$$

To obtain Eq. (9.68a, b), the following relations are used: $\int_0^1 \frac{\phi_1\phi_2}{(1+q_1\phi_1)^3}\,\mathrm{d}\bar{x} = 0$, $\int_0^1 \frac{\phi_2}{(1+q_1\phi_1)^2}\,\mathrm{d}\bar{x} = 0$. For the asymmetric deformations ($q_2 \neq 0$), Eq. (9.68b) can be further reduced to

$$\phi_2:\ b_{22} - \alpha^* s_{11}s_{22}q_0^2 + \lambda_s s_{22} + \alpha^* s_{11}s_{22}q_1^2 = 2\beta_v^* I_3^*(q_1) \tag{9.70}$$

Express β_v^*, respectively, from Eqs. (9.68a) and (9.70), equilibrate these expressions, and we obtain the following equation for the asymmetric bifurcation points:

$$\begin{aligned} &2\alpha^* s_{11}^2 I_3^* q_1^3 + \alpha^* s_{11}s_{22} I_1^*(q_1,0)q_1^2 + 2\left(b_{11} - \alpha^* s_{11}^2 q_0^2 + \lambda_s s_{11}\right)I_3^* q_1 \\ &+ (b_{22} + \lambda_s s_{22})I_1^*(q_1,0) - 2b_{11}I_3^* q_0 - \alpha^* s_{11}s_{22}I_1^*(q_1,0)q_0^2 = 0 \end{aligned} \tag{9.71}$$

Taking $\lambda_s = 2$ in Eq. (9.71), we solve the obtained equation numerically and show the results in Fig. 9.7. It is seen that the dimensionless initial arch rise q_0 should be larger than a critical value $q_0^{\min}$ for the existence of the asymmetric bifurcation points. It is also seen that at $q_0^{\min}$, q_1 is near 0. So as a first approximation of $q_0^{\min}$, we take $q_1 = 0$ in Eq. (9.71) and find

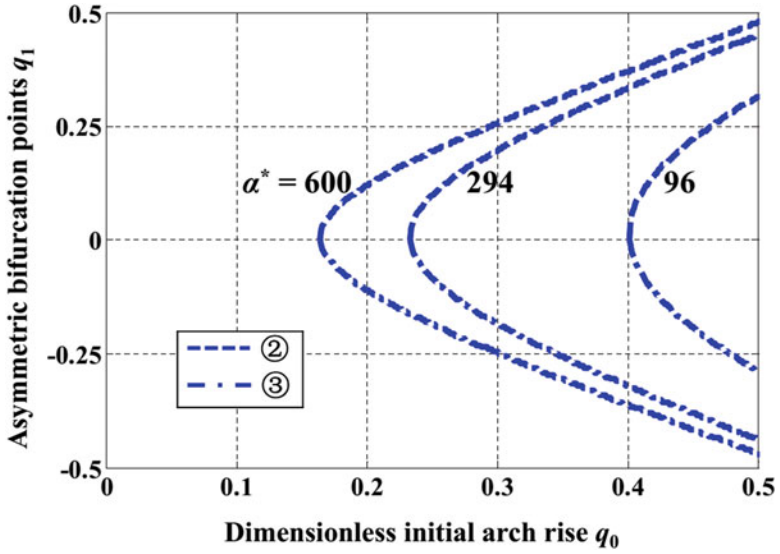

Fig. 9.7 Evolutions of asymmetric bifurcation points (② and ③) with dimensionless initial arch rise at different levels of the stretching parameter α^*

$$q_0^{\min} = \sqrt{\frac{b_{22} + \lambda_s s_{22}}{\alpha^* s_{11} s_{22}} + \left(\frac{b_{11} m_{22}}{\alpha^* s_{11} s_{22} f_1}\right)^2} - \frac{b_{11} m_{22}}{\alpha^* s_{11} s_{22} f_1} \tag{9.72}$$

where b_{11}, b_{22}, s_{11}, s_{22}, f_1, and m_{22} are given in Table 9.3. In Eq. (9.72), replace the non-dimensional quantities (q_0, α^*, λ_s) with the expressions in Table 9.1, and we obtain the necessary symmetry-breaking criterion as follows:

$$\left(\frac{r}{h}\right)_{\min} = \sqrt{\frac{b_{22}}{6 s_{11} s_{22}}\left(1+4\frac{1}{\frac{h}{E^s/E^*}+2}\right)+\frac{4}{s_{11}}\left(\frac{L}{h}\right)^2\left(\frac{1}{\frac{h}{E^s/E^*}+2}\right)\frac{\tau^0}{E^s}+\left(\frac{b_{11} m_{22}}{6 s_{11} s_{22} f_1}\left(1+4\frac{1}{\frac{h}{E^s/E^*}+2}\right)\right)^2\left(\frac{h}{g_0}\right)^2} - \frac{b_{11} m_{22}}{6 s_{11} s_{22} f_1}\left(1+4\frac{1}{\frac{h}{E^s/E^*}+2}\right)\frac{h}{g_0} \tag{9.73}$$

Equation (9.73) is plotted in Fig. 9.8, from which it is found that the positive residual surface tension ($\tau^0/E^s > 0$ in Fig. 9.8a, $\tau^0/E^s < 0$ in Fig. 9.8b) increases $(r/h)_{\min}$, while the negative one decreases it. The positive surface tension (traction)

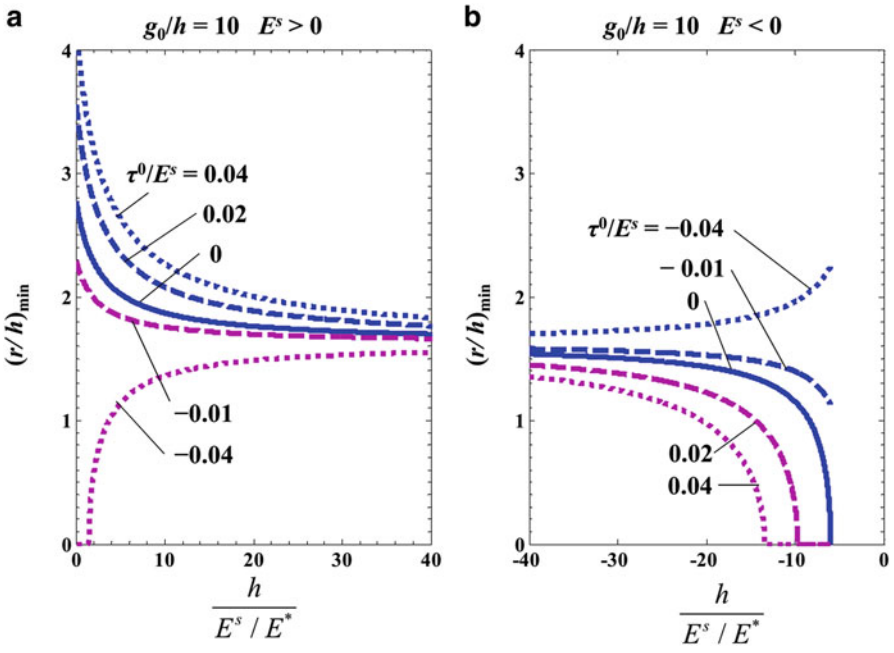

Fig. 9.8 Minimum allowable ratio $(r/h)_{\min}$ between the initial arch rise r and the beam thickness h for the asymmetric bifurcation at different levels of beam thickness h (normalized as $h/(E^s/E^*)$) and residual surface tension τ^0 (normalized as τ^0/E^s). The beam length-to-thickness ratio $L/h = 25$

reduces the arch rise, so larger initial arch rise (larger $(r/h)_{\min}$) is required for the existence of asymmetric bifurcation, and vice versa for the negative surface tension (compression).

It is also found from Fig. 9.8 that the beam size (thickness h, normalized as $h/(E^s/E^*)$) affects $(r/h)_{\min}$. Such size dependency of $(r/h)_{\min}$ can be explained by the influences of the effective Young's modulus $(E)_{\text{eff}}$ and the residual surface tension τ^0. In the case of positive surface Young's modulus E^s (refer to Fig. 9.8a), the effective Young's modulus $(E)_{\text{eff}}$ increases with the decrease of h (see Eq. (9.62)), so the nanobeam becomes stiffer, which will lead to an increase of $(r/h)_{\min}$. On the other hand, since the effective axial stiffness decreases when decreasing h (see Eq. 9.61), the negative surface tension τ^0 will induce more arch rise, so the required initial arch rise ($(r/h)_{\min}$) for asymmetric bifurcation is reduced. When τ^0 is small (i.e., negative residual surface tension is large enough), the influence of τ^0 is dominant, so $(r/h)_{\min}$ appears to decrease when reducing h (see the curve at $\tau^0/E^s = -0.04$ in Fig. 9.8a). When τ^0 is large, $(E)_{\text{eff}}$ is dominant, so $(r/h)_{\min}$ increases when reducing h (see the curve at $\tau^0/E^s = -0.01$). Both positive τ^0 and $(E)_{\text{eff}}$ have the effect of increasing $(r/h)_{\min}$ when reducing h (see the curves at $\tau^0/E^s = 0.02$ and 0.04). The size effect on $(r/h)_{\min}$ in the case of negative surface Young's modulus (refer to Fig. 9.8b) can be explained in the similar way.

It is noted that in Fig. 9.8, $(r/h)_{\min}$ is plotted in the range (i.e., $h/(E^s/E^*) \leq -6$ and ≥ 0) where the effective Young's modulus (Eq. (9.62)) is nonnegative. Moreover, if $(r/h)_{\min}$ is negative or an imaginary number, the asymmetric bifurcation may take place in an initially straight beam. In this case, $(r/h)_{\min}$ is taken to be 0 in the figure.

9.4 Conclusions

In this chapter, we examine the instability behaviors of the electrostatically actuated micro/nanobeam. The governing equations are developed with the aid of Euler-Bernoulli beam theory and are solved using Galerkin decomposition method. The symmetric snap-through of the microbeam is studied first. The fringing field effect, the beam size effect, and the intermolecular forces are accounted for in the model formulation. Our results, which are based on the first mode approximation, reveal that the size of the microbeam plays a major role in dictating the existence of the snap-through behavior of the beam, while the fringing field and intermolecular forces play an insignificant role. In the second part, the asymmetric bifurcation of the nanobeam is investigated. The surface effects at nanoscale are accounted for in the beam model. Our results, which are based on the reduced-order model of two degrees of freedom, show that the beam size and the residual surface tension play significant roles in the symmetry-breaking criterion.

Acknowledgements The financial support provided by the Natural Sciences and Engineering Research Council of Canada, the Discovery Accelerator Supplements, and the Qatar National Research Foundation under the National Priority Research Program is gratefully acknowledged.

References

Asthana, A., Momeni, K., Prasad, A., Yap, Y.K., Yassar, R.S.: In situ observation of size-scale effects on the mechanical properties of ZnO nanowires. Nanotechnology **22**, 265712 (2011)

Ballestra, A., Brusa, E., De Pasquale, G., Munteanu, M.G., Soma, A.: FEM modelling and experimental characterization of microbeams in presence of residual stress. Analog Integr. Circ. Sig. Process **63**, 477–488 (2010)

Batra, R.C., Porfiri, M., Spinello, D.: Electromechanical model of electrically actuated narrow microbeams. J. Microelectromech. Syst. **15**, 1175–1189 (2006)

Batra, R.C., Porfiri, M., Spinello, D.: Review of modeling electrostatically actuated microelectromechanical systems. Smart Mater. Struct. **16**, R23–R31 (2007)

Belardinelli, P., Lenci, S., Brocchini, M.: Modeling and analysis of an electrically actuated microbeam based on nonclassical beam theory. J. Comput. Nonlin. Dyn. **9**, 031016 (2014)

Carr, D.W., Evoy, S., Sekaric, L., Craighead, H.G., Parpia, J.M.: Measurement of mechanical resonance and losses in nanometer scale silicon wires. Appl. Phys. Lett. **75**, 920–922 (1999)

Casimir, H.B.G.: On the attraction between two perfectly conducting plates. Proc. Kon. Ned. Akad. Wetensch. Ser. B **51**, 793–795 (1948)

Cammarata, R.C.: Surface and interface stress effects in thin films. Prog. Surf. Sci. **46**, 1–38 (1994)

Charlot, B., Sun, W., Yamashita, K., Fujita, H., Toshiyoshi, H.: Bistable nanowire for micromechanical memory. J. Micromech. Microeng. **18**, 045005 (2008)

Chen, T., Chiu, M.-S., Weng, C.-N.: Derivation of the generalized Young-Laplace equation of curved interfaces in nanoscaled solids. J. Appl. Phys. **100**, 074308 (2006)

Cuenot, S., Frétigny, C., Demoustier-Champagne, S., Nysten, B.: Surface tension effect on the mechanical properties of nanomaterials measured by atomic force microscopy. Phys. Rev. B **69**, 165410 (2004)

Das, K., Batra, R.C.: Pull-in and snap-through instabilities in transient deformations of microelectromechanical systems. J. Micromech. Microeng. **19**, 035008 (2009a)

Das, K., Batra, R.C.: Symmetry breaking, snap-through and pull-in instabilities under dynamic loading of microelectromechanical shallow arches. Smart Mater. Struct. **18**, 115008 (2009b)

Dequesnes, M., Rotkin, S.V., Aluru, N.R.: Calculation of pull-in voltages for carbon-nanotube-based nanoelectromechanical switches. Nanotechnology **13**, 120–131 (2002)

Dingreville, R., Qu, J., Cherkaoui, M.: Surface free energy and its effect on the elastic behavior of nano-sized particles, wires and films. J. Mech. Phys. Solids **53**, 1827–1854 (2005)

Eringen, A.C.: On differential equations of nonlocal elasticity and solutions of screw dislocation and surface waves. J. Appl. Phys. **54**, 4703–4710 (1983)

Farokhi, H., Ghayesh, M.H., Amabili, M.: Nonlinear dynamics of a geometrically imperfect microbeam based on the modified couple stress theory. Int. J. Eng. Sci. **68**, 11–23 (2013)

Fleck, N.A., Hutchinson, J.W.: A reformulation of strain gradient plasticity. J. Mech. Phys. Solids **49**, 2245–2271 (2001)

Fleck, N.A., Muller, G.M., Ashby, M.F., Hutchinson, J.W.: Strain gradient plasticity: theory and experiments. Acta Metall. Mater. **42**, 475–487 (1994)

Fu, Y., Zhang, J.: Size-dependent pull-in phenomena in electrically actuated nanobeams incorporating surface energies. Appl. Math. Model. **35**, 941–951 (2011)

Fu, Y., Zhang, J., Jiang, Y.: Influences of the surface energies on the nonlinear static and dynamic behaviors of nanobeams. Phys. E. **42**, 2268–2273 (2010)

Goll, C., Bacher, W., Büstgens, B., Maas, D., Menz, W., Schomburg, W.K.: Microvalves with bistable buckled polymer diaphragms. J. Micromech. Microeng. **6**, 77–79 (1996)
Gurtin, M.E., Murdoch, A.I.: A continuum theory of elastic material surfaces. Arch. Ration. Mech. Anal. **57**, 291–323 (1975)
Gurtin, M.E., Murdoch, A.I.: Surface stress in solids. Int. J. Solids Struct. **14**, 431–440 (1978)
Gurtin, M.E., Weissmüller, J., Larché, F.: A general theory of curved deformable interfaces in solids at equilibrium. Philos. Mag. A **78**, 1093–1109 (1998)
He, J., Lilley, C.M.: Surface effect on the elastic behavior of static bending nanowires. Nano Lett. **8**, 1798–1802 (2008)
Hu, Y.C., Chang, C.M., Huang, S.C.: Some design considerations on the electrostatically actuated microstructures. Sens. Actuators A Phys. **112**, 155–161 (2004)
Intaraprasonk, V., Fan, S.: Nonvolatile bistable all-optical switch from mechanical buckling. Appl. Phys. Lett. **98**, 241104 (2011)
Israelachvili, J.N.: Intermolecular and Surface Forces, 3rd edn. Academic, Waltham, MA (2011)
Jia, X.L., Yang, J., Kitipornchai, S.: Pull-in instability of geometrically nonlinear micro-switches under electrostatic and Casimir forces. Acta Mech. **218**, 161–174 (2011)
Jing, G.Y., Duan, H.L., Sun, X.M., Zhang, Z.S., Xu, J., Li, Y.D., Wang, J.X., Yu, D.P.: Surface effects on elastic properties of silver nanowires: contact atomic-force microscopy. Phys. Rev. B **73**, 235409 (2006)
Ke, C.-H., Pugno, N., Peng, B., Espinosa, H.D.: Experiments and modeling of carbon nanotube-based NEMS devices. J. Mech. Phys. Solids **53**, 1314–1333 (2005)
Kinaret, J.M., Nord, T., Viefers, S.: A carbon-nanotube-based nanorelay. Appl. Phys. Lett. **82**, 1287–1289 (2003)
Kong, S.: Size effect on pull-in behavior of electrostatically actuated microbeams based on a modified couple stress theory. Appl. Math. Model. **37**, 7481–7488 (2013)
Krylov, S., Ilic, B.R., Schreiber, D., Seretensky, S., Craighead, H.: The pull-in behavior of electrostatically actuated bistable microstructures. J. Micromech. Microeng. **18**, 055026 (2008)
Lam, D.C.C., Yang, F., Chong, A.C.M., Wang, J., Tong, P.: Experiments and theory in strain gradient elasticity. J. Mech. Phys. Solids **51**, 1477–1508 (2003)
Li, Y., Meguid, S.A., Fu, Y., Xu, D.: Unified nonlinear quasistatic and dynamic analysis of RF-MEMS switches. Acta Mech. **224**, 1741–1755 (2013)
Li, X., Ono, T., Wang, Y., Esashi, M.: Ultrathin single-crystalline-silicon cantilever resonators: fabrication technology and significant specimen size effect on Young's modulus. Appl. Phys. Lett. **83**, 3081–3083 (2003)
Lifshitz, E.M.: The theory of molecular attractive forces between solids. Sov. Phys. JETP **2**, 73–83 (1956)
Ma, Q., Clarke, D.R.: Size dependent hardness of silver single crystals. J. Mater. Res. **10**, 853–863 (1995)
Ma, H.M., Gao, X.-L., Reddy, J.N.: A microstructure-dependent Timoshenko beam model based on a modified couple stress theory. J. Mech. Phys. Solids **56**, 3379–3391 (2008)
McFarland, A.W., Colton, J.S.: Role of material microstructure in plate stiffness with relevance to microcantilever sensors. J. Micromech. Microeng. **15**, 1060–1067 (2005)
Medina, L., Gilat, R., Krylov, S.: Symmetry breaking in an initially curved micro beam loaded by a distributed electrostatic force. Int. J. Solids Struct. **49**, 1864–1876 (2012)
Medina, L., Gilat, R., Krylov, S.: Symmetry breaking in an initially curved pre-stressed micro beam loaded by a distributed electrostatic force. Int. J. Solids Struct. **51**, 2047–2061 (2014a)
Medina, L., Gilat, R., Krylov, S.: Experimental investigation of the snap-through buckling of electrostatically actuated initially curved pre-stressed micro beams. Sens. Actuators A **220**, 323–332 (2014b)
Miller, R.E., Shenoy, V.B.: Size-dependent elastic properties of nanosized structural elements. Nanotechnology **11**, 139–147 (2000)
Mindlin, R.D.: Second gradient of strain and surface tension in linear elasticity. Int. J. Solids Struct. **1**, 417–438 (1965)

Moghimi Zand, M.: The dynamic pull-in instability and snap-through behavior of initially curved microbeams. Mech. Adv. Mater. Struct. **19**, 485–491 (2012)
Pane, I.Z., Asano, T.: Investigation on bistability and fabrication of bistable prestressed curved beam. Jpn. J. Appl. Phys. **47**, 5291–5296 (2008)
Park, S., Hah, D.: Pre-shaped buckled-beam actuators: theory and experiments. Sens. Actuators A Phys. **148**, 186–192 (2008)
Patricio, P., Adda-Bedia, M., Ben Amar, M.: An elastic problem: instabilities of an elastic arch. Physica D **124**, 285–295 (1998)
Pippard, A.B.: The elastic arch and its modes of instability. Eur. J. Phys. **11**, 359–365 (1990)
Poncharal, P., Wang, Z.L., Ugarte, D., de Heer, W.A.: Electrostatic deflections and electromechanical resonances of carbon nanotubes. Science **283**, 1513–1516 (1999)
Reddy, J.N.: Microstructure-dependent couple stress theories of functionally graded beams. J. Mech. Phys. Solids **59**, 2382–2399 (2011)
Rokni, H., Seethaler, R.J., Milani, A.S., Hosseini-Hashemi, S., Li, X.-F.: Analytical closed-form solutions for size-dependent static pull-in behavior in electrostatic micro-actuators via Fredholm integral equation. Sens. Actuators A Phys. **190**, 32–43 (2013)
Roodenburg, D., Spronck, J.W., van der Zant, H.S.J., Venstra, W.J.: Buckling beam micromechanical memory with on-chip readout. Appl. Phys. Lett. **94**, 183501 (2009)
Ruzziconi, L., Bataineh, A.M., Younis, M.I., Cui, W., Lenci, S.: Nonlinear dynamics of an electrically actuated imperfect microbeam resonator: experimental investigation and reduced-order modeling. J. Micromech. Microeng. **23**, 075012 (2013)
Sadeghian, H., Goosen, H., Bossche, A., Thijsse, B., van Keulen, F.: On the size-dependent elasticity of silicon nanocantilevers: impact of defects. J. Phys. D. Appl. Phys. **44**, 072001 (2011)
Sadeghian, H., Yang, C.K., Goosen, J.F.L., van der Drift, E., Bossche, A., French, P.J., van Keulen, F.: Characterizing size-dependent effective elastic modulus of silicon nanocantilevers using electrostatic pull-in instability. Appl. Phys. Lett. **94**, 221903 (2009)
Salvetat, J.-P., Briggs, G.A.D., Bonard, J.-M., Bacsa, R.R., Kulik, A.J., Stöckli, T., Burnham, N. A., Forro, L.: Elastic and shear moduli of single-walled carbon nanotube ropes. Phys. Rev. Lett. **82**, 944–947 (1999)
Shin, M.K., Kim, S.I., Kim, S.J., Kim, S.-K., Lee, H., Spinks, G.M.: Size-dependent elastic modulus of single electroactive polymer nanofibers. Appl. Phys. Lett. **89**, 231929 (2006)
Tilmans, H.A.C., Legtenberg, R.: Electrostatically driven vacuum-encapsulated polysilicon resonators: part II. theory and performance. Sens. Actuators A Phys. **45**, 67–84 (1994)
Toupin, R.A.: Elastic materials with couple-stresses. Arch. Rational Mech. Anal. **1**, 385–414 (1962)
van der Meijs, N.P., Fokkema, J.T.: VLSI circuit reconstruction from mask topology. Integr. VLSI J. **2**, 85–119 (1984)
Verbridge, S.S., Shapiro, D.F., Craighead, H.G., Parpia, J.M.: Macroscopic tuning of nanomechanics: substrate bending for reversible control of frequency and quality factor of nanostring resonators. Nano Lett. **7**, 1728–1735 (2007)
Wang, G.-F., Feng, X.-Q.: Effects of surface elasticity and residual surface tension on the natural frequency of microbeams. Appl. Phys. Lett. **90**, 231904 (2007)
Wang, G.-F., Feng, X.-Q.: Surface effects on buckling of nanowires under uniaxial compression. Appl. Phys. Lett. **94**, 141913 (2009)
Xu, F., Qin, Q., Mishra, A., Gu, Y., Zhu, Y.: Mechanical properties of ZnO nanowires under different loading modes. Nano Res. **3**, 271–280 (2010)
Yang, F., Chong, A.C.M., Lam, D.C.C., Tong, P.: Couple stress based strain gradient theory for elasticity. Int. J. Solids Struct. **39**, 2731–2743 (2002)
Zhang, Y., Wang, Y., Li, Z., Huang, Y., Li, D.: Snap-through and pull-in instabilities of an arch-shaped beam under an electrostatic loading. J. Microelectromech. Syst. **16**, 684–693 (2007)
Zhu, H.X.: Size-dependent elastic properties of micro- and nano-honeycombs. J. Mech. Phys. Solids **58**, 696–709 (2010)

Index

S.A. Meguid (ed.), *Advances in Nanocomposites*,
DOI 10.1007/978-3-319-31662-8